A COMPARATIVE STUDY OF THE BIDIRECTIONAL REFLECTANCE DISTRIBUTION FUNCTION OF SEVERAL SURFACES AS A MID-WAVE INFRARED DIFFUSE REFLECTANCE STANDARD

THESIS

Bradley Balling, Captain, USAF

AFIT/GE/ENP/09-M01

DEPARTMENT OF THE AIR FORCE
AIR UNIVERSITY

AIR FORCE INSTITUTE OF TECHNOLOGY

Wright-Patterson Air Force Base, Ohio

A COMPARATIVE STUDY OF THE

BIDIRECTIONAL REFLECTANCE DISTRIBUTION FUNCTION

OF SEVERAL SURFACES AS A MID-WAVE INFRARED

DIFFUSE REFLECTANCE STANDARD

THESIS

Presented to the Faculty

Department of Engineering Physics

Graduate School of Engineering and Management

Air Force Institute of Technology

Air University

Air Education and Training Command

in Partial Fulfillment of the Requirements for the

Degree of Master of Science in Electrical Engineering
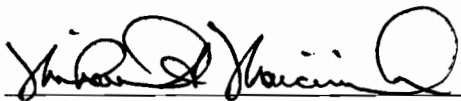
Bradley Balling, MBA, BSEE

Captain, USAF

March 2009

A COMPARATIVE STUDY OF THE

BIDIRECTIONAL REFLECTANCE DISTRIBUTION FUNCTION

OF SEVERAL SURFACES AS A MID-WAVE INFRARED

DIFFUSE REFLECTANCE STANDARD

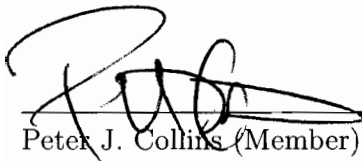Bradley Balling, MBA, BSEE
Captain, USAF

Approved:

_____
Micheal A. Marciniak (Chairman)

20 Nov 09
_____
Date

_____
Peter J. Collins (Member)

18 MAR 2009
_____
Date

_____
Michael R. Hawks (Member)

18 MAR 2009
_____
Date

AFIT/GE/ENP/09-M01

Abstract

The Bi-Directional Reflectance Distribution Function (BRDF) has a well defined and well studied diffuse measurement standard in the ultraviolet (UV), visible, and near infrared (NIR), Spectralon®. It is predictable, stable, repeatable, and has low surface variation because it is a bulk scatterer. In the mid-wave IR (MWIR) and long-wave IR (LWIR), there is not such a well-defined standard. There are well-defined directional hemispherical reflectance (DHR) standards, but the process of integrating BRDF measurements into DHR for the purpose of calibration is problematic, at best. Direct BRDF measurement standards are needed. This study systematically investigates the BRDF and its variation for eight potential MWIR diffuse BRDF standards. The currently recognized reflectance standard in the MWIR, Infragold®, is compared against two alternative gold electroplated arc-sprayed aluminum samples, a silver-painted arc-sprayed aluminum sample, a black-paint sample, a novel laser beam diffuser that has been gold coated, and Spectralon®which does not have published BRDF information in the MWIR. Diffuseness is compared by fitting the data to BRDF models, and repeatability is measured by using the standard deviation and percent difference from the mean calculated from multiple BRDF measurements across the surface of the samples. Although Spectralon®has been dismissed as a reflectance standard in the MWIR due to its spectral dependence, this document shows comparatively that it is an excellent candidate for a diffuse MWIR BRDF standard regardless of its reflectance.

Acknowledgements

First and foremost, I would like to thank my thesis advisor Dr. Michael Marciniak for his guidance, help, and advice in this effort. I would also like to thank Dr. Leonard Hanssen, Dr. Thomas Germer, and everyone else at NIST I worked with. They have provided much advice and experimental samples to measure. I would also like to thank the Air Force Research Laboratories Optical Measurement Facility for their support and the measurements they have provided.

<div align="right">Bradley Balling</div>

Table of Contents

List of Figures

List of Tables

List of Symbols

List of Abbreviations

A COMPARATIVE STUDY OF THE BIDIRECTIONAL REFLECTANCE DISTRIBUTION FUNCTION OF SEVERAL SURFACES AS A MID-WAVE INFRARED DIFFUSE REFLECTANCE STANDARD

I. Introduction

This thesis is primarily concerned with investigation and proposition of an Infrared (IR) Bidirectional Reflectance Distribution Function (BRDF) standard. This is because at the writing of this document, an IR *BRDF* standard does not exist, although an IR *reflectance* standard does. This makes the validation of IR BRDF measurements mathematically correct, at best, but problematic in practice. Furthermore, even the current BRDF standard in the visible spectrum, Spectralon®, is not that well defined as a BRDF standard, although it has been thoroughly researched. It is most completely defined as a spectral Directional Hemispheric Reflectance (DHR) standard, and the current IR 'standards' are only defined this way.

1.1   Importance of the BRDF

There is a long list of reasons why the BRDF is important. If common speech is used, it describes how the light rays reflect when they are incident upon a surface. One of the main uses of the BRDF or a model of it is in scene rendering and simulation. There are really three parts to this problem, the physical space and its properties, the light sources, and the observer's view. If the observer's view is the unknown, this view can be generated with knowledge of the physical space, its properties, specifically the BRDF, and the light sources. This applies to computer graphics industry and

military engagement simulations. Figure 1 shows an example of a scene generated using IR BRDFs.

Another very important usage of the BRDF is in the measurement of surface properties, specifically surface roughness. This mathematical relationship between surface roughness and the BRDF is established in Appendix B. These BRDF measurements are used, 'as a nondestructive probe to measure surface quality, optical performance, smoothness, appearance, defects, and contamination on a wide variety of materials'[6].

1.2   Motivation for an IR BRDF Standard

BRDF models fitted to BRDF measurements are used to generate engagement scenarios from which an asset's survivability is assessed, but there is an obvious limitation in that this assessment can be no more accurate than the BRDF models and data used to create it. In contrast to the civilian computer graphics industry, the accuracy of these simulations can be a matter of life and death for military personnel who may be faced with an IR threat. Calibration is required for accurate IR BRDF measurements, and the process of calibration requires some type of IR BRDF standard. Thus, the establishing the motivation for this study. IR reflectance and BRDF standards also help to ensure accurate measurements in the field, which ensure the properties of assets under test are not degraded and perform as required.

Essentially, the same sample should give the same BRDF independent of the measurement techniques, and equipment used. Unfortunately, this is often not the case. The surface structure and materials that determine the BRDF are on such a small scale that a precise *a priori* mathematical solution for a diffuse sample has not been achieved. Therefore, only consistent and comparative measurements can be used in order to evaluate and validate a DHR or BRDF measurement system; this is
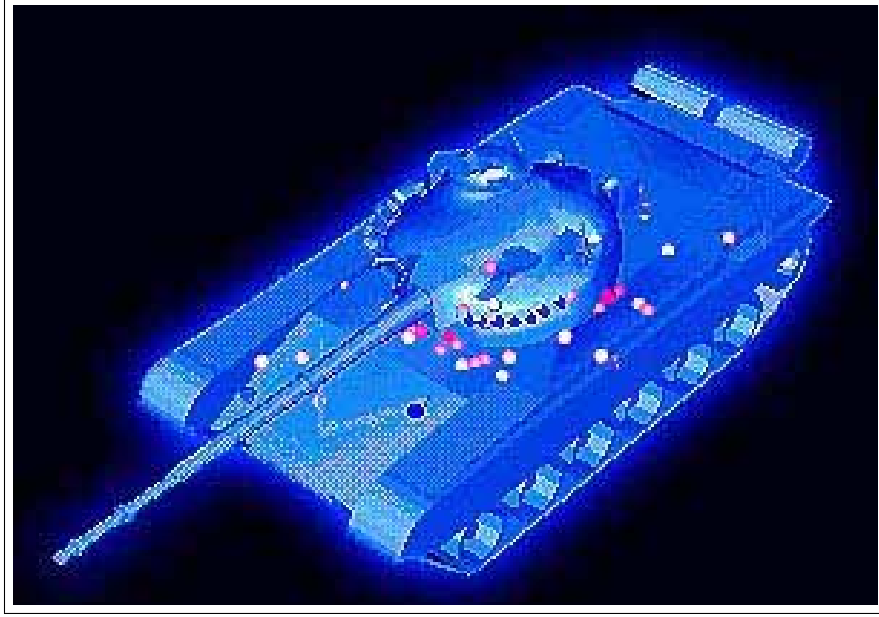
Figure 1. An example of an IR scene generated using a BRDF[3].

done using a standard. At the writing of this document, an IR BRDF standard does not exist, and IR comparisons of samples between laboratories are scarce. There are two examples of a laboratory comparison of standards in the IR, 'Results of a NIST-led Inter-laboratory Comparison of Infrared Reflectance', which has only evaluated the spectral reflectance at near normal incidence[30] and 'BRDF Round Robin Test of ATSM E1392'[40] which does not contain a very good description of its diffuse standards. This document is meant to address this issue.

1.3   Organization

This thesis is organized in such a way as to tell a logical story of the development of this effort in progressive steps until all the tools and requirements necessary to achieved the objective have been developed. These tools are then used to evaluate potential IR BRDF standard samples, which are the ultimate objective of this study. As with any pursuit, this study is motivated by a problem. This problem and

motivation has just been established in Sections 1.1 and 1.2.

Next, an understanding of the the BRDF, its development, and BRDF models is required to understand what exactly it is and what it is not. This is presented in Chapter II. A review of the radiometry required to understand the BRDF is presented in Appendix A. The mathematics for describing optical scatter using electromagnetic methods, i.e. a truly physical BRDF model, is presented in Appendix B.

A description of the methods to obtain BRDF measurements is required as the logical next step. Chapter III links the mathematical development in Chap II to the measurement form of the BRDF because they are different conceptually. It also gives a description of the instrument used to obtain the measurements, the Air Force Institute of Technology (AFIT)'s recently acquired Schmidt Measurement Services (SMS) Complete Angle Scatter Instrument (CASI®). Non-standard procedures for operation are also listed in this chapter.

A calibration of the CASI® 's measurements and the techniques used to accomplish this are demonstrated in Chapter IV. This chapter investigates the current visible standard Spectralon®to validate these techniques, and it is also used as a reference for what an IR BRDF standard should look like.

In similar fashion, Chapter V calibrates and verifies measurements in the IR at $\lambda = 3.39 \mu m$ using three well defined samples. The BRDF measurement sets for each of these samples is presented to describe the samples behavior. These samples have precisely measured DHR values and are then used to calibrate the AFIT BRDF measurements in the IR. Additional independent BRDF measurements are then used to validate the calibration. These are the measurements presented in this study.

Finally, Chapter VI first investigates current IR reflectance standards and what BRDF information on them is available. It next presents the additional samples for comparison. Finally, it presents the BRDF characteristics for each of these

samples and analyzes all the samples in the IR to determine which sample is the best candidate for an IR BRDF standard. The organization of this information in bullet format is listed here.

- Chapter I: The absence of an IR BRDF standard creates an obvious problem for precise measurement.

- Chapter II: An overview of BRDF development, definition, and current models.

- Chapter III: An overview of Measurement Methods, Procedures, and Equipment used in this effort.

- Chapter IV: Definition of an ideal BRDF standard, the BRDF to DHR transformation, fitting techniques, and the verification of techniques by application to the visible BRDF standard.

- Chapter V: IR calibration by measurement of certified DHR samples, their presentation, and calibration verification using independent IR BRDF measurements.

- Chapter VI: Investigation and analysis of other samples for possible IR standards.

- Chapter VII: Conclusions and future research.

- Appendix A: A radiometry review.

- Appendix B: An overview of deterministic BRDF models.

II. A Physical and Mathematical Understanding of the BRDF

This chapter introduces the definition and mathematical development of the BRDF, including many of the models used to represent various types of samples. A progression of the models is described for completeness and in the sense that some of these models are used to describe the 'diffuseness' of the samples later in Chapter VI. This chapter also presents a wide variety of BRDF models as a courtesy to the reader. It must also be noted that the BRDF is only one half of the Bidirectional Scatter Distribution Function (BSDF). The other half, which includes transmission scatter, is the Bidirectional Transmission Distribution Function (BTDF).

> ! It may be useful to read Appendix A if unfamiliar with radiometry, or quickly examine it for the symbology used in this document before reading this chapter.

2.1 BRDF Development

In this section, the BRDF will first be briefly be introduced. Then, a logical progression will be followed beginning with the simpler concept of total reflectance. It will then be extended to directional reflectance, and finally to the BRDF. A key distinction must be made here between reflectance and reflectivity to avoid confusion. Reflectance is a ratio of the total flux (energy) reflected off of a surface divided by the the flux (energy) incident on it, where as reflectivity denotes a measure of *energy density* reflected off of a surface. The BRDF is really reflectance per unit steradian at a specific location, and hence, a reflectance distribution. It is differential because it describes the reflectivity at this infinitely small point only. Furthermore,

a distribution describes the variation of a density. Thus, the BRDF could also be called the Bidirectional Reflectivity Function if one was so inclined. This is important because the BRDF is a measure of *reflectivity* and *not reflectance.*

The BRDF was initially defined by Nicodemus[48] in 1977, but it has limitations in that form, such as the assumption of an isotropic BRDF. The generally accepted full definition is the ratio of the *radiance* reflected from a surface into a unit solid angle in a *given direction* to the incident *irradiance* from a *given direction.*

$$BRDF(\theta_i, \phi_i, \theta_r, \phi_r, \lambda) = \frac{dL_r(\theta_i, \phi_i, \theta_r, \phi_r, \lambda)}{dE_i(\theta_i, \phi_i, \lambda)} \left[\frac{1}{sr} \right], \tag{1}$$

or alternatively,

$$f(\theta_i, \phi_i, \theta_r, \phi_r, \lambda) = \frac{dL_r(\theta_i, \phi_i, \theta_r, \phi_r, \lambda)}{dE_i(\theta_i, \phi_i, \lambda)} \left[\frac{1}{sr} \right]. \tag{2}$$

! Recall that as used here, the BRDF, f, is a differential reflectivity, and ρ is a reflectance. They are not equivalent.

Figure 2 shows the geometry and definitions used through this study for the measurements made and the models. It is drawn on a Cartesian coordinate system, with the incident light vector $\mathbf{L}$, the reflected light vector $\mathbf{R}$, the sample area dA, and the sample normal $\mathbf{N}$. The BRDF is typically notated such that it is a function of incident zenith, θ_i, incident azimuth, ϕ_i, reflected zenith θ_r, and reflected azimuth ϕ_r. This is shown in Figure 2.

The BRDF is not only a function of the variables shown in Figure 2, but it can also be a function of wavelength, λ, polarization, and often the position on and orientation of the sample. BRDFs can even be time varying[55]! The inclusion of polarization is typically done by representing the BRDF as a Mueller matrix[8]. Many
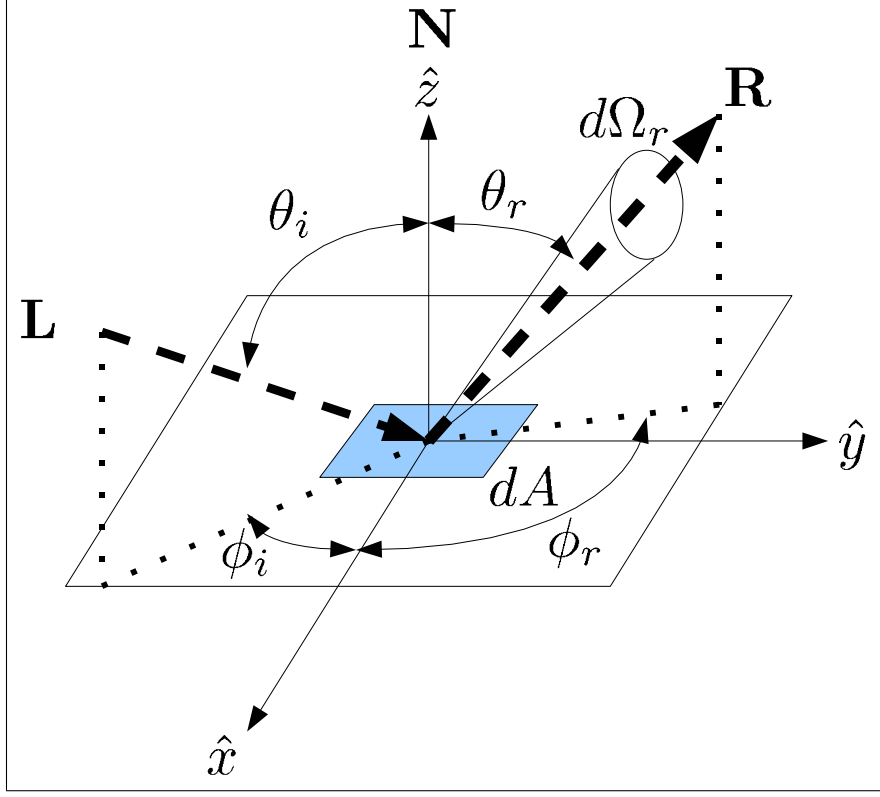
Figure 2. The definition of the coordinate system for the BRDF with incoming light vector, L, and out going light vector, R, shown.

representations of the BRDF are simplifications and this should be kept in mind. An excellent way to quickly understand the BRDF intuitively is to see a three-dimensional spherical plot of the function or data. This is presented in Figure 3.

2.1.1   Reflectance and the BRDF.

This section will radiometrically link the simpler concept of reflectance and to the more complex BRDF starting with the definition of reflectance. Also, the distinction between reflectance and the BRDF is an important concept in phenomenological models discussed later. Reflectance as defined in Appendix A is

$$\rho = \frac{\Phi_{reflected}}{\Phi_{incident}}, \tag{3}$$
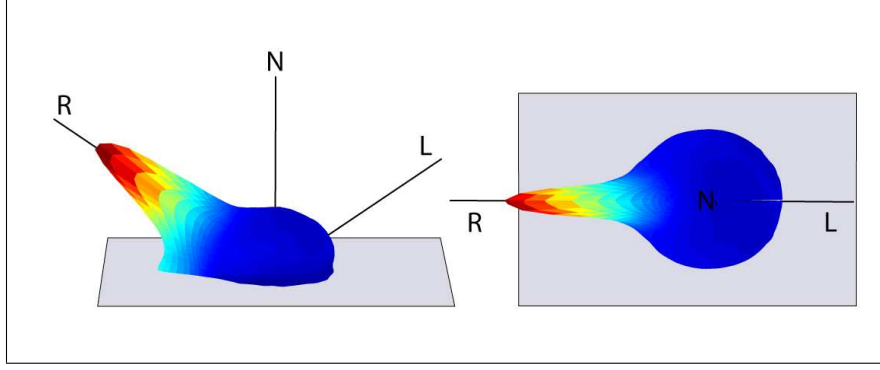
Figure 3. An example of three-dimensional spherical BRDF plot where the shape and the color indicates the magnitude of the BRDF. The vector L is the incoming light vector, N is the surface normal, and R is the mirror reflection vector[47].

where Φ is flux. This can be extended because the area of the the radiometric reflected 'source', A_s, and the area of the radiometric incident 'detector', A_d, are the same piece of real estate when considering reflectance. This leads to

$$\rho = \frac{\Phi_{reflected}/A_s}{\Phi_{incident}/A_d},\tag{4}$$

which using the radiometric definitions in Appendix A, reduces to

$$\rho = \frac{M_r}{E_i},\tag{5}$$

where M_r is reflected exitance and E_i is incident irradiance.

In the context of the BRDF, the subscript i is typically used to denote an incident quantity and r is used to denote a reflected quantity. This makes this development easier to follow and more concise. This formulation is also important because it will be used throughout this document.

One more relationship is needed in order to tie reflectance to the BRDF. The exitance over the entire hemisphere is related to the radiance, L, of a Lambertian

source by,

$$M = \pi L. \tag{6}$$

This relationship is valid because the reflector has no directional dependence in this case. This is called a perfectly diffuse reflector, or a Lambertian reflector. After inserting this relationship into Equation (5), the result is

$$\rho = \frac{\pi L_r}{E_i}. \tag{7}$$

After rearranging terms, the diffuse BRDF is

$$f = \frac{L_r}{E_i} = \frac{\rho}{\pi}. \tag{8}$$

Thus, a perfectly diffuse BRDF is simply the reflectance divided by π. If we have a perfectly diffuse reflector and $\rho = 1$, the BRDF is

$$f = \frac{1}{\pi}. \tag{9}$$

Unfortunately in practice, the reflectance, ρ, is never independent of the incidence angle of the light, but it can be a decent approximation for a diffuse only term in a BRDF. This relationship will be used in Chapter III in the definition of an ideal BRDF standard.

2.1.2 Directional Reflectance and the BRDF.

Directional reflectance , also known as the Directional Hemispheric Reflectance, is the ratio of the total energy reflected from a surface into the subtending hemisphere to that incident on the surface *from a given direction*[43]. This is no different than the reflectance except that the direction of the incident light is considered. Thus,

the directional reflectance as a BRDF is simply a sphere when plotted in spherical coordinates that changes 'size' based upon the incident light direction. The rigorous definition of this is shown in Equation (10). Now ρ can be represented as $\rho(\theta_i, \theta_i)$ resulting in,

$$
\begin{aligned}
\rho(\theta_i, \theta_i) &= \frac{\Phi_r}{\Phi_i} \\
&= \frac{\int \int L_r \cos\theta_r d\Omega_r dA_s}{\int \int L_i \cos\theta_i d\Omega_i dA_d} \\
&= \frac{\int_{A_s} \int_0^{2\pi} \int_0^{\pi/2} L_r \cos\theta_r \sin\theta_r d\theta_r d\phi_r dA_s}{\int_{A_d} \int_{\phi_i} \int_{\theta_i} L_i \cos\theta_i \sin\theta_i d\theta_i d\phi_i dA_d} \\
&\approx \frac{\int_0^{2\pi} \int_0^{\pi/2} L_r \cos\theta_r \sin\theta_r d\theta_r d\phi_r}{L_i \cos\theta_i \sin\theta_i \Delta\theta_i \Delta\phi_i}
\end{aligned}
\tag{10}
$$

where the approximation is used because the incident beam is assumed to have a uniform amplitude across the beam, and sufficiently narrow to approximate the integration with a product. This also allows the integration over the detector and source areas to cancel because they are the same area and the beam is considered to be uniform.

If this derivation is then applied to the BRDF, we can put the directional reflectance inside the BRDF itself. The definition of the BRDF is

$$
L_r(\theta_i, \phi_i, \theta_r, \phi_r) = f(\theta_i, \phi_i, \theta_r, \phi_r) E_i(\theta_i, \phi_i).
\tag{11}
$$

Reflectance, incident flux, and reflected flux are defined as

$$
\begin{aligned}
\rho(\theta_i, \phi_i) &= \frac{\Phi_r}{\Phi_i} \\
\Phi_r &= \int \int f(\theta_i, \phi_i, \theta_r, \phi_r) E_i(\theta_i, \phi_i) \cos\theta_r dA_i d\Omega_r \\
\Phi_i &= \int E_i(\theta_i, \phi_i) dA_i.
\end{aligned}
\tag{12}
$$

11

If these definitions are combined, the result is the directional reflectance as a part of the BRDF. The assumptions here are the same as those used in the derivation of the directional reflectance. The assumptions are that the reflector is Lambertian, $f(\theta_i, \phi_i, \theta_r, \phi_r) = f_d(\theta_i, \phi_i)$, which is constant over the reflected hemisphere, and that the irradiance is uniform. The resulting derivation is,

$$\rho(\theta_i, \phi_i) = \frac{\int\int f(\theta_i, \phi_i, \theta_r, \phi_r) E_i(\theta_i, \phi_i) cos\theta_r dA_i d\Omega_r}{\int E_i(\theta_i, \phi_i) dA_i}$$

$$\rho(\theta_i, \phi_i) = \int_0^{2\pi} \int_0^{\pi/2} f(\theta_i, \phi_i, \theta_r, \phi_r) cos\theta_r sin\theta_r d\theta_r d\phi_r$$

$$\rho(\theta_i, \phi_i) = 2\pi f_d(\theta_i, \phi_i) \int_0^{\pi/2} cos\theta_r sin\theta_r d\theta_r$$

$$\rho(\theta_i, \phi_i) = \pi f_d(\theta_i, \phi_i)$$

$$f_d(\theta_i, \phi_i) = \frac{\rho(\theta_i, \phi_i)}{\pi} \tag{13}$$

Thus, the result is that the reflectance is now a function of the incident light direction, or vector.

2.1.3   The Bi-Directional Reflectance Distribution Function.

In the previous two sections, it has been shown how the BRDF for a diffuse scatterer is obtained using reflectance. This leaves a problem, because no physical object has been found to be totally diffuse. If the incident angle of the light is near grazing, $\theta_i \lesssim 90°$, just about any physically realizable object becomes specular. An example of this is seeing a reflection when looking down a long hallway even if surface is dull when looking straight down.

For a generic BRDF formulation, an additional component is needed: the specular reflection. The simplest way to handle this is to create what is commonly referred to as a perfectly diffuse/fractional-specularity model [43]. In this model, a perfectly

diffuse, or Lambertian, component is simply added to a specular component.

$$f(\theta_i, \phi_i, \theta_r, \phi_r) = f_s(\theta_i, \phi_i, \theta_r, \phi_r) + f_d(\theta_i, \phi_i) \qquad (14)$$

The diffuse component is typically at most only a function of the incident angle only, because as the incident ray moves away from the surface normal, the diffuse component, f_d, gets less intense, and at the same time, the specular lobe gets larger. This is about as far as the discussion can be taken without looking a specific models. A three dimensional depiction of the diffuse component, specular component, and full fractional specularity BRDF model is shown in Figure 4.

(a)   (b)   (c)
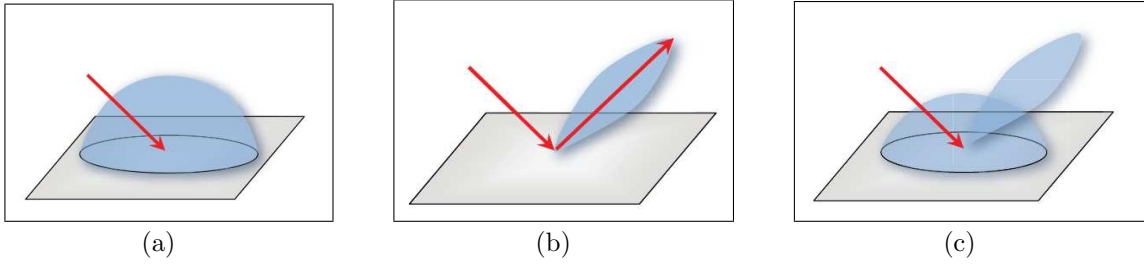
Figure 4. The components of the fractional specularity BRDF model. (a) Lambertian diffuse component only. (b) Specular component only. (c) Both components added together to form the full fractional specularity model[31].

2.1.4   BRDF Model Classification.

There are really three main types of models from this author's perspective: empirical, phenomenological, and deterministic BRDFs. This is the author's own re-branding of the BRDF family tree borrowing nomenclature from Shell [52], Ngan [47], and Marciniak [43]. The logic behind this structure follows the intent and physical insight involved in the derivation for the BRDF. Empirical methods are mathematically-based data fits or interpolations of the data. Phenomenological, or representative, methods are still data fits, but they use some sort of physical in-

sight within the fitted model's functions. Finally, deterministic methods attempt a derivation using electromagnetic theory to approximate the BRDF without any data collection. A technical report from Purdue University, written by Yinlong Sun [56], gives a good overview of the different methods used to approximate the BRDF. His classification is very similar to the classification system that is used in this study. Table 1 visually depicts this classification system.

Table 1. The BRDF Model Family Tree.

- Empirical BRDFs
    - Interpolation of Data
    - Basis Function Fits (Spherical Wavelets)
- Phenomenological BRDFs
    - Perfectly Diffuse/Snell's Law Based Specular Lobe
    - Perfectly Diffuse/Fresnel Based Specular Terms
    - Directional Diffuse/Fresnel Based Specular Terms
    - Very Strongly Energy Conserving (Infrared Based)
- Deterministic BRDFs
    - Kirchhoff Diffraction Theory
    - Rayleigh-Rice Vector Perturbation Theory
    - Limited Simulations

Empirical BRDFs tend to be some type of data representation. Typically, they are spherical harmonic representations and have been used due the nature of the scatter and the nature of the spherical coordinate system[9]. These functions are orthogonal and map to certain BRDFs very well. As they are not the focus of this thesis, they are only mentioned for completeness.

Deterministic BRDFs which are completely derived from physics and electromagnetics are presented in Appendix B. This is because it is quite cumbersome and

difficult to follow. The results also are not used in the body of this study, but are still a revelant part of the research conducted.

2.2 Phenomenological BRDF Models

This section addresses the mathematical construct of a few of the common phenomenological, or representative, BRDF models in a manner where each model builds upon the previous. This development is pertinent because the Ward and Cook-Torrance models are used in Chapter VI to provide a measure of 'diffuseness'. They are also pertinent because, ultimately, they are used for the scene generation described in Chapter I. The models include the Phong, Blinn-Phong, Ward, Ward-Duer, Cook-Torrance, Maxwell-Beard, Oren-Nayar, and Sandford Robinson.

2.2.1 Less-Physically Based Phenomenological BRDFs.

This grouping of BRDFs typically covers those that are a simple approximation to Snell's law for the location of specular lobe with some type of arbitrary shaping, and also have a perfectly diffuse component that is independent of incident angle. They tend to be computationally efficient because they are simple, and they are often used for real-time computer graphics renderings. The progression of models presented here adds complexity step by step for each model building upon the previous. This is an attempt at telling a coherent story of BRDF development, but it leads to a story that facilitates the reader in understanding the development to more and more physically based models that is lacking in many presentations of BRDF models. An excellent overview of these models is provided in Ngan's PhD thesis[47]. Notations common to each of these models is included in Table 2. Bold notation denotes a vector.

Table 2. Common Notations for BRDF Models.

Symbol	Description
N	Surface Normal Vector
V	Observation Vector (View)
L	Incident Vector (Light)
R	Mirror Reflection of **L**
H	Bisecting Vector of **V** and **L**
δ	Angle Between **N** and **H**

2.2.1.1   The Phong Model.

This is really the first BRDF chronologically and most well known of all BRDFs in computer graphics[47]. The basic idea behind the Phong model is that Snell's law is obeyed in a mirror direction within the plane of incidence defined by the incoming light vector, **L**, and the normal to the surface, **N**. To describe the fall-off of BRDF values around the mirror direction vector, or the specular lobe, a cosine fall-off to an arbitrary power is modeled. Phong's original formulation is,

$$f(\mathbf{L}, \mathbf{V}) = \frac{\rho_d}{\pi} + \rho_s \frac{(\mathbf{V} \cdot \mathbf{R})^n}{\mathbf{N} \cdot \mathbf{L}}, \tag{15}$$

where ρ_d is the diffuse reflectance term, ρ_s is the specular reflectance term, $\cdot$ is a vector dot product, the mirror reflectance vector is defined by $\mathbf{R}(1, \theta_r, \phi_r) = \mathbf{L}(1, \theta_i, \phi_i + \pi)$, and all other definitions are given by Table 2. Given that a perfectly diffuse BRDF is simply ρ_d/π, one can already know that this model is not physically plausible, and is more of a intuitively based curve fit. As are all of the models that follow. A modification to the Phong model that ensures reciprocity and energy conservation to make it more physically plausible is

$$f(\mathbf{L}, \mathbf{V}) = \frac{\rho_d}{\pi} + \frac{\rho_s}{2\pi}(n + 2)(\mathbf{V} \cdot \mathbf{R})^n. \tag{16}$$

2.2.1.2 The Blinn-Phong Model.

The Blinn-Phong[13] model is simply a variant that is based on the half angle vector, **H**, instead of the mirror vector, **R**. This variation is important because it changes the shape of the specular lobe. Using the original Phong formulation, the specular lobe remains a constant cone for all incident angles, but using the Blinn-Phong formulation the specular lobe becomes oblate. Figure 5 shows the relationship between the vectors. A physically based reason that one could plausibly give for using this geometry is that, as one moves away from the center of the lobe in the ϕ direction, the incident angle with regards to the Fresnel reflectance changes more abruptly than it would in the θ direction.
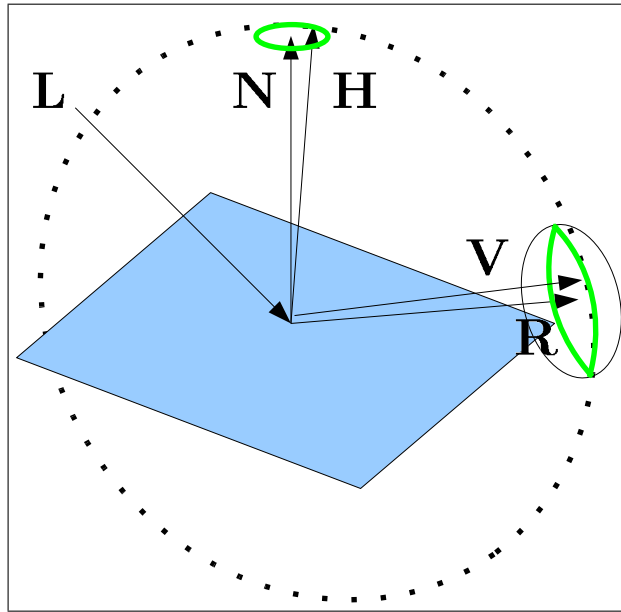
Figure 5. An illustration of the effect of using V·R defined lobe vs. a H · N defined lobe. The green line indicates the cooresponding V and H paths.

Although Ngan gives no mention to a physical explanation for this phenomenon, it is shown in Ngan's thesis that the halfway vector approach definitely renders more

realistic scenes when grazing angles are involved. The Blinn-Phong model is

$$f(\mathbf{L}, \mathbf{V}) = \rho_d/\pi + \frac{\rho_s}{2\pi}(n+2)(\mathbf{H} \cdot \mathbf{N})^n. \tag{17}$$

2.2.1.3 The Ward Model.

This model uses a Gaussian distribution opposed to the cosine distribution that the Blinn-Phong model uses[58]. This is a more physically based model because the distribution of scattering centers, or micro-facets, typically is Gaussian. In addition, it is based upon the halfway vector that the Blinn-Phong model uses. This model is also able to account for anisotropic distribution of scattering centers, meaning that there is a term describing the Gaussian distribution in both the ϕ and θ axes; this is opposed to one term for both. This paper also shows the reduction of the anisotropic model to the isotropic model, because the isotropic model is required when the measurements are in-plane only. This model is reciprocal, but not strongly energy conserving. The anisotropic model is

$$f(\mathbf{L}, \mathbf{V}) = \frac{\rho_d}{\pi} + \rho_s \frac{1}{\sqrt{(\mathbf{N} \cdot \mathbf{L})(\mathbf{N} \cdot \mathbf{V})}} \frac{e^{-tan^2(\delta)(cos^2(\phi_h)/\alpha^2 + sin^2(\phi_h)/\beta^2)}}{4\pi\alpha\beta}, \tag{18}$$

where α and β describe width of the specular lobe in the ϕ and θ axes respectively, and ϕ_h is the angle between the projection of $\mathbf{H}$ onto the sample surface and $\phi = 0$. When $\alpha = \beta$, the expression reduces to

$$f(\mathbf{L}, \mathbf{V}) = \frac{\rho_d}{\pi} + \rho_s \frac{1}{\sqrt{(\mathbf{N} \cdot \mathbf{L})(\mathbf{N} \cdot \mathbf{V})}} \frac{e^{-tan^2(\delta)/\beta^2}}{4\pi\beta^2}. \tag{19}$$

2.2.1.4 The Ward-Duer Model.

This model is simply a modification to the Ward model that makes the model strongly energy conserving; this modification can also be applied to the anisotropic

model[21]. This model is given by,

$$f(\mathbf{L}, \mathbf{V}) = \frac{\rho_d}{\pi} + \rho_s \frac{1}{(\mathbf{N} \cdot \mathbf{L})(\mathbf{N} \cdot \mathbf{V})} \frac{e^{-tan^2(\delta)/\beta^2}}{4\pi\beta^2}. \tag{20}$$

2.2.2 More-Physically Based Phenomenological BRDFs.

These models tend to be much more physically based, and hence, much more complicated. Most tend to be based off of what is called a microfacet model. Although some of the previous models did use a Gaussian microfacet distribution-like term, they do not have obscuration functions. Many authors prefer to make a distinction between these microfacet models, but the mathematics of a few of the previously presented models have the same microfacet distribution term. The previous models also do not attempt to adjust for the Fresnel effects that change the magnitude of the scatter with θ_i. Figure 6 shows the masking and shadowing of light rays that microfacets would cause, and this demonstrates the physical need for such a term especially at high incident angles for rough surfaces.

(a)   (b)
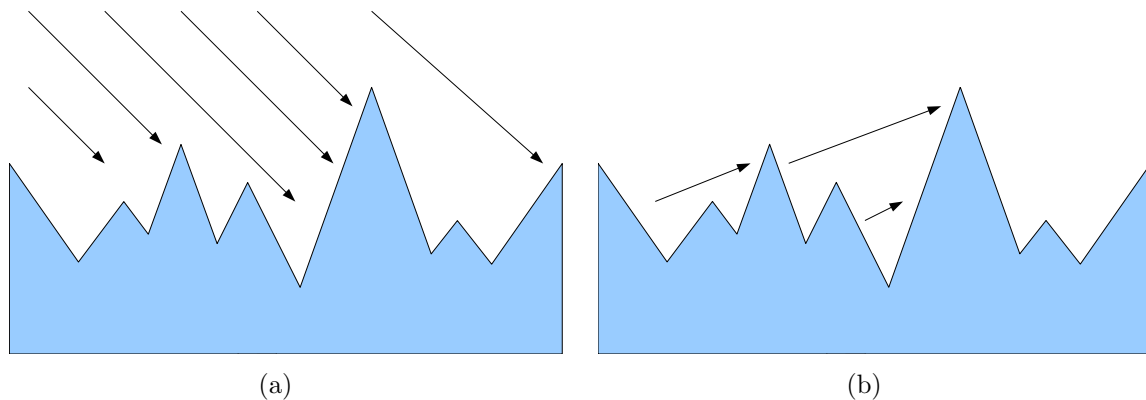
Figure 6. Depiction of microfacet obscuration function. (a) Depiction of microfacets shadowing others. (b) Depiction of reflections being masked by other microfacets.

2.2.2.1 The Cook-Torrance Model.

This model is the first of the microfacet models[17]. These models are loosely based upon geometrical optics. The terms that were just described will be mathematically defined in this model and used in further models. Table 3 shows the additional terms used in these models, but their definitions often vary by model. One must take care to not assume that they are the same for different models although the notation may be the same.

This first microfacet model gives a good overview of the make up of these models. The first and most important term that makes these models more physical is the Fresnel term, which is based upon electromagnetics. This describes the familiar effect that most surfaces become increasingly specular near grazing incidence. For the rigorous development of the Fresnel reflection equations, the reader is referred to Hecht[33]. Although this term can be used, a simplification has been provided by the computer graphics community to simplify the process of fitting functions to the data. This also makes the function computationally more efficient.

The normal condensed formulation of the Fresnel equation for unpolarized light, given by the average of both polarizations, is

$$F(\theta_i, \theta_r) = \frac{1}{2} \left(\frac{sin^2(\theta_i - \theta_t)}{sin^2(\theta_i + \theta_t)} + \frac{tan^2(\theta_i - \theta_t)}{tan^2(\theta_i + \theta_t)} \right),$$ (21)

Table 3. Common Notations for More Physically-Based BRDF Models.

Symbol	Description
F	Fresnel Term
G	Geometric Attenuation (Shadowing)
D	Microfacet Distribution (Typically Gaussian)

20

where θ_t is the transmission angle given by Snell's law of refraction, which requires the index of refraction for the material. If this is simplified for computational efficiency, the result is

$$F(\theta_i, \theta_r) = \frac{1}{2}\frac{(g-c)^2}{(g+c)^2}\left(1 + \frac{(c(g+c)-1)^2}{(c(g-c)+1)^2}\right), \tag{22}$$

where $c = cos(\theta_i) = \mathbf{L} \cdot \mathbf{H}$ uses the half angle instead of the mirror vector, and $g = \sqrt{n^2 + c^2 - 1}$. This simplification is only valid where $n = n_t/n_i > 1$ because of the square root in the g term. The refractive index of the medium the incident wave is propagating in is n_i, which in air is approximately 1, and n_t is the refractive index of material the incident wave is incident upon.
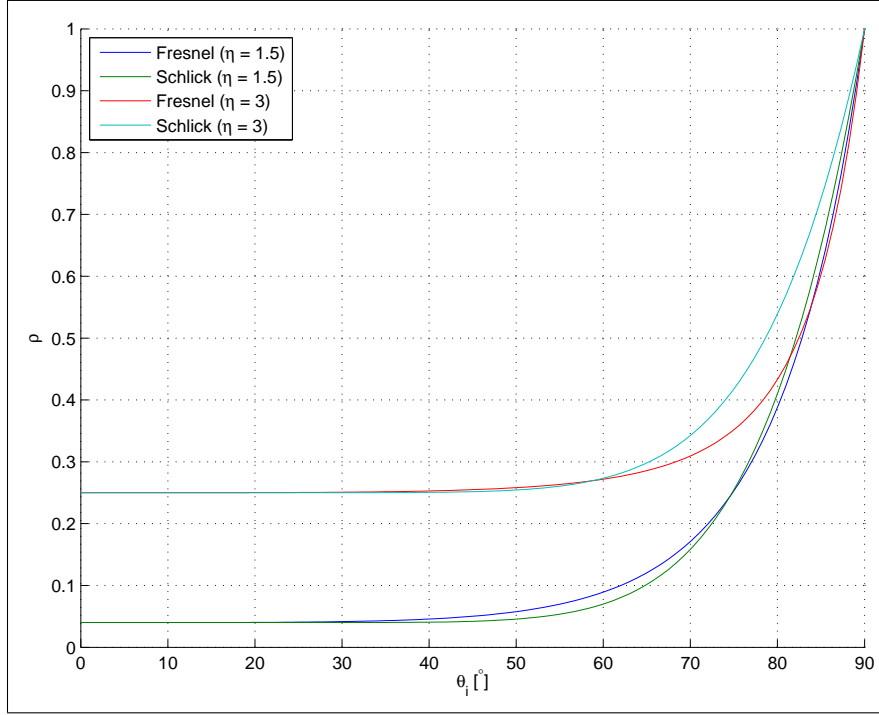
Figure 7. A comparison a Fresnel function and Schlick approximation, this approximation simplifies the function and increases computational speed.

An approximation for computational efficiency is given by Schlick[50] as

$$F(\theta_i) = F(0) + (1 - F(0))(1 - cos(\theta_i))^5, \tag{23}$$

21

where θ_i is the incident angle and $F(0)$ is the Fresnel reflectance at $\theta_i = 0$. This approximation was initially proposed for metallic surfaces, which have a very high index of refraction. This is because the index of refraction is defined electrically as $n = \sqrt{\epsilon/\mu}$. The permeability of most objects that are not magnetic is typically $\mu \approx 1$, and metals have very high permittivities, $\epsilon > 50$[10]. Figure 7 shows a test of this approximation at $n = 1.5$ and $n = 3$ versus θ_i. This shows that the approximation is relatively effective even at lower indices of refraction.
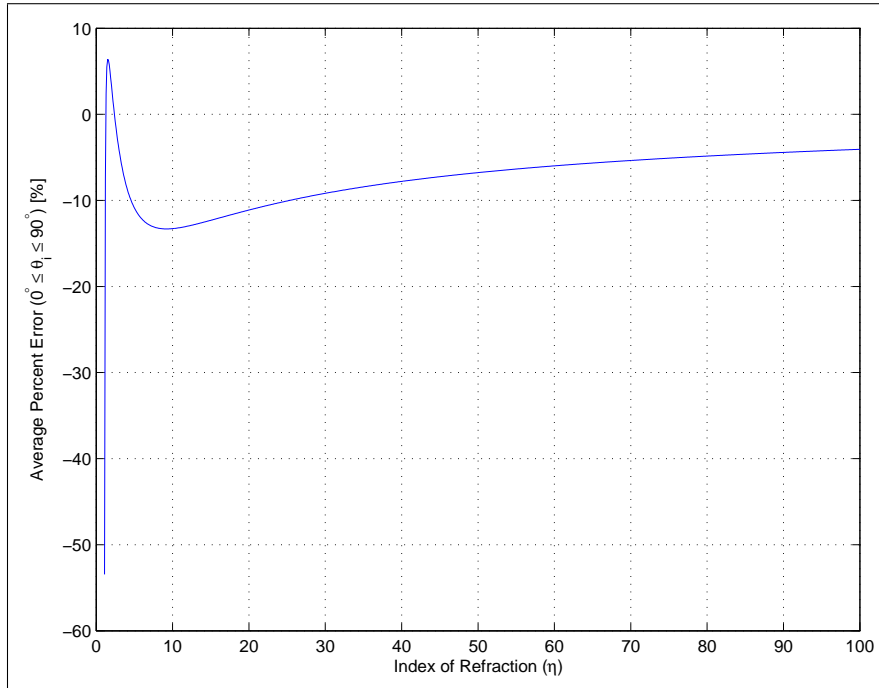
Figure 8. A comparison a Fresnel function and Schlick approximation, this approximation simplifies the function and increases computational speed.

Figure 8 shows a more complete test of this approximation. It plots the average percent error in the range, $0° \leq \theta_i \leq 90°$, for increasing values of n which are closer to the metal coatings presented later in this study. This shows the error trend as n is varied, which shows it is stable in the limit of n. Therefore, it is valid where $n \gtrsim 1.5$. This approximation is presented because it is used in this study when fitting the Cook-Torrance model to the measured data in later chapters.

The next term to be considered is the geometric occlusion term, which was depicted in Figure 6. This term in the Cook-Torrance model describes the shadowing and masking effects, and is derived strictly from the geometry of a Gaussian rough surface. This term is given by,

$$G = min\left(1, \frac{2(\mathbf{N} \cdot \mathbf{H})(\mathbf{N} \cdot \mathbf{V})}{(\mathbf{V} \cdot \mathbf{H})}, \frac{2(\mathbf{N} \cdot \mathbf{H})(\mathbf{N} \cdot \mathbf{L})}{(\mathbf{V} \cdot \mathbf{H})}\right), \tag{24}$$

where the $min()$ function selects the least of the arguments. The first term in the minimum function is where no occlusion of any kind is occurring, the second term accounts for masking because it doesn't have a L term, and the third term is the shadowing term.

Lastly, the microfacet distribution term, D, represents the distribution for microfacet normals about the average surface normal. This distribution is typically assumed to be Gaussian in nature. This term is given by,

$$D = \frac{1}{m^2 cos^4(\theta_h)} e^{-(tan(\theta_h)/m)^2}, \tag{25}$$

where m is a fitting term similar to the standard deviation of a Gaussian distribution.

Thus, with all the terms needed to describe the Cook-Torrance model, the expression is

$$f(\mathbf{L}, \mathbf{V}) = \frac{\rho_d}{\pi} + \frac{\rho_s}{\pi} \frac{D\ G\ F}{(\mathbf{N} \cdot \mathbf{L})(\mathbf{N} \cdot \mathbf{V})}. \tag{26}$$

As shown in Ngan's thesis, this tends to give excellent results for rough surfaces when compared to all the previously defined models. This should not be a surprise as this function is more physically based.

2.2.2.2   The Oren-Nayar Model.

This model is similar to the Cook-Torrance model, but it models the diffuse portion of the BRDF. This is important for materials like sand and concrete. The difficulty with this model is that multiple reflections are encountered because the reflections are in all directions. A simplification of the more general model is given by Oren and Nayar [46] as

$$
\begin{aligned}
f =& \frac{\rho_d}{\pi} cos\theta_i (A + B \ max(0, cos(\phi_i - \phi_r)))... \\
& sin(max(\theta_i, \theta_r)) tan(min(\theta_i, \theta_r))), \\
A =& 1 - \frac{1}{2} \frac{\sigma^2}{\sigma^2 + 0.33}, \\
B =& 0.45 \frac{\sigma^2}{\sigma^2 + 0.09},
\end{aligned}
\tag{27}
$$

where σ is the standard deviation of the surface.

2.2.2.3   The Maxwell-Beard Model.

This model is also microfacet based, and logically follows the development presented up to this point. It was originally developed for the IR response of painted surfaces[44]. This model adjusts for a non-Lambertian diffuse, or volume, scatter as described in the original paper. This volume scatter is also often referred to as a bulk scatter. This effectively adds a directional diffuse term. It also uses the Fresnel, occlusion, and distribution based terms for the specular, or surface, scatter.

2.2.2.4   The He-Torrance Model.

The last model in this subset of microfacet based models is very similar to the Maxwell-Beard model, but this model takes polarization and other wave phenomena into account[32]. It is considered the most physically based of the microfacet models.

24

This model is also very complex, and would be a good candidate for further research.

2.2.3 Energy Based Phenomenological BRDFs.

2.2.3.1 The Sandford-Robinson Model.

This model takes a different approach to BRDF modeling motivated by the conservation of energy, or Kirchhoff's law, described in Appendix A. It was modeled this way because it was developed for the IR signatures of paint, and thus, Kirchhoff's law must be obeyed for accurate predictions. The original document by Sandford[49] is hard to come by, so this presentation loosely follows that of Shell [52] and Marciniak [43]. It is presented in such a manner to remain consistent with this paper.

The first term of consequence in this model is an approximation to the Fresnel reflectance term, and is given by

$$g(\theta, b) = \frac{1}{1 + b^2 tan^2(\theta)}. \tag{28}$$

where b, the diffuse shaping term, determines the directional dependence of the diffuse reflectivity. In order to maintain energy conservation and counteract the perturbations of the shaping, a normalization term is introduced. This normalization is given by

$$\begin{aligned} G(b) &= \frac{1}{\pi} \int g(\theta, b) cos\theta sin\theta d\theta \\ &= \frac{1 + \frac{b^2 ln(b^2)}{1-b^2}}{1 - b^2}. \end{aligned} \tag{29}$$

When this is included, the strongly energy conserving diffuse term is

$$f_d(b, \rho_d, \theta_i, \theta_r) = \frac{\rho_d}{\pi} \frac{g(\theta_i, b)g(\theta_r, b)}{G(b)^2}. \tag{30}$$

Next, the specular term is derived. The specular lobe shaping is given by

$$h(\chi, \theta_i, \phi_i, \theta_r, \phi_r) = \frac{1}{(\chi^2 cos^2(\delta) + sin^2(\delta))^2}, \tag{31}$$

where χ determines the lobewidth and δ is the halfway angle previously defined. Again, a normalization factor is used, given by

$$H(\chi, \theta_i) = \frac{1}{4\pi} \int h(\chi, \theta_i, \phi_i, \theta_r, \phi_r) d\Omega_r$$
$$= \frac{1}{2\chi^2} \left((1 - \chi^2) cos(\theta_i) + \frac{2\chi^2 + (1 - \chi^2)^2 cos^2(\theta_i)}{\sqrt{(1 - \chi^2)^2 cos^2(\theta_i) + 4\chi^2}} \right). \tag{32}$$

In order to keep this model strongly energy conserving, Kirchhoff's law is used to derive an expression for the specular reflectance. The specular reflectance is,

$$\rho_s(\rho_d, \epsilon_o, b, \theta_i) =$$
$$1 - 2\pi \int_0^{\pi/2} f_d(b, \rho_d, \theta_i, \theta_r) cos(\theta_r) sin(\theta_r) d\theta_r - \epsilon(\epsilon_o, b, \theta_i), \tag{33}$$

where the directional emittance is

$$\epsilon(\epsilon_o, b, \theta_i) = \epsilon_o \frac{g(\theta_i, b)}{G(b)}. \tag{34}$$

This follows the previous development of the directional dependence of the diffuse reflectivity. When this is combined with the specular portion of the BRDF, the Sandford-Robinson model is

$$f_s(\rho_d, \epsilon_o, b, \chi, \theta_i, \theta_r, \phi_r) = \frac{1}{4\pi} \rho_s(\rho_d, \epsilon_o, b, \theta_i) \frac{h(\chi, \theta_i, \phi_i, \theta_r, \phi_r)}{H(\chi, \theta_i)} \frac{1}{cos(\theta_r)}. \tag{35}$$

Additionally there is a problem with this, the specular reflection at $\theta_r = 90^o$ becomes

infinite. In order to negate this effect, the f_s can be multiplied by the term,

$$\frac{1}{1 + b^2 tan^2(\theta)}.\tag{36}$$

Smooth $\longrightarrow$ Rough

	Smooth	Rough
Specular	Mirror BRDF Delta Function	Cook-Torrance BRDF Off Specular Lobe
Diffuse	Lambertian BRDF No View Dependence	Oren-Nayar BRDF View Dependence
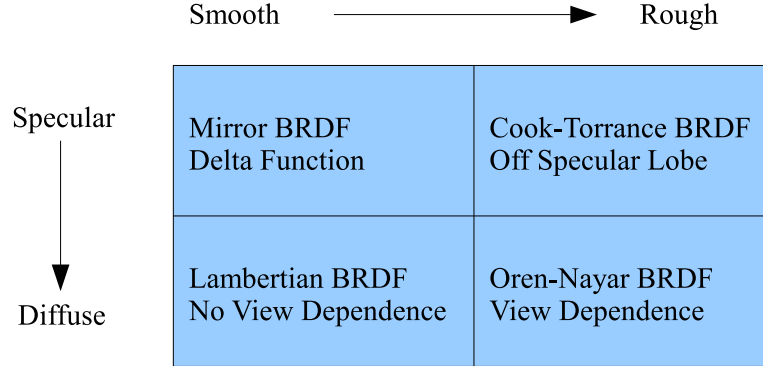
Figure 9. An illustration for the areas of where different phenomenological BRDF models are best suited for application.

There are many options for representing a BRDF that have been demonstrated here, and the model to use really depends upon the material and accuracy desired. Nevertheless, the model for that material should end up with the lowest MSE error when used for a fit. Figure 9 is a good visualization of surface roughness versus specular/diffuse material qualities and which BRDF model to use.

2.3 Chapter Conclusion

This chapter has laid down the foundation for the remainder of this document. It presented a mathematical development and definition of the BRDF. This is important in understanding what exactly BRDF measurements are, because they do not fit the strict definition of the derivative quantity as which the BRDF is mathematically defined. This chapter then presented the different models that represent the BRDF. In the process of representing the BRDF with models, the physical processes

at work creating these different BRDF characteristics were represented with mathematics. This physical insight will be key when interpreting the results of BRDF measurements. Additionally, these models will also make it possible to quantify the different parameters of these models. This will allow the quantification of 'diffuseness' or 'specularity' for a set of BRDF measurements.

III. Measurement Methods, Equipment, and Procedures

This chapter describes the measurement methods, equipment, and procedures used in this effort. First, the mathematical formulation of the BRDF will be modified in order to be applicable to physical measurements. Next, the equipment used in this research will be described and the geometrical definitions that apply will be defined. Finally, the specific procedures in the IR used with this equipment in order to set it up and align samples will be covered. This is because it has not been a trivial task.

3.1 BRDF Measurement Formulation

The BRDF is formally defined in Section 2.1 as a differential measurement, which means it is only defined at a infinitely small point in space, or rather a direction. This is not possible to measure because any optical measurement device has a finite aperture and a detector which needs a certain amount of flux to provide a measurable response. Thus, the BRDF definition must be modified for measurements. The definition of the BRDF is

$$BRDF = \frac{dL_r}{dE_i}. \tag{37}$$

If a substitution is made for the incident differential irradiance, dE_i, the form becomes

$$BRDF = \frac{dL_r}{L_i \ cos\theta_i \ d\Omega_i}. \tag{38}$$

The definition of the radiance is then substituted in, and careful cancellation of terms produces the BRDF in measurement form,

$$BRDF = \frac{dP_r/d\Omega_r}{P_i \ cos(\theta_r)} \left[\frac{1}{sr}\right], \tag{39}$$

where dP_r is the differential received power, $d\Omega_r$ is the differential solid angle sub-tended by the aperture, P_i is the power of the incident beam on the sample, and θ_r is the angle between the sample normal and the detector as shown in Figure 10. This figure also places the other terms of Equation (39) on the BRDF measurement device used in this research. When making these substitutions to change the form, one must recall that the ratio of measured power, or signal, is equivalent to flux, Φ. This result agrees with results defined by Stover[53]. There are many measurement methods that have been proposed for the BRDF, but the most common scientific instrument is a gonio-reflectometer, or scatterometer. An example of this type of instrument and a relation to the parts of the BRDF measurement Equation (39) are shown in Figure 10.
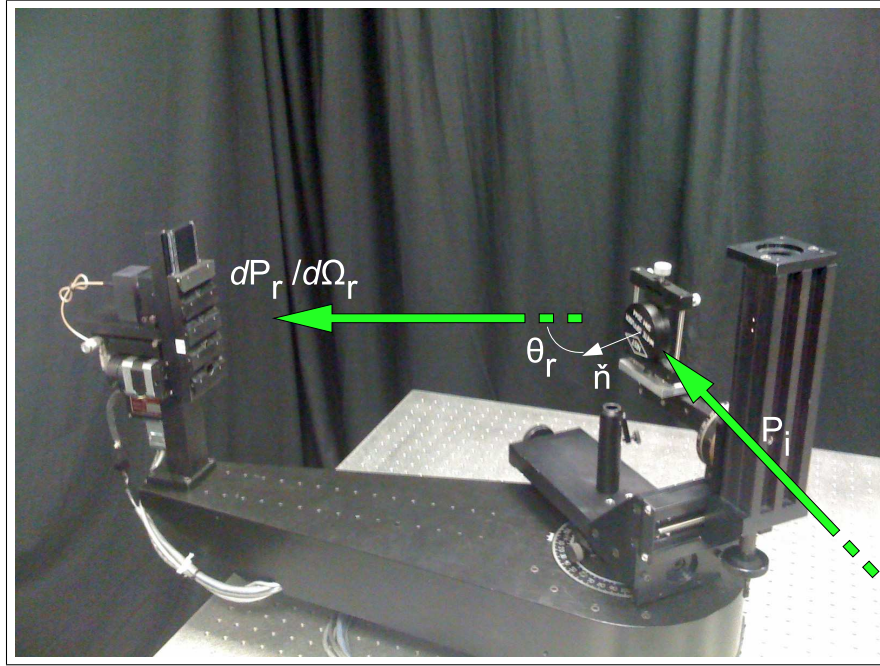
Figure 10. A physical depiction of the BRDF measurement Equation (39) super imposed upon the CASI® .

3.2 Equipment: the CASI®

This section gives a description of the main instrument used for BRDF measurement in this study. The CASI® was developed in the late eighties by Stover, et al.[36]. SMS, formerly TMA, then produced the instrument commercially. SMS considers it 'the world's most advanced and accurate light scatter instrument'[6]. The AFIT CASI® was previously used by the Air Force Research Laboratories (AFRL) Optical Measurement Facility, and it was refurbished by SMS in 2008 and delivered to AFIT in August of that year. The official CASI® product brochure[5] lists its advertised capabilities as a scientific instrument. Table 4 gives a partial listing of these capabilities relevant to the AFIT CASI® .

The AFIT CASI® consists of 5 main parts: the two source enclosures, the main rotation stage, the control and power electronics, and the control computer. A thorough treatment of the hardware is listed in the official hardware reference[51]. A photo of the entire CASI® system is shown in Figure 11. Although the manufacturer's documentation is available, it is still necessary to document the equipment in order to understand the assumptions and limitations of the measurements. This also provides a more concise overview for the reader. This overview is presented in an order

Table 4. Listing of AFIT CASI® capabilities.

Item	Specification
Wavelength	$544nm$, $632.8nm$, $3.39\mu m$, $10.6\mu m$
Total System Accuracy	5%
Total System Linearity	2%
Repeatability	2%
Noise Equivalent BRDF	5×10^{-8}
Resolution	$0.001°$
Accuracy	$0.05°$
Aperatures	$300\mu m$, $1.1mm$, $4mm$, and $13.85mm$

beginning at the beam's source and ending at the detector. A more design-oriented description of the CASI® is available in Stover's original design paper[36].
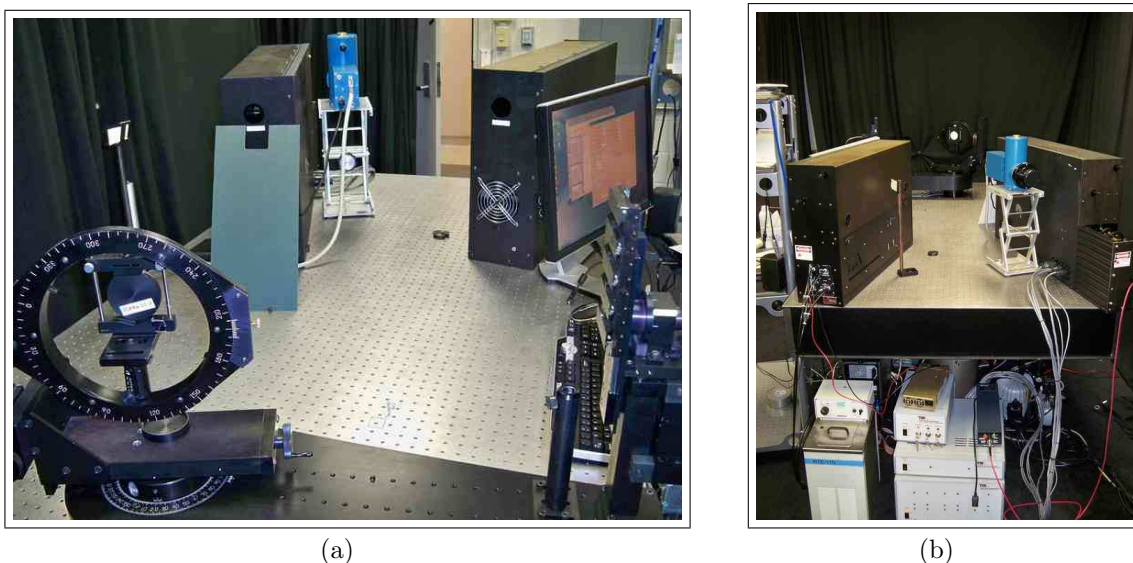
Figure 11. (a) The AFIT CASI® from source end of optics table.
(b) The AFIT CASI® from sample end of optics table.

The sources enclosures unique to AFIT's CASI® are shown in Figures 12 and 13. Figure 12 shows the $3.39\mu m$ HeNe Mid-wave (MW) IR laser, the $544nm$ green HeNe laser, and the $650nm$ red alignment laser co-aligned with the MWIR laser that is intended ensure sample alignment with the IR source. Figure 13 shows the $10.6\mu m$ CO_2 Long-wave (LW) IR laser, the $632.8nm$ red HeNe laser, and the $650nm$ red alignment laser. Each enclosure has the same basic configuration.

The first beam alignment components are encountered just after the laser sources. Beam splitters and turning mirrors are used to co-align the optical axises of the beams in each source box. After the beam splitter, there is a chopper that provides modulation for the optical lock-in so that ambient light and other noise can be filtered out. This helps ensure that only the laser's scatter is measured. Next, there is another beam splitter and wide band detector. This is used to cancel out any instability the lasers may experience during the measurement. The last component in the lower half
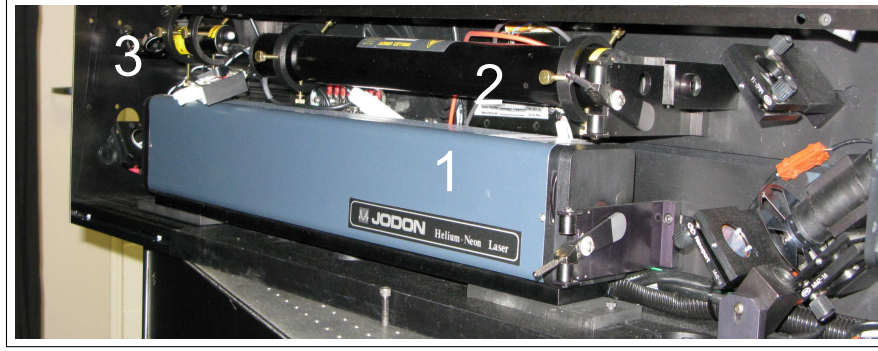
Figure 12. Lower half of the AFIT CASI® 's source enclosure #1, components include (1) a $3.39\mu m$ laser, (2) a $544nm$ laser, and (3) a $650nm$ alignment laser.

of each source box is a turning mirror that sends the beam to the upper half of the source boxes and is used for alignment with the objective in the upper half of the source box.
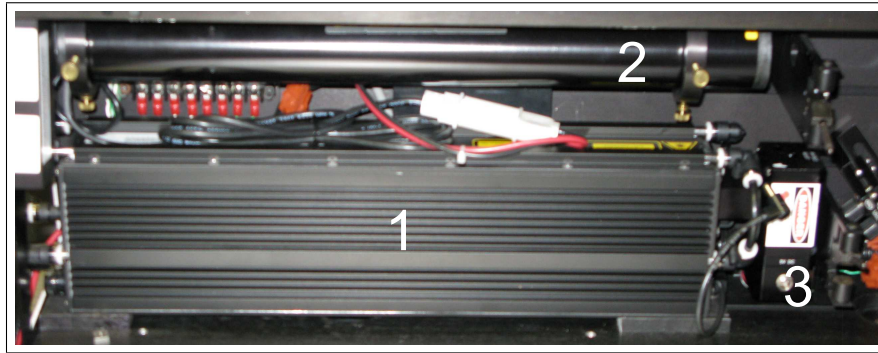
Figure 13. Lower half of AFIT CASI® 's source enclosure #2, components include (1) a $10.6\mu m$ laser, (2) a $632.8nm$ laser, and (3) a $650nm$ alignment laser.

Figure 14 shows the upper half of the source boxes which are identical for each source box in the AFIT CASI® system. First, a turning mirror is used to direct the beam to an objective. Its focal point is to be placed at the center of the subsequent spatial filter in order to reduce diffraction, and thus, ensure a more uniform illumination and reduce unintended illumination of the sample's surface. The objective and spatial filter are placed on a moveable track in order to allow the focus of the beam at the detector when its aperture is centered on the beam. The last component in

the source box is the Off-Axis Parabolic (OAP) mirror which directs the beam at the sample and allows the adjustment of the optical axis so it may be aligned with the gonio arm's center of rotation and the center of the detector. A half wave plate within the source box and a polarizer at the detector can be used for full polarmetric measurements. IR polarizers and half-wave plates were not used for this study.
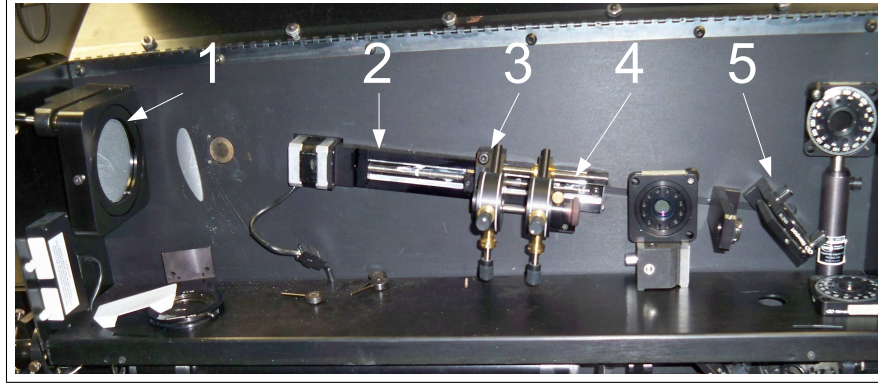
Figure 14. Upper half of the AFIT CASI® 's source boxes, components include (1) OAP mirror, (2) a focus track, (3) a spatial filter, (4) a focusing objective, and a (5) turning mirror.

The light from the beam is scattered when the beam reaches the sample. An assumption is made here, the definition of the BRDF calls for a completely collimated illumination beam incident upon the sample, but the beam is actually still converging when it hits the sample because it is focused on the detector. This assumption is valid because the beam width is narrow enough that a small angle approximation can be used.

Figure 15 shows the components of the main rotation stage and the coordinate system of the CASI® . This is important because the CASI® software assumes it is making an in-plane measurement. This means that the normal to the sample's surface is aligned with the z axis of the BRDF. This puts the incident beam and the center of the reflected solid angle in the x-z plane. Therefore, only θ_i, the angle between the z-axis and the incident beam, and θ_r, the angle between the z-axis and detector,

are varied in the measurement. This forces $\phi_i = 0°$ and $\phi_r = 180°$. This type of measurement is used for all the measurements in this study because the samples were assumed to be isotropic, because of their diffuse nature. A sample is isotropic if the measurement is independent of rotation on the z-axis. Nevertheless, it is possible to vary the sample mount's out-of-plane stage, to take out-of-plane measurements, but this also varies the polarization and θ_i each time when the gonio-arm is moved. This must be accounted for in the data processing. Lamott's master's thesis has a good example of how to do this as it relates to the AFIT CASI® 's coordinate system[38].
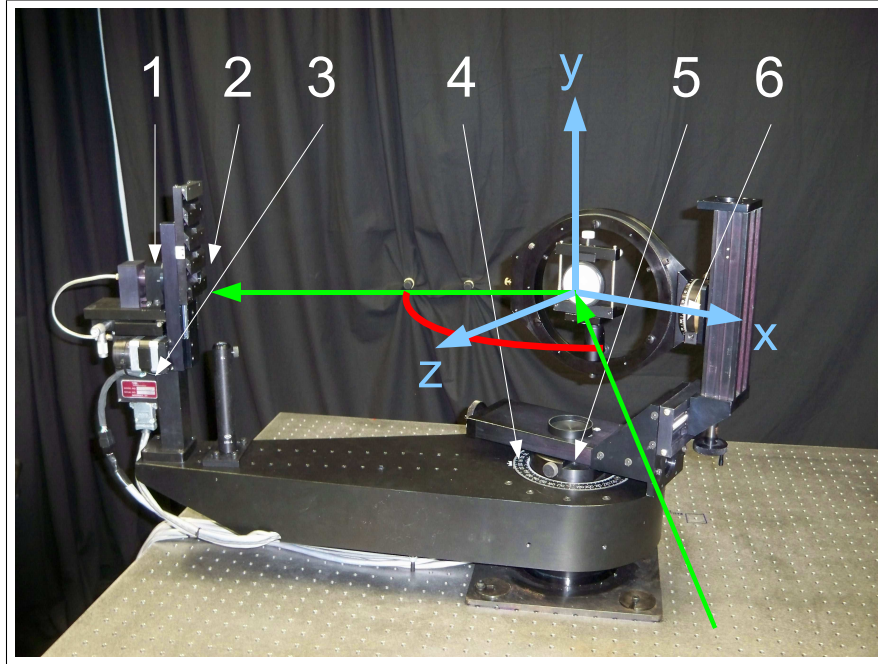
Figure 15. The AFIT CASI® 's main rotation stage, components include (1) a detector, (2) a variable aperture, (3) a detector pre-amp, (4) the detector stage and gonio-arm, (5) the sample stage, and (6) the sample out-of-plane stage.

The last noteworthy assumption the CASI® makes when performing measurements is the aperture size. It allows for the selection of four different aperture sizes $13.85mm$, $4mm$, $1.1mm$, and $300\mu m$. Therefore, the CASI® 's measurement is not the true BRDF of the sample, but it is the average BRDF over the aperture's solid angle, which was discussed in Section 3.1. The step size of θ_r during a sweep corre-

sponds to the arc length at the aperture of 1/2 the aperture size. Thus, the aperture size actually determines the angular resolution and sampling of the true BRDF. The CASI® is able to change apertures throughout a scan to more finely sample the specular return, but this is not needed with the diffuse samples and is not used in this study. All measurements in this study are performed using the 13.8mm aperture. After the aperture, the scatter from the sample is finally detected. The AFIT CASI® has four detectors, one appropriate for each laser's wavelength. The integration time is dependent on each detector and the measured signal. This is determined in the CASI® software. The detectors are listed in Table 5.

3.3 Description of DHR Measurements

DHR measurements are currently used for the calibration BRDF data. It is therefore only appropriate that they are discussed in general so that the difference between the two measurements is illustrated. If one was to make a BRDF measurement with an aperture large enough to create a solid angle that covers the entire hemisphere over a sample's surface, the relation between this measurement and the DHR would simply be

$$\rho_{DHR} = \pi \, f_{BRDF}, \tag{40}$$

where f_{BRDF} is this fictional BRDF measurement and ρ_{DHR} is the measured DHR.

In practice, this measurement is performed with an integrating sphere. It is de-

Table 5. Listing of AFIT CASI® detectors.

Detector Type	Wavelength
Gallium(III) Arsenide (GaAs) (Optically filtered)	544nm
GaAs (Optically filtered)	632.8nm
Indium Antimonide (InSb) (Liquid Nitrogen (LN_2) Cooled)	3.39μm
Mercury Cadmium Telluride (HgCdTe) (LN_2 Cooled)	10.6μm

signed to focus all of the light scattered off of a sample to a detector. This received flux and the flux received from a reference beam split off before entering the sphere are ratioed to give the DHR. Figure 16 shows a geometry that the National Institute of Standards and Technology (NIST) uses to make DHR measurements[28].
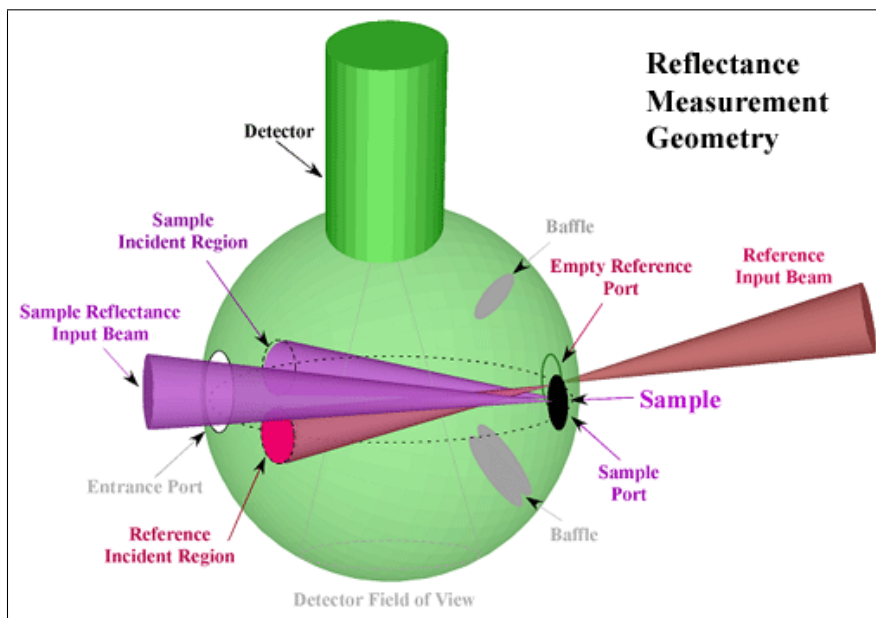
Figure 16. A depiction of a DHR measurement geometry used by NIST[28].

3.4   IR Setup Procedures

Procedures for the setup of the CASI® in the visible spectrum are straight forward and are supplied in AFIT's own procedures specification written by Dominic Maga[41]. Nevertheless, the setup procedures in the IR are tricky and can cause variation in the data. For this reason, they are documented here. A second concern not listed in the procedures is the sample's alignment, which has proven to be critical to precise BRDF measurement. Therefore, sample alignment procedures are also covered in Section 3.5.

There are two basic ways to setup and align the CASI® itself. The first is done

using only the CASI® 's own detector. First, the visible source in the box is aligned to get the IR source 'in the ballpark'. Next, the detector is placed in the beam path without a sample mounted using the largest aperture. The same steps are followed that would be completed if the setup was being performed with the visible source except that the detector's output during each adjustment is used to maximize the signal. The only obvious difference is that when adjusting the objective, the projection plate is not used because it would block the signal. The setup in the IR using only the CASI® 's detector is possible, but it is time consuming and has some uncertainty.

An IR Focal Plane Array (FPA) was available, so it was used to confirm IR alignment. It confirmed that when only the CASI® 's detector is used, the setup is not always satisfactory. It was then used for the alignment of the system, and its use produces much better results in the signature scan, which confirms this method.

> ! The FPA is only sensitive to wavelengths between $1 - 6\mu m$, thus this method is only applicable to the $3.39\mu m$ source.

The first step in the setup is to correctly align the optical axis inside the source box. This is achieved with the two primary turning mirrors and the adjustable apertures as shown in Figures 17 and 18. This procedure is same as the optical setup process except that the FPA is used instead of the naked eye. The objective is that the beam should decrease in radius uniformly when the apertures are shut.

The next step is to align the objective with the optical axis, and then to adjust the spatial filter so that it is centered on the optical axis and at the objective's focal point. This step is shown in Figure 19. The $3.39\mu m$ source uses the $80mm$ Calcium Floride (CaF) objective, and the $350\mu m$ spatial filter. The projection cover is placed on the large aperture with the FPA focused on it. The procedure is the same as if the beam was visible, but once again the FPA is used as an aid.

(a)   (b)
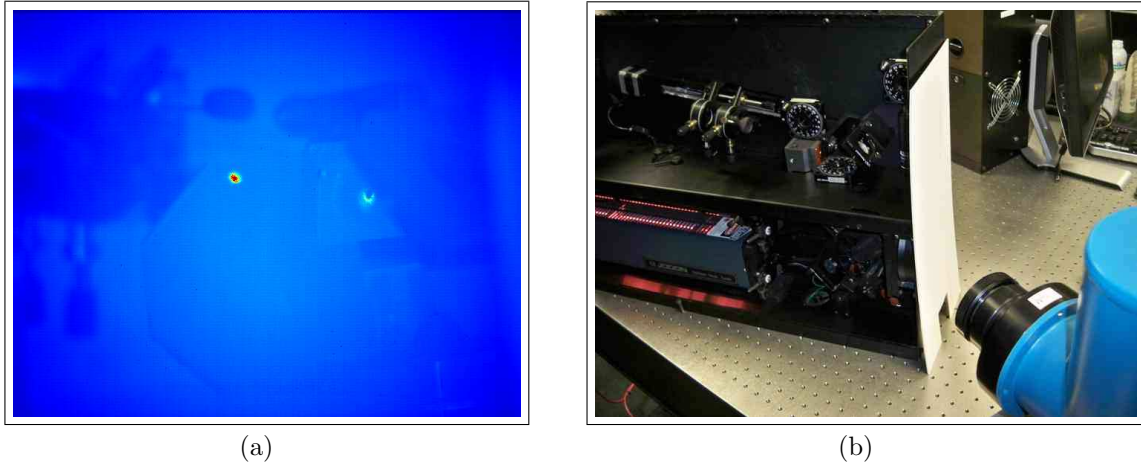
Figure 17. Internal alignment of the beam axis in the source box. (a) IR picture of beam on the first, smaller variable aperture. (b) Visible photo of the physical layout.
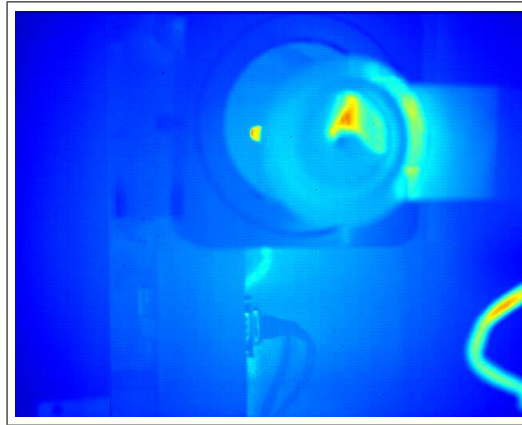
Figure 18. Internal alignment of the beam axis in the source box on the second, larger variable aperture.

The next step, shown in Figure 20, is to align optical axis of the beam to pass directly over the gonio-arm's center of rotation. This is done using a variable aperture mount at the gonio-arm's center of rotation as a reference. This step is completed exactly the same way as it is in the visible, but using the FPA as an aid.

Next, the optical axis is the centered on a plane parallel to the optical bench that bisects the detector. This is shown in Figure 21, this step is slightly modified from the procedure in the visible. A reference card is aligned with the outer markings on the detector, but a small slit in the reference card is used instead of a visible line.

39

(a)   (b)
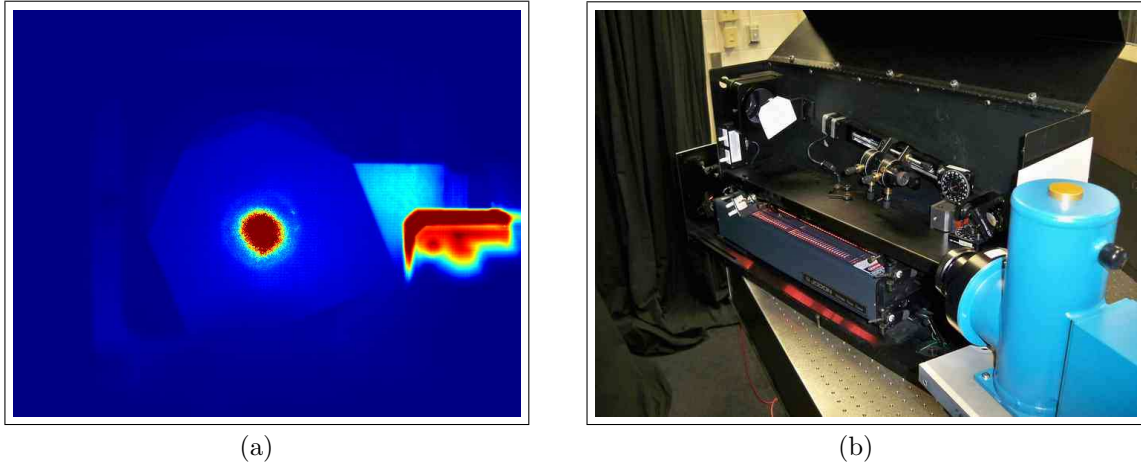
Figure 19. Alignment of the objective and the filter in the IR. (a) IR picture of the beam on the projection plate to check for beam centering and diffraction rings. (b) Visible photo of the physical layout.

(a)   (b)
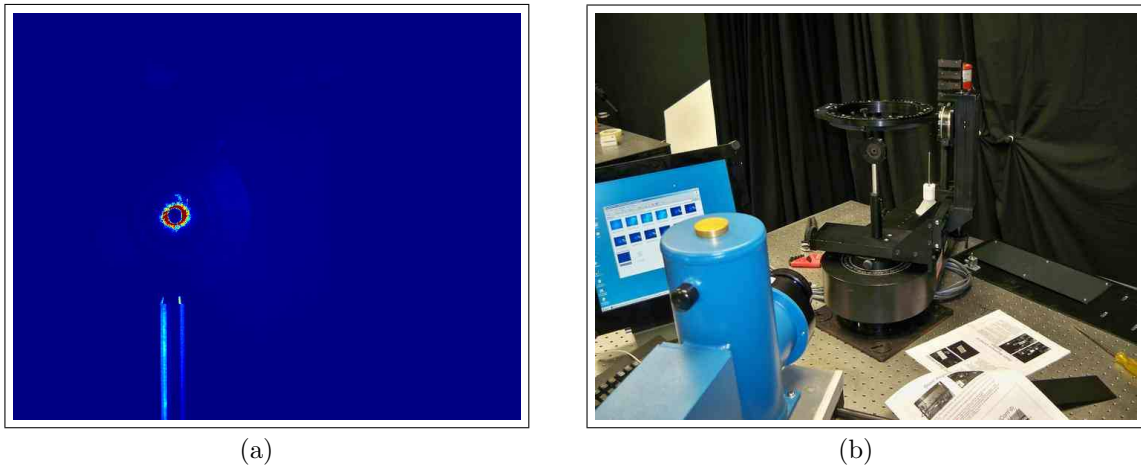
Figure 20. Alignment of the beam axis over the gonio-arm's center of rotation. (a) IR picture of beam alignment with gonio arm center of rotation. (b) Visible photo of physical layout.

This is done because the line on the reference card is not visible through the FPA.

The next step, shown in Figure 22, shows the alignment and focusing of the detector on a semi-opaque sample. Masking tape was used as the semi-opaque sample here. This sample must be over the axis of rotation for the detector to be correctly focused on the sample; this is achieved by making sure the beam position does not move on the sample when θ_i is varied. The FPA can be used to ensure this, but if

40
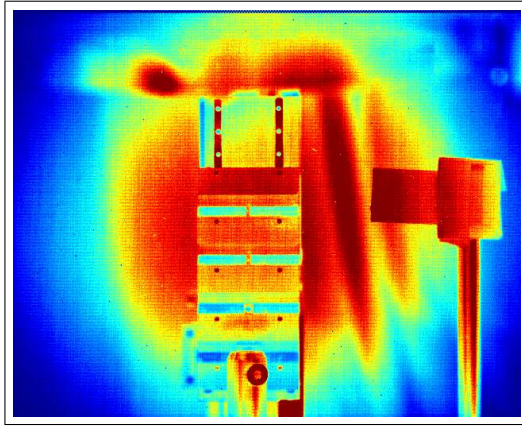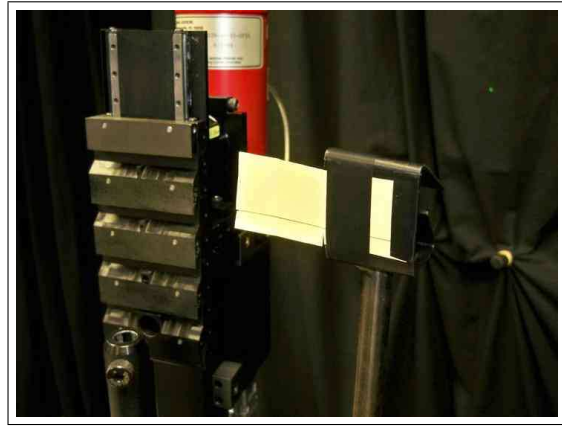
(a)   (b)

Figure 21. Alignment of beam axis with the detector's center in the plane perpendicular to the optical bench. (a) IR picture of beam alignment with center of detector aperture. (b) Visible photo of the physical setup.
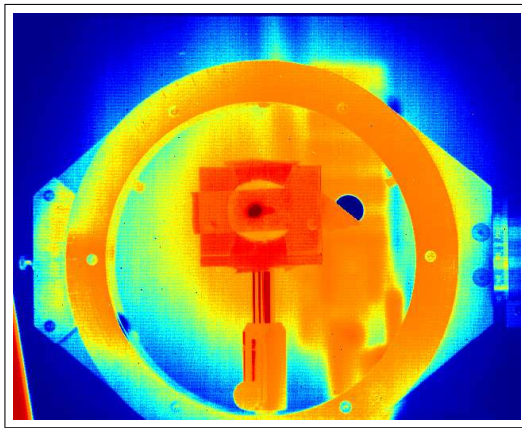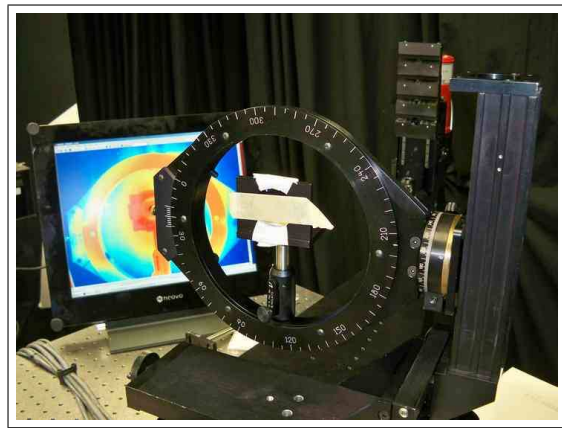
(a)   (b)
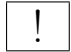
Figure 22. Alignment and focusing of the IR detector. (a) IR picture of beam on masking tape for detector alignment and focusing. (b) Visible photo of physical layout with masking tape in the sample location.

the procedure is being done without the FPA, the co-aligned sample alignment beam must be used. The focusing and alignment of the detector follows the same procedure as in the visible, where the detector's output is used to perform the adjustment. The semi-opaque sample is left in position for the next step even though the beam has not been focused on the detector.

3.5 IR Sample Alignment

There are basically two methods for sample alignment, just as there are in the visible. The first is the 'eyeball' method. It follows the general idea that if a mirror is placed upon the surface of the sample, the mirror's normal and the sample's normal should be co-aligned. Then, if the reflection from the mirror is aligned with the beam's axis, the sample's normal should also be aligned if $\theta_i = 0°$. The full development of this method in the IR, as presented here, follows this assumption.

The second alignment method relies upon the assumption that every sample eventually becomes specular at high incidence angles. The highest incidence angle the CASI® can achieve is $\theta_i = 85°$. After setting θ_i, θ_r is also set to $85°$. The sample is then adjusted until the highest detector response is achieved. Unfortunately, the very diffuse samples used in this study have proven this method to be highly inaccurate when cross checked with the 'eyeball' method, whose maximum error is on the order of a few degrees.

> ! This is the observation that leads to the recommendation in the conclusion of a sample mount jig that has a mirror whose normal can be made parallel with the sample's normal, or vice versa. After alignment using the mirror, the entire jig could be rastered to place the illumination upon the sample. The disagreement between the two current methods of sample alignment create the need for an alignment jig. This jig is illustrated in Section 7.2.

The first step in this process is to align a large variable aperture just outside of the source box with the beam's optical axis. This aperture can then be used as a reference to reflect the specular return from the mirror on the sample to the FPA. This return can then be used to align the sample. A 'half-step' is used here to help with the horizontal alignment of the beam. Figure 23 shows that the aperture's mount can be used to obstruct the beam to center it horizontally.

(a)   (b)
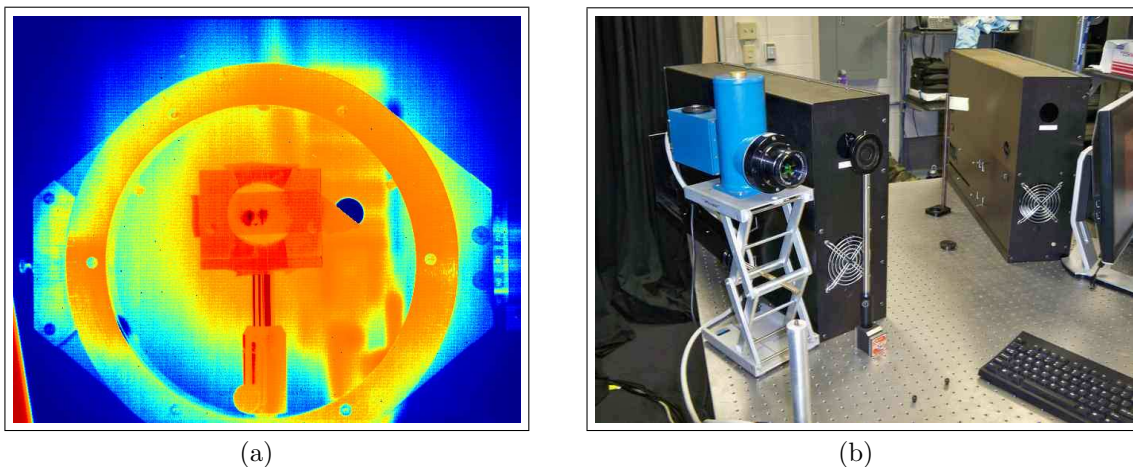
Figure 23. **Alignment of the sample alignment aperture immediately following the source box. (a) IR picture of beam split by aperture mounting to center it in the beam axis. (b) Visible photo of the physical layout.**

The next step is to fine tune the horizontal and vertical alignment of the aperture external to the source box until the aperture appears to close down uniformly on the beam's image on the semi-opaque sample. Figure 24 shows an example of what this should look like in the FPA. When this is completed, make sure the aperture is fully open, remove the semi-opaque sample, and focus the beam on the detector.
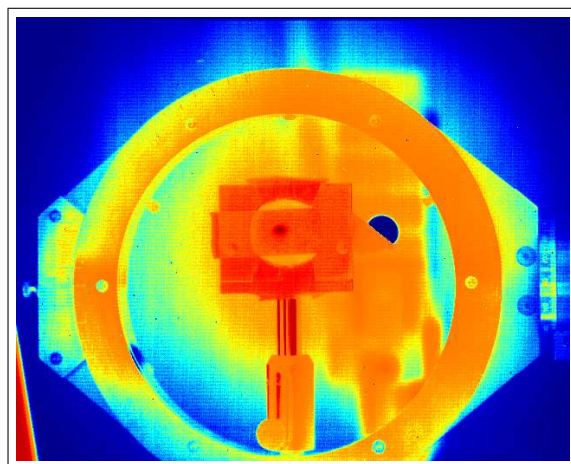
Figure 24. Alignment of sample alignment aperture in all directions in the IR.

Next, the sample is mounted with its normal as close as possible to the beam's

axis using visual inspection. The illuminated area of the sample is to be placed such that when θ_i increases, the illuminated area does not project off the sample. Next, θ_i is varied while the FPA is used to make sure that the illuminated area does not move across the face of the sample, just as it was done in the visible spectrum. If the FPA is not being used, one must use the sample alignment laser to ensure that the beam spot does not change position when θ_i is varied. This is difficult because the alignment laser is very dim. This process using the FPA is shown in Figure 25.
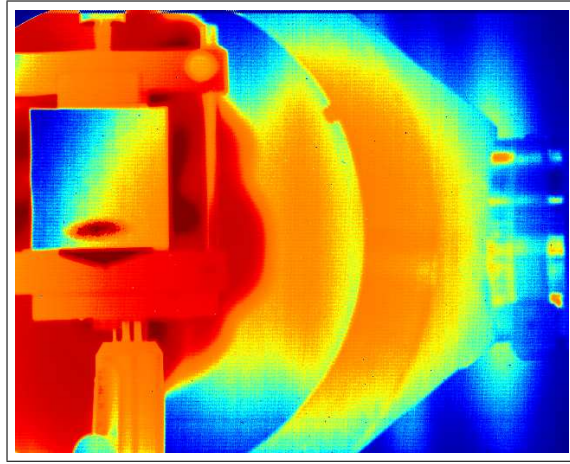
Figure 25. IR picture of beam pattern at a high angle of incidence confirming the illuminated location does not change with θ_i.

The final step is then to ensure that the sample's normal is aligned with the incident beam when $\theta_i = 0°$. First, the large aperture is closed down until it only allows beam to pass through to provide a reflective surface for alignment. Figure 26 shows a mirror placed upon the sample's face using the protective sheet provided with the mirror between the sample face and the mirror. This protective sheet should not harm the sample's surface, but it should be cleaned with compressed air to ensure nothing has been left on the face of the sample prior to measurement.

The specular reflection from the mirror and then the aperture is aligned with the center of the large external aperture in the FPA display. This should ensure the the sample's normal is aligned with the beam path within a few degrees, assuming that
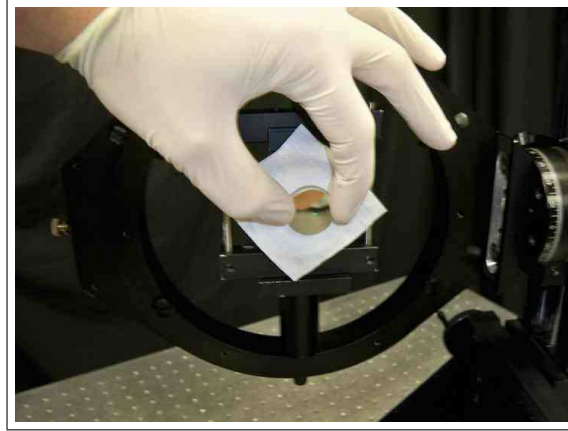
Figure 26. Photo of mirror used to provide specular return for sample alignment.

the mirror's normal is aligned with the sample's normal. Figure 27 shows an example of this, where the beam's path is not aligned so the reflection off of the aperture can be shown.
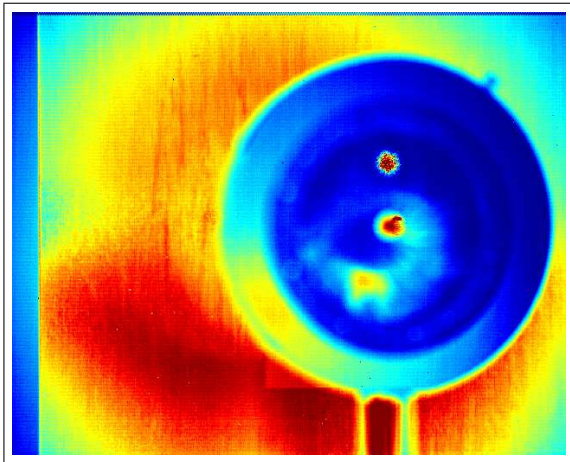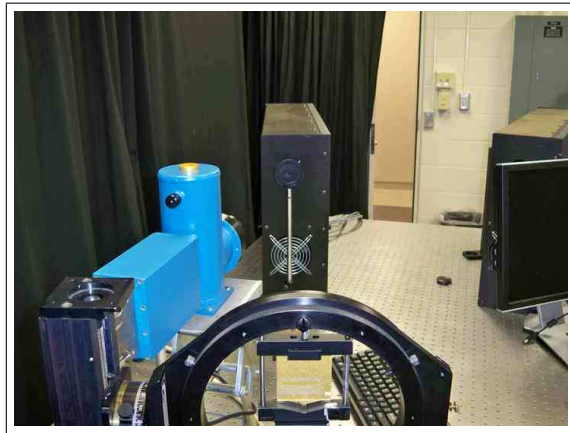
(a)   (b)

Figure 27. (a) Alignment of specular return with the beam path in the IR using the FPA. (b) Visible photo of physical layout.

! The reflections from any of the apertures in the IR could be a specular because they may be bare metal surfaces. Thus, the FPA needs to be placed near the specular direction of the reflection in order to see it. In this case, it needs to be as close to the sample as possible.

3.6 Matlab®Reflectance Software Suite

Table 6. Listing of Matlab®Reflectance Commands.

Function	Purpose
findDirectories()	Finds subdirectories containing a search string
readCASI()	Reads a CASI ASCII file
readCASIBatch()	Reads multiple CASI ASCII files
extractSet()	Extracts values or a range of values from a matrix
plot2DBSDF()	2D plotting utility
findInPlaneDHR()	Finds a DHR given a in-plane BRDF sweep
plotSampleRepeatability()	Plots all measurements in a set or percent difference
plotSampleComparision()	Plots the mean and/or standard deviation of a single incident angle for different samples
plotSampleCharacteristics()	Plots the mean and/or standard deviation for all incident angles for a single sample
plotSampleCharacteristics3D()	Same as plotSampleCharacteristics() except uses a 3D plot
plotPerecentDifferenceComparision()	Plots a single measurement comparison to a set of measurements

All plotting and data analysis in this thesis has been done using a MATLAB®reflectance software suite that was created for this study. It was inspired by the AFIT radar MATLAB®software suite. Table 6 shows a listing of the functions created for this study. The purpose of this software is to have a standard set of processing and plotting functions available to future students. The structure of this library is such that the common bond between all functions is the BRDF matrix. These functions read data formats, manipulate it, and then plots it. The current form of this BRDF matrix has all the information listed in columns, and this is done specifically to address the posibility of additional parameters if the CASI® is upgraded. If so, then only another column needs to be added to the standard format. The current variable represented in each column is in the order: θ_i, ϕ_i, θ_r, ϕ_r, λ, and BRDF value (from left to right). Future additions may include the sample position, polarized values instead of a single

BRDF value, or a cell array where the BRDF value is a Mueller matrix. Polarized measurements were not available in the IR during this effort, so this capability was not added. This software can be obtained by contacting the author.

3.7   Chapter Conclusion

This chapter has illustrated the difference between the mathematical definition of the BRDF and the nature of the physical BRDF measurements. The measurement equipment was thoroughly introduced, and the in-plane geometry of the measurements was also presented graphically. This concept of in-plane measurement is critical to understanding the analysis of the data. Finally, the process of aligning and setting up the sample in the IR was presented in order to document the process and address any issues it may cause in the subsequent analysis. Finally, a listing of the software used is provided to let the reader know it is available for use by contacting the author.

IV. The Math of Measurement and A **Spectralon**®Standard

T his chapter's primary purpose is establish procedures for calibration with well defined samples. It first investigates what an ideal BRDF standard would be if one existed. The best performing physically realizable sample in the visible spectrum is Spectralon®. Spectralon®is the universally accepted standard for reflectance and BRDF in the visible spectrum. The current state of this standard and those like it, including any available published information about it, is presented to lay down the framework for its measurement and analysis. In order to measure Spectralon®and confirm these results, the mathematical constructs and techniques necessary to calibrate, verify, and analyze the measurements in this study are presented. Finally, the measurements of Spectralon®are used to verify these methods and the AFIT CASI® in the visible, where this problem is much more well defined. It also provides a benchmark for standards in the IR.

4.1 An Ideal BRDF Standard

An ideal BRDF standard is a mathematical construct. The derivation of a purely Lambertian reflector was provided in Section 2.1.1, and the result is

$$f_{BRDF} = \frac{1}{\pi} = 0.3183. \tag{41}$$

These mathematical properties are self evident, but there are also other properties that are highly desired in a physical sample other than just 'diffuseness'. The first is the low variation of the BRDF across the surface of the sample; this is the property of repeatability for a single sample. This means that the BRDF should be independent of the location on the sample. The second property is that of reproduceability, as defined here, or that each independent sample produces the same characteristics and

BRDF. These properties are listed in Table 7.

Table 7. Ideal BRDF Standard Characteristics.

Property
Isotropic, not a function of ϕ_i
Not a function of sample surface position
Perfect Repeatability
Perfect Reproducibility
Perfectly Diffuse, $f_{BRDF} = \frac{\rho}{\pi}$
Not Transmissive, $\tau = 0$
Not Absorptive, $\alpha = 0$
Perfectly Reflective, $\rho = 1$
Not a function of θ_i, remains diffuse

4.2 Spectralon®

Unfortunately, there is no such thing as the ideal standard described in Section 4.1, but the next best thing is Spectralon®and its Polytetrafluoroethylene (PTFE) derivatives. Spectralon is 'a solid, thermoplastic based upon PTFE that exhibits the highest diffuse reflectance of any material or coating, up to 95% from 250-2500 nm, and 99% from 400-1500 nm.'[4]. Spectralon®is produced by Labsphere®, and is so diffuse because the scattering is primarily a bulk interaction. Another very similar standard is pressed PTFE powder, and it is also a bulk reflector with its properties based upon the compression of the powder. This is no surprise as it is made of the same material and only the preparation differs. The third derivative of this family of standards is sintered PTFE, where PTFE is exposed to heat to bond the PTFE power together for durability. Unfortunately, sintered PTFE exhibits much more surface reflection and is less diffuse[22].

4.2.1 History and Standards.

Initial research into PTFE goes all the way back to the late 1970's[59]. Published laboratory intercomparision studies, often called round robins, using this standard date to 1985[60]. The study of PTFE and Spectralon®has been quite extensive. A good description of the effect of polarization on Spectralon®, and why it behaves the way it does, is contained in Haner's paper[26]. A large body of knowledge responsible for the study of Spectralon®has been motivated by space-based remote sensing applications where it is used for instrument calibration[18; 22].
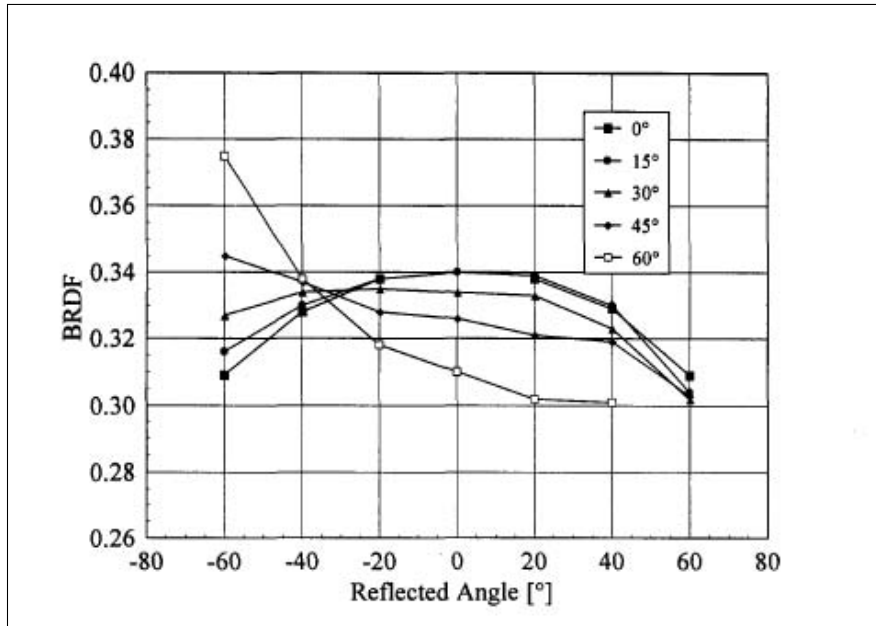
Figure 28. BRDF as a function of reflected angle at 632.8nm for a pressed PTFE plaque at the indicated incident angles. The relative expanded uncertainties of the BRDF, less than 0.2 percent, are within the sizes of the symbols.[11, pg. 28]

Nevertheless, while the spectral DHR characteristics are well defined from many sources, standard information for BRDF measurement is often vague and lacking. The National Institute of Standards and Technology (NIST) lists its special publication 250-48[11] as its BRDF reflectance standard. This special publication's only BRDF information is supplied in Figure 28 with its original caption. Unfortunately, these

50

measurements are for pressed PTFE and not Spectralon®. There is not a significant difference in their BRDFs when compared to other materials, but the difference is large enough to be a problem for calibration. A comparison of these two samples is presented in Early's study[22], and it is shown in Figure 29.
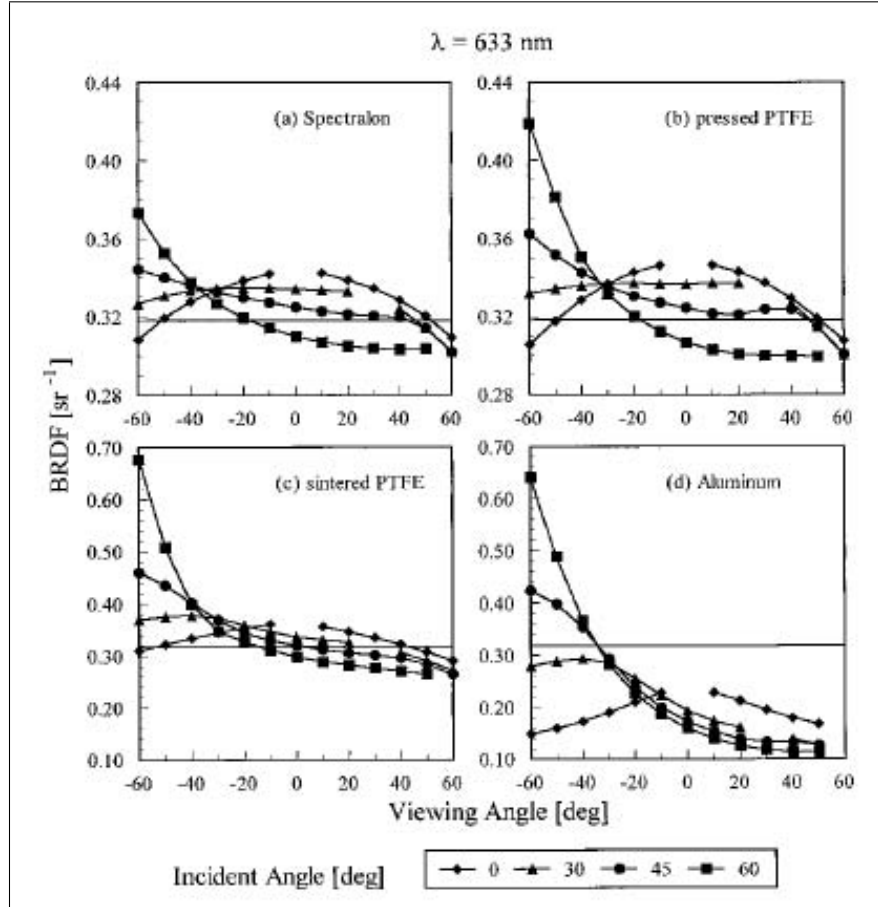
Figure 29. An intercomparision of BRDF from 4 different samples listed in Early's study. Measurements listed were performed at NIST as a function of viewing angle at a wavelength of 633nm from the NIST measurements. The horizontal line is the ideal value of $1/\pi \mathrm{sr}^{-1}$. [22, pg. 1082]

A search of Labsphere®'s standards did not produce a full set of Spectralon®BRDF measurements either. Actual Spectralon®samples obtained from Labsphere®contained only spectral DHR information. Labsphere®'s website links to two sources, the first is a standards brochure that contains only DHR information[4], and the second is

51

a technical report labeled 'A Guide to Reflectance Coating and Materials'[45]. The only BRDF information contained in this document is shown in Figure 30. The fact that there are only two incident angles provided and no repeatability information leaves it lacking for a source of BRDF information to be used for verification.
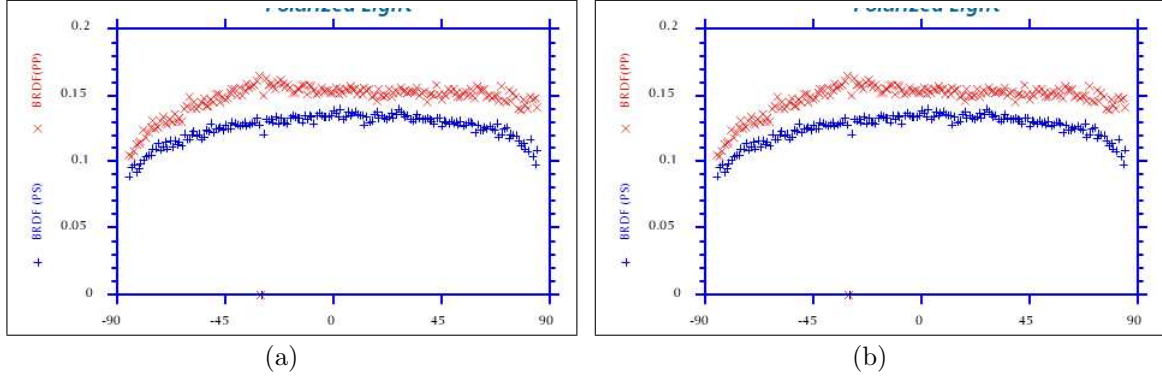
Figure 30. **Spectralon**®**BRDF Standard Information from Labsphere**®**'s technical report(a) Polarized BRDF information($\lambda = 633\text{nm}, \theta_i = 30°$). (b) Polarized BRDF information($\lambda = 633\text{nm}, \theta_i = 60°$)[45, pg. 14]. Reproduced at original size.**

The best source of Spectralon®measurements comes from a laboratory intercomparision of various samples performed by Early[22]. It has a respectable set of measurements for Spectralon®, and these measurements come from a reliable source, NIST. These are the measurements used in this study to verify the AFIT CASI® BRDF measurements of Spectralon®. Nevertheless, there are two limitations to this set of data. First, there is not a polarization listed. A safe assumption is that of an SU measurement where the incident beam is polarized perpendicular to the plane of incidence, or s-polarized, and the detector is unpolarized. The s-polarization is generally the default laser orientation to avoid the Brewster angle for transmissive samples. The second problem is that there is not a table of values from which to create the data. In order to create a data set, the open source program *Enguage Digitizer* was utilized. This program allows the creation of a data set from a figure alone[2]. This reproduction of Early's data is presented in Section 4.4.2.

52

4.2.2 A Standard Set of Measurements.

Labsphere®'s technical report references the American Society for Testing and Materials (ASTM) Standard E1392-90 as an 'extremely detailed and lucid treatment of the subject of BRDF measurement'[45, pg. 14]. This standard was replaced by ASTM standard E1392-96 in 2002, but unfortunately, it has since been withdrawn in 2003 without a replacement[1]. In light of this information, it was decided to adhere to the incident angles listed in NIST's BRDF standard document and Early's study.

If NIST's BRDF standard document[11] and Early's study[22] is used to decide on the θ_i's to be used in this study, θ_i should be 0°, 15°, 30°, 45°, and 60° with a detector span of $-60° \leq \theta_r \leq 60°$. It appears that Early neglects $\theta_i = 15°$ because the BRDF values are so close to the $\theta = 0°$ values for Spectralon®. In this document, $\theta_i = 0°, 15°, 30°, 45°, 60°$, and 75° will be used. This is because the extra information provides more data to fit a BRDF model to. A span of $-85° \leq \theta_r \leq 85°$ was also chosen for the reflected angle range for purposes of DHR conversion and BRDF model fitting.

4.3 Measurement Conversion, Processes, and Fitting

4.3.1 BRDF to DHR Conversion.

Before any BRDF measurements with reference to a calibrated reflectance samples are presented, the method of translating an in-plane BRDF measurement to DHR must be understood. A key point to be made here is the intuitive relationship between DHR and the BRDF. A good conceptual analogy would be that of the relationship between instantaneous speed, analogous to the BRDF, and distance traveled, analogous to the DHR. The integration of the instantaneous speed over time giving distance, is conceptually similar to the integration of the BRDF over the hemisphere

centered at the sample's surface. This relationship is

$$\rho_{DHR}(\theta_i, \phi_i) = \int_{2\pi} f_{BRDF}(\theta_i, \phi_i, \theta_r, \phi_r)cos(\theta_r)d\Omega_r. \tag{42}$$

Unfortunately, it is very time and resource prohibitive to get measurements over the entire hemisphere. Therefore, the in-plane measurement is often all that is available, but it is all that is needed if the sample is isotropic. Figure 15 showed a very good physical depiction of what in-plane measurement is. The mathematical definition of an in-plane measurement is that, $\phi_i = \phi_r + 180°$. In a strict sense, it is dependent upon ϕ_i, but if a sample is isotropic, $\phi_i = 0°$ by convention.

If the sample is truly isotropic, and $\theta_i \approx 0°$, this creates symmetry in every possible in-plane cut of the hemisphere, or stated alternatively, the cross-section of the BRDF in the hemisphere does not change as this plane is rotated about the z-axis. Therefore, a single in-plane BRDF near normal incidence should be all that is required to calculate the DHR from the BRDF.

The second problem is that BRDF measurements are simply an average over the solid angle of the aperture used for the measurement, and therefore, it is only a sampling of the actual function. Using this knowledge and a Riemann sum for discrete integration, it can be stated that the continuous integration stated in Equation (42) then becomes,

$$\rho_{DHR} = \pi \sum_{n=1}^{N-1} \Delta\theta_r \overline{f_{BRDF}} cos(\overline{\theta_r})sin(\overline{\theta_r}), \tag{43}$$

$$where,$$

$$\Delta\theta_r = |\theta_r(n = i + 1) - \theta_r(n = i)|,$$

$$\overline{f_{BRDF}} = (f_{BRDF}(n = i + 1) + f_{BRDF}(n = i))/2, and$$

$$\overline{\theta_r} = (\theta_r(n = i + 1) + \theta_r(n = i))/2.$$

The final issue in this conversion is introduced by the CASI® itself. Unfortunately, there is a 4° occlusion on either side of the retro-reflection from the gonio-arm and detector. In addition, the measurement range for θ_r is only valid from $-85°$ to $85°$ according to the manufacturer SMS. Thus, there must be some type of interpolation or function fitting used when calculating the BRDF.

There are many different functions that could be used to estimate the missing data. Every available function in the MATLAB®data fitting toolbox was evaluated for fitting to these profiles. Obviously, a straight interpolation was one possibility, but a three-term Gaussian fit and what is known as a rational fit both worked very well. After much experimentation, it was clear that the Gaussian fit was best suited because it is already used in most of the phenomenological models, and it was the most resilient to odd distributions and outliers. Thus, a three-term Gaussian best fit function is used to calculate DHR and its bounds for the rest of this study, unless otherwise noted. Figure 31 shows an example of these fits applied to the Spectralon®sample data at $544nm$. Because a fit must be used, there is always a certain amount of uncertainty in the DHR calculated from BRDF.

The other point that must be mentioned here is the idea of reflectance factor which is often used in technical reports. Reflectance factor is not a reflectance, or DHR. Where as reflectance factor is a function of θ_i, ϕ_i, θ_r, ϕ_r, and λ. Reflectance is only a function of λ, and DHR is only a function of θ_i and λ. This is simply a way to convert a single BRDF data point to DHR, and it makes the assumption that the BRDF is completely Lambertian. Reflectance factor is

$$R_{factor}(\theta_i, \phi_i, \theta_r, \phi_r, \lambda) = \pi f(\theta_i, \phi_i, \theta_r, \phi_r, \lambda). \qquad (44)$$
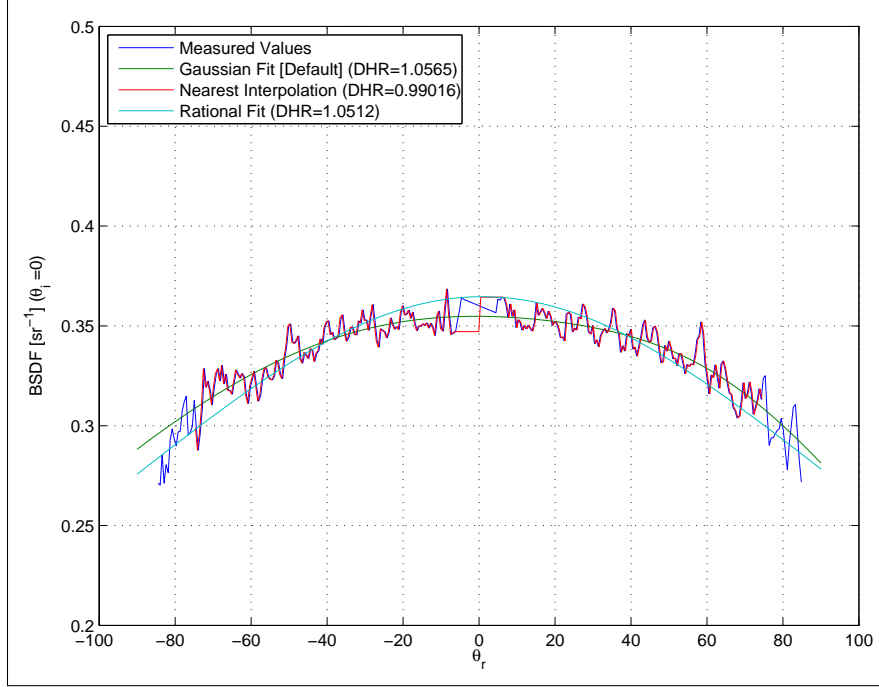
Figure 31. A fit of the mean of the data to a three term Gaussian used to calculate DHR from the measurement.

4.3.2 Sample Repeatability Measurement Process.

A good BRDF standard should have some amount of repeatability, which means that the BRDF measurement should be relatively constant over a single sample's surface. Reproduceability is the ability to demonstrate this over multiple samples, which is beyond the scope of this effort. This demonstration of repeatability is necessary because it is not possible to get the same exact illumination area each time the sample is mounted. There are two ways presented in this study to estimate this repeatability. The first is using the percent difference from the measurement set's mean, or Percent Difference from the Set Mean (PDM), and the second is using a relative standard deviation, which is used in later analysis and presented in Section 6.4.5.

Using standard deviation alone requires multiple samples for some statistical significance, but it is also sensitive to the magnitude of the measurement. On the other hand, a percent difference only requires a reference. The percent difference method

56

has been used extensively in published robin-round studies for the intercomparision of measurements made by different labs for both DHR and BRDF measurements; an example is shown in Early's round-robin paper[22]. This thesis primarily uses the PDM technique. The down side to using this technique only is that it does not consider the distribution of the error.

Depending on how the sample alignment and sample's illuminated position change, there are three forms of variance between measurements. These are deviations from the equipment, from the alignment, and from the sample itself. To isolate deviation, or variance, from the equipment, one can just repeatedly measure the same position on the sample. An example of this using the CASI® and Spectralon®will be shown in Figure 37 later in the chapter. It shows the percent difference from the mean for each measurement in the set. There is still some variance due to the sample, as will be shown, but this is the best method availble for isolating the measurement variance.
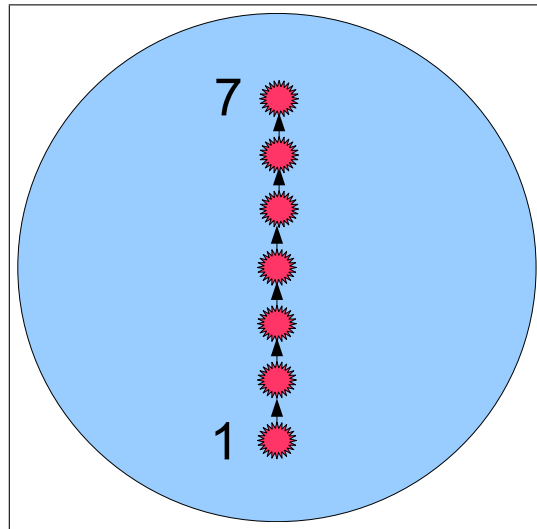
Figure 32. A description of how multiple measurements are taken on a single sample to demonstrate repeatability.

The remaining two sources of variance cannot be isolated without the variance from the equipment, but the variance due to the sample's surface variance can be isolated from the sample alignment variance. To do this, one must make all the

measurements with the same sample alignment, and raster the illuminated position on the sample, as depicted in Figure 32. Unfortunately, if these measurements are compared to measurements taken by different equipment, all three sources of variance will manifest themselves. This must be kept in mind when comparing data.

The raster procedure used on each sample in this study is depicted in Figure 32. It was most efficient to lower the sample, or conversely raise the beam accross the face of the sample. The time available for this study was limited, so the arbitrary choice of seven measurements across the face of the sample was chosen. The first measurement in a set is aligned so that even at higher incident angles, the entire beam is still on the face of the sample.

4.3.3 Model Fitting Techniques.

The last analysis technique needed is the fitting of the phenomenological BRDF models, presented in Section 2.2, to the measured data. Fitting techniques are used in this study in order to provide a way to quantify the differences in 'diffuseness' between the measured samples and to provide a three dimensional representation of the data. The fitting techniques used in this thesis minimize the Mean Squared Error (MSE) between the data and the model. The MSE is defined here as

$$\sigma_{MSE} = \sqrt{\frac{1}{N} \sum [f_{model}(\lambda, \theta_i, \theta_r, \phi_r) - f_{meas}(\lambda, \theta_i, \theta_r, \phi_r)]^2}, \qquad (45)$$

where σ_{MSE} is the MSE, N is the number of samples taken, f_{model} is the BRDF calculated by the model, and f_{meas} is the measured BRDF.

A slight variation on this technique presented by Torrance[57, pg. 14] emphasizes θ_r near the sample normal in fits by means of using a $cos(\theta_r)$ in the MSE function as shown in Equation (46). Although, this may have some potential for analysis, this thesis will not use any weighting in the fits because the objective of fitting to the

functions is to have a metric for 'diffuseness'.

$$\sigma_{MSE} = \sqrt{\frac{1}{N}\sum[[f_{model}(\lambda, \theta_i, \theta_r, \phi_r) - f_{meas}(\lambda, \theta_i, \theta_r, \phi_r)] \times cos(\theta_r)]^2} \qquad (46)$$

Fitting a BRDF model to data is not a trivial task because of the number of variables to must be varied. The dependent variables, $\lambda, \theta_i, \theta_r,$ and ϕ_r, and independent variables unique to each model, typically three or more, must all be varied when fitting a model to the data. Figure 33 demonstrates this process of finding the least MSE for the Cook-Torrance model and Spectralon®data at $\lambda = 633nm$.
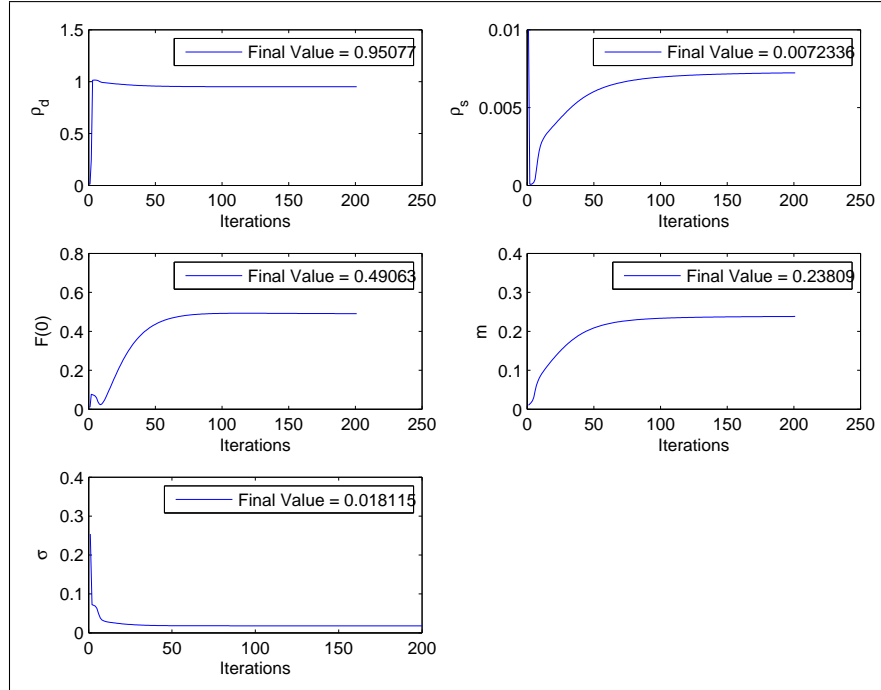
Figure 33. An example of the convergence of the Cook-Torrance model to measured data. Each variable is varied until there is stability in the solution.

The key to fitting these models efficiently is to find the minimum of the MSE function with a non-linear multivariable equation solver. The MATLAB®function of choice for this task is $fminunc()$. The choice of unconstrained variables is due to

59

the fact that the convergence of the independent variables is stable and tends to be independent of initial conditions. The key here is to cycle through each independent variable separately finding the minimum MSE, one variable at a time, using the previous solution when solving for the next variable. The fit convergence is always a good check on whether the solution is stable and valid. For this study, most fits converged to a stable solution within about one hundred iterations.

4.4   Measurement

4.4.1   Spectralon®Sample Description.

(a)   (b)
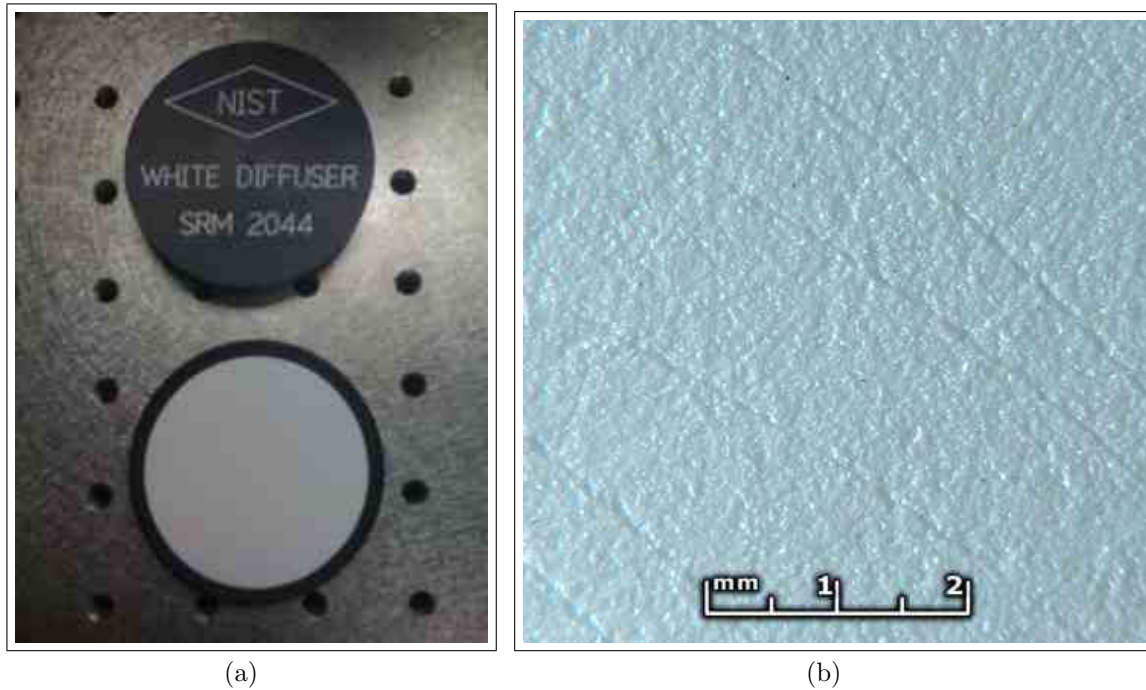
**Figure 34. (a) Photo of NIST calibrated Spectralon®sample 2044a-01-2.
(b) Surface microscope photo of NIST calibrated Spectralon®sample 2044a-01-2**

Figure 34 shows the Spectralon®sample used in this study. It is a NIST calibrated sample, serial number 2044a-01-2. NIST refers to Spectralon®as Standard Reference Material (SRM) 2044a. This specific sample's Certificate of Analysis was granted on

April 2, 2003 and expired on October 1, 2005. Nevertheless, Spectralon®has been shown to be a material that is very stable, and it should still be suitable for this research[25]. Sample 2044a-01-2 is a Spectralon®disk with a diameter of $5.1cm$ press fitted into a round Delrin container with a diameter of $6cm$ and a thickness of $1.5cm$.
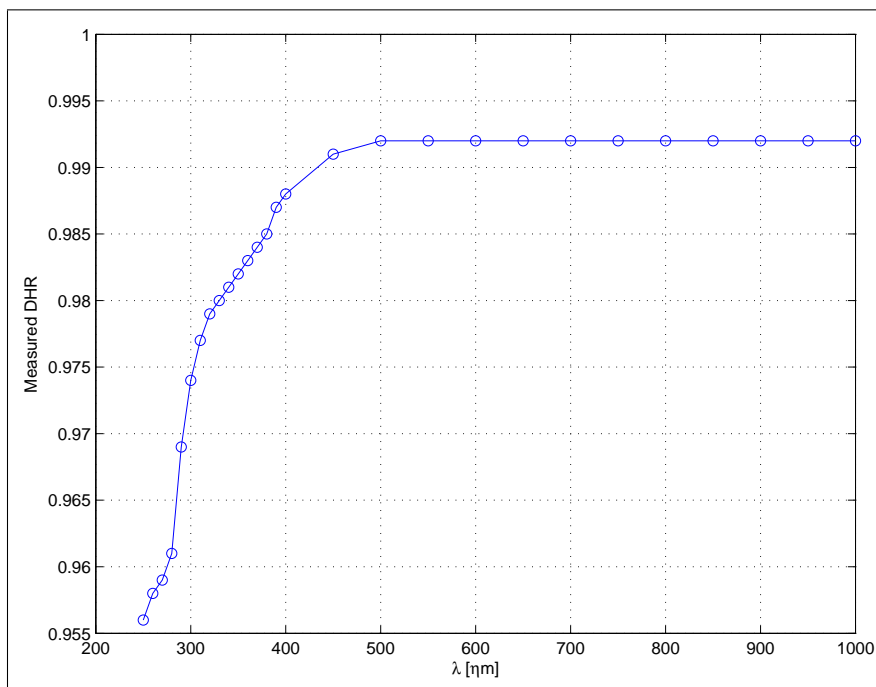
Figure 35. A DHR vs. wavelength plot reproduction from the calibration certificate for Spectralon®sample 2044a-01-2.

The calibrated spectral DHR for this sample from $\lambda = 250nm$ to $\lambda = 1000nm$ is shown in Figure 35. The importance to this study are the values at wavelengths of $544nm$ and $633nm$ which both have a DHR of 0.992. This will allow us to calibrate the CASI® later in the analysis, and then compare our calibrated data to Early's BRDF measurements. It also shows Spectralon®'s flat spectral characteristics in the visible and near IR spectrums.

4.4.2 Early's Data.
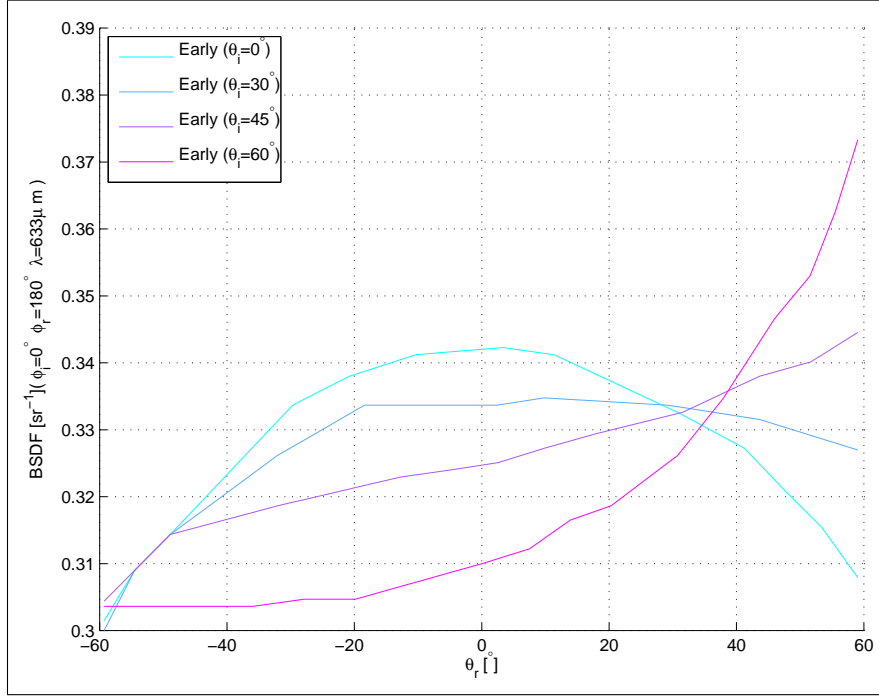
Figure 36. A reproduction of Early's Spectralon®measurements made at NIST ($\lambda = 633$nm)[22].

Early's figures must be turned into data in order to analyze and compare Early's

Spectralon®measurements made at NIST with those made by AFIT's CASI® . Un-

fortunately, the process of converting the figure into data leads to some uncertainty,

but it is tolerable because it is still more advantageous than only comparing to DHR

values without any validation. The reproduction of the Spectralon®data in Figure 29

is presented in Figure 36. The main difference between the two is that Early uses

negative reflected angles for forward scatter whereas the convention in this study is

to use positive angles for forward scatter. The data shows that Spectralon®is very

diffuse especially at angles near normal incidence, but it can be seen, as θ_i goes to

higher angles of incidence, the sample does become more specular. This is to be

expected as the bulk interaction becomes a Fresnel surface reflection. Nevertheless,

even these values are much lower than any other diffuse presented in the literature.

4.4.3 Spectralon®Measurements.

This section presents the repeatability of the CASI® at visible wavelengths, the mean of the entire measurement set for Spectralon®, and the repeatability of Spectralon®. DHR calculations, measurement comparisons, and removal of any measurement errors are presented in the analysis section. The data in this section is uncalibrated. Therefore, this section only shows the characteristics of Spectralon®sample and its repeatability. This must be kept in mind when evaluating the data in this section. This section is further broken down into measurements for each of the visible wavelengths available on the AFIT CASI® .

4.4.3.1   544nm.
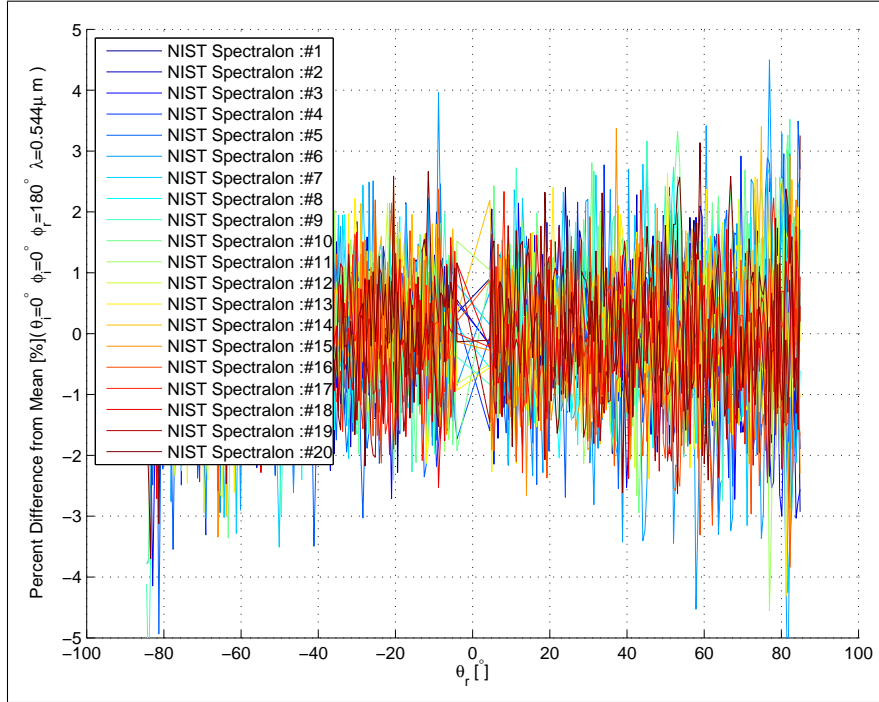
Figure 37.   A plot of the percent difference from the mean for 20 measurements at the same point and alignment on Spectralon®sample 2044a-01-2 at $\lambda = 544$nm.

Figure 37 shows the PDM for a measurement set where the illumination spot and

sample alignment is kept the same for 20 measurements. This primarily demonstrates the CASI® 's repeatability using this sample. It shows that for the vast majority of the measurements that the PDM is typically less than ±2%. This is good because it agrees with the CASI® 's literature and documentation, which is presented in Section 3.2.
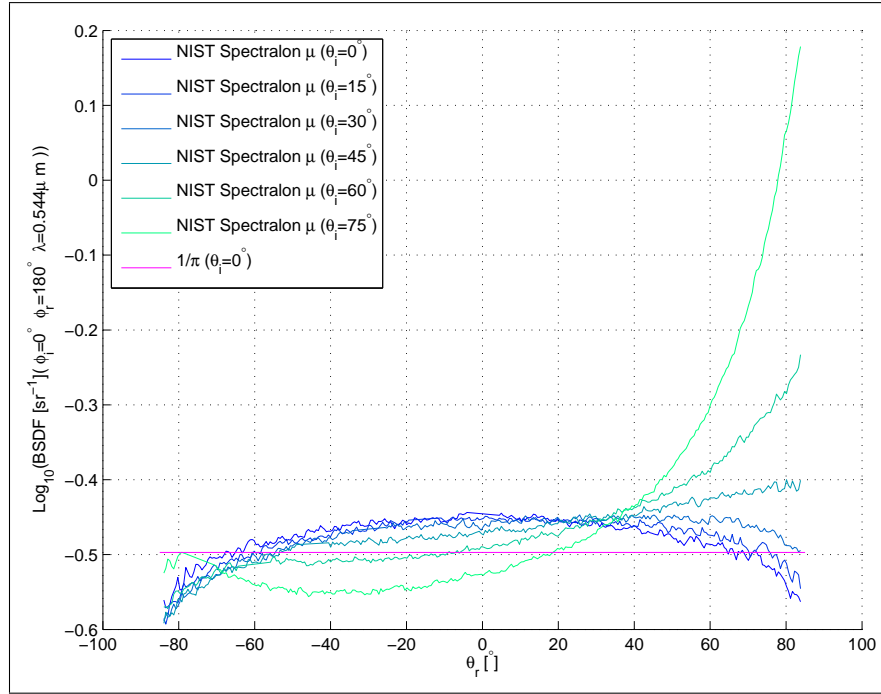
Figure 38. **BRDF Measurements of NIST calibrated Spectralon®sample at** $\lambda = 544$nm.

Figure 38 presents a logarithmic plot of the mean for the full measurement set with the same alignment discussed in Section 4.2.2. It also adds the value of an ideal BRDF standard, $1/\pi$, for reference and comparison. The profile of the measurements, or shape, seems to agree with Early's data, and it remains very diffuse up to about $\theta_i = 60°$. The standard deviation is also so low for this sample that it only works to clutter the plot, and it is not plotted along with the mean values. Another very interesting effect to be mentioned is that regardless of the incident angle, Spectralon®has nearly the same BRDF value at approximately, $\theta_r = 30°$. It is not immediately clear why

this happens, but it is definitely noteable.

The last parameter to mention is the repeatability of the measurement accross the face of the sample, which is a direct indication of the confidence that can be had in the measurement. Figure 39 (a) shows the repeatability approaches that of the instrument when $\theta_i = 15°$, but it can definitely be seen that it is dependent on θ_r. This effect is even more obvious in Figure 39 (b) when $\theta_i = 75°$. This is due to the fact that there is more surface scatter and the BRDF is more dependent on the surface of the sample than on the uniformity of the bulk material.

4.4.3.2   633nm.

Next, the same measurements at $\lambda = 633nm$ presented with the same format. This is also the set of measurements that will be directly compared with Early's data because they are at the same wavelength. Figure 40 shows the same measurement made 20 times with the same alignment and position on the sample. In this case, the results are still encouraging, but not quite as good as the $\lambda = 544nm$ case. Regardless, the percent difference from the mean of the measurements is still typically $\pm 2\%$.

Figure 41 shows the mean from the full set of measurements. A BRDF very similar to the measurements at $\lambda = 544nm$ is expected, and the results tend to confirm this. Nevertheless, there are some notable differences. The first is that the measurements are much higher, this is due to the lack of calibration and is explained in the analysis section. The second difference is the fact that the intersection of the each θ_i has moved to $\theta_r \approx 40°$. This is most likely due to the fact that although the wavelength has changed, the size of the particles in the bulk structure has not.

Figure 42 shows the repeatability for $\lambda = 633nm$ at $\theta_i = 15°$ and $\theta_i = 75°$, as shown previously for $\lambda = 544nm$. There is not an appreciable difference of any kind other than the PDM at $\theta_i = 75°$ seems to be a little cleaner.
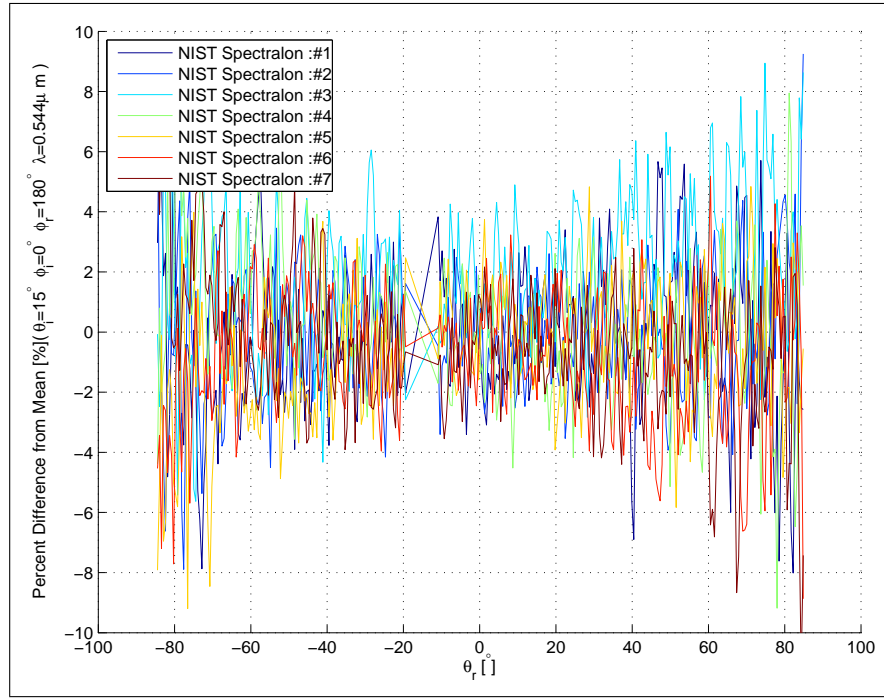
(a)
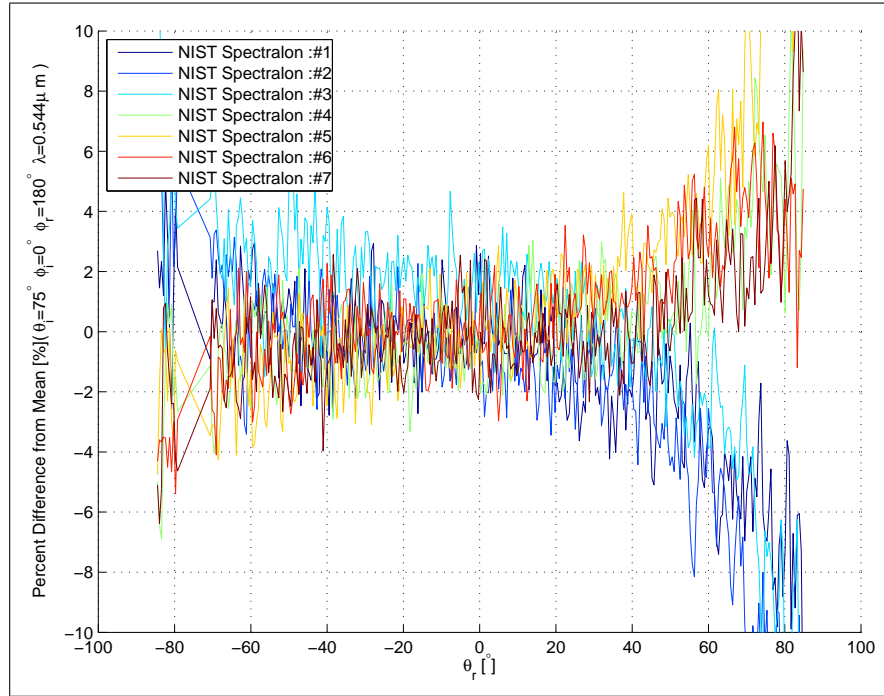
(b)

Figure 39. (a) Sample repeatability demonstrated as a percent difference from the mean where $\theta_i = 15°$. (b) Sample repeatability demonstrated as a percent difference from the mean where $\theta_i = 75°$.
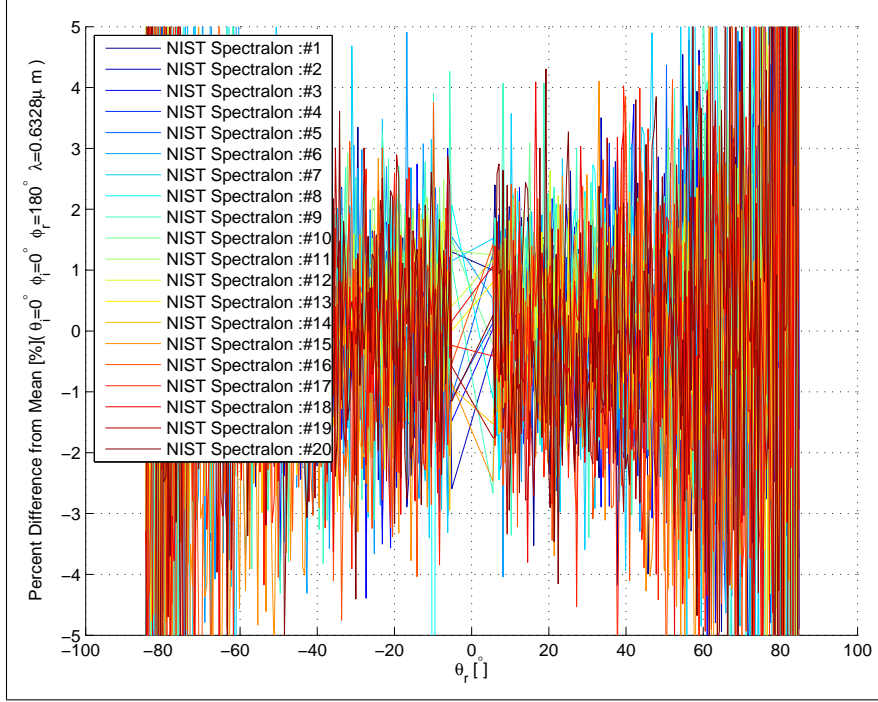
Figure 40. A plot of the percent difference from the mean for 20 measurements at the same point and alignment on Spectralon®sample 2044a-01-2 at $\lambda = 633$nm.

4.5 Analysis

In this section, the AFIT BRDF measurements are calibrated to the DHR measurements, and the calibration is validated by comparison with the BRDF data from Early's study. This section will demonstrate the necessity of calibrating BRDF measurements.

4.5.1 DHR Confirmation of Early's Data.

An analysis of Early's data is presented here to check its validity without making any assumptions about it. If a DHR calculated from this BRDF data matches a standard Spectralon®DHR value, it will validate Early's data. This data then can be used later to validate the BRDF calibration of the AFIT measurements.

Figure 43 shows a three-term Gaussian fit to Early's data. In this specific case,
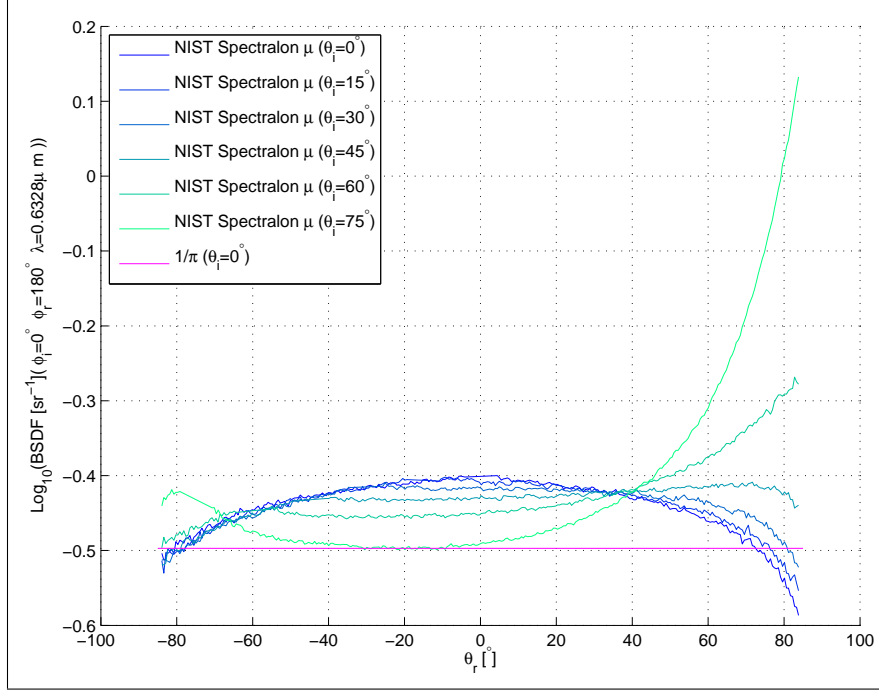
Figure 41. BRDF Measurements of NIST calibrated Spectralon®sample at $\lambda = 633$nm.

the fit is very important because the data only extends from $-60° \leq \theta_r \leq 60°$, and data in the range $-90° \leq \theta_r \leq 90°$ is needed. This adds some uncertainty to this calculation, but it must also be noted that the most important data is near $\theta_r \approx 45°$. This because of the radiometry and calculus that leads to the discrete in-plane DHR calculation introduced in Equation (43). Section 5.5 quantifies this argument for measurements taken by the CASI® . The DHR calculation from the Gaussian fit is 0.997. This is very close to the DHR of 0.99 that Spectralon®would be expected to have at this wavelength from the published standards. As DHR measurements from this specific sample are not available, this comparison will have to suffice. The results from this specific case do much to validate this process even with the limited data.
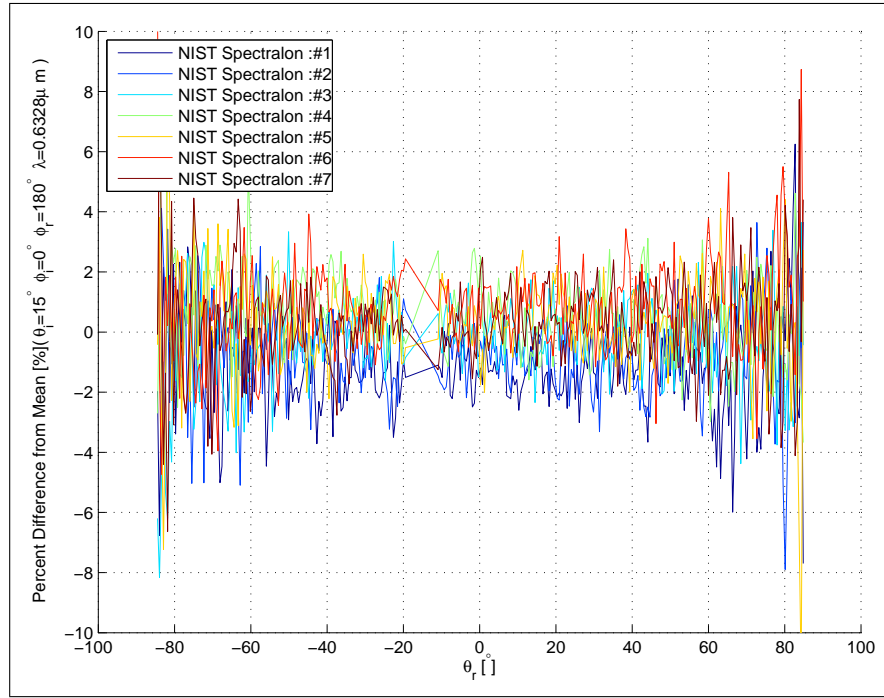
(a)
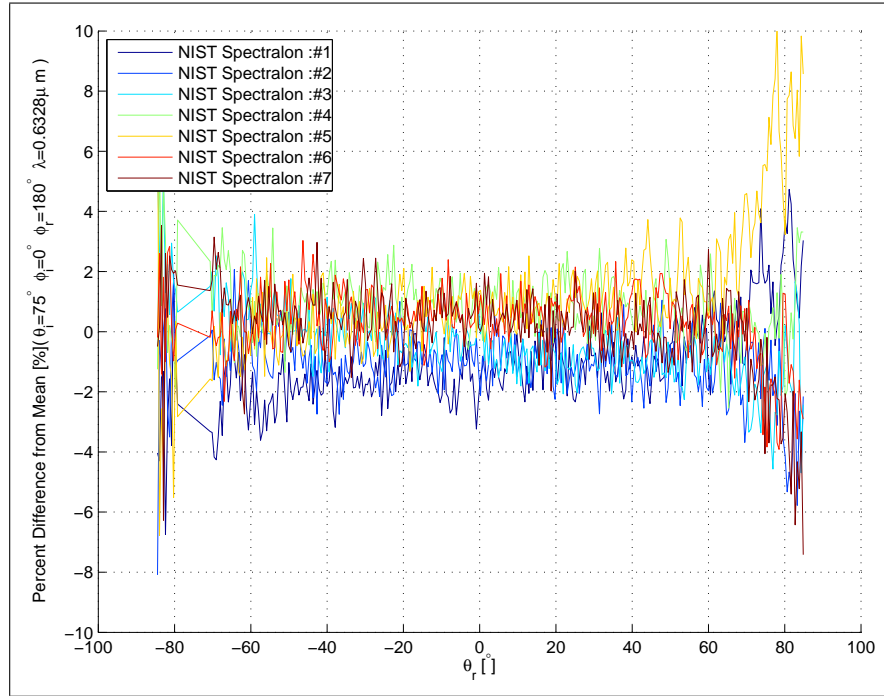
(b)

Figure 42. **(a) Sample repeatability demonstrated as a percent difference from the mean where $\theta_i = 15°$. (b) Sample repeatability demonstrated as a percent difference from the mean where $\theta_i = 75°$.**

69
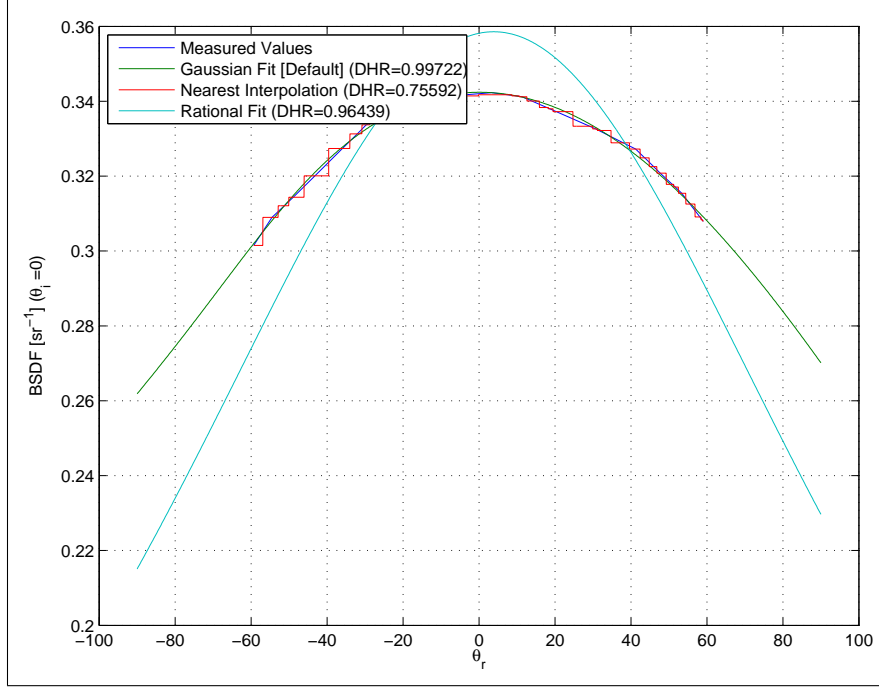
Figure 43. Plot of a three term Gaussian fit and DHR calculation from Early's data.

4.5.2 DHR Calculation.

Figure 44 shows the BRDF comparison and calculation of DHR from the AFIT measured NIST Spectralon®sample at $\lambda = 544nm$, $\lambda = 633nm$, and from Early's Spectralon®sample at $\lambda = 633nm$ before any calibration is performed on the AFIT data. At first inspection, it appears the AFIT measurements are both quite high and it looks like an additive bias, but this is not the case. This is because all the terms of BRDF measurement equation are multiplicative. This can be shown if a value is added to compensate; the BRDF profiles at $\lambda = 633nm$ do not match. The DHR values also do not match the NIST calibrated Spectralon®sample, which has a DHR of 0.992 at both $\lambda = 544nm$ and $\lambda = 633nm$.

Figure 45 shows the BRDF comparison and DHR calculation after the calibration of the AFIT measurements. The adjustments applied to the data are simple multiplicative ratios between the DHR calculated from the BRDF measurements and the
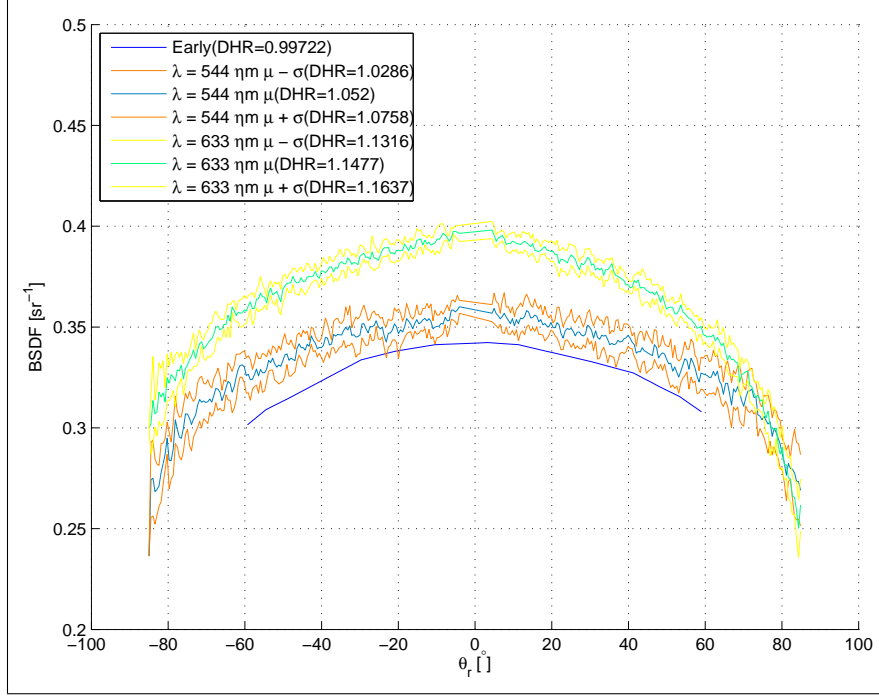
Figure 44. DHR comparison of uncalibrated measurements of NIST Spectralon®sample and those taken from Early's paper.

measured DHR. The corrective factor is

$$C.F.(\lambda) = \frac{DHR_{DHR}(\lambda)}{DHR_{BRDF}(\lambda)}, \tag{47}$$

where $C.F.(\lambda)$ is the corrective factor to be applied to each BRDF measurement point, $DHR_{DHR}(\lambda)$ is the measured DHR, and $DHR_{BRDF}(\lambda)$ is the DHR calculated from the BRDF measurements. After this corrective factor is applied, the BRDF measurements and their profiles agree very closely with each other and Early's data. In addition, the DHR also agrees very closely with that of the measured DHR.

Although this method is technically correct because all the BRDF measurements would be off by the same multiplicative factor, it is using a weighted integration to calculate the DHR and subquently this factor. Therefore, the measurements near $\theta_r \approx 45°$ are much more important than other BRDF values in this calibration method

71
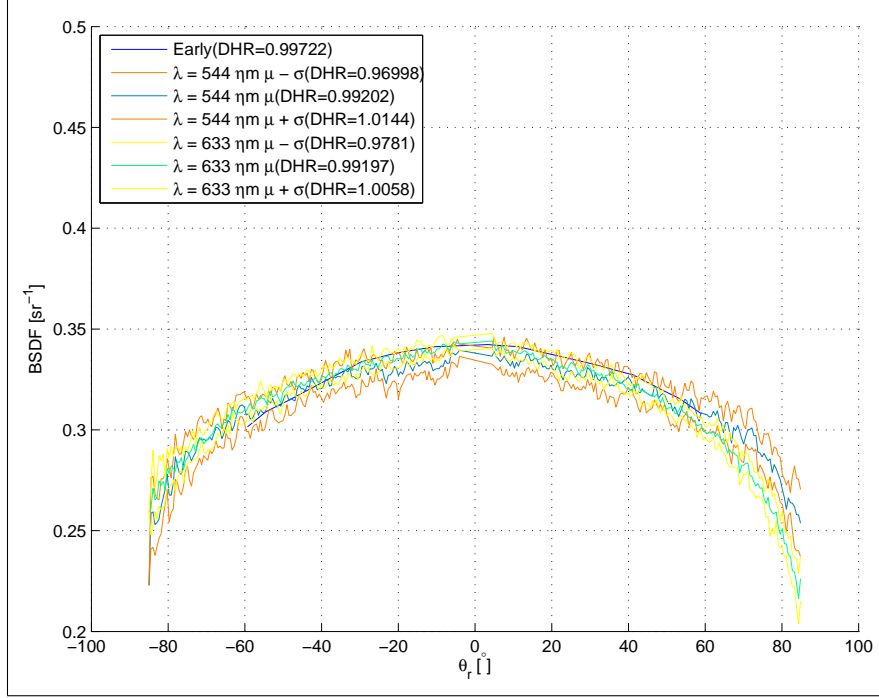
Figure 45. DHR comparison of calibrated measurements of NIST calibrated Spectralon®sample and those taken from Early's paper with calibration.

due to the $sin(\theta_r)cos(\theta_r)$ term in Equation (43), which is used for the calculation of DHR. If one was calibrating to BRDF measurements only, an average multiplicative corrective factor would be calculated from the entire measurement set. This is something that needs to be kept in mind when using DHR measurements to calibrate BRDF measurements. This is another reason why direct BRDF values should be used for calibration.

> ! A BRDF calibration using measured DHR weights the relative importance of BRDF data with a $sin(\theta_r)cos(\theta_r)$ term, making BRDF measurements near $\theta_r \approx 45°$ more important for this type of calibration.
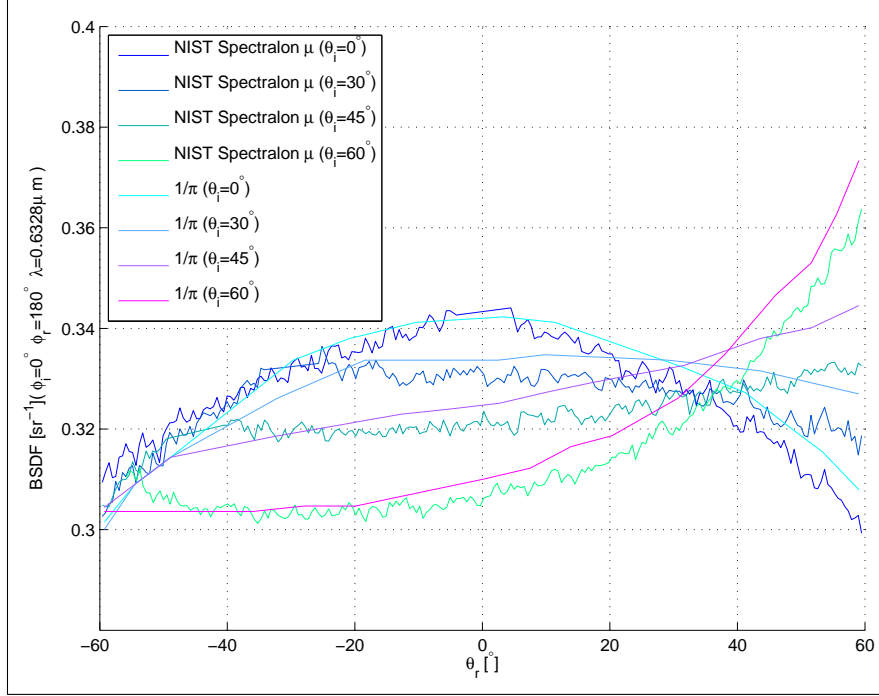
Figure 46. The comparison between Early's **Spectralon**®full measurement set and measurements of NIST **Spectralon**®sample 2044a-01-2 made with **AFIT's CASI**® at $\lambda = 633$nm.

4.5.3 BRDF Measurement Validation.

The last step is to validate the DHR calibration. This is done by directly comparing AFIT's calibrated BRDF data to Early's BRDF data to verify it visually and using a percent difference. It is not necessarily productive to compare BRDF measurements at different wavelengths because, as was seen in the measurements section, the 'crossover' point was not the same at different wavelengths. Thus, the BRDF is not the same at different wavelengths for the entire BRDF. Figure 46 shows the direct comparison between Early's **Spectralon**®measurements and the measurements made with the AFIT CASI® at $\lambda = 633nm$. The values line up relatively well considering how the data was obtained from Early's paper and after considering the fact that there could be some misalignment in the AFIT data.

Figure 47 (a) shows the percent difference between the AFIT measurements and

73
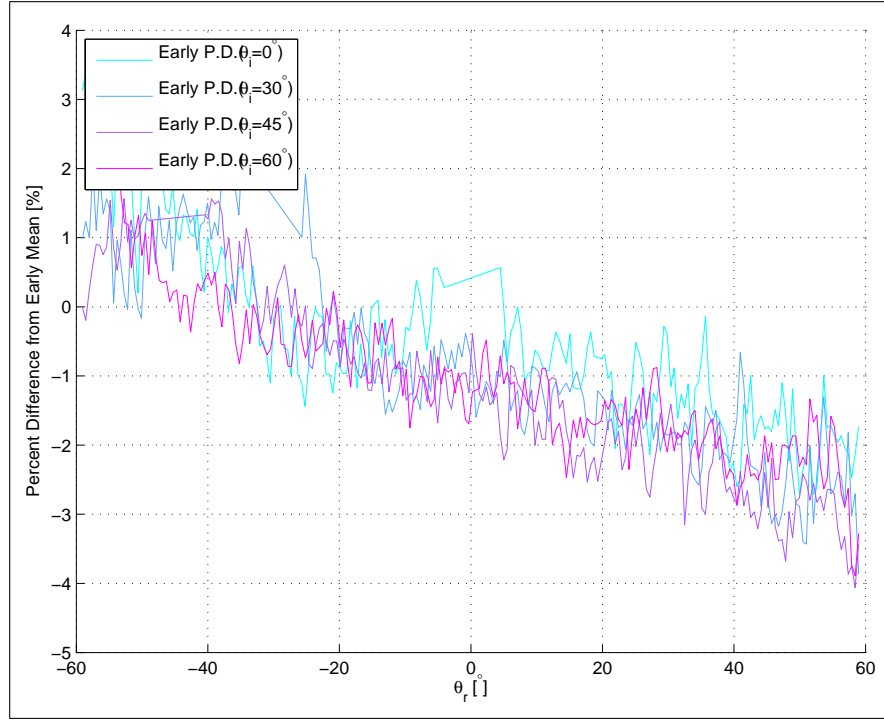
(a)
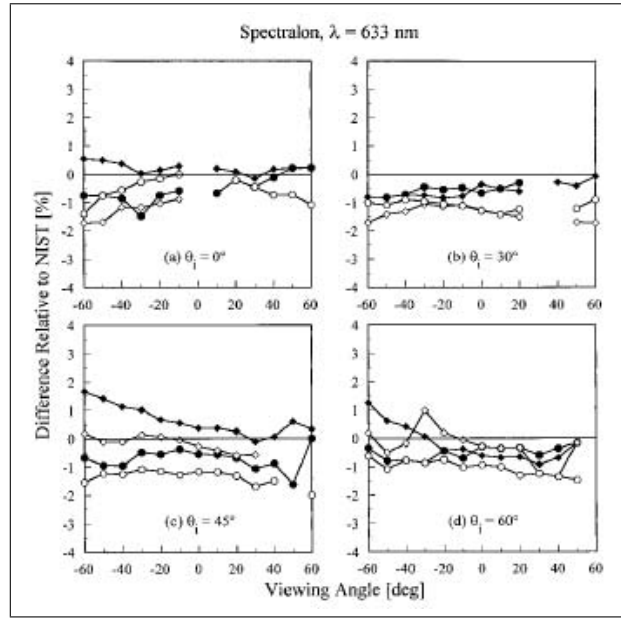
(b)

Figure 47. Interlab comparisons at $\lambda = 633$nm (a) AFIT's percent difference from Early's measurement set (b) Early's published inter-lab comparison percent difference

74

Early's data. These results compare nicely with Early's intercomparision percent difference between labs shown in Figure 47 (b). All the measurements tend to have a percent difference error from Early's measurements at NIST of less than approximately three percent. This result validates the calibration method used here, and the measurements themselves.

4.5.4 Fitting.

In this section, the Ward and Cook-Torrance models are fit to the Spectralon®measurements at $\lambda = 633nm$. The convergence plots of the variables for each fit, as demonstrated earlier in Section 4.3.3, are not shown because there was not any convergence or instability issues for these fits. The results of the fit are what is important here, and they are shown in Table 8. Also, only the Ward and Cook-Torrance models are presented in the fitting because they are relatively simple to implement and have a single diffuse term. Having only a single diffuse term is important when the fitting is used to determine the 'diffuseness'.

Figure 48 shows visually that the Cook-Torrance model obviously provides a better fit to the data. This is because the diffuseness of the sample is modeled better with the Fresnel term in the Cook-Torrance model. The obscuration term also helps at larger angles of incidence. Although the Ward model does not do the best at fitting to these diffuse measurements, the Cook-Torrance model actually does not fit significantly better in this case when one compares the MSE results.

Table 8. Spectralon®BRDF Model Fitting Results.

Sample	Ward Model				Cook-Torrance Model				
	ρ_d	ρ_s	β	σ	ρ_d	ρ_s	m	F_o	σ
Spectralon®	0.926	0.200	0.188	0.0503	0.951	0.00723	0.238	0.491	0.0181
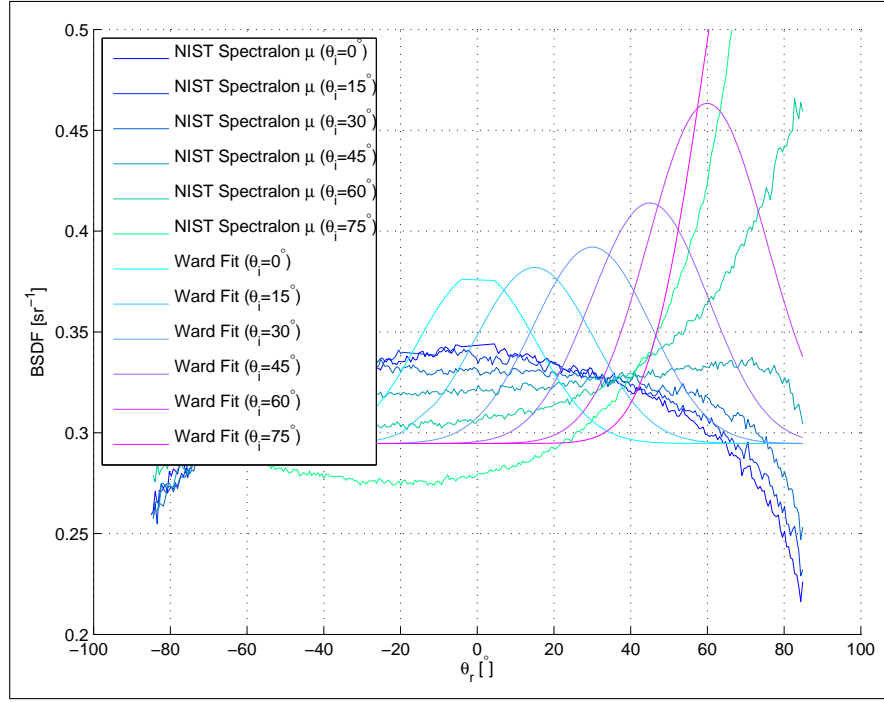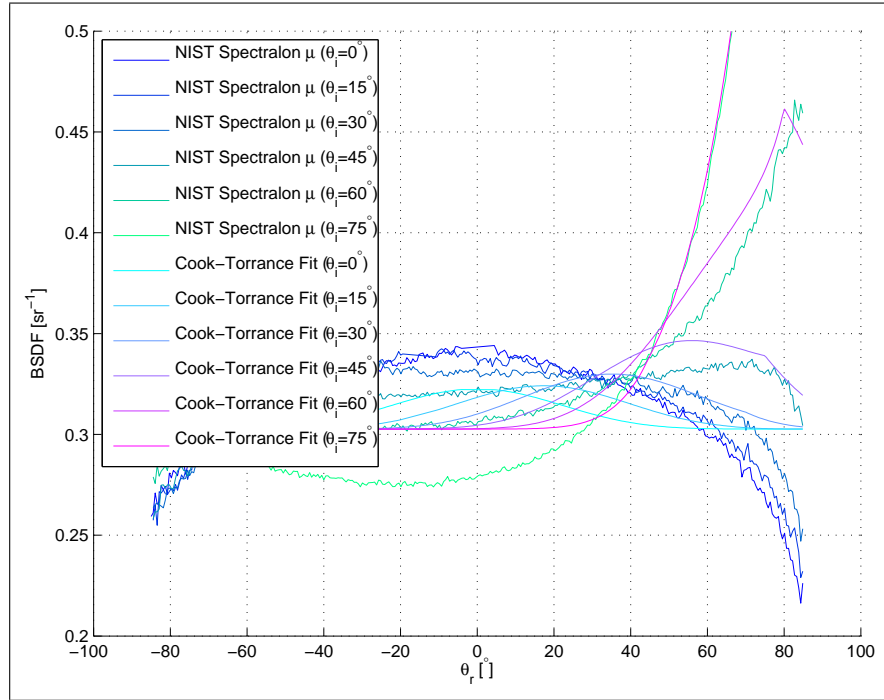
Figure 48. (a) Comparison of calibrated **Spectralon**®measurements and a fitted Ward
BRDF model. (b) Comparison of calibrated **Spectralon**®measurements and a fitted
Cook-Torrance BRDF model.

Table 8 shows the numerical results of each model's fit to the data. These fitting results will be useful in Chapter VII to have a standard to compare to when the potential samples are analyzed for 'diffuseness'. This data can also be used to present three dimensional BRDF representations of the different samples, which is shown in the next section.

4.6   Three Dimensional Modeling

<table>
<tr><td>(a)</td><td>(b)</td></tr>
</table>
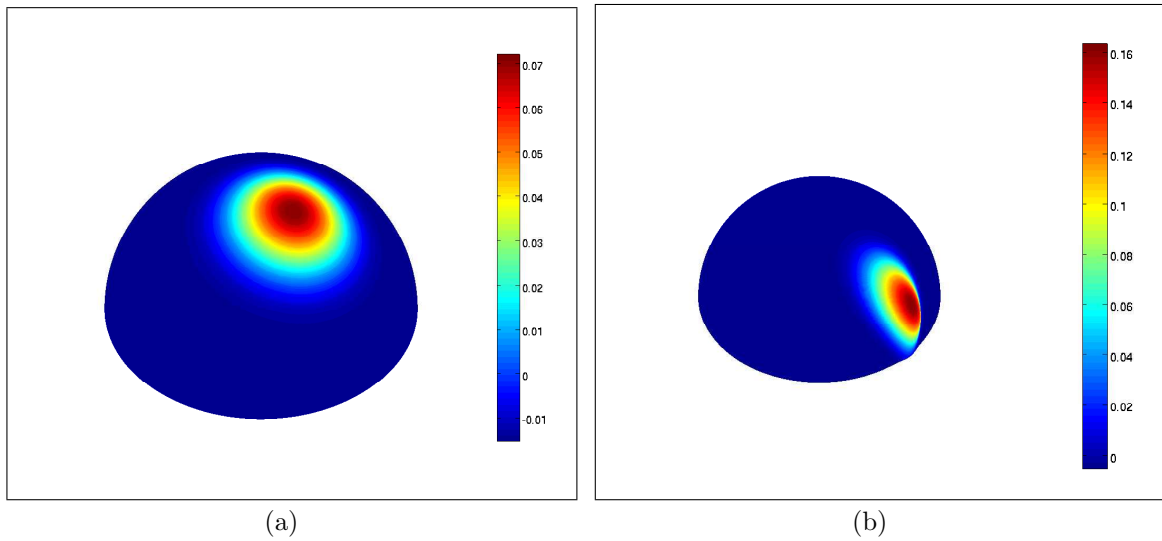
Figure 49. Spectralon®Ward BRDF model three dimensional representations showing the full scatter of the models. (a) $\theta_i = 0°$. (b) $\theta_i = 60°$.

This section takes the results from the fitting in Section 4.5.4 and applies them to create three dimensional representations for each model in spherical coordinates with the radial magnitude and color representing the BRDF value of the scatter. This is very useful for an intuitive representation of the each model and the sample it represents. It must also be mentioned that the plotting function also interpolates the data points over the surface to create a solid figure. This means that these figures are for comparative and intuitive demonstrations only.

4.6.1 Ward 3D Model.

The first three dimensional representation is based upon the Ward model of the Spectralon®data. Figure 49 shows just how diffuse Spectralon®really is, even in the large incident angle case. It must also be noted that the scale is different for each subfigure. The lobe shape is a result of the model itself.

4.6.2 Cook 3D Model.
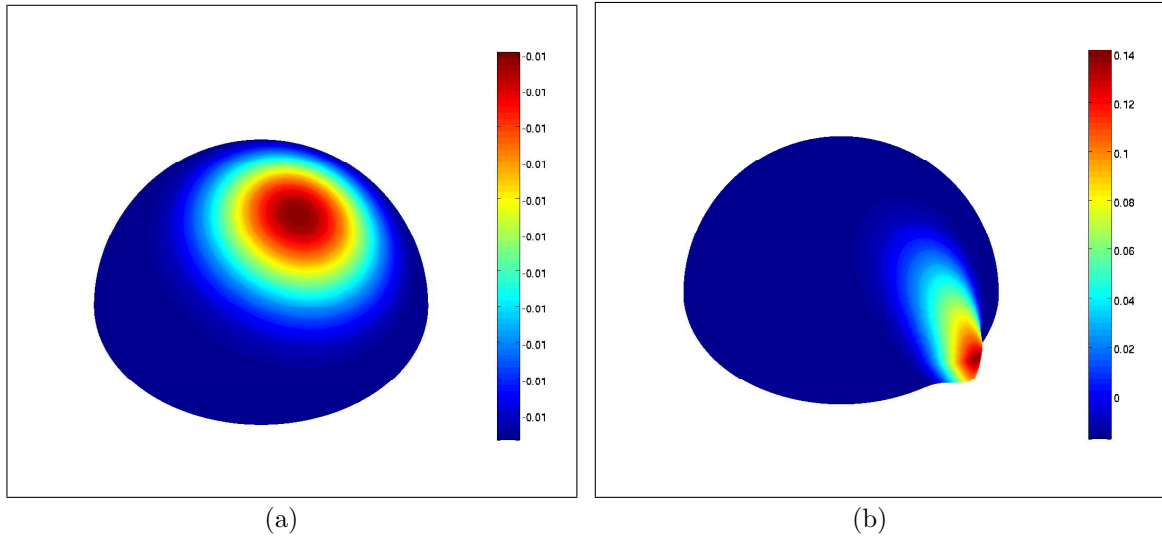
Figure 50. Spectralon®Cook BRDF model three dimensional representations showing the full scatter of the models. (a) $\theta_i = 0°$. (b) $\theta_i = 60°$.

Figure 50 is the Cook-Torrance model's representation of the Spectralon®data. This model really shows quite a difference in lobe shape and size with changes in the incident angle just as the data does, but this is due more to the model than the data. Nevertheless, it gives a moderately realistic representation of Spectralon®, as was demonstrated with the two dimensional in-plane comparison to the measurements in Figure 48 (b).

4.7   Chapter Conclusion

This chapter has introduced all the concepts necessary to understand what a diffuse BRDF standard should be, and the tools needed to analyze measurements from one of these samples. The current visible standard, Spectralon®, is a good starting point for comparison with IR BRDF standards. The fact that the measurements at $\lambda = 633nm$ were so far off of calibrated BRDF values demonstrates the need for calibration, and the calibration process produced good results. Finally, the comparative BRDF measurements validated this conclusion. These tools and procedures will be necessary when looking at standards in the IR.

V. Infrared Calibration and Validation

Τhis chapter's primary purpose is to perform the calibration of the CASI® at $\lambda = 3.39 \mu m$ using the procedures that were established in Chapter IV. Three diffuse samples with calibrated and well verified DHRs produced by NIST will be used to accomplish this task. There are also reliable BRDF measurements for these samples, which to validate the calibrations with, which is why these samples are being used. There are other calibrated reflectance samples in the IR, but there really is not a standard like Spectralon®that has been thoroughly studied. This will be explored in more detail later in Chapter VI. In addition, there is very little published BRDF information available for these IR reflectance standards, which is a second reason why these alternate samples have been chosen. These samples will also be used in the comparison of possible IR BRDF standards in the next chapter.

5.1 DHR Study and Reference Samples

The samples used in this calibration came from a DHR 'round robin' intercomparision study between 20 various laboratories coordinated by NIST as the pilot lab[30]. All these labs are considered certified laboratories, they include NIST, AFRL, Arnold Engineering Development Center, Boeing, General Electric, Lockheed Martin, MIT Lincoln Laboratory, Sandia National Laboratory, United States Geological Survey, and others. The results from this study were encouraging because they showed better agreement than past studies in the IR, but BRDF measurements were not performed in this study. Regardless, this provides well defined DHRs with which the BRDF measurements made in this study can be calibrated when a DHR for a specific sample is not available. The samples used in this study were on loan from AFRL, but each lab had its own set of samples in the DHR study. The three diffuse samples

from the study have low, medium, and high DHR values. Each of these samples will be presented with its results from the DHR study. The numbering on the samples is used for brevity in this thesis, and it was derived from the protective casings for them.

5.1.1 D51A01: Gold on Nickel on Arc-sprayed Aluminum.

The first sample shown in Figure 51 is very similar to Infragold®; it is an 'electroplated gold on nickel on arc-sprayed aluminum on [a] machined brass substrate'[30, pg. 10]. This sample was considered to be the high reflectance diffuse standard to be measured in the DHR study. This is because gold has a very high reflectance in the IR. The microscope photo in Figure 51 (b) shows that the arc-sprayed aluminum creates a very rough surface to distribute the normally specular reflections from a smooth gold surface into a diffuse pattern.

(a)   (b)
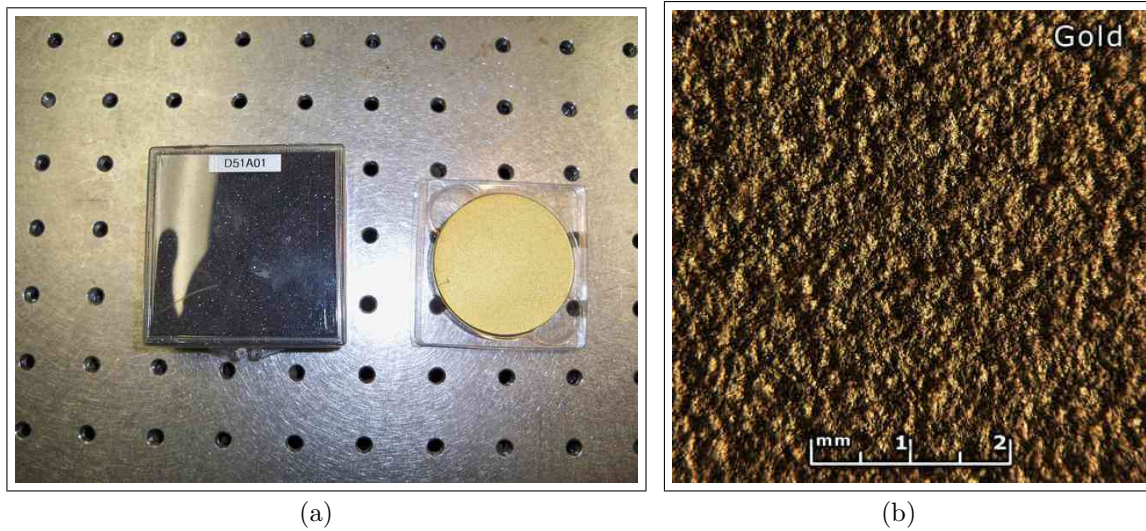
Figure 51. D51A01: Gold on nickel on arc-sprayed aluminum on brass substrate (a) Photo of sample and container (b) Surface microscope photo of sample

The study found the DHR of this sample to be approximately 0.9675 at $\lambda = 3.39\mu m$, as shown Figure 52 (a). Both the NIST mean and the mean of the labs

(a)   (b)
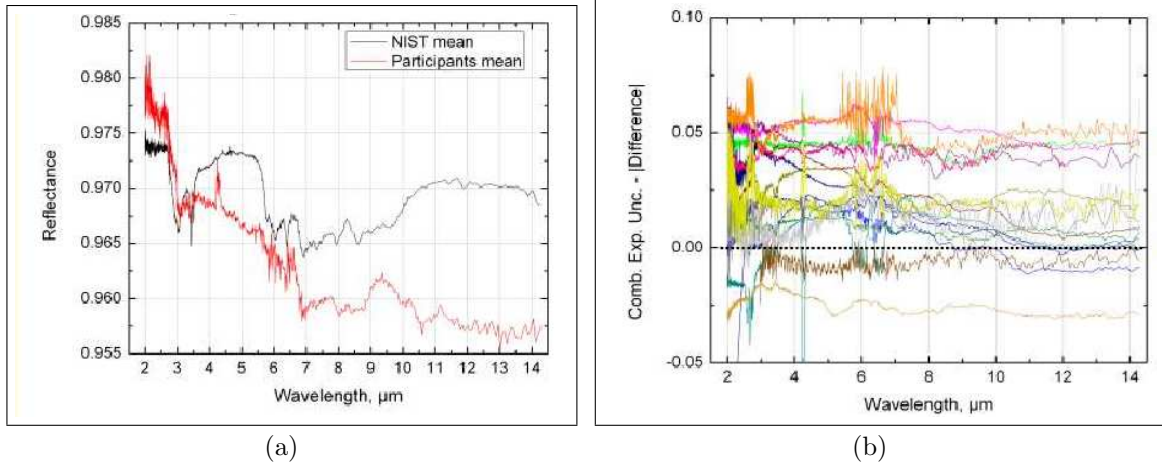
Figure 52. D51A01: DHR Intercomparision Results (a) NIST average vs. lab's average (b) Agreement criterion for each lab.

agree well at this wavelength. Unfortunately, it is not apparent exactly what the uncertainty is from the all the measurements in the presentation, but it appears that the average uncertainty is about 0.02. Figure 52 (b) shows the agreement criterion; a value above zero meets the criterion. Mathematically defined the agreement criterion is

$$Criterion(Lab, \lambda) = \sqrt{(\sigma_{NIST}(\lambda)^2 + \sigma_{Lab}(\lambda)^2)} - |\overline{\rho_{NIST}(\lambda)} - \rho_{Lab}(\lambda)|, \qquad (48)$$

where $\sigma_{NIST}(\lambda)$ is the wavelength-dependent standard deviation of the reflectance from NIST's measurements, $\sigma_{Lab}(\lambda)$ is the wavelength-dependent standard deviation of the reflectance from each of the lab's measurements, $\overline{\rho_{NIST}(\lambda)}$ is NIST's average reflectance value, and $\rho_{Lab}(\lambda)$ is the lab's measured reflectance. If the criterion is above 0, it falls within the σ confidence bounds. In determining the DHR to use for calibration of BRDF data, it is fair to say that if the NIST mean and the average from all the labs in Figure 52 (a) agree, it can be used for this study as a calibration value.

5.1.2 D51C01: Nextel Black Paint.

(a)   (b)
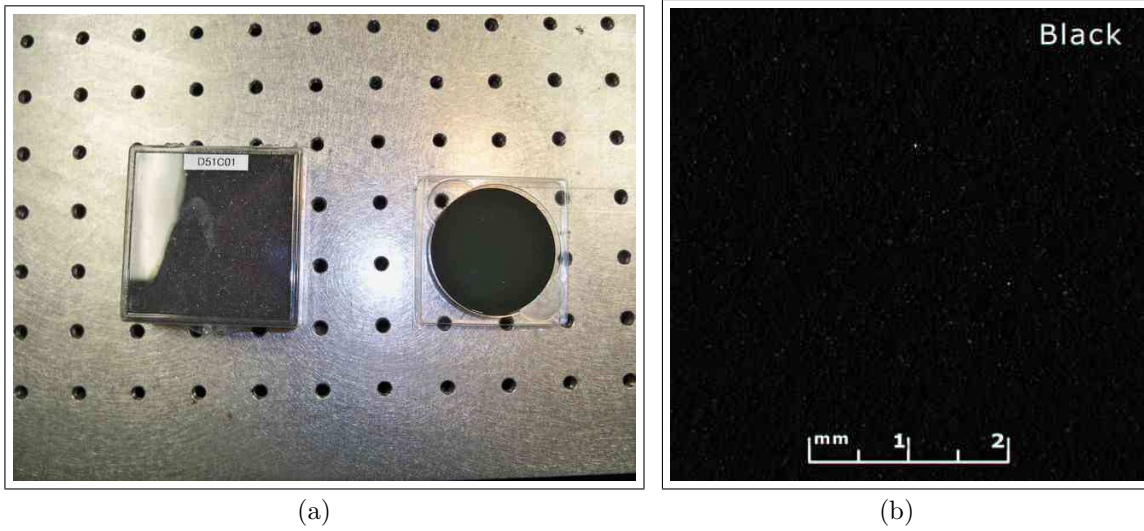
Figure 53. D51C01: Nextel Black Paint on brass substrate (a) Photo of sample and container (b) Surface microscope photo of sample

(a)   (b)
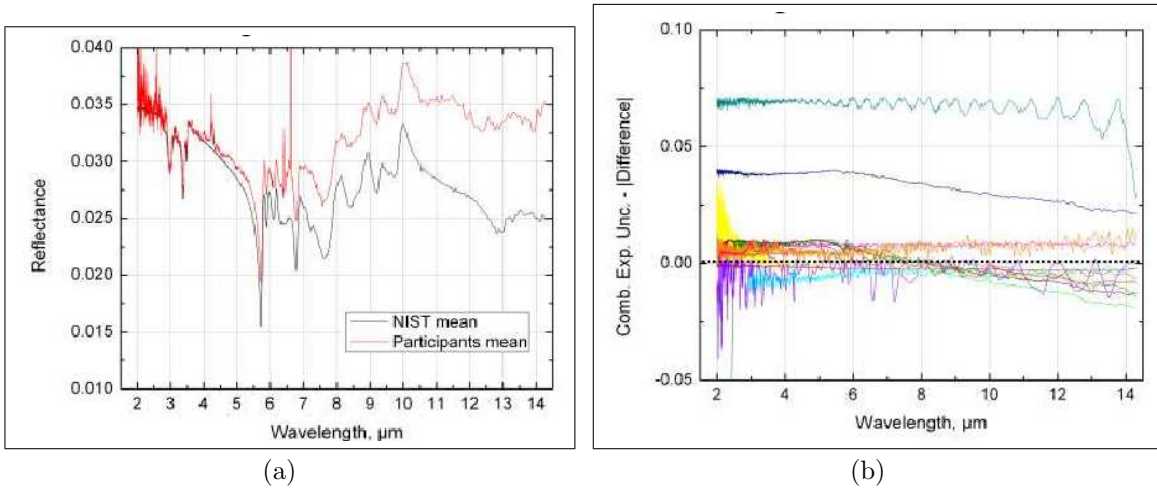
Figure 54. D51C01: DHR Intercomparision Results (a) NIST average vs. lab averages (b) Agreement criterion from each lab.

The second sample in the study is Nextel black paint on a machined brass substrate, shown in Figure 53. This is the diffuse low reflectance sample from the DHR study. Figure 54 shows the results from the study. The DHR at $\lambda = 3.39\mu m$ appears to be approximately 0.030, but it is difficult to tell because there appears to be an

absorption line right around $\lambda = 3.5\mu m$. Also Figure 54 (b) shows that the agreement between participants was not quite as good for this sample. This creates some uncertainty about the DHR value being used for calibration.

5.1.3 D51D01: Krylon Silver Paint on arc-sprayed aluminum.
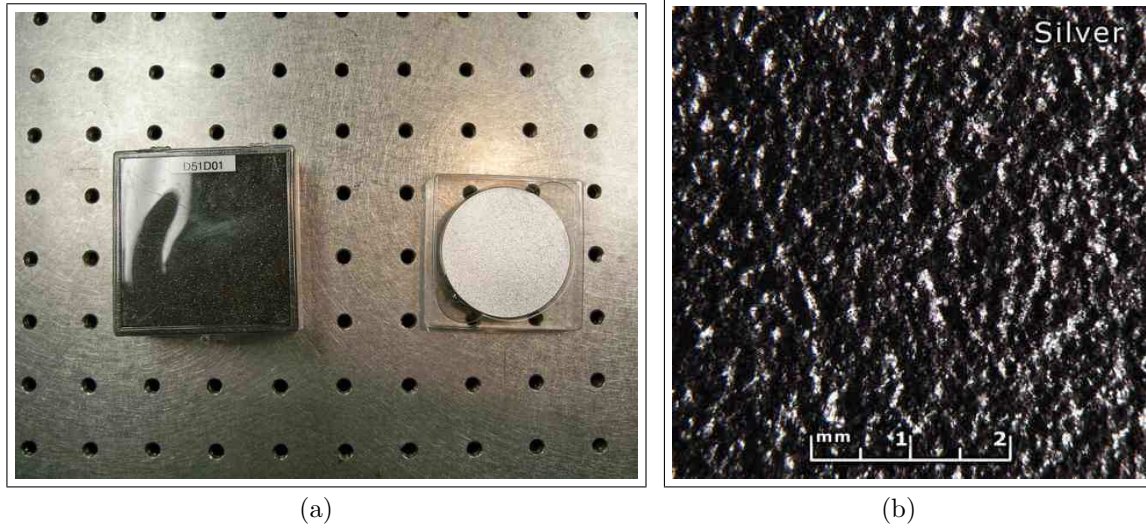
Figure 55. D51D01: Krylon silver paint on arc-sprayed aluminum on brass substrate (a) Photo of sample and container (b) Surface microscope photo of sample
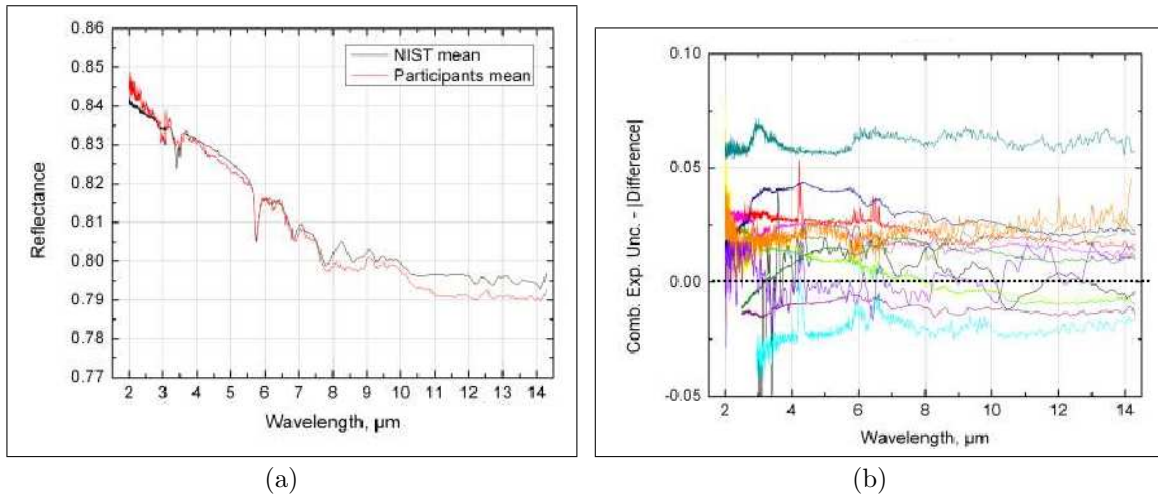
Figure 56. D51D01: DHR Intercomparision Results (a) NIST average vs. lab averages (b) Agreement criterion from each lab.

The last sample is Krylon silver paint on arc-sprayed aluminum on a machined brass substrate[30, pg. 10]. This sample is shown in Figure 55. Figure 56 presents the results from the DHR intercomparision study, which shows good agreement at $\lambda = 3.39 \mu m$. Therefore, there is no uncertainty about the value to be used for BRDF calibration with this sample. The measured DHR for this sample is 0.83.

5.2 AFIT BRDF Measurements

This section presents the AFIT CASI® measurements without a DHR calibration performed. Therefore, this section just explores the general characteristics of each sample's measurements. The first figures for each sample are logarithmic Cartesian plots because the entire set is more easily seen on the same plot. This plot also adds standard deviation error lines. The second plot is a logarithmic polar plot, which is a more intuitive look at the data and the sample's behavior. The last two figures for each sample address the repeatability. The calculation of DHR will be addressed in the calibration section because it is more appropriate to address it there.

5.2.1 D51A01: Gold on nickel on arc-sprayed aluminum.

Figure 57 shows the standard measurement set established in Chapter IV for the rough gold sample, D51A01. It is apparent that the arc-sprayed surface creates a very diffuse surface and the gold plating leads to a high reflectance from surface scattering. The surface scattering does not remain as diffuse as the Spectralon®did, but a clear set of specular lobes does not form. The standard deviation is also high relative to Spectralon®. Even though there is not a specular lobe, it does become more specular in the sense that the distribution shifts with an increase in the incident angle. The polar plot shown in Figure 58 gives a good intuitive idea of how diffuse this surface is. The grid lines in the figure also correspond to the incident angles of the measurements.
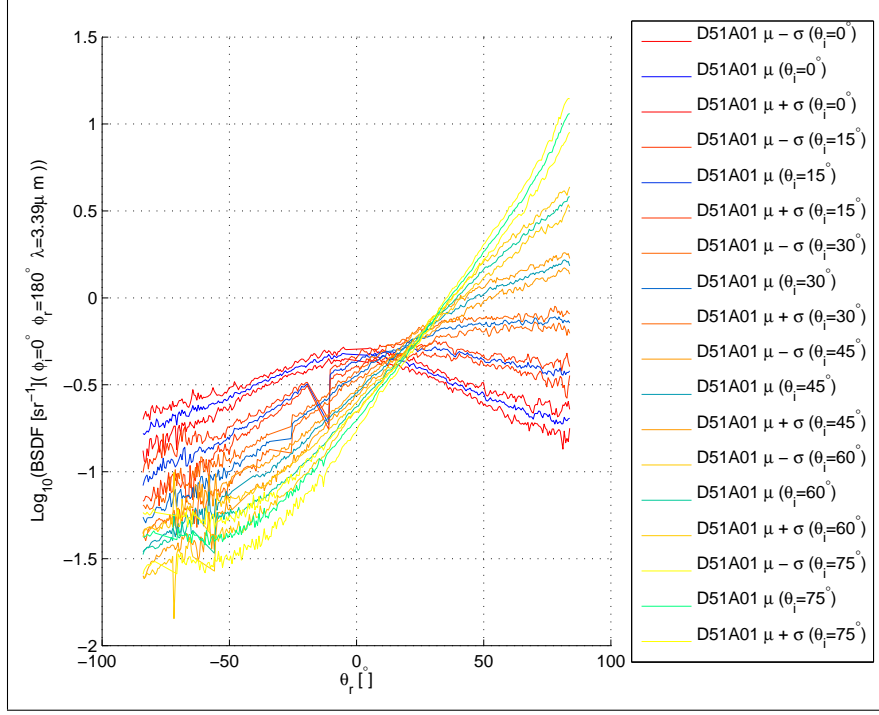
Figure 57. BRDF logarithmic plot with standard deviation added for sample D51A01.
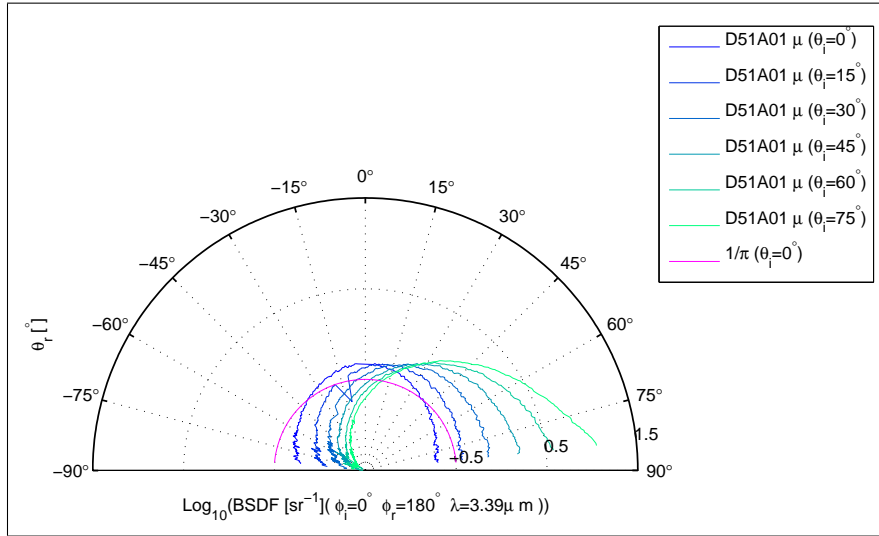
Figure 58. BRDF logarithmic polar plot for sample D51A01.

Figure 59 (a) shows the PDM value of the measurements when the incident location on the sample was not rastered and $\theta_i = 0°$. Thus, the measurement should not change and the PDM should be near zero, but this is not the case. When
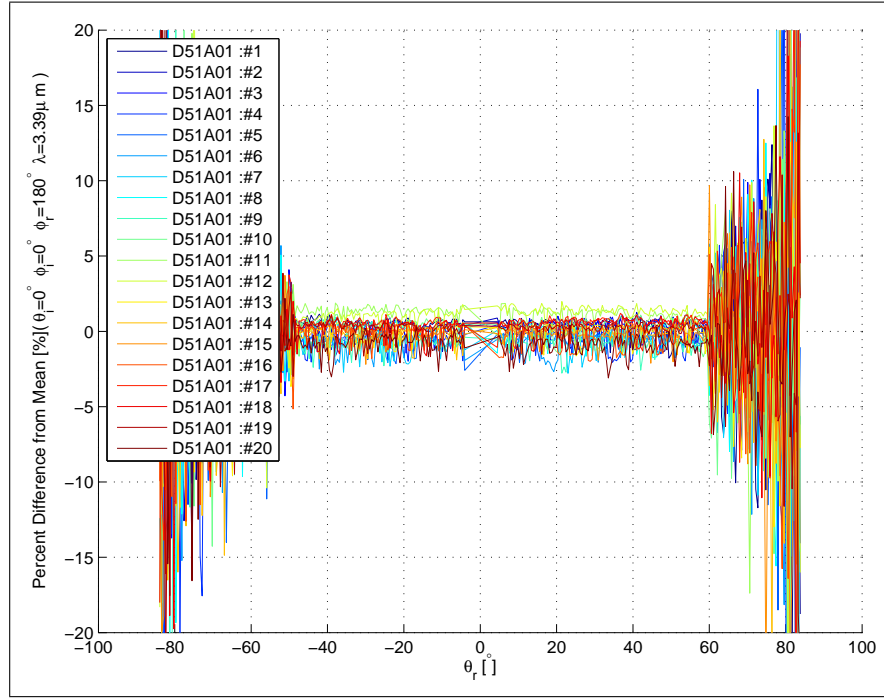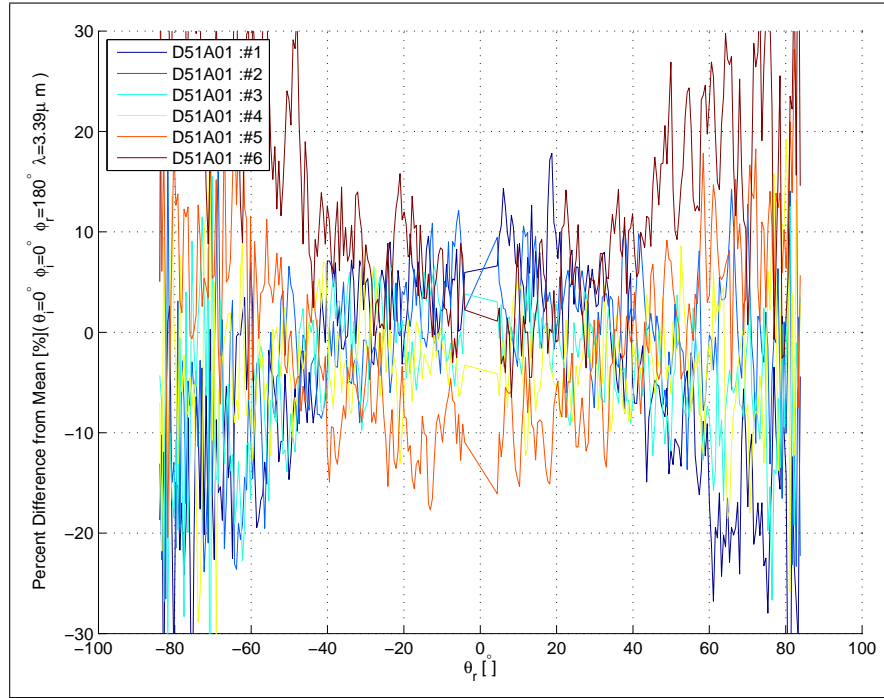
Figure 59. D51A01: Uncalibrated Repeatability (a) Percent difference from the mean of 20 measurements without changing illumination. (b) Percent difference from the mean of six measurements while changing the position of illumination.

$-60° \leq \theta_r \leq 60°$, the PDM value for each measurement is typically less than $\pm2\%$. This is an encouraging result showing that the CASI® is working correctly. Nevertheless, the PDM value remains very low until the reflected angle reaches approximately $\pm60°$, then gets considerably larger. This is mostly likely due to the randomness of the surface and the nature of the surface scatter.

Figure 59 (b) shows the percent difference when the illuminated spot on the sample is rastered across its surface. It is apparent that the arc-sprayed surface that creates a very diffuse BRDF, but it also decreases the repeatability even when uncalibrated. This repeatability, shown as a PDM value, appears to be about $\pm10\%$ between $-60 \leq \theta_r \leq 60°$ when $\theta_i = 0°$.

5.2.2 D51C01: Nextel Black Paint.
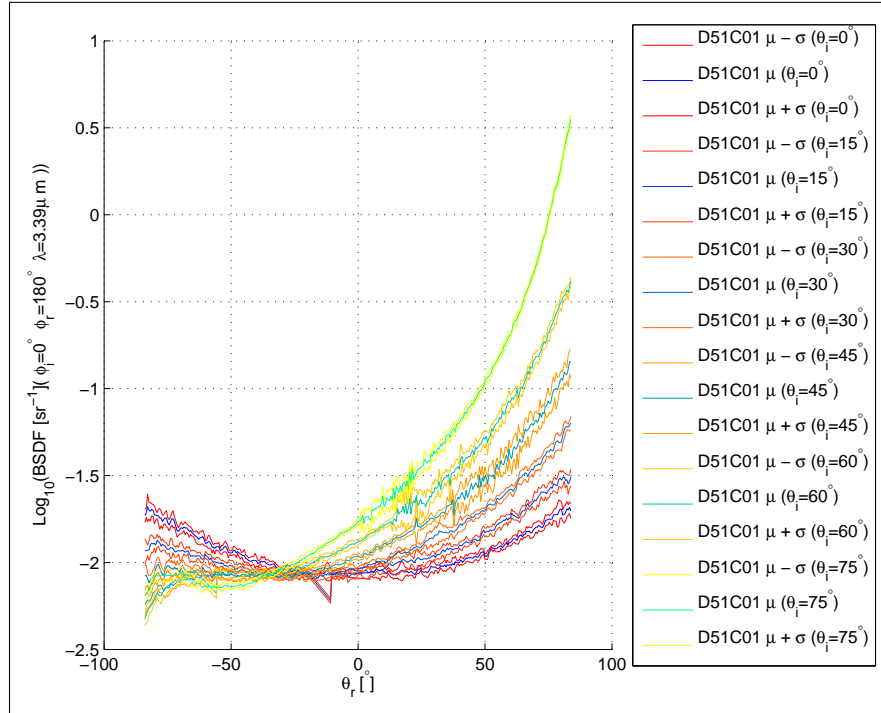
Figure 60. BRDF logarithmic plot with standard deviation added for sample D51C01.

Figure 60 shows the standard measurement set established in Chapter IV for

the Nextel black paint sample, D51C01. This is the low reflectance value sample, meaning it also has low BRDF values. The first interesting characteristic is the fact that, at normal incidence, the reflectance is actually higher farther from specular values resulting in a bowl-shaped BRDF on a Cartesian plot, which is atypical. This supports the idea that a bulk interaction is responsible for the scatter at these values, even perhaps absorption and re-emission. Next, it is apparent that the standard deviation is also much lower in this sample. Lastly, it also shows that although the reflectance is generally low, the reflectance increases greatly when θ_i is increased. This shows that the scattering changes from a mostly bulk interaction to a surface interaction as one would expect with an increase in θ_i.
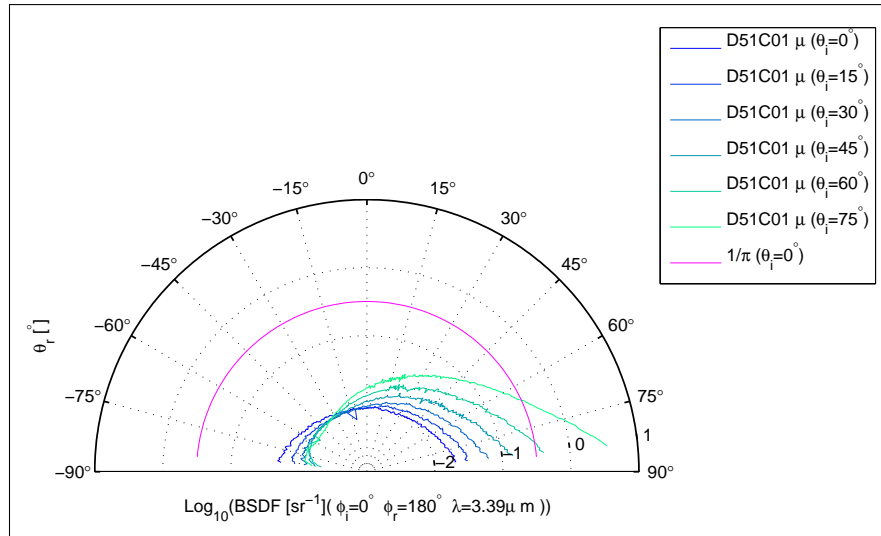
Figure 61. BRDF logarithmic polar plot for sample D51C01.

Figure 61 shows this same data in the polar logarithmic format, and it becomes clear how low the BRDF values are when θ_i is near normal incidence. It is a full two orders of magnitude below a BRDF value of 1 sr^{-1}, its peak value at $\theta_i = 75°$, which corresponds to 0 $log(sr^{-1})$.

Figure 62 (a) shows the PDM value for the measurements when the incident location on the sample was not rastered and $\theta_i = 0°$. For this sample, one can observe

89
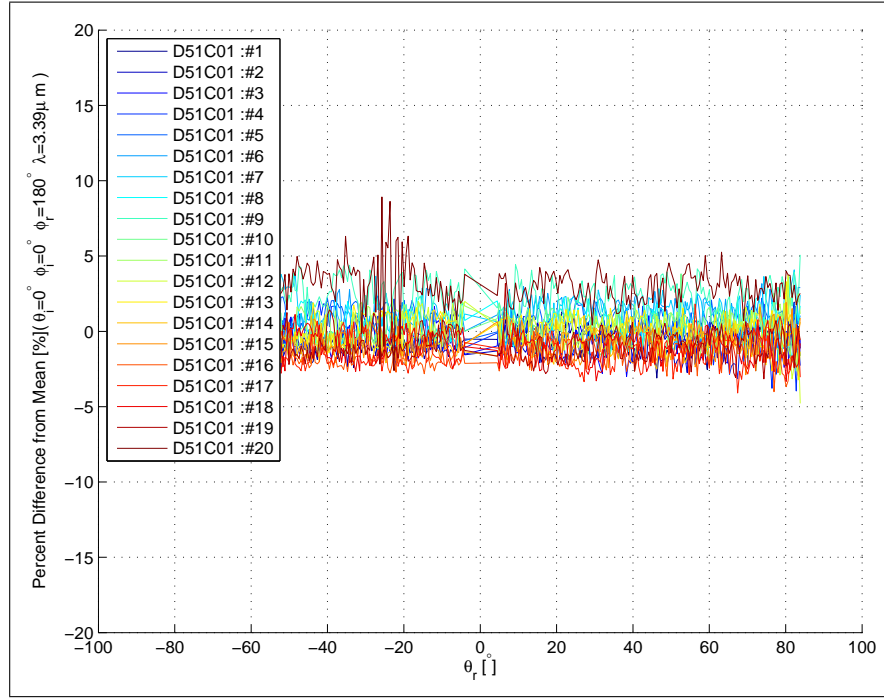
(a)
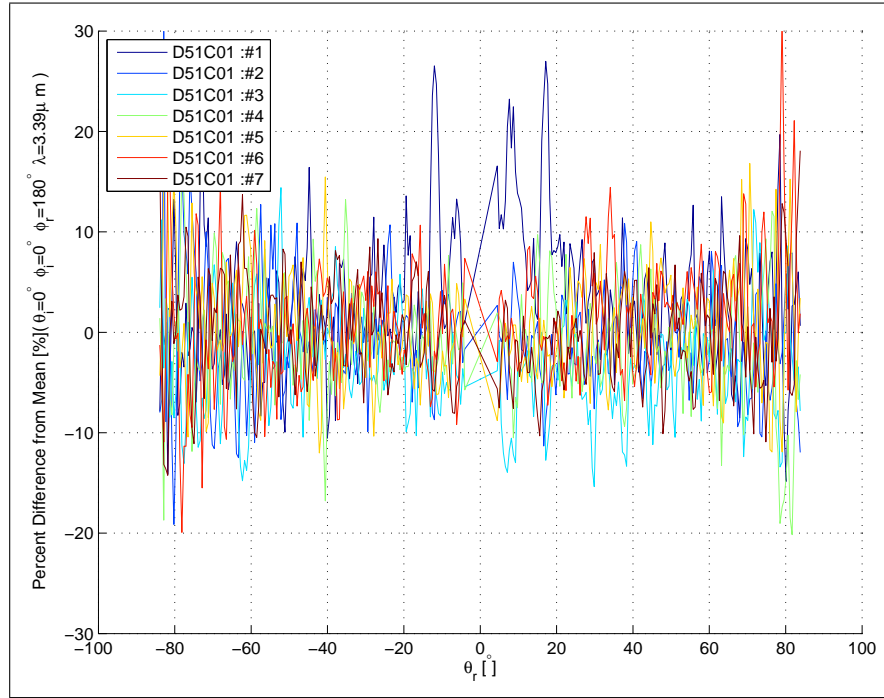
(b)

Figure 62. D51C01: Uncalibrated Repeatability (a) Percent difference from the mean of 20 measurements without changing illumination. (b) Percent difference from the mean of seven measurements while changing the position of illumination.

90

an interesting behavior when compared to the last sample. The percent difference from the mean does not get significantly greater when $\theta_r > \pm 60°$. This is most likely due to the fact it is a bulk interaction. This also supports the idea that discrete increase in PDM near $-60 \leq \theta_r \leq 60°$ in Figure 59 (b) is due to the nature of surface scatter. This is an even more encouraging result than that for D51A01, the rough gold sample, showing that the CASI® is working correctly and properly set up.

Figure 62 (b) shows the PDM value for when the sample is rastered between each measurement set at $\theta_i = 0°$. This result is much better than for the rough gold sample, D51A01. The percent difference remains below $\pm 10\%$ in the majority of cases, and is usually below $\pm 5\%$. Once again, this is most likely due to the uniformity of the bulk interaction in the black paint.

5.2.3 D51D01: Krylon Silver Paint on Arc-sprayed Aluminum.
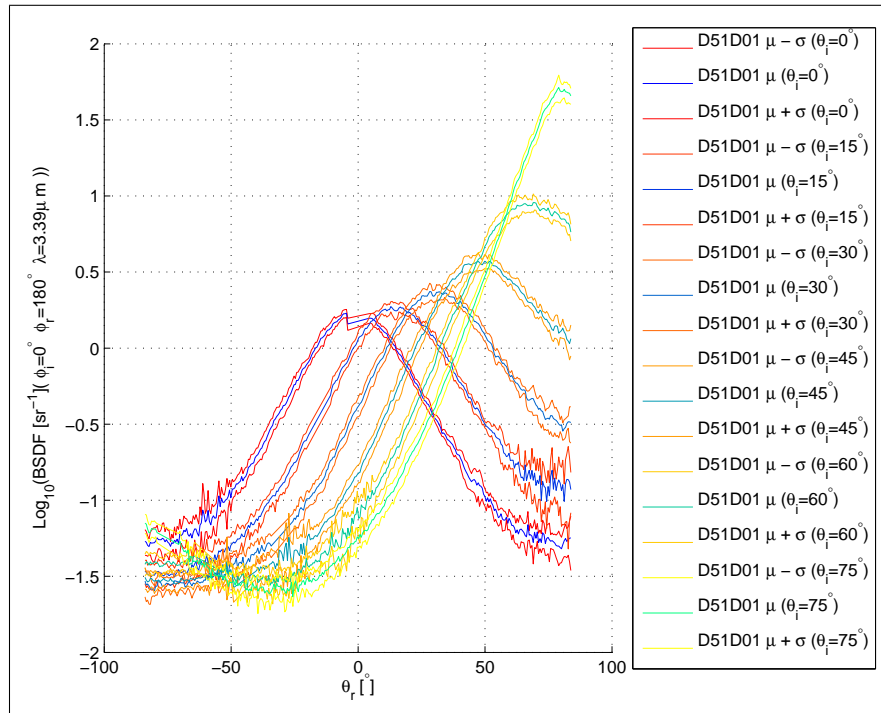
Figure 63. BRDF logarithmic plot with standard deviation added for sample D51D01.

Figure 63 shows the standard measurement set established in Chapter IV for the Krylon silver paint sample, D51D01. This is the medium reflectance value sample used in the DHR laboratory intercomparision. The first characteristic of this sample, when compared to the previous two, is that it is comparatively much more specular. It clearly has specular lobing, but it is still considered a diffuse sample. It is most likely more specular because of the paint 'filling' in the valleys in its surface roughness created by the arc-spraying process. This is supported by the microscope picture of the sample presented in Figure 55 (b). The standard deviation of the measurements in this case appears to be approximately the same as the rough gold sample, D51A01.
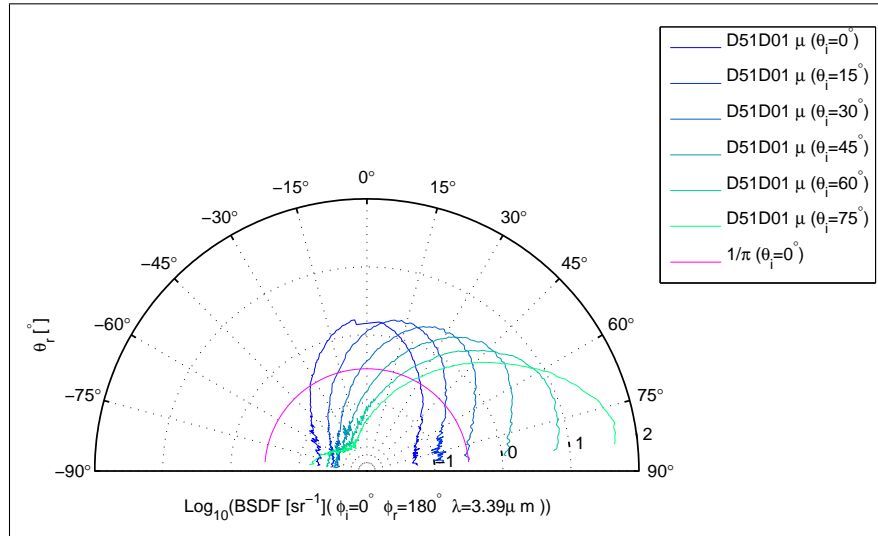
Figure 64. BRDF logarithmic polar plot for sample D51D01.

Figure 64 also makes it apparent, because of the alignment of the specular lobe, that there was some small misalignment in the measurements of this sample. This cannot be observed with the previous two samples because they do not exhibit clear specular lobes. This is most apparent at when the incident angle is the higher. In Figure 63 when $\theta_i = 45°$, the specular lobe appears to be almost at $\theta_r = 50°$. It appears to be about 3 degrees misaligned toward positive θ_r values, unless this is due to masking.
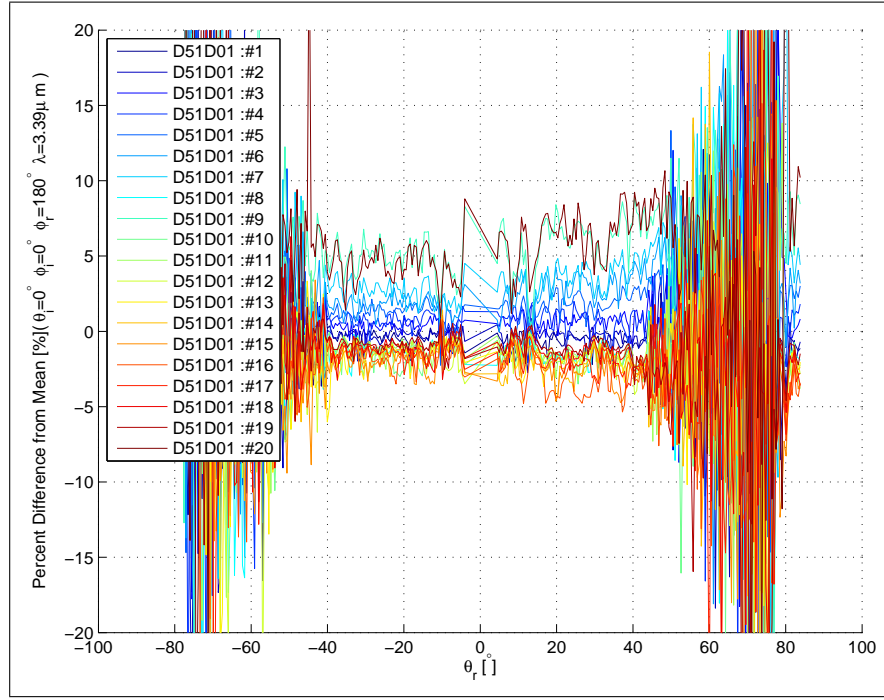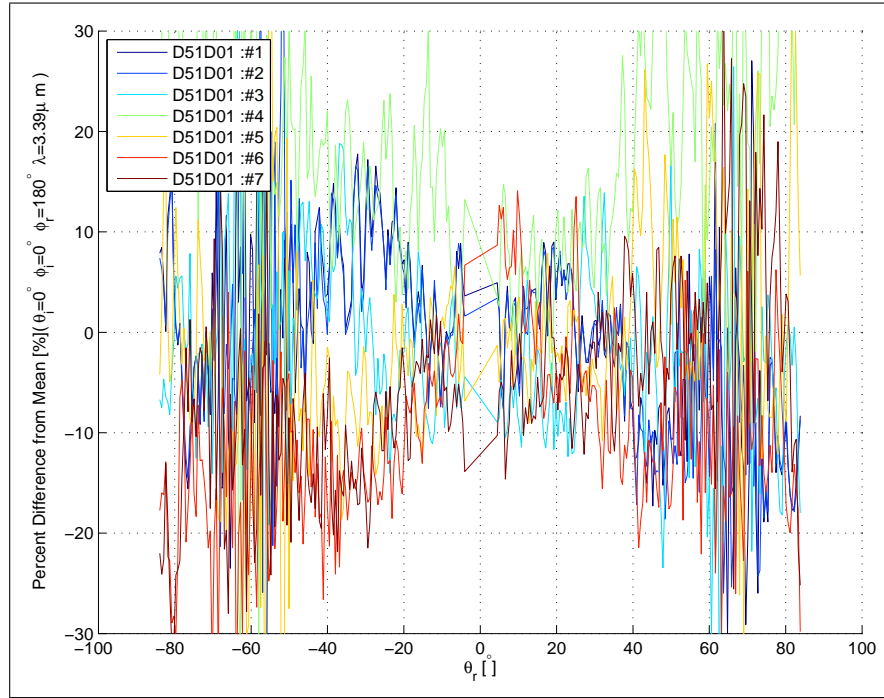
Figure 65. D51D01: Uncalibrated Repeatability (a) Percent difference from the mean of 20 measurements without changing illumination. (b) Percent difference from the mean of seven measurements while changing the position of illumination.

Figure 65 (a) shows similar repeatability performance that the rough gold sample, D51A01, exhibited. The change is that the percent difference is significantly higher when $-40 \leq \theta_r \leq 40°$, opposed to breaking around $60°$ for the rough gold sample. The similar behavior could be explained with the fact that they are both surface scatterers, and their surfaces were created with the same process. It is possible that because the silver sample is the more specular one; it changes the break point. Nevertheless, it is a very interesting result that is difficult explain because the measurement is not being altered, and the BRDF values are not relatively any smaller, which could create a higher PDM, than those for the Nextel black paint sample. Figure 65 (b) shows PDM values when measurements are taken across the face of the sample. When comparing these values to those of the rough gold, this sample actually shows worse repeatability. This is most likely because it is more specular, which then makes the non-specular averages smaller and this creates a higher PDM.

5.3   AFRL BRDF Measurement Capabilities

A second set of BRDF measurements for these samples has also been made available, but before these measurements are used, the measurement equipment, procedures, and quality of these measurements are discussed. These BRDF measurements, which are used for validation in this chapter, were made by the Optical Measurements Facility (OMF), which is directed and operated by AFRL. This facility first used the AFIT CASI® , but it now has a more complete BRDF measurement system. In addition, they have considerable experience in this field as they have been making these types of measurements for over 30 years. They are generally considered a leader in the field of IR BRDF measurement.

The OMF found that taking out-of-plane measurements with the CASI® could often be very difficult and time consuming. AFRL contracted with System Research

94

<center>(a)   (b)</center>
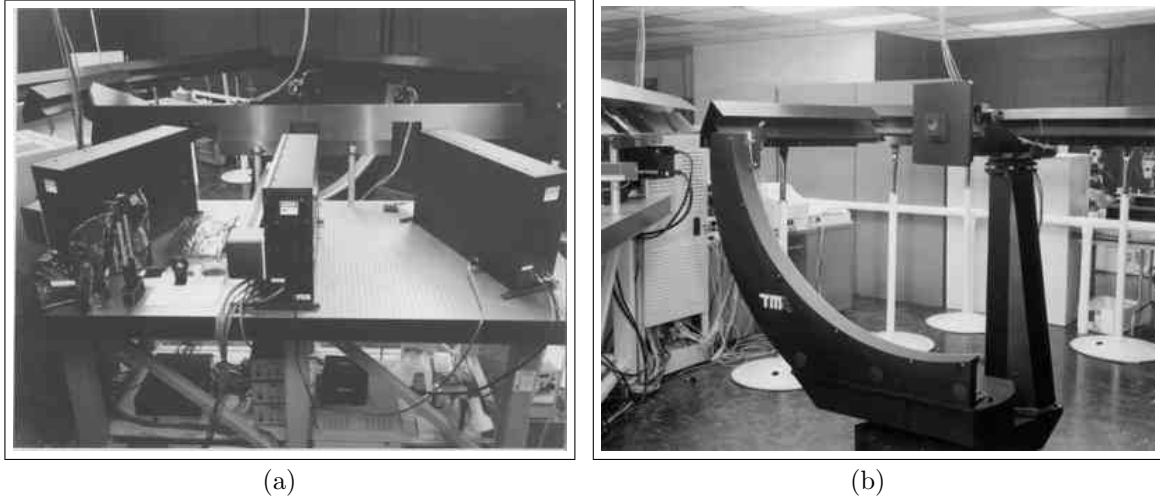
Figure 66. (a) Picture of AFRL hemispherical laser scatterometer source boxes (b) Picture of AFRL hemispherical laser scatterometer goniometer[14].

Laboratories and TMA, the original manufacturers of the CASI® , to create a very similar instrument to the CASI® , but with the added abilities and precision. This instrument is shown in Figure 66. A summary of this capability upgrade from the CASI® is shown in Table 9.

<center>**Table 9. Laser Scatterometer Capabilities at the OMF[14].**</center>

Capability	TMA CASI® Laser Scatterometer	TMA Hemispherical Laser Scatterometer
Wavelength	$\lambda = 0.544, 0.633,$ 3.39, and 10.6 μm	$\lambda = 0.544, 0.633, 1.06,$ 3.39, and 10.6 μm
Angle of Incidence	$0° \leq \theta_i \leq 85°$	$0° \leq \theta_i \leq 89°$
Angle of Reflection	$0° \leq \theta_r \leq 88°$	$0° \leq \theta_r \leq 89°$ $0° \leq \phi_r \leq 360°$
Receiver Obstruction	$\pm 6°$	$\pm 1.5°$
Polarization	s-pol Source Unpolarized Receiver	Linear (s,p, or variable) Source Linear (s,p, or variable) Receiver
Sample Temperature	Ambient	$-65° \leq T \leq 204°$ C

A significant difference between this system and the CASI® is that the sample

<center>95</center>

itself is rapidly rotated about its z-axis during the measurement. Figure 66 (b) shows this mounting system. The beam is positioned so that it is incident upon the center of rotation. This has the effect of averaging the BRDF variation due to the non-uniformity in the surface roughness of the sample. This is why the measurements from this system do not have the standard deviation information available, as it has been demonstrated with the AFIT CASI® measurements.

There are two other noteable statements from the 'OMF Final Report' for this measurement system that are of interest to this study. The first is the confirmation of the calibration technique, where the BRDF measurements are integrated and compared with DHR measurements to calibrate the data. This is provided verbatim in the following quote.

> Calibration procedures are needed for both laser scatterometers, based on an approach that includes integration of the BRDF over the reflected hemisphere for a normal-incident angle and comparison with the DHR of the sample tested. If significant differences are found, the effective aperture can be calibrated such that the integrated BRDF of a reference standard equals its measured DHR. Furthermore, if the sample is homogeneous and isotropic, only an unpolarized in-plane scan at normal incidence is required[14].

The second notable quote that applies to these measurements relates to the tolerance in the comparison of DHR measurements to the integration of the BRDF in-plane data. It states that if the results are within the design goal of 10%[14], this is a satisfactory result. This gives us some amount of tolerance that can be expected in Section 5.5, where the BRDF measurements are calibrated using DHR values and then compared against each other.

5.4 AFRL BRDF Measurements and Uncalibrated Comparison

In this section, the measurements made at the OMF are presented without any calibration. This section will also be used to compare the AFIT CASI® measurements to the AFRL measurements without any calibration. Calibration will be evaluated in the following section so that both the AFIT and AFRL measurements can be compared at the same time.

5.4.1 D51A01: Gold on Nickel on Arc-sprayed Aluminum.
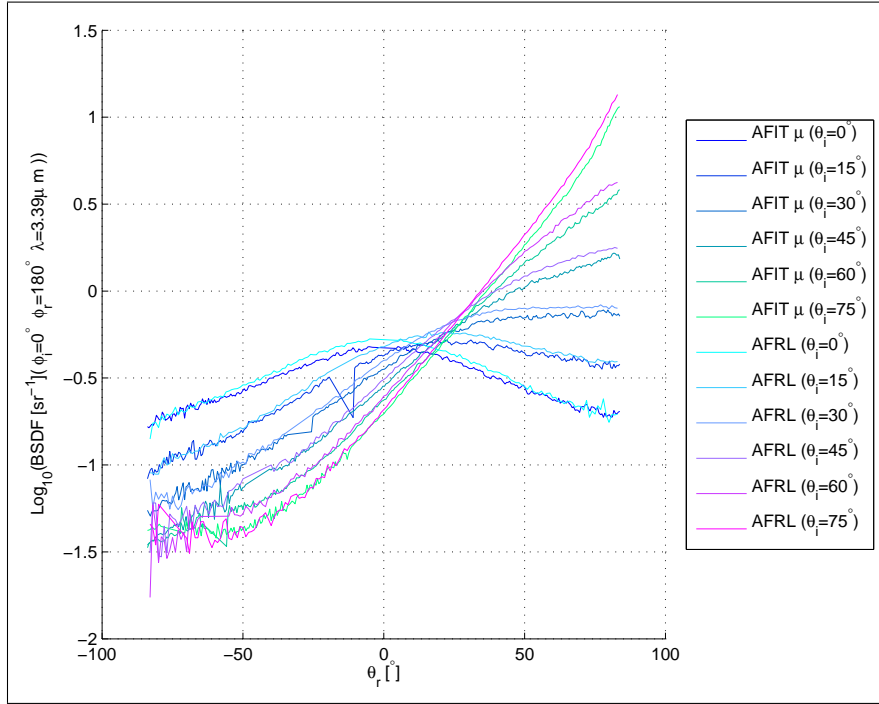
Figure 67. Comparison of uncalibrated AFIT CASI® measurements and AFRL OMF measurements of the rough gold sample, D51A01.

Figure 67 shows the comparison of the two data sets for the rough gold sample. The values and characteristics are almost the same as one would expect. Only the differences will be addressed as the characteristics of each sample have already been discussed. The single trend seen here is that it appears that the AFIT measurements

have a relatively consistent offset when compared. The AFRL measurements tend to give higher values in this case only.

5.4.2   D51C01: Nextel Black Paint.
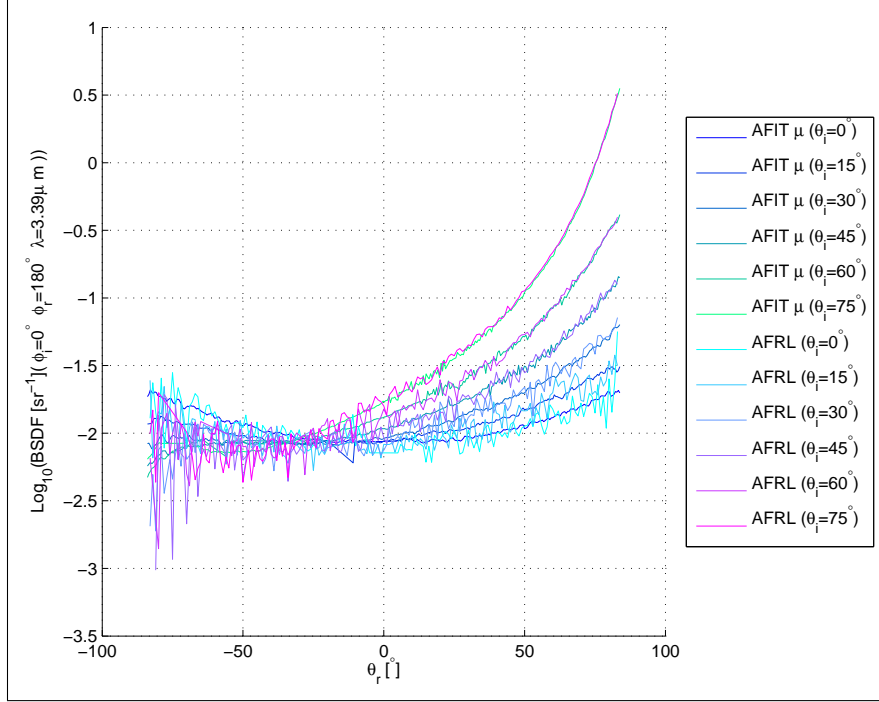
Figure 68. Comparison of uncalibrated AFIT CASI® measurements and AFRL OMF measurements of the Nextel black sample, D51C01.

Figure 68 shows the comparison of the two data sets for the Nextel black paint sample. It is not clear which set gives higher measurements, but both data sets agree well. Another observation is that the AFRL measurements have become noticeably noisier. This noise appears at approximately at $-1.5\ log(sr^{-1})$, and is most likely due to the low BRDF values approaching the noise floor of the equipment. This noise is consistent with the previous measurements.
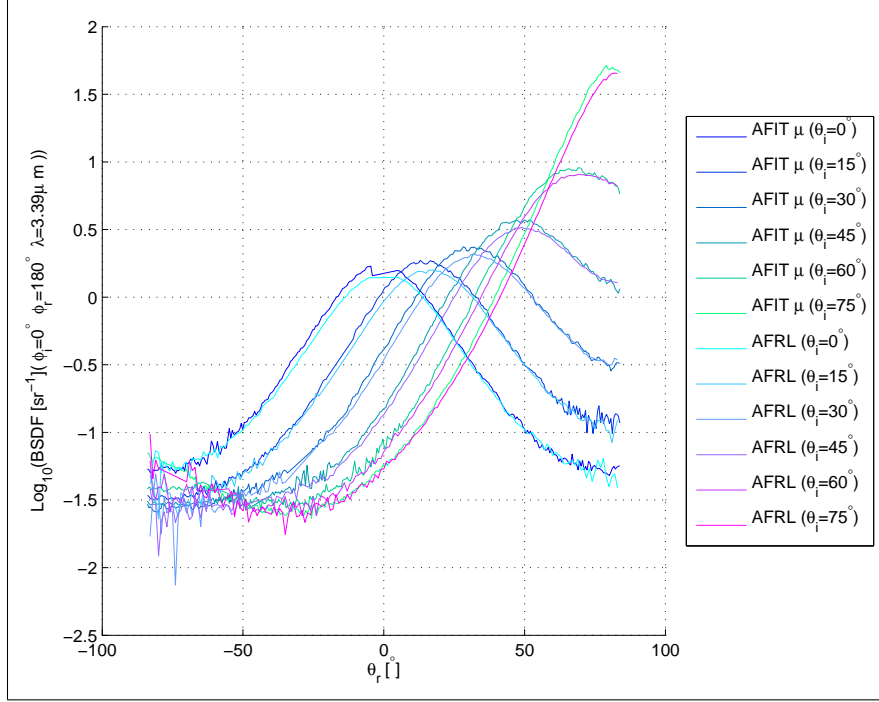
Figure 69. Comparison of uncalibrated AFIT CASI® measurements and AFRL OMF measurements of the rough Krylon silver sample, D51D01.

5.4.3 D51D01: Krylon Silver Paint on Arc-sprayed Aluminum.

Figure 69 shows the comparison of the two data sets for the rough Krylon silver paint sample. The trend here does not follow the first sample. The AFRL measurements are not higher in this case, but the AFIT CASI® measurements are. This is most likely due to the fact that the AFIT measurements of the rough gold sample seem to have an alignment error. This is considered in the calibration section. There also appears to be a slight misalignment between the two measurements, which if the AFRL measurements were properly aligned, confirms a slight misalignment of the AFIT measurements.

5.5   Calibration by Calculated DHR

This section addresses the application of using the measured DHR from the DHR study to calibrate the BRDF measurements. Although this technique was already addressed, a short discussion is added to illustrate that some regions of the Gaussian fit used to calculate the BRDF are more important than others. Figure 70 shows a plot of the $sin()cos()$ term from Equation (43), which is used to calculate DHR from the BRDF. This figure shows that the missing regions of the data, where it is either obstructed or does not exist, have very little effect on the DHR even if the fit is not perfect in these areas. It is important to realize that less than 3% of the data is estimated by the fit in these areas, as shown in the Figure 70. The fit just needs to agree where the data does exist, especially when $\theta_r \approx 45°$. For this reason, unless the fit is poor, $R^2 \leq 0.97$, the quality of the fit will not be addressed.
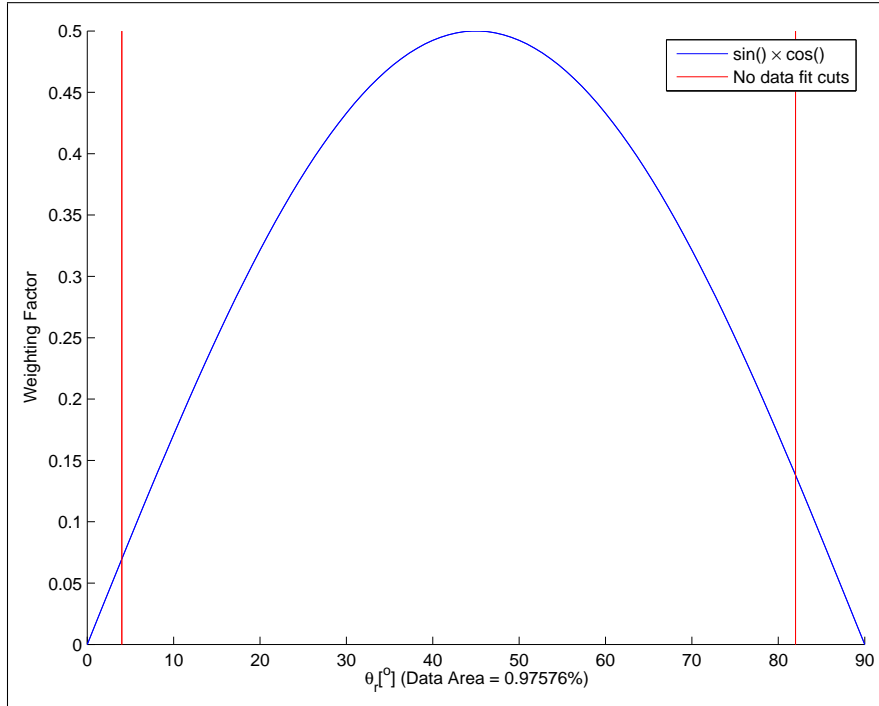
Figure 70. A depiction of the weighting factors used in the DHR calculation to show where the Gaussian fit is most critical.

5.5.1 D51A01: Gold on Nickel on Arc-sprayed Aluminum.

Figure 71 (a) shows the AFIT CASI® uncalibrated measurement average with standard deviation added and the uncalibrated AFRL OMF measurements at $\theta_i = 0°$,. The DHRs are shown in the legend of the figure. To calculate the DHR, a Gaussian distribution is fit, and then the DHR is calculated from it, as described in Chapter IV. The measured DHR from the round robin study was 0.9675 for this sample. A value very close to this is what one would expect from all the measurements when the DHR is calculated, but this is not what happens.

The AFRL measurements produce a DHR of 1.02, and the AFIT measurements produce a DHR of 0.954. These calculated values and the actual DHR measurements are then used to calibrate the data using the technique shown in Section 4.5.2. After this calibration has been applied to the data, the DHR from the BRDF measurements is recalculated. The results after calibration for the rough gold sample are shown in Figure 71 (b). After the application of this multiplicative correction factor, the DHRs agree very well with the measured DHR, and the BRDF profiles themselves generally agree. The slight mismatch of the BRDF profiles here will have consequences later in the analysis.

5.5.2 D51C01: Nextel Black Paint.

Figure 72 (a) shows the uncalibrated comparison of the AFRL and AFIT measurements for the Nextel black paint sample at $\theta_i = 0°$. In this case, both the AFIT and AFRL measurements agree very well with each other, but they both produce DHR values that are too high. The sample itself has a measured DHR of about 0.03, whereas, the calculated DHR from the AFRL BRDF data produces 0.036 and the AFIT BRDF data produces 0.037. It is interesting that they both agree with each other well, and this will be addressed in the analysis section when comparing to the
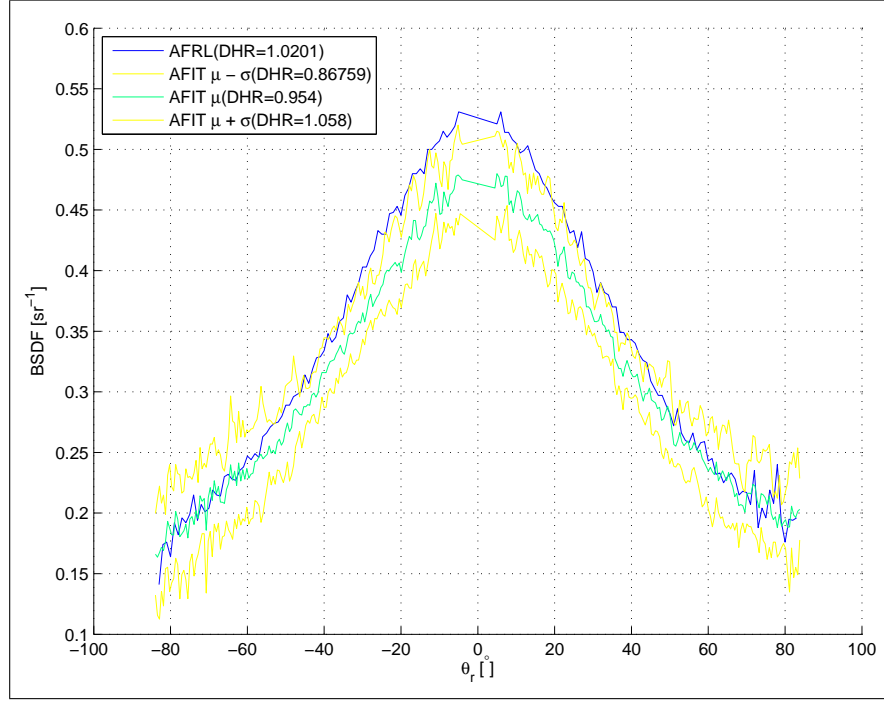
(a)
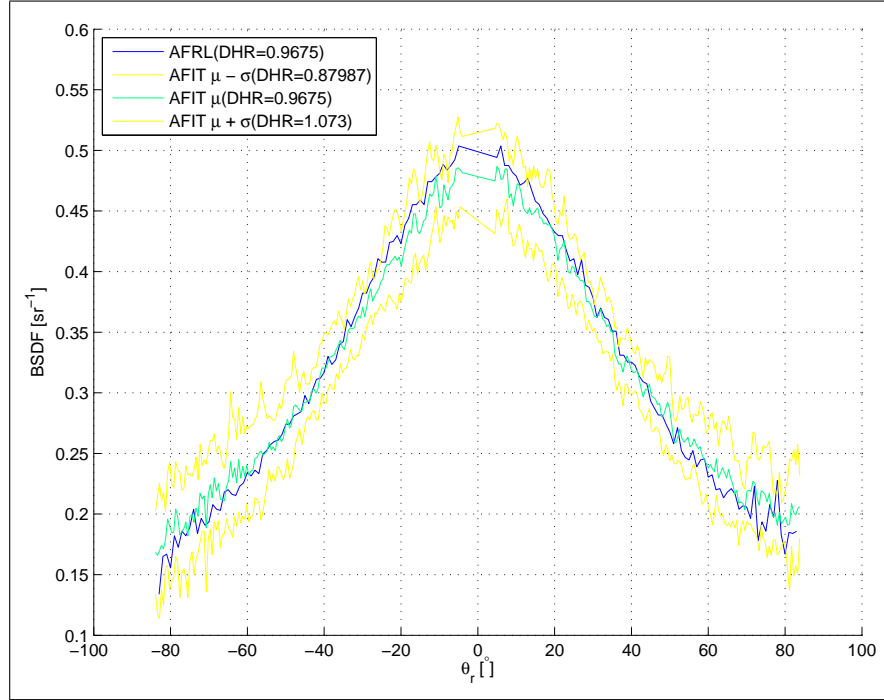
(b)

Figure 71. D51A01: Calibrated and Uncalibrated DHR Comparisons (a) DHR calculated from uncalibrated data for sample D51A01. (b) DHR calculated from data calibrated using the DHRs from Figure a.

102

other sample's measurements. Figure 72 (b) shows the results after the application of the corrective factor.

5.5.3 D51D01: Krylon Silver Paint on Arc-sprayed Aluminum.

Figure 73 (a) shows the uncalibrated comparison of the AFRL and AFIT measurements for the rough Krylon silver paint sample at $\theta_i = 0°$. The AFIT measurements and calculated DHRs are actually higher than the AFRL measurements as they were with the Nextel black paint sample. The AFRL measurements produce a calculated DHR of 0.87 and the AFIT measurements produce a DHR of 0.97, whereas, the sample was measured at 0.83. Figure 73 (b) shows the profile after the application of the corrective factor and a recalculation of the DHR. The BRDF profiles and DHRs match extremely well in this case, but a slight misalignment is still there.

5.5.4 Analysis of Calibration.

Table 10 shows a summary of the results of the DHR measurements and DHR calculations from the BRDF measurements. The corrective factors for each sample measured by the AFIT CASI® , with the same aperture, should agree very well. The same should be true of the corrective factors calculated from the AFRL data. Interestingly enough, this is not the case.

Table 10. Comparison of DHR and DHR Calculated from BRDF.

Sample	DHR	AFIT DHR	AFRL DHR	AFIT C.F.	AFRL C.F.
D51A01	0.9675	0.9540	1.2010	1.0142	0.8056
D51C01	0.0300	0.0371	0.0362	0.8094	0.8294
D51D01	0.8300	0.9562	0.8728	0.8680	0.9510
Average				0.8932	0.8597
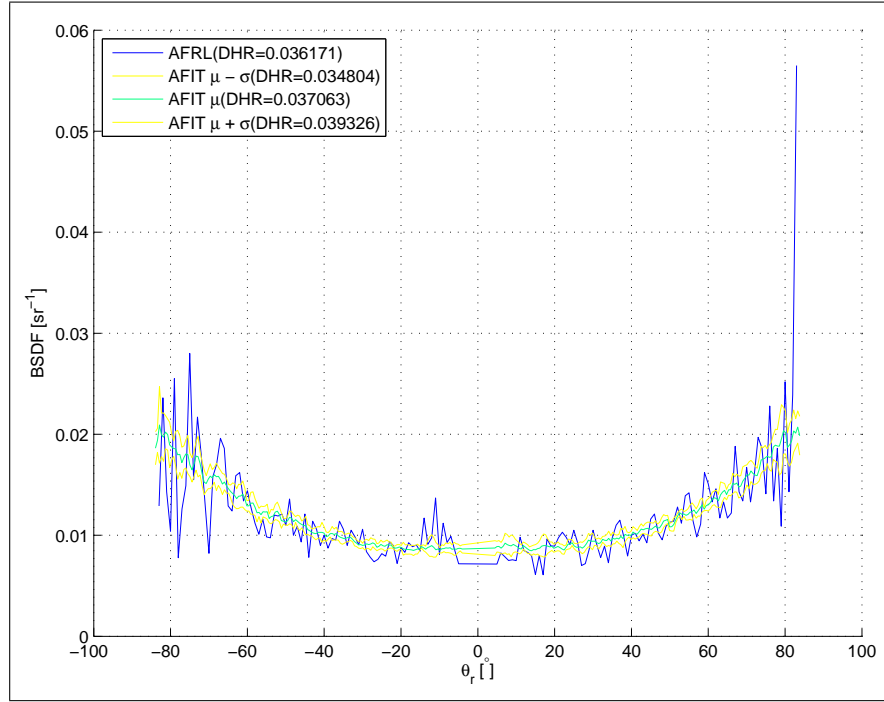
(a)
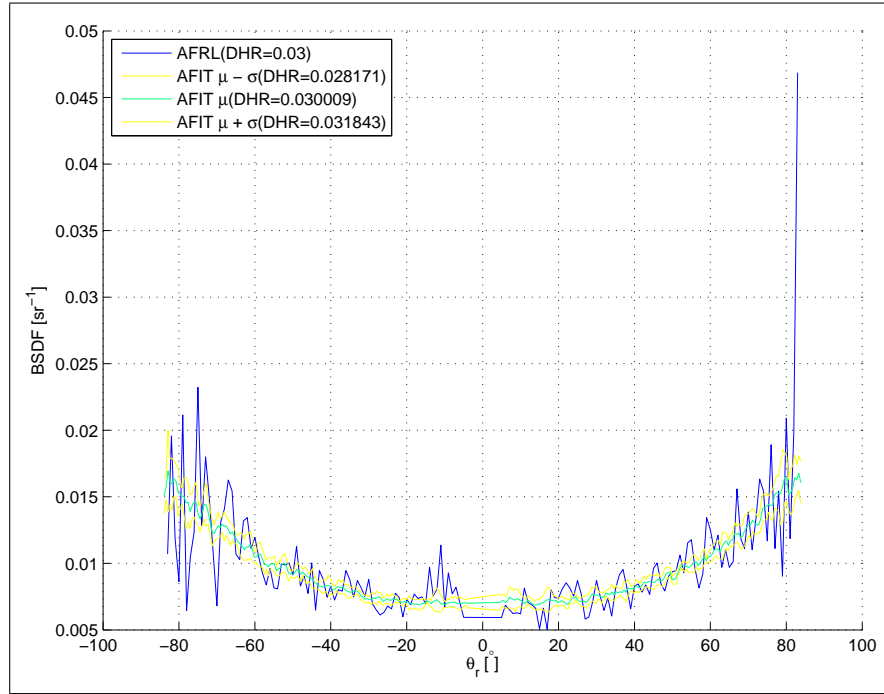
(b)

Figure 72. D51C01: Calibrated and Uncalibrated DHR Comparisons (a) DHR calculated from uncalibrated data for sample D51C01. (b) DHR calculated from data calibrated using the DHRs from Figure a.

104
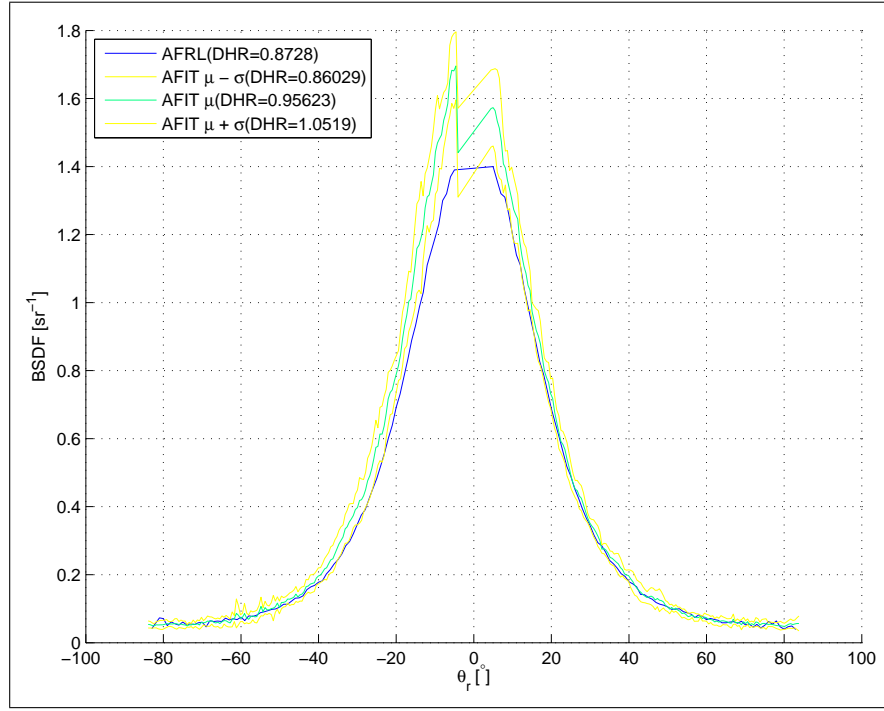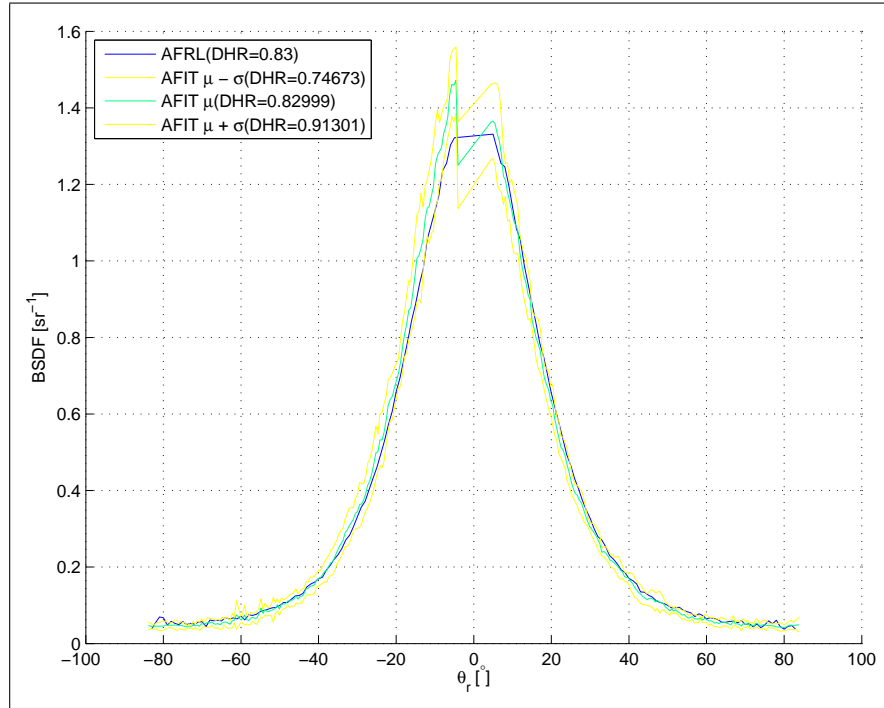
Figure 73. D51D01: Calibrated and Uncalibrated DHR Comparisons (a) DHR calculated from uncalibrated data for sample D51D01. (b) DHR calculated from data calibrated using the DHRs from Figure a.

The first step in deciding what corrective factor to use when DHR measurements are not available for calibration is to look closely at the outliers and decide if they should be used. The obvious outlier in Table 10 is the AFIT corrective factor for sample D51A01, which is greater than 1. The reason why this value is suspect is that Figure 71 (b), after the application of the corrective factor, shows that the BRDF profiles do not match very well when compared with the other calibrated comparisons at $\theta_i = 0°$. This is indicative of a significant misalignment error. The comparison of all the calibrated measurements for D51A01 is shown in Figure 74, this confirms the misalignment when it is compared to Figure 75 for the Nextel black paint sample and Figure 76 for the rough Krylon silver paint sample.
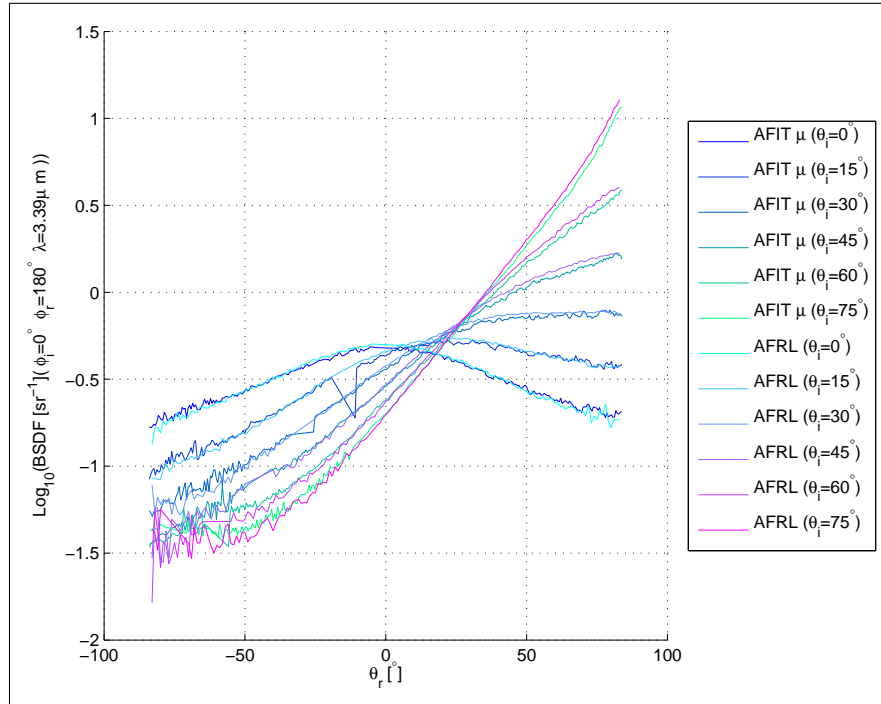
Figure 74.   Comparison of calibrated AFIT CASI® measurements and AFRL OMF measurements of the rough gold sample, D51A01.

Only alignment error in the plane of measurement will be obvious from the plots of the BRDF measurements, because it would only change the location of the specular lobe not the magnitude of it. In this case, the profile would still be much the same.

This is impossible to assess without comparative BRDF measurements. On the other hand, alignment error perpendicular to this plane of measurement would create two effects. The first would be an effect similar to an apparent scaling of the data to make the specular lobe's peak smaller. The second effect, which is related to the first, is that it would not just be scaled, the shape, or profile, of the BRDF would also change. This is because a slice of the BRDF is being taken that does not line up with the specular peak in three dimensions. Then, if the profiles are not the same, it is very likely that there is an out-of-plane alignment issue. This is the case in Figure 71 (b), which plots the rough gold sample, where $\theta_i = 0°$ and the scale is linear for clarity. Therefore, the rough gold sample, D51A01, has an out-of-plane alignment issue that caused the BRDF values to be low relative to the AFRL data. Thus, this corrective factor is high and should not be used to determine the overall corrective factor to use with the measurements in the Chapter VI when DHR is not available for calibration.
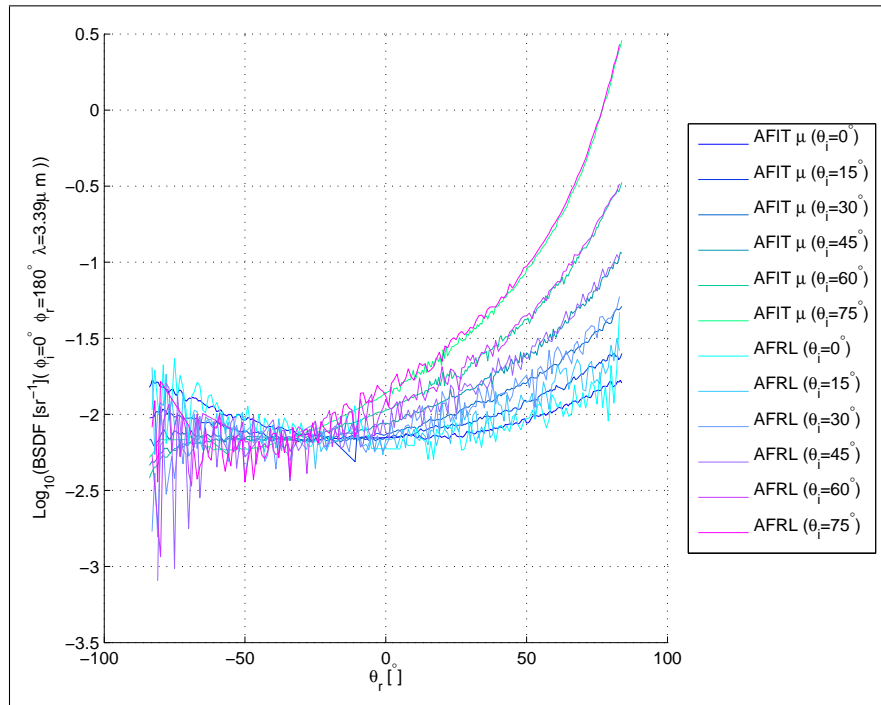
Figure 75. Comparison of calibrated AFIT CASI® measurements and AFRL OMF measurements of the Nextel black paint sample, D51C01.

107

The AFIT CASI® corrective factor should then be the average of the calculated corrective factor from samples D51C01 and D51D01, which is 0.84. Without an exhaustive study of induced alignment error and its effects, it is impossible to know if these samples are actually well aligned. Thus, the assumption must be made that they are even though it is known that the Krylon silver sample, D51D01 has a slight misalignment. This is reasonable because of the agreement in the BRDF profiles for the full set of AFIT measurements with the full set of AFRL measurements shown in Figures 75 and 76. Higher incident angles also tend to make this effect more pronounced. The linear plots in Figures 72 (b) and 73 (b), where $\theta_i = 0°$, can also be used to confirm this.
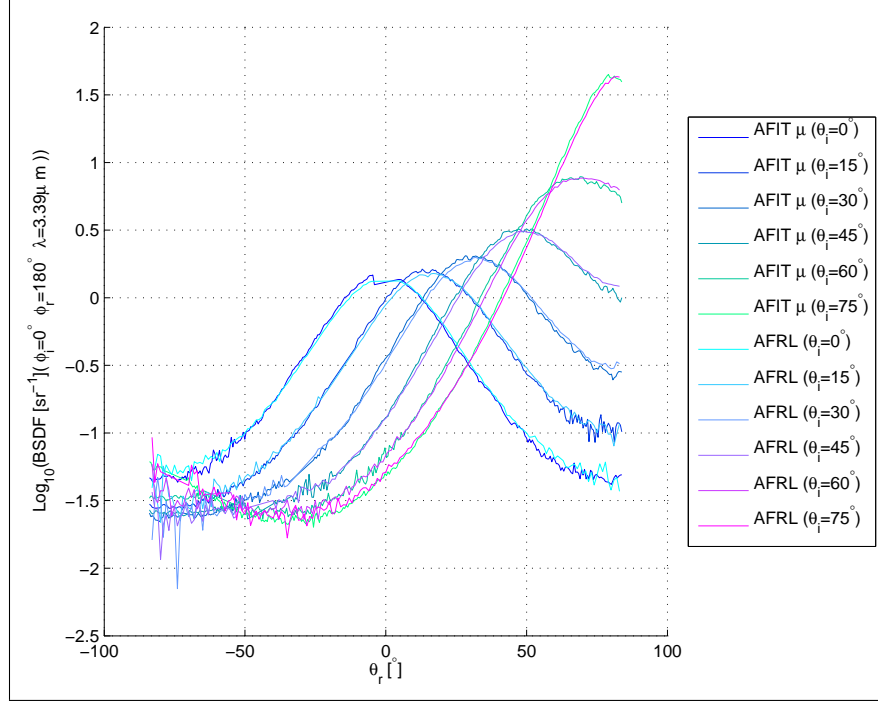
Figure 76. Comparison of calibrated AFIT CASI® measurements and AFRL OMF measurements of the rough Krylon silver paint sample, D51D01.

In addition, the AFRL corrective factors also do not agree as well as they should, but they fall in line with each other well enough to be considered accurate by the standards laid out in the 'OMF Final Report'[14]. Therefore, all of the AFRL mea-

108

surements could be used if futher measurements were to be made with this equipment. From this analysis, it appears that each individual sample requires a measured DHR to calibrate the BRDF.

5.6   Chapter Conclusion

This chapter established the corrective factor, 0.84, to be used with the AFIT CASI® 's largest aperture at $3.39\mu m$, when DHR is not available, to produce measurements that can be considered accurate enough for the analysis of all the remaining samples considered in this study as a MWIR BRDF standard. The samples presented here will also be included in the consideration of an MWIR BRDF standard in Chapter VI.

It is apparent from this chapter that the alignment of a sample, even if diffuse, is very important when using it for calibration. It would be necessary to have DHR measurements for each sample measured to calibrate the BRDF measurements to ensure accurate results using the DHR calibration method only. The use of direct BRDF measurements for comparison provided the ability to ensure the accuracy and throw out the outliers. The ideal case for accurate BRDF measurements is to have a standard with actual BRDF measurements to compare against, get it aligned correctly, and apply the corrective factor. If the unknown sample is mounted in the same physical plane as a mirror and a standard, the mirror could be used for alignment and the standard for calibration. This mounting device would then provide the ability to preserve the alignment between the sample, the standard, and the mirror. This idea will be investigated further in the conclusion.

VI.   Evaluation of Potential BRDF IR Standards

T he IR spectrum is typically, but not always, classified into five bands depending upon the source and the application, these bands are listed in Table 11. This chapter focuses on the MWIR, as did the previous chapter. This chapter uses the methods and procedures previously established to evaluate seven different samples at $\lambda = 3.39 \mu m$ in the MWIR to determine which one would be best suited to be used as a diffuse BRDF standard in the MWIR.

Table 11. Typical IR band Classification [15]

Band	Wavelength	Description
Near Infrared (NIR)	$0.7 \leq \lambda \leq 1.4 \mu m$	Night Vision
Short-wave Infrared (SWIR)	$1.4 \leq \lambda \leq 3 \mu m$	Telecommunications
Mid-wave Infrared (MWIR)	$3 \leq \lambda \leq 8 \mu m$	High Temperature Signatures
Long-wave Infrared (LWIR)	$8 \leq \lambda \leq 14 \mu m$	Low Temperature Signatures
Far Infrared (FIR)	$14 \leq \lambda \leq 1,000 \mu m$	Heating Applications

This chapter first investigates the current reflectance standards and searches for any trace of a published MWIR BRDF standard. Three additional samples being considered for a diffuse MWIR BRDF standard are then described. BRDF measurements of these samples and Spectralon®at $\lambda = 3.39 \mu m$ are then presented. The measurements from all the samples presented in this study are then analyzed and compared before making an assessment on which would be the most suitable for use as a diffuse MWIR BRDF standard at $\lambda = 3.39 \mu m$. The sample's characterization, reflectance, diffuseness, repeatability, and standard deviation are used as parameters to determine its suitability as a diffuse MWIR BRDF standard.

6.1 Investigation of IR Reflectance and IR BRDF Standards

If Spectralon®was such a well performing sample in the visible spectrum, why is Spectralon®not used as a IR reflectance standard as well? The answer is rather simple, the spectral reflectance is not constant and drops off above $\lambda \approx 2.5\mu m$. One of the most desired characteristics of a diffuse reflectance standard, but not necessarily for a BRDF standard, is a consistent spectral reflectance, typically near 1. Rough gold samples such as Infragold®usually provide this in the IR, but Spectralon®has been used in the NIR band for reflectance calibration as well. An example of Spectralon®being used in the NIR at $1.5\mu m$ is presented in a paper by Hanssen[29, pg. 300], but there are not any examples of it being used past this point into the SWIR. This is because the bulk interaction in the Spectralon®, or PTFE, becomes absorptive. Although this is true, Spectralon®at $3.39\mu m$ will also be evaluated in this study.

The current solution to the IR BRDF problem has been to use of rough gold diffuse IR reflectance standards as BRDF standards. The the gold provides a surface with high reflectance that is spectrally flat, and the roughness makes it diffuse much in the same manner that the microfacet BRDF models work. The problem with this is that although the spectral reflectance of gold is predictable in the IR; the rough surface is not. The current commercially available IR alternative to Spectralon®in the IR spectrum is Infragold®. The Labsphere®technical report lists Infragold®as having a $92 - 96\%$ reflectance in the spectral range of $1 \leq \lambda \leq 16\mu m$[45, pg. 7]. Infragold®is recommended for use in the NIR and MWIR, and the reflectance is approximately a constant 95.5% beyond $2\mu m$. Unfortunately, there is not a BRDF standard for this material. There is also another commercially available variant of Infragold®, Infragold-LF®, which is recommended for use in the LWIR band. Infragold-LF®is much rougher and tends to be more diffuse. The reflectance of this material is simply listed as $90 - 94\%$, and has nearly the same spectral characteristics except that it is scaled.

These published spectral reflectance standards are shown in Figure 77.

(a)   (b)
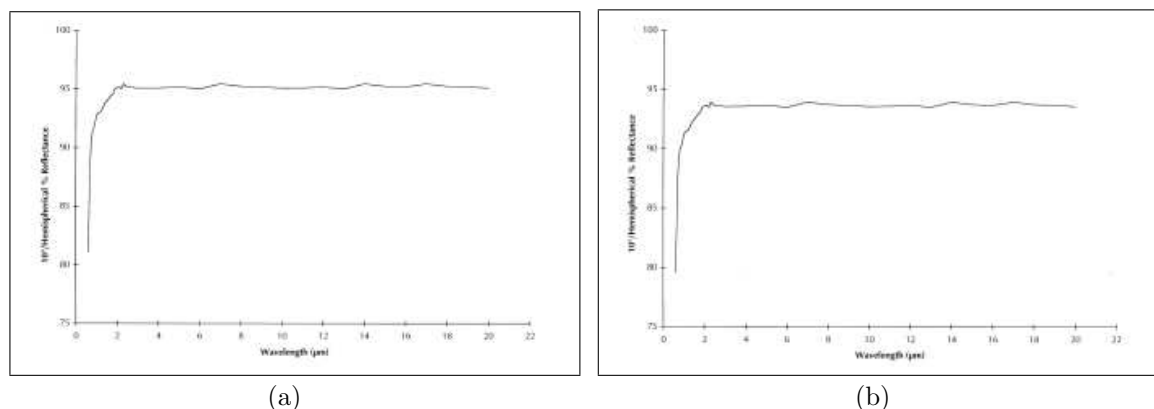
Figure 77. (a) **Labsphere**®published spectral reflectance of **Infragold**®. (b) **Labsphere**®published spectral reflectance of **Infragold-LF**®. Reproduced at original size[45, pg. 7].

Published IR BRDF standards have proven to be much more elusive than published BRDF **Spectralon**®standards. Most IR BRDF studies have been concentrated on the NIR and **Spectralon**®. Most of the available research has not focused on the BRDF in the SWIR and beyond, which is the focus of this document. A few alternative IR reflectance standards have been published in the literature. One of these reflectance standards in the NIR is **Spectralon**®placed behind a rare earth metal transmissive plate, this effectively controls the absorptive bands in the NIR spectrum[16, pg. 1]. This is mostly used to calibrate spectral instruments. A second related effort was the investigation of Silicon (Si) as a specular IR reflectance standard from $2 - 5\mu m$[35]. These might be good future materials to investigate, if available.

Documents that have published IR BRDF measurements in general are rare. There have been several studies of the IR characteristics of flat black coatings[37], and these studies have been mostly conducted for IR scene modeling purposes[34]. The first published IR BRDF measurements of standard reference materials appears in a 'round robin' study published by at NIST[40]. The results from this BRDF round robin varied by as much as three orders of magnitude, and the descriptions of the
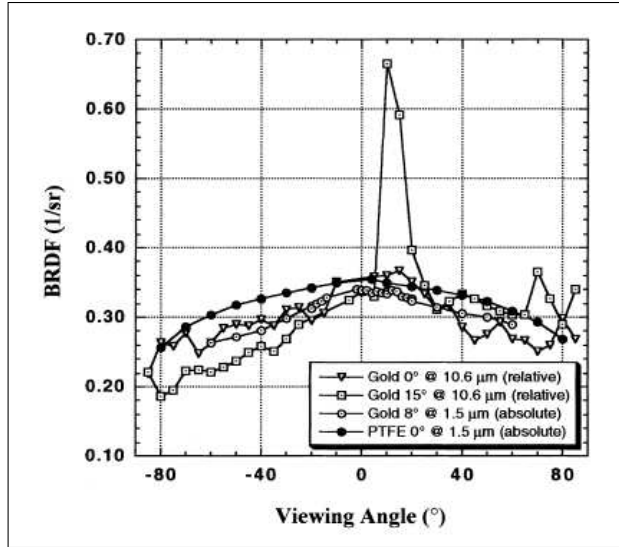
Figure 78. Hanssen's published IR BRDF measurements of **Spectralon**®and **Infragold**®[29].

samples measured are vague. Therefore, this information is not necessarily an option for this study. The first serious consideration put into the research of a IR BRDF standard was published by Hanssen. It focused on the parameters required of a diffuse material if it was to be used as a reflectance and BRDF standard in the IR[27]. The requirements presented were so strict that there has not been any follow-on research located where they have been met. The best source of IR BRDF data presented as a scientific measurement of a standard was published by Hanssen in 'Infrared diffuse reflectance instrumentation and standards at NIST'[29]. This data as published is shown in Figure 78. The current state of the art leaves much to be desired in IR BRDF measurement.

6.2 Additional Sample Descriptions

The Spectralon®sample has already been described in Section 4.4.1, so it will not be repeated here, but this section describes the other possible candidates being evaluated for use as a MWIR BRDF standard that have not been previously presented.

6.2.1 Infragold®.
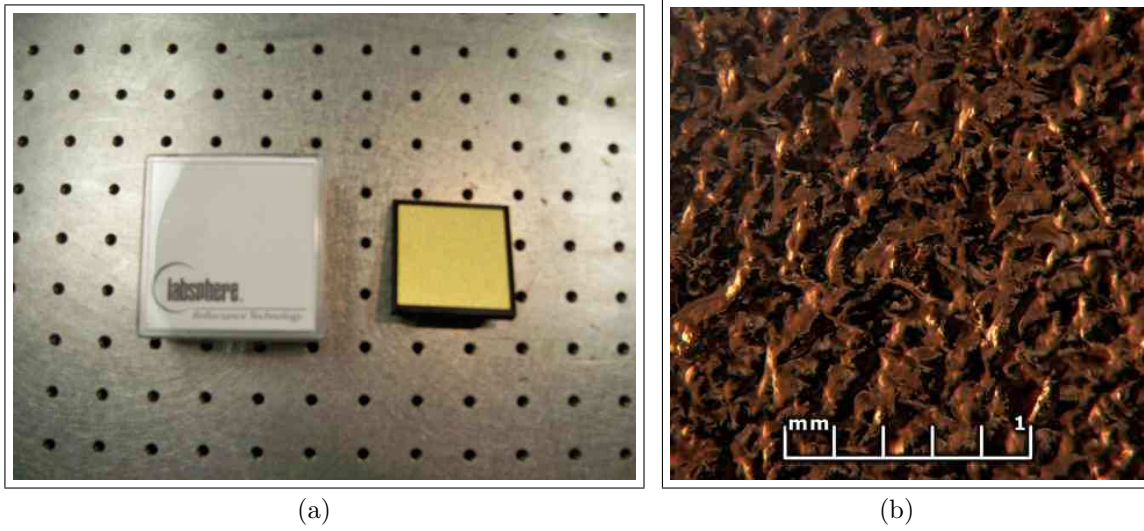
Figure 79. Infragold®(a) Photo of sample and container. (b) Surface microscope photo of sample.

The Infragold®sample used in this study was a calibrated reflectance sample purchased from Labsphere®. As Infragold®has already been discussed, Figure 79 is provided for documentation. The calibration documentation lists the reflectance for this specific sample as 0.95 at $\lambda = 3.39 \mu m$.

6.2.2 Infragold-LF®Prototype Sample.

Figure 80 shows one of the original prototypes for Infragold-LF®. This sample was on loan from the AFRL OMF. It has a flame-sprayed aluminum coating on a substrate which was then gold coated. The surface roughness of this sample is much greater than any of the other samples that are presented in this study. This is confirmed by the microscope photo shown in Figure 80 (b). The intent of the rougher surface is to make the sample even more diffuse, but it also has the consequence of higher surface variance.
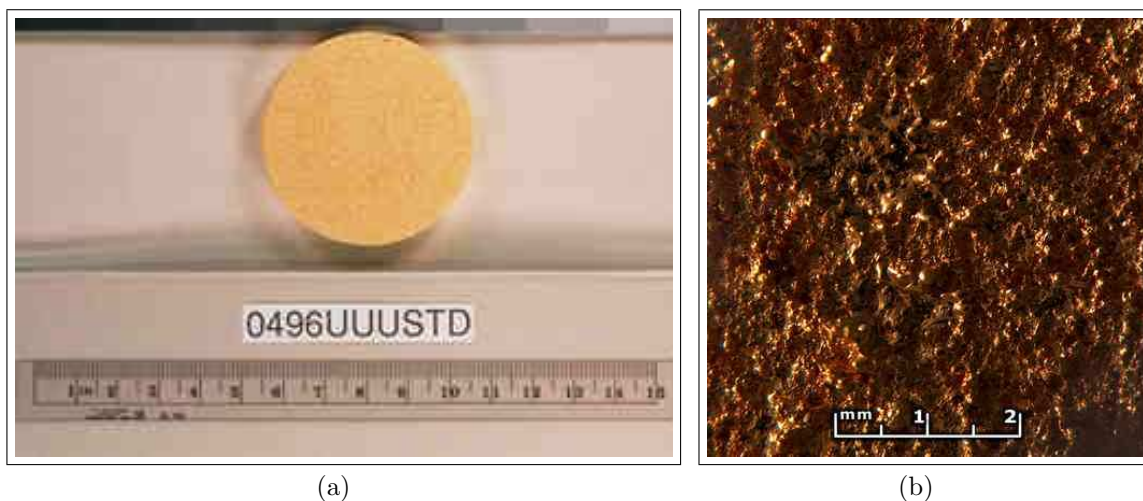
Figure 80. Infragold-LF®Prototype (a) Photo of sample and container. (b) Surface microscope photo of sample.

6.2.3 Gold Deposited on the Surface of a RPC®Laser Beam Diffuser.
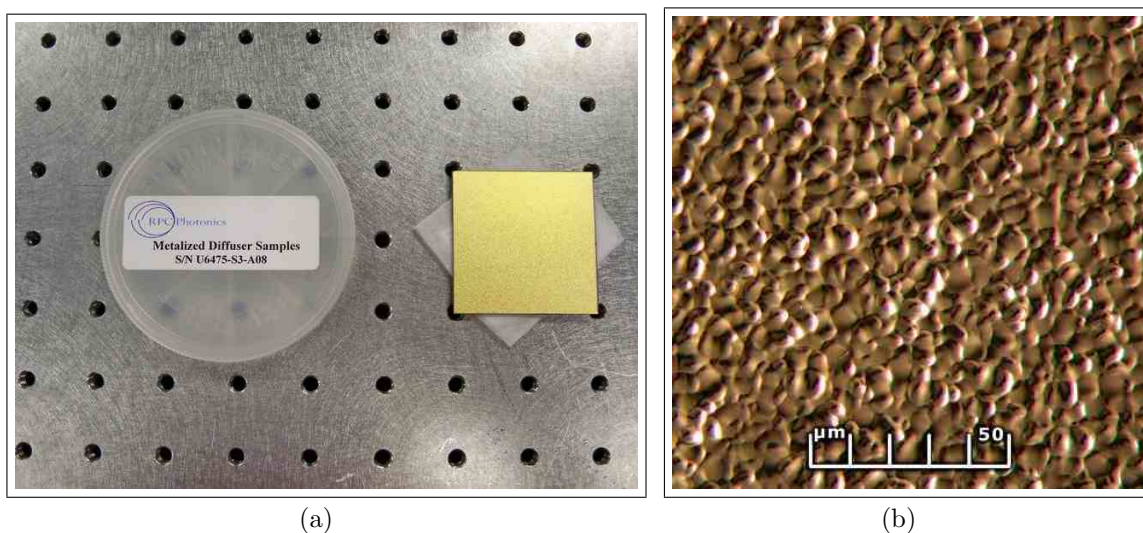
Figure 81. Gold deposited on the surface of a RPC®laser beam diffuser (a) Photo of sample and container. (b) Surface microscope photo of sample.

Figure 81 shows the most experimental sample in this study. The manufacturer of this sample, RPC®Photonics, 'designs and manufactures optical components with precision structured surfaces, refractive and/or diffractive, that can be used to control and distribute light in an efficient way, for illumination and display systems and

115

other light-control applications'[7]. This sample was first proposed by NIST for consideration as an IR BRDF standard because the roughness created on the surface of the RPC®laser diffuser has a surface of randomly spaced and sized half-spheres. The surface of this sample, which is a replicated polymer on a glass substrate, was gold coated with a sputtering process for this study. In theory, this should create a more consistent BRDF profile than the arc or flame sprayed aluminum providing the surface roughness. Figure 81 (b) shows a microscope photo of the sample illustrating the sample's surface profile.

6.3 Additional Sample Measurement Sets

In this section, the measurement set for each of the additional samples will be presented individually and the primary scattering mechanisms will be discussed, as well as each sample's repeatability profile. The corrective factor of 0.84, determined in Chapter V, is used to calibrate all additional measurements in this section with the exception of Infragold®, which has a calibrated DHR. This assumption is necessary because direct DHR measurements were not available to calibrate each of these samples individually.

6.3.1 Spectralon®at 3.39 μm.

This set of measurements was conducted in order to see what happens when Spectralon®is measured out of its intended range because such results could not be found in the literature. Figures 82 and 83 show a direct comparison of Spectralon®at $\lambda = 633\eta m$ and $\lambda = 3.39\mu m$ with a perfect Lambertian scatterer added for reference between the figures. Considering it has not been used as a reflectance standard in the MWIR, it was expected to have very poor performance in the IR due to absorption, but as shown in the direct comparison, the performance is not as poor
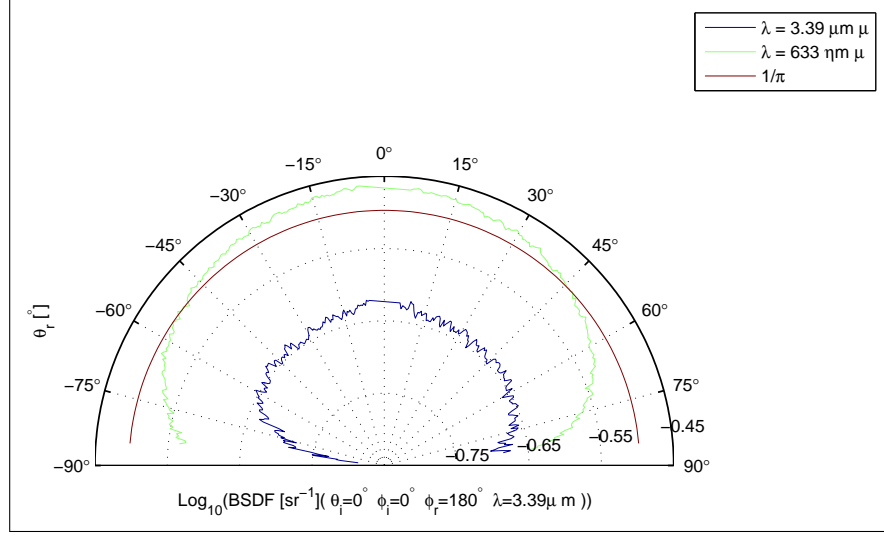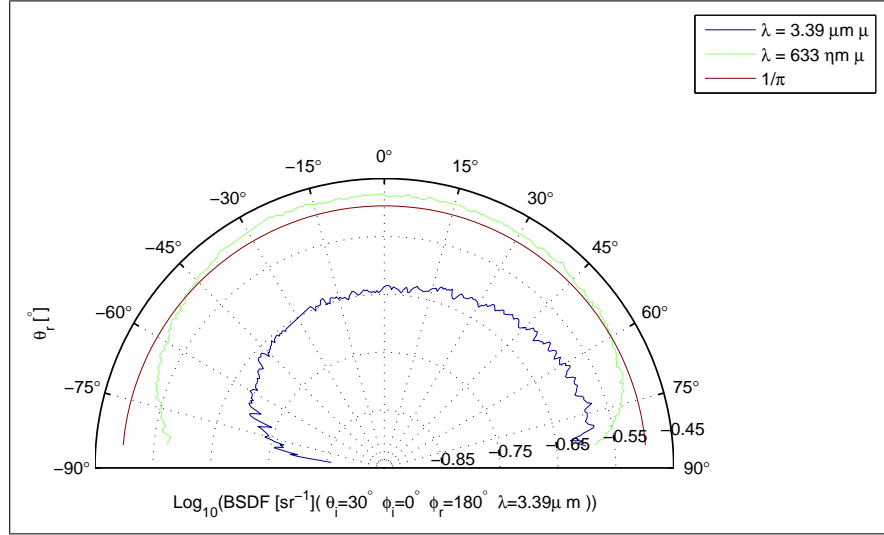
Figure 82. Comparison of **Spectralon**®measurements at $\lambda = 633\eta$m and $\lambda = 3.39\mu$m at (a) $\theta_i = 0°$. (b) $\theta_i = 30°$.

as expected. The DHR calculated from the BRDF is 0.70 at $\lambda = 3.39\mu m$; this is actually better than some of the gold coated samples. The calculated DHRs will be further investigated in the analysis section, but it is of interest to note here because of **Spectralon**®'s extensive use a spectral reflectance standard.

Figure 82 shows the comparison of the in-plane BRDF at $\theta_i = 0°$ and $\theta_i = 30°$. This figure demonstrates that at near normal incidence angles, the BRDF at $\lambda =$
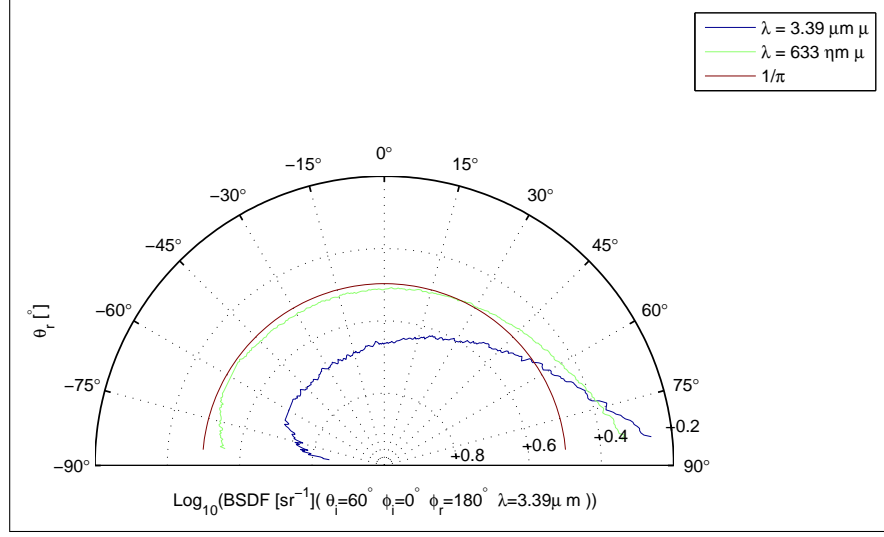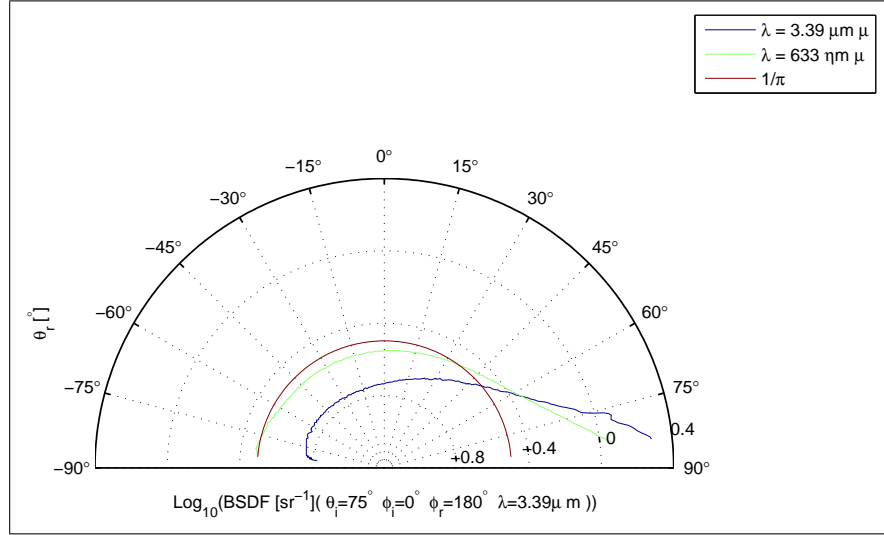
Figure 83. Comparison of Spectralon®measurements at $\lambda = 633\eta$m and $\lambda = 3.39\mu$m at (a) $\theta_\mathbf{i} = 60°$. (b) $\theta_\mathbf{i} = 75°$.

$3.39\mu m$ appears to be only scaled from its profile at $\lambda = 633\eta m$. On the other hand, Figure 83 shows that at $\theta_i = 60°$ and $\theta_i = 75°$ Spectralon®gets much more specular than at $\lambda = 633\eta m$. This is most likely due to a change in the index of refraction, which is the square root of the ratio of electrical emissivity and permeability, in the material due to the change in wavelength. This result agrees with the common Fresnel equation, Equation (21). Figure 84 (a) shows the in-plane Spectralon®measurements

118

at $\lambda = 3.39\mu m$ on a Cartesian plot with the standard deviation added, and subfigure (b) shows the more intuitive polar plot with the ideal perfect Lambertian BRDF value added for reference.

Figure 85 (a) shows the PDM values at $\theta_i = 0°$; this is very consistent with the results in the visible and shows excellent repeatability compared to other samples in the IR. This is most likely due to the nature of the bulk scatter. Figure 85 (b) shows the PDM values at $\theta_i = 75°$, which also shows very good repeatability right up to when the scatter becomes specular, confirming the consistency of the bulk scatter.

6.3.2   Infragold®.

Figure 86 shows the full measurement set for the Infragold®sample. This sample is very similar to the rough gold sample, D51A01, used in the round robin DHR study. Thus, it would be expected to have a very similar measurement set, and it does. This sample is the sole case of the measurements presented in this chapter where a calibrated measured DHR was available for calibration. Thus, the corrective factor determined in Chapter V was not used. The corrective factor in this case was 0.95, which is reasonably close when compared with the other corrective factors. Figure 86 (b) shows that this sample does not exhibit clear specular lobing, and it behaves similar to the other rough gold samples.

Figure 86 (a) shows that the standard deviation lies close to the mean values except when the condition, $\theta_i - 50° \gtrsim \theta_r \gtrsim \theta_i + 50°$, is met. This is likely due to the fact that the microfacet surfaces causing this scattering may be experiencing multiple reflections, shadowing, and masking. This increases the uncertainty in the path of the light ray, which causes in an increase in the standard deviation of the BRDF. The PDM plots shown in Figure 87 confirm this assertion. This sample obviously does not perform as well as the Spectralon®at $\lambda = 3.39\mu m$ in terms of repeatability. The
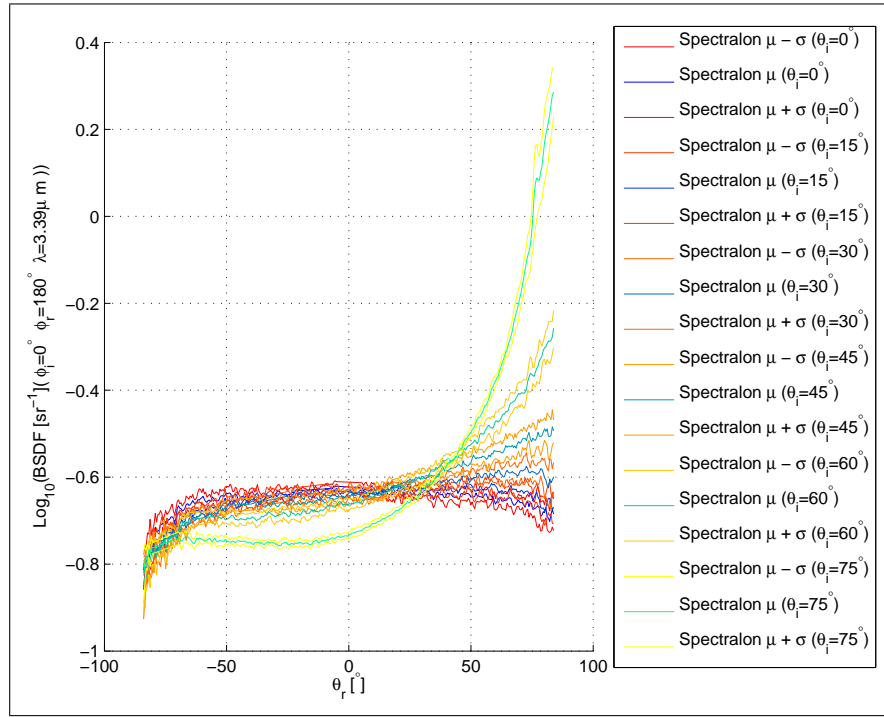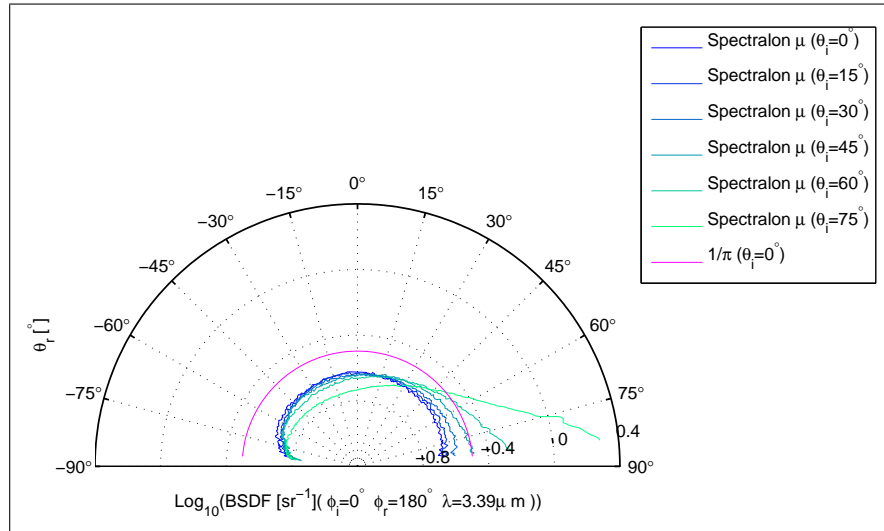
Figure 84. Measurements of **Spectralon**®sample conducted with **AFIT CASI**® at $3.39\mu\text{m}$
(a) Logarithmic Cartesian plot of full measurement set with standard deviation added.
(b) Logarithmic polar plot of full measurement set.
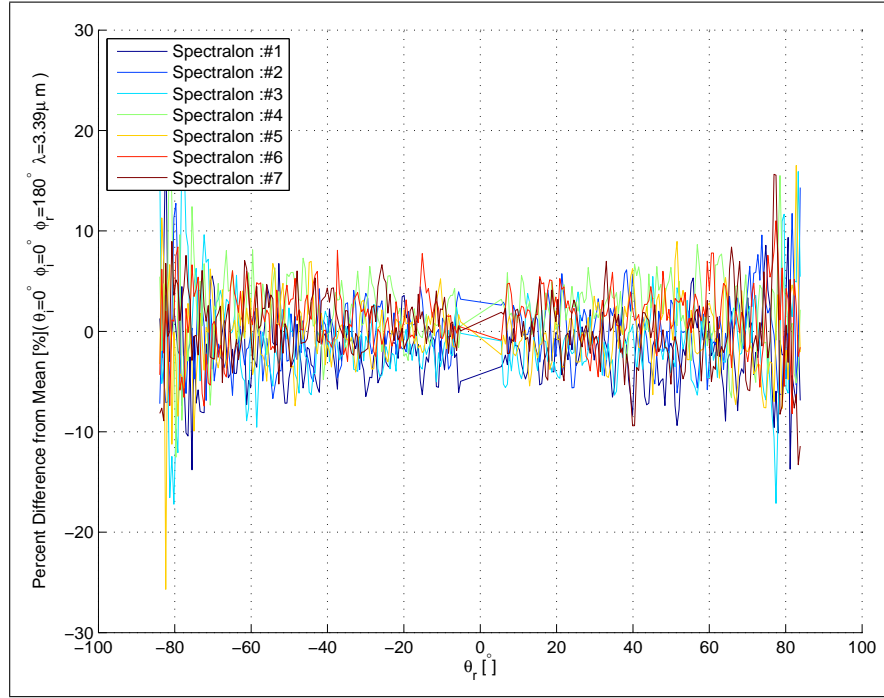
(a)
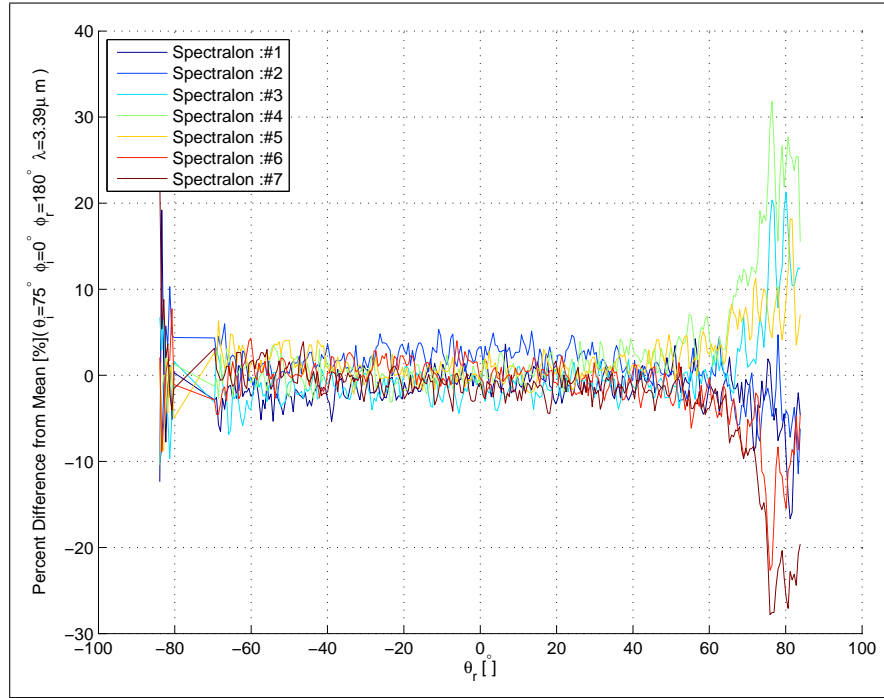
(b)

Figure 85.   Percent difference from the mean for each measurement made of **Spectralon**®with the **AFIT CASI**® at (a) $\theta_i = 0°$ and $\lambda = 3.39\mu$m.   (b) $\theta_i = 75°$ and $\lambda = 3.39\mu$m.

121
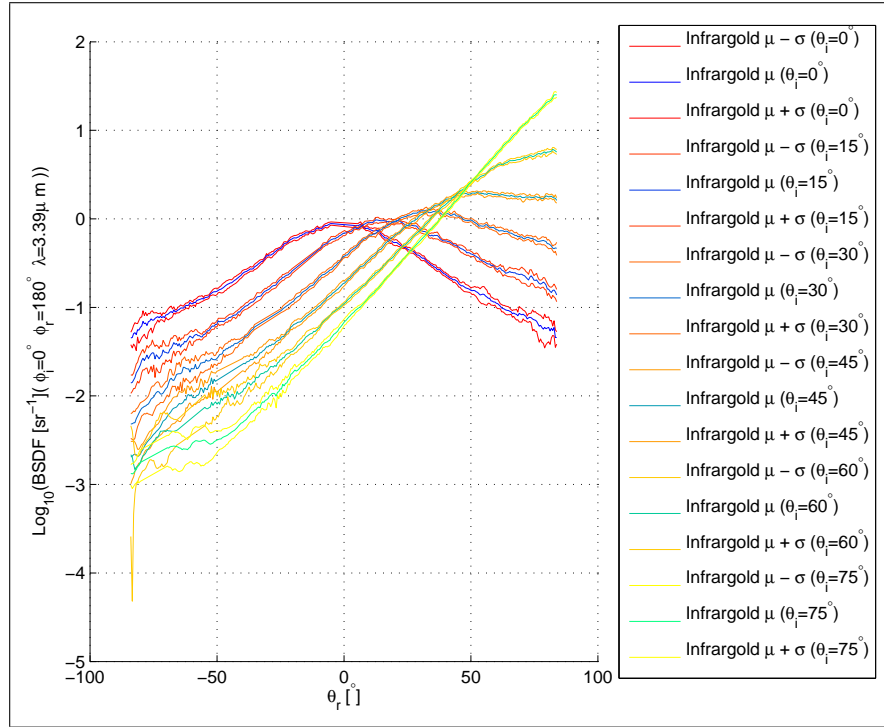
(a)
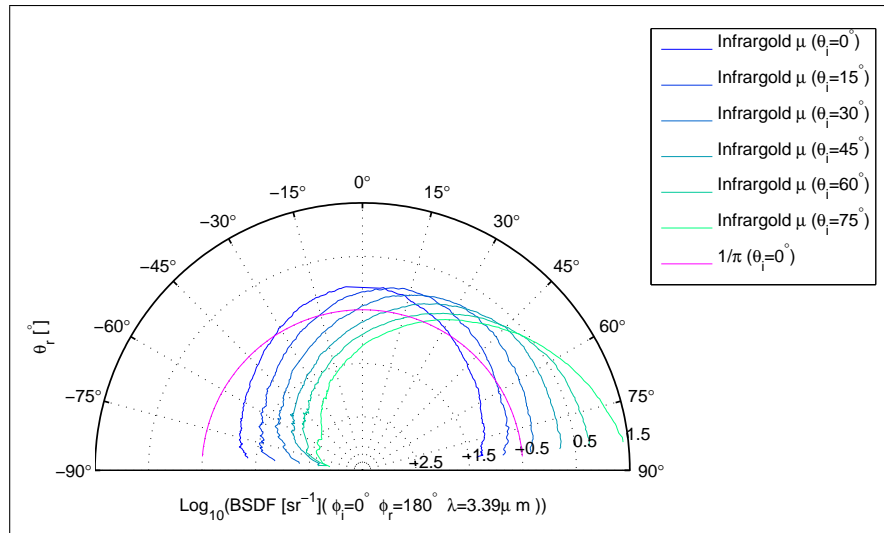
(b)

Figure 86. Measurements of **Infragold**®sample conducted with **AFIT CASI**® at **3.39**μm
(a) Logarithmic Cartesian plot of full measurement set with standard deviation added.
(b) Logarithmic polar plot of full measurement set.

PDM values for the retroreflection at $\theta_i = 75°$ are likely high because of significant shadowing occurring on the face of the sample at high incidence angles.

6.3.3 Infragold-LF®Prototype Sample.

This sample is physically almost the same as the Infragold®except that the surface is much rougher. This has the effect of creating a much more diffuse distribution, but it is obvious that this also greatly increases the standard deviation and the PDM. This, in turn, adversely affects the repeatability of the sample. Figure 88 (a) shows that the variance of the surface roughness across the face of the sample is so high that it not only creates extremely high values of standard deviation, but causes noise in the mean of the measurement set. Figure 88 (b) shows that this sample provides a very diffuse BRDF profile, even at higher angles of incidence.

Figure 89 shows the PDM plots for this sample, and this is where the surface variance becomes an immediately apparent problem. The interesting characteristic seen here is that the PDM actually *decreases* with the increase in the incidence angle. This is very diffcult to explain, because this behavior is not seen in any of the other samples. The only possible explanation is that the distribution of surfaces is such that there are actually fewer multiple reflections at higher incident angles.

6.3.4 Gold Deposited on the Surface of a RPC®Laser Beam Diffuser.

This sample actually shows some very interesting characteristics that have not been demonstrated with other samples. The consistent hemispheres on the surface most likely create many multiple reflections that are distributed by the shape of the hemispheres. Figure 90 (a) shows the full measurement set with standard deviation. The standard deviation is actually very well behaved in this sample regardless of θ_r and θ_i. The interesting effect of the small lobes at $\theta_r \approx \pm 80°$ is unusual because it
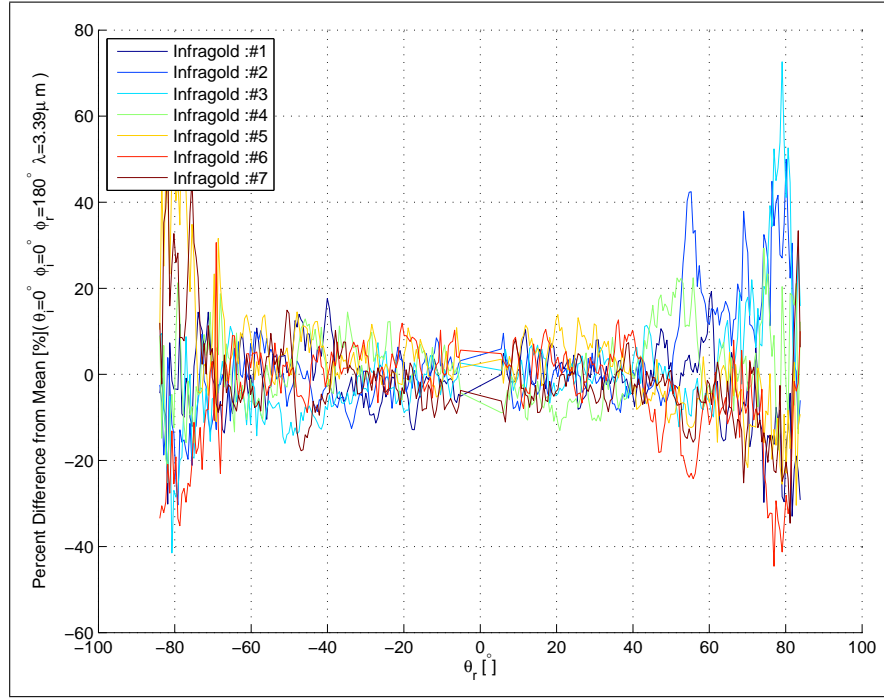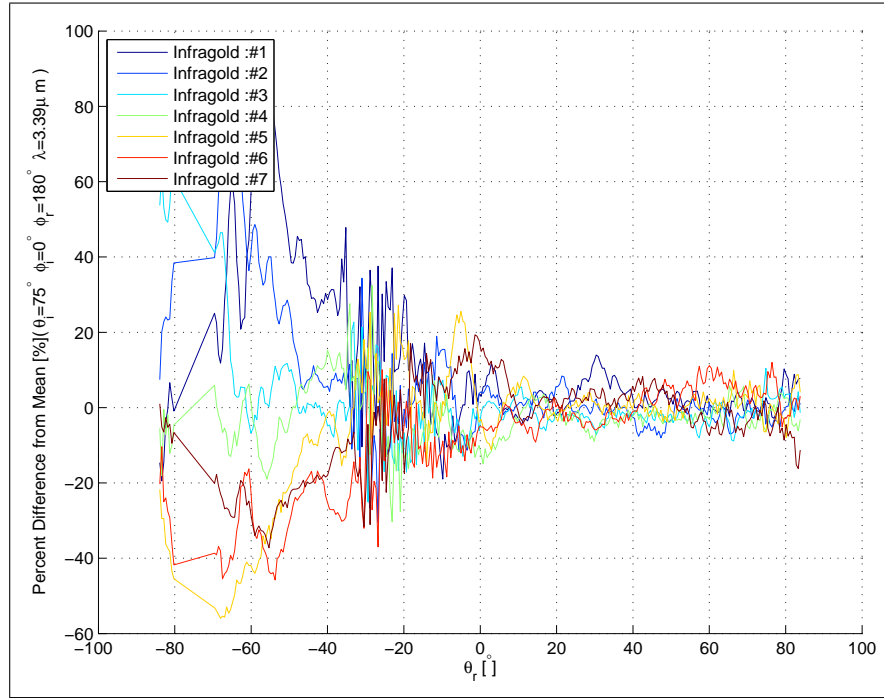
Figure 87. Percent difference from the mean for each measurement made of **Infragold**®with the **AFIT CASI**® at (a) $\theta_{\mathrm{i}} = 0°$ and $\lambda = 3.39\mu$m. (b) $\theta_{\mathrm{i}} = 75°$ and $\lambda = 3.39\mu$m.

124
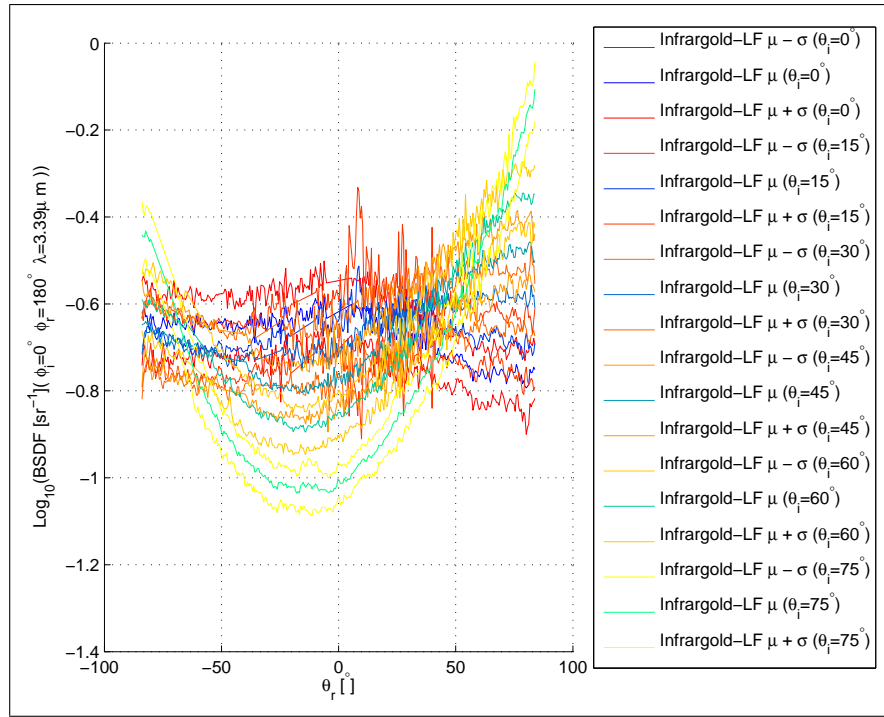
(a)
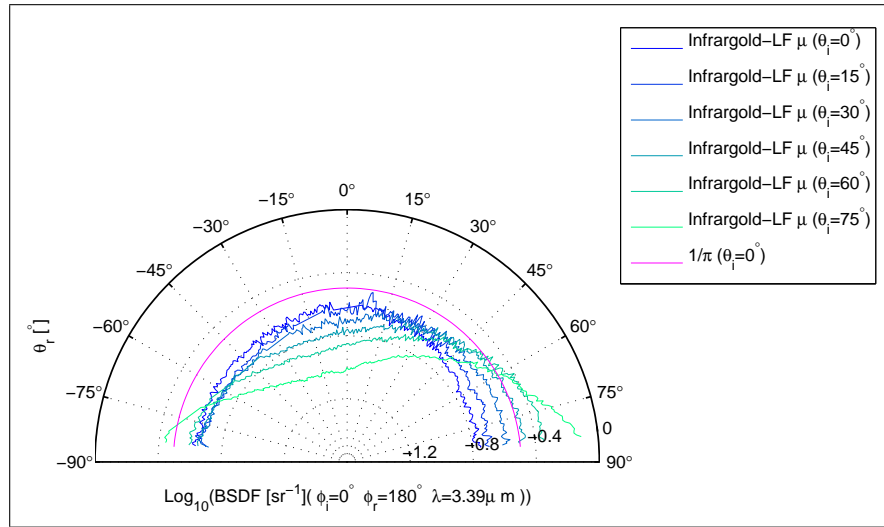
(b)

Figure 88. Measurements of **Infragold-LF**®sample conducted with **AFIT CASI**® at 3.39μm (a) Logarithmic Cartesian plot of full measurement set with standard deviation added. (b) Logarithmic polar plot of full measurement set.
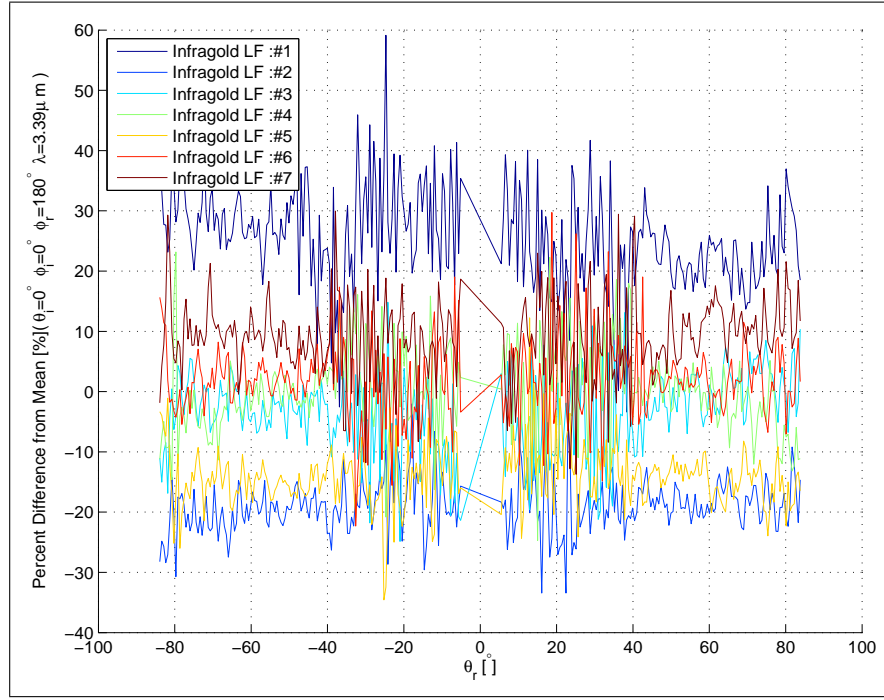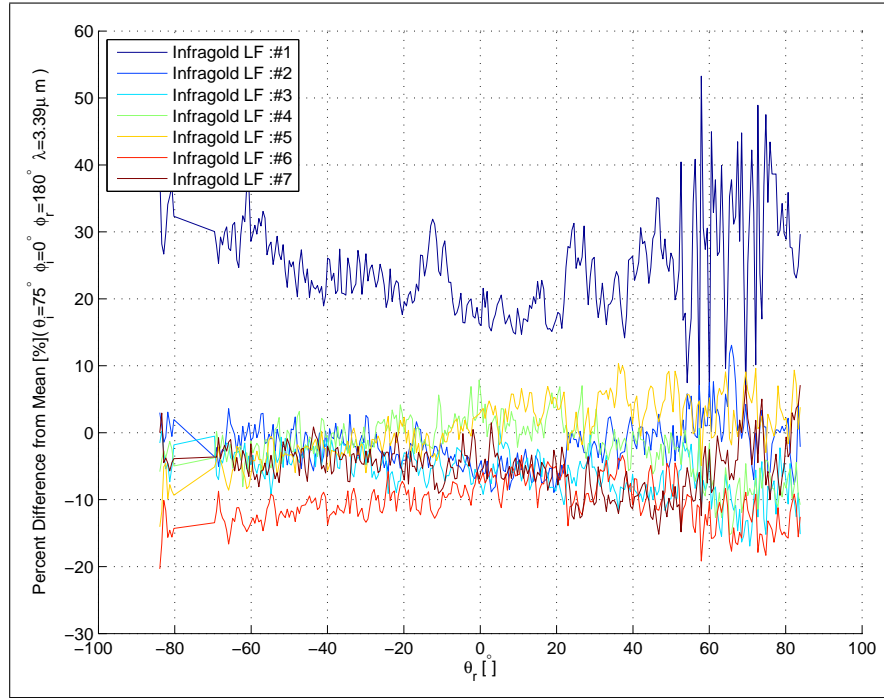
Figure 89. Percent difference from the mean for each measurement made of **Infragold-LF**®with the **AFIT CASI**® at (a) $\theta_i = 0°$ and $\lambda = 3.39\mu$m. (b) $\theta_i = 75°$ and $\lambda = 3.39\mu$m.

occurs in both forward and reverse scatter, and its location is relatively independent of the incident angle. Another unique characteristic is that there are two small diffuse lobes on either side of the specular lobe. Furthermore, the specular lobe shows up at $\theta_i \gtrsim 60°$. This is likely due to a specular reflection off of the top surface of the small hemispheres that does not experience any multiple reflections or shadowing.

Figure 91 shows the PDM plots for this sample. The PDM when $\theta_i = 0°$ is not as good as one would expect with the relatively regular nature of the surface. Each measurement tends to be consistently high or low. This may suggest that the hemisphere size is large enough that the beam is being reflected more in one direction than another when the illuminated location changes. This effect gets even more pronounced at $\theta_i = 75°$, and the errors get larger. This shows the importance of using the PDM to see how each measurement is different. The large PDM errors in the backward reflection are due to the smaller BRDF values and shadowing.

6.4   Analysis

This section comparatively analyzes all samples considered in this study for its suitability as a diffuse MWIR BRDF standard. The first step is to directly compare all the samples against one another in the same figure in order to understand their differences. Although this is a qualitative analysis, it is valuable. Secondly, the reflectance, diffuseness, average PDM, and average relative standard deviation are all quantitatively analyzed. These parameters and the qualitative analysis are then combined to compare their suitability as a diffuse MWIR BRDF standard.

There are also additional parameters that would need to be considered for the analysis of a diffuse MWIR BRDF standard, but they are beyond the scope of this study. The manufacturing, reproduceability, and cost of the candidates are just a few of the possible additional parameters that could be considered. A final study would

127
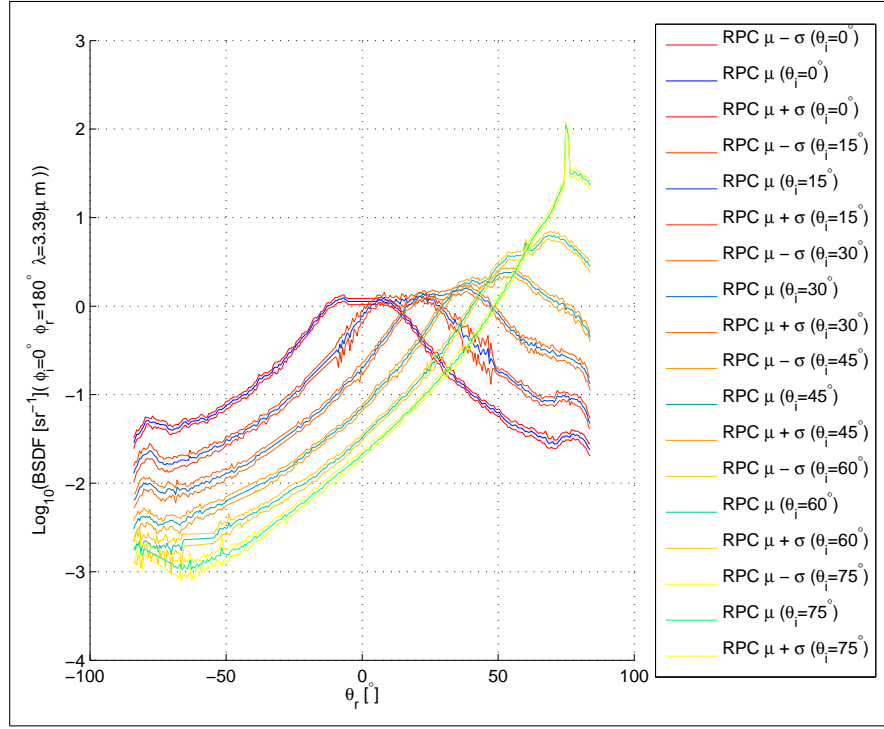
(a)
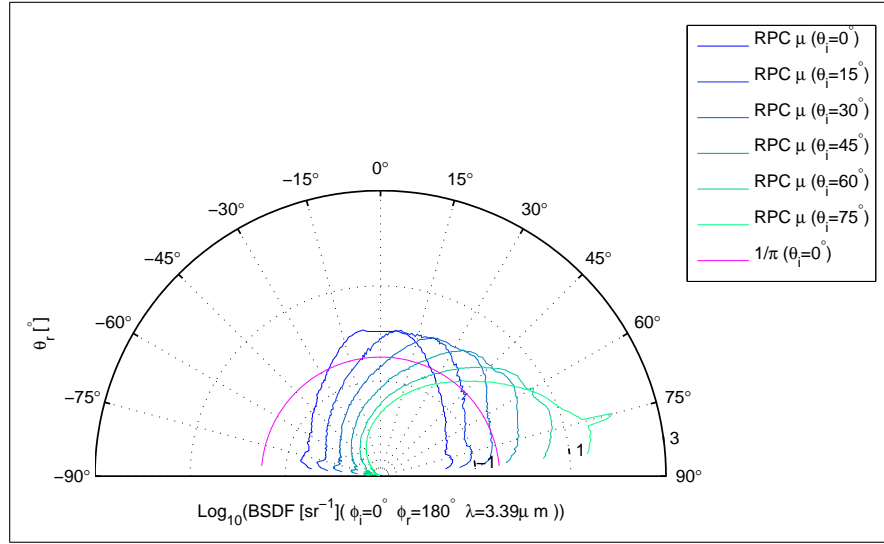
(b)

Figure 90. Measurements of metalized RPC®laser beam diffuser sample conducted with AFIT CASI® at 3.39μm (a) Logarithmic Cartesian plot of full measurement set with standard deviation added. (b) Logarithmic polar plot of full measurement set.
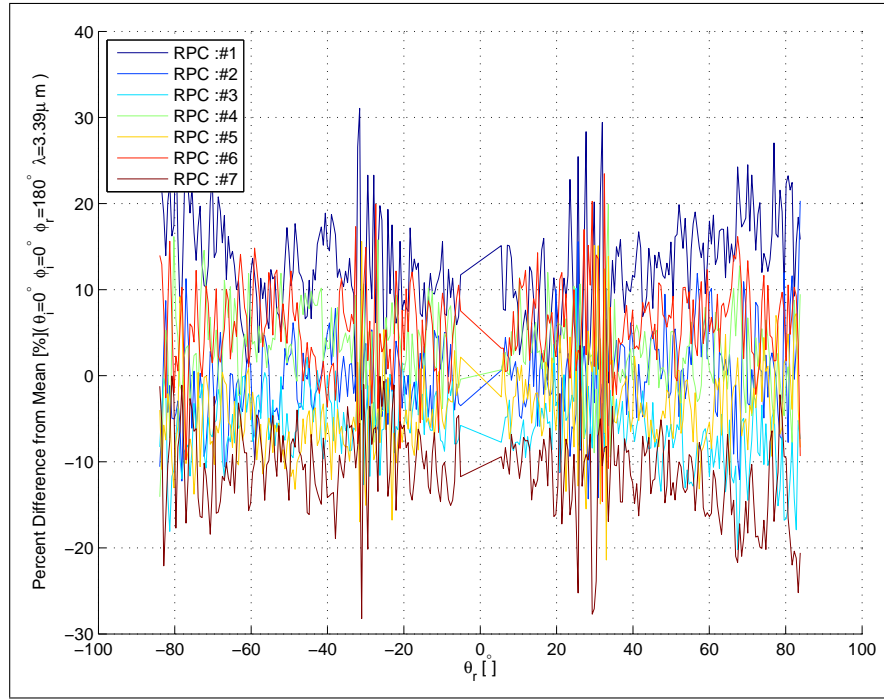
(a)
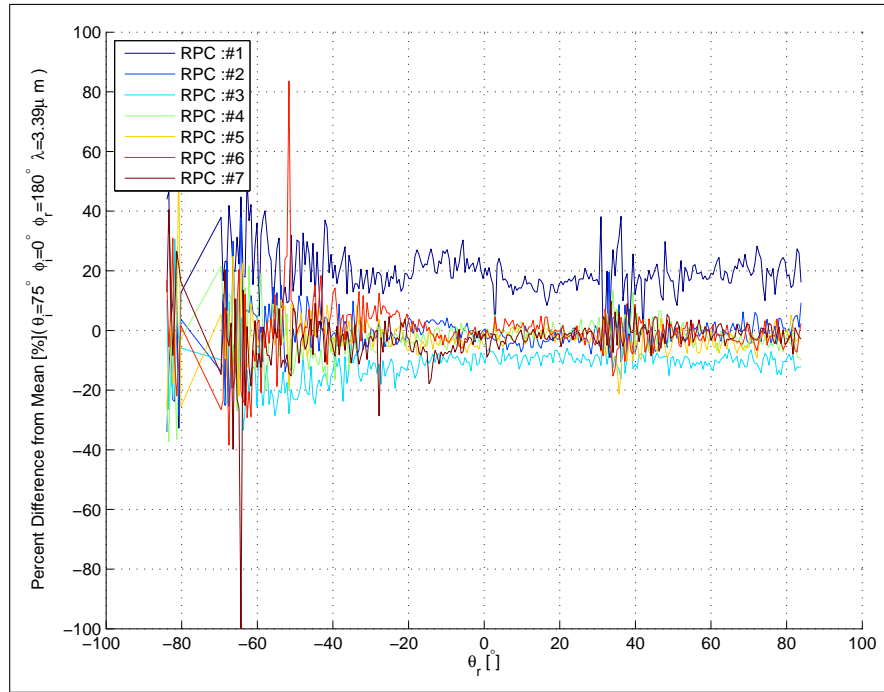
(b)

Figure 91. Percent difference from the mean for each measurement made of the metalized RPC®laser beam diffuser sample with the AFIT CASI® at (a) $\theta_i = 0°$ and $\lambda = 3.39\mu$m. (b) $\theta_i = 75°$ and $\lambda = 3.39\mu$m.

129

also require multiple samples and a much larger measurement set. This study is just a preliminary comparative analysis that is focusing on the sample's characteristics themselves.

6.4.1   Characterization.

This section presents a visual comparison of all the sample's mean values for each measurement set against one another in order to compare their differences. It also adds a perfect Lambertian reflector as a reference between figures. Each successive figure increases the incident angle 15 degrees, beginning at an incidence angle of zero and ending at 75 degrees.

Figure 92 (a) shows the comparison of all the samples at $\theta_i = 0°$. If they are visually rated in order from least diffuse to most diffuse, the order is RPC®metalized diffuser, Krylon Silver paint, Infragold®, rough gold, Infragold-LF®, Spectralon®, and finally the Nextel black paint, which is actually 'over' diffuse. It is apparent that the RPC®metalized diffuser, Krylon silver paint, and the Infragold®are all very similar samples with similar BRDF profiles. The rough gold has a similar shape, but the difference is more noticeable. The Infragold-LF®and Spectralon®have almost identical responses, except for the noise on the Infragold-LF®.

In Figure 92 (b), the incidence angle is increased to 15 degrees. The RPC®metalized diffuser, Krylon silver paint, Infragold®, and rough gold all respond accordingly, but it appears that the Spectralon®and Infragold-LF®stay almost completely diffuse. The Nextel black sample also begins to develop a specular lobe. Figure 93 (a) shows the same basic trend at $\theta_i = 30°$, with no immediately obvious changes.

Figure 93 (b) at $\theta_i = 45°$ begins to show the first clear break from this overall trend. First, the rough gold is becoming relatively more specular compared to the RPC®metalized diffuser, Krylon silver paint, and Infragold®when this figure is com-

pared to $\theta_i = 0°$. In addition to this relative comparison, the Infragold®has become almost as specular as the RPC®metalized diffuser. The other significant difference is that the Infragold-LF®is starting to clearly break from the Spectralon®and become relatively less diffuse. The Nextel black paint has also developed a significant signature, not in the expected specular direction, but near grazing reflected angles. This is most likely caused by whatever phenomena caused this sample's bowl shaped BRDF profile at $\theta_i = 0°$.

Figure 94 (a) at $\theta_i = 60°$ shows the same trends continuing, and the Nextel black paint's signature in the grazing forward scatter direction has almost reached the level of the other samples' values. The one big difference here is that the RPC®metalized sample has developed a significant narrow specular lobe located at the mirror reflection angle. Figure 94 (b) at $\theta_i = 75°$ shows most of the same trends continuing, but the difference is that the Infragold-LF®develops a significant backscatter and Spectralon®shows more of a forward scatter. This is most likely due to the differing nature of their scattering mechanisms. The Spectralon®is just starting to get an actual surface scatter, whereas, the very rough surface of the Infragold®is showing the effects of significant shadowing and masking. The Nextel black paint's forward scatter near grazing angles is now more prevalent than all, but the more specular samples. Finally, the RPC®metalized diffuser has grown its narrow specular peak.

6.4.2 Reflectance.

The reflectance is the first quantitative parameter that is compared in the analysis section. Nevertheless, judgment must still be used in the comparison of these numbers, because a data fit is involved in the estimation of the missing data. In addition to this, misalignment will also cause errors in the calculation of the DHR from the BRDF values. Regrettably, this has not been quantified. Figure 95 shows a linear plot of
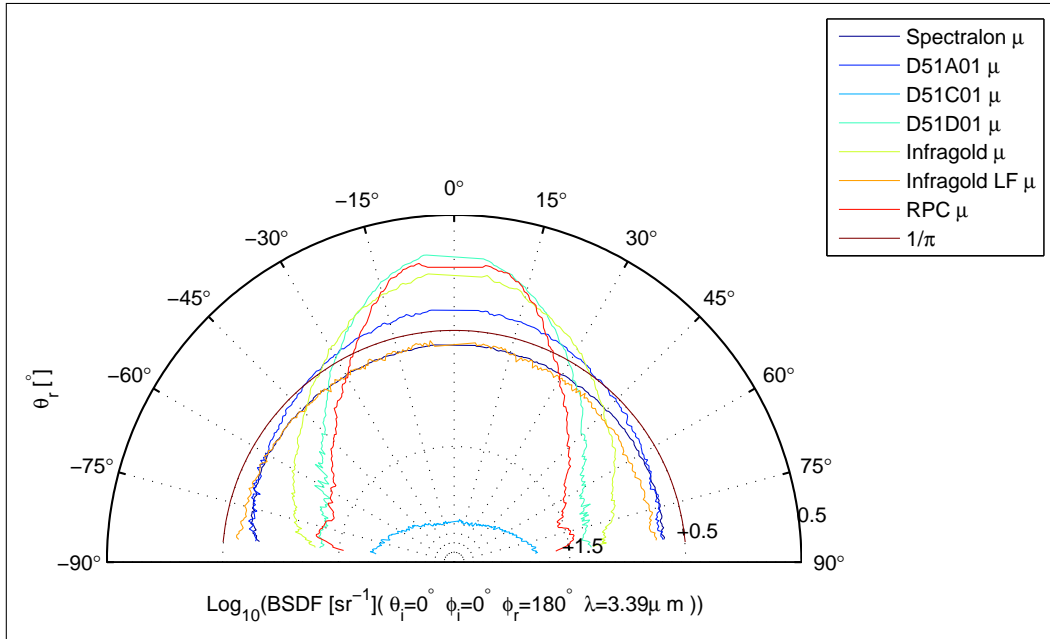
(a)
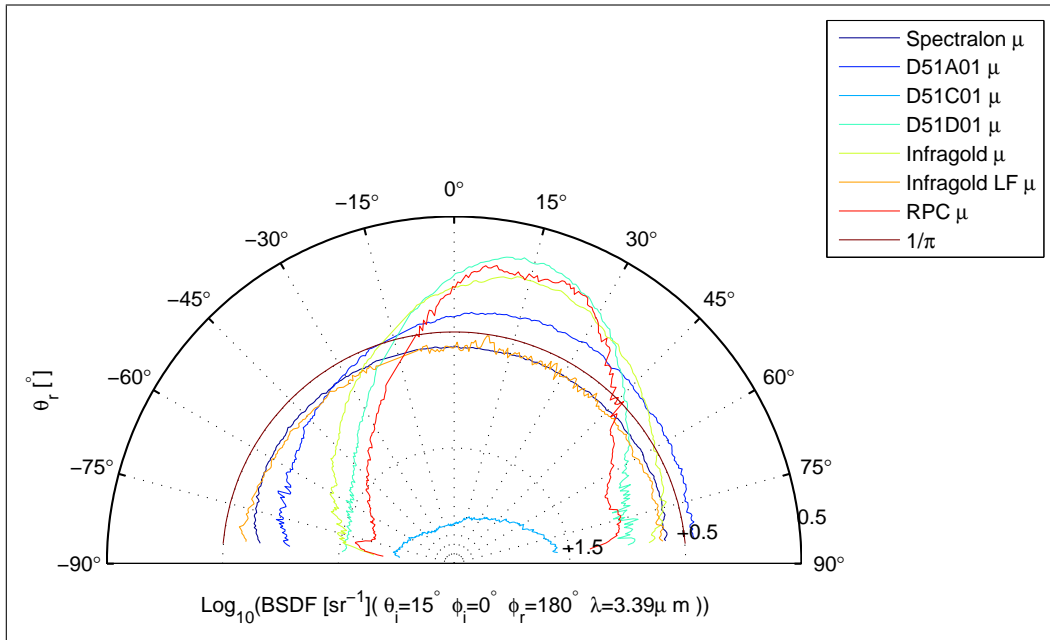
(b)

Figure 92. The comparison of the BRDFs measured by the AFIT CASI$^{\textregistered}$ at (a) $\theta_i = 0^\circ$ and $\lambda = 3.39\mu$m. (b) $\theta_i = 15^\circ$ and $\lambda = 3.39\mu$m.

132
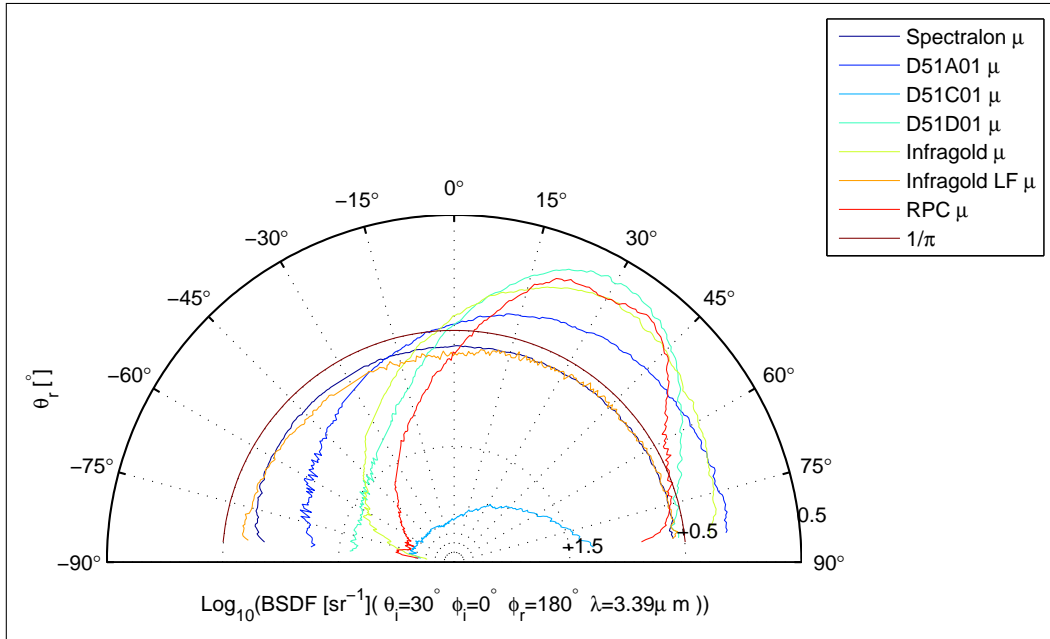
(a)
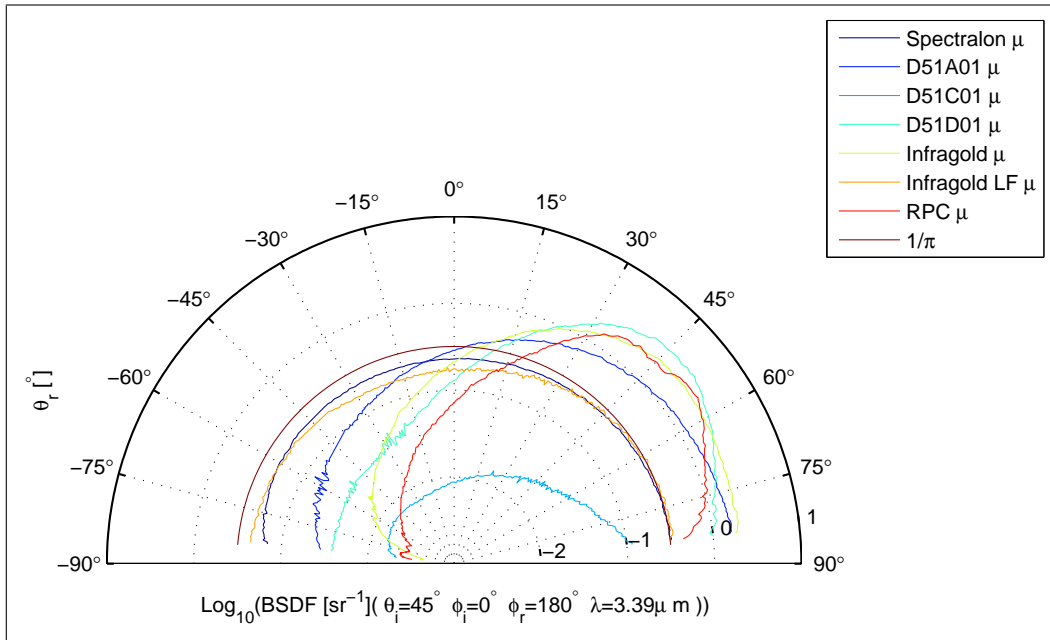
(b)

Figure 93. The comparison of the BRDFs measured by the AFIT CASI® at (a) $\theta_i = 30°$ and $\lambda = 3.39\mu m$. (b) $\theta_i = 45°$ and $\lambda = 3.39\mu m$.

133
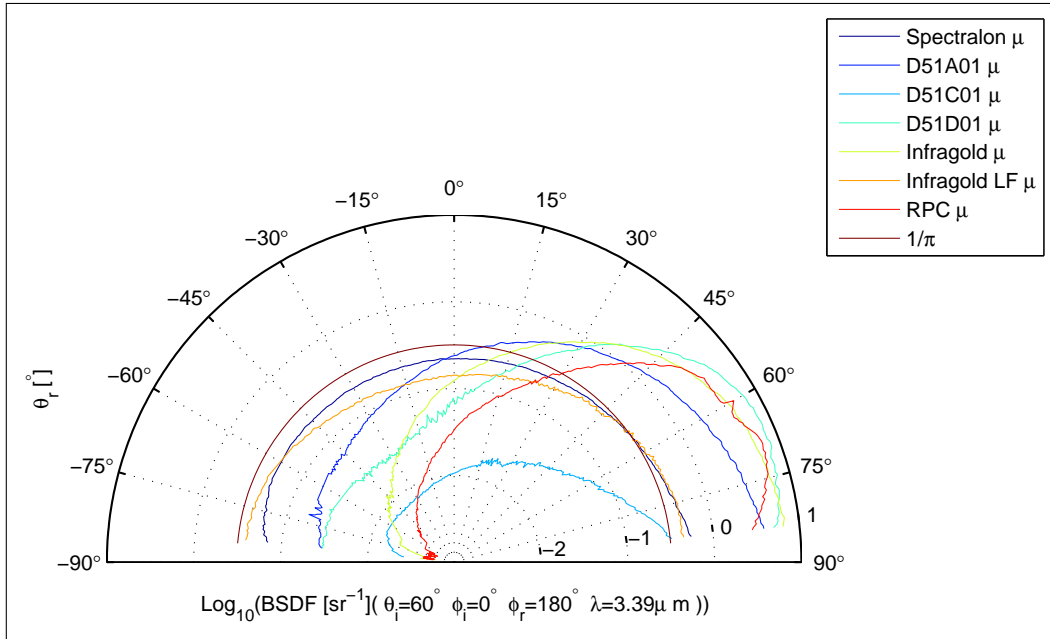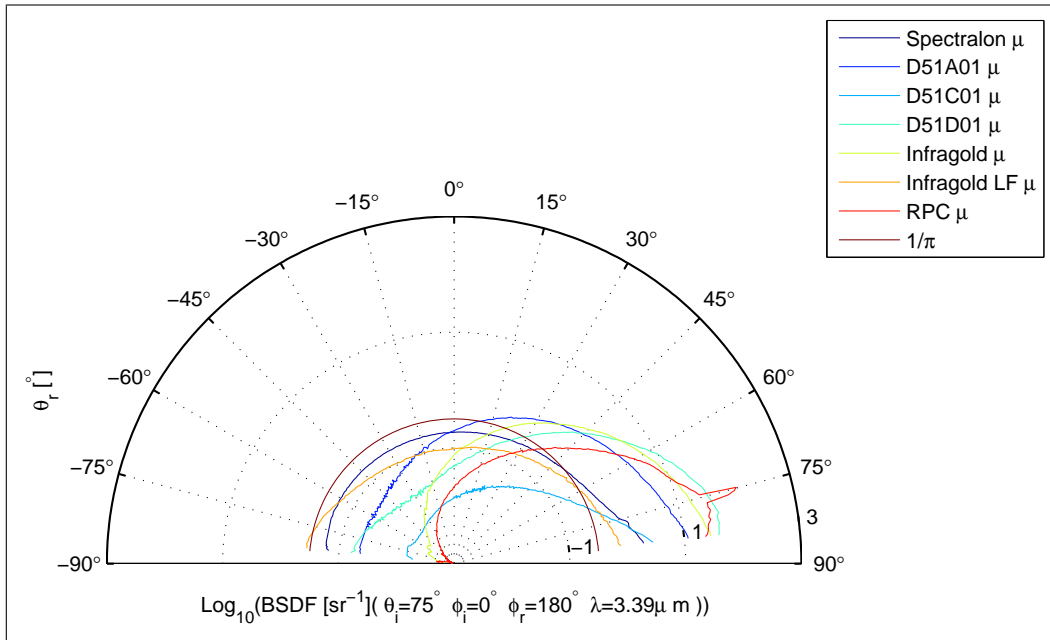
Figure 94. The comparison of the BRDFs measured by the AFIT CASI® at (a) $\theta_i = 60°$ and $\lambda = 3.39\mu$m. (b) $\theta_i = 75°$ and $\lambda = 3.39\mu$m.

134

all the samples at $\theta_i = 0°$ with the calculated DHR values shown in the legend. The linear scale gives one a better idea of the actual BRDF values and how different the BRDF profiles actually are. One must also recall that the stated goal in the OMF Final Report was to be able measure BRDF and calculate DHR values within 10%. So although the computed DHR may not be perfect, it should be relatively close enough to the actual measured values that it can be considered in this comparative study.
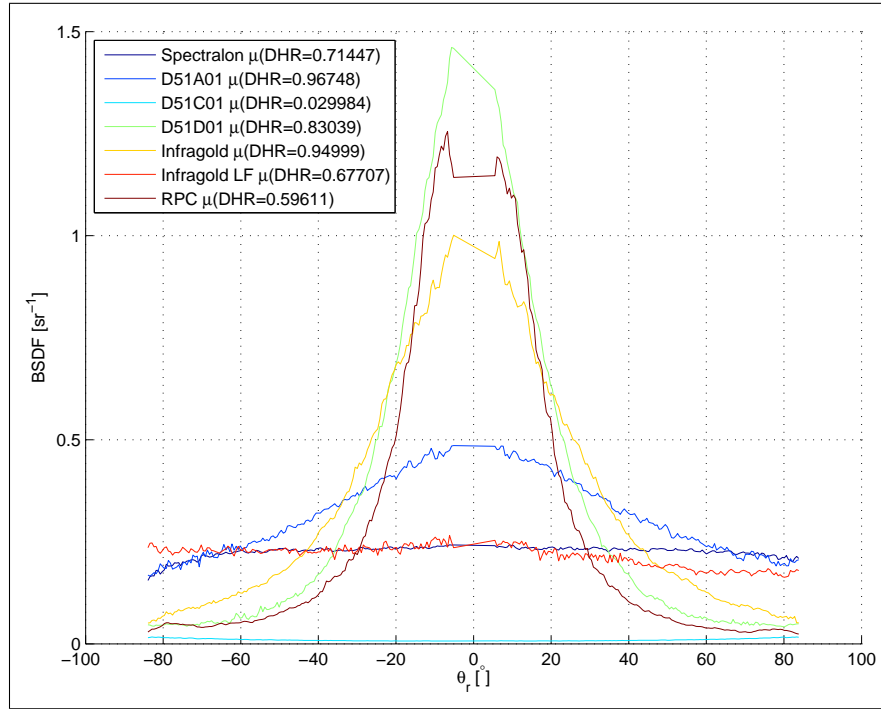
Figure 95. A calibrated comparison of DHR calculated from BRDF values at $\theta_i = 0°$ and $\lambda = 3.39\mu m$.

Table 12 presents all the calculated DHR values listed in descending order. The actual measurement values are also listed to show which samples had measured DHR values. One must evaluate the calculated DHRs from the samples that have not been calibrated using a DHR measurement carefully, because these values have a definitely un-measureable uncertainty associated with them. The rough gold and Infragold®perform well in this comparison of DHRs. This was expected because of

Table 12. Calculated DHRs of All Studied Samples.

Sample	Calculated DHR	Measured DHR
D51A01	0.9675	0.9675
Infragold®	0.9500	0.9500
D51D01	0.8304	0.8300
Spectralon®	0.7060	N/A
Infragold-LF®Prototype	0.6690	N/A
RPC®Metalized Diffuser	0.5890	N/A
D51C01	0.0300	0.0300

their gold surfaces. The most surprising results here are for the Spectralon®, the Infragold-LF®prototype, and the RPC®metalized diffuser samples, which have DHRs of 0.71, 0.67, and 0.59, respectively. The Spectralon®value is interesting because it is much higher than what one would expect given that most of the published spectral DHR information for Spectralon®does not extend beyond $2.5\mu m$. It has not been used because the reflectance is wavelength dependent in the IR, and it has not been used as a reflectance standard for this reason. This reflectance and the BRDF profile suggests that Spectralon®is still a good performer in this study even at this wavelength.

The Infragold-LF®and RPC®metalized diffuser are both surprising because the gold coating should produce higher DHRs. In addition, the Infragold-LF®prototype's sample average is very noisy which made the fit poor. The Infragold-LF®sample should have a DHR closer to 0.95. It is also possible that either it is misaligned, because it appears that the BRDF profile is not symmetric, or that the part of the surface measured had a bias towards that direction.

6.4.3 Diffuseness.

To numerically quantify the 'diffuseness' of a sample the measurements are fit to a physically based BRDF model with a diffuse reflectance term and a specular reflectance term. One problem with this method is that the specular reflectance

terms are model dependent. This means only values from the same model can be compared. A second problem is that if only the diffuse term is used to comparatively rank the data; one would be comparing *absolute diffuse reflectance* and not the *relative diffuseness*. Thus, a ratio between the diffuse reflectance and total reflectance is necessary. This definition of this ratio is

$$Diffuseness \ Ratio = \frac{\rho_d}{\rho_d + \rho_s}. \tag{49}$$

Thus, this ratio provides how 'diffuse' the data is relative to other data fits of the same model to each sample's measurements. A value of ≈ 1 is the most diffuse the ratio can be. In order to use this ratio, an assumption must be made that the fit is valid, and not every measured BRDF will always fit well to a single function. Table 13 presents the results of the fitting routines when applied to the measurements.

Table 13. Fitting Results for All Samples.

Sample	Ward Model				Cook-Torrance Model				
	ρ_d	ρ_s	β	σ_{MSE}	ρ_d	ρ_s	m	F_o	σ_{MSE}
Spectralon®	0.63	0.33	0.17	0.09	0.66	0.03	0.29	0.29	0.02
D51A01	0.16	3.99	0.25	0.61	0.28	0.13	1.40	0.36	0.10
D51C01	-0.02	0.29	0.13	0.14	0.04	0.05	0.02	0.26	0.01
D51D01	-0.84	10.69	0.12	2.48	0.30	0.09	1.45	0.14	0.74
Infragold®	-0.37	7.65	0.17	1.46	0.18	0.15	1.23	0.23	0.22
Infragold-LF®	0.58	0.24	0.22	0.05	0.59	0.00	5.50	0.32	0.04
RPC®Diffuser	-0.08	6.78	0.07	3.53	1.37	0.07	0.14	0.05	2.67
Spectralon®$(633\eta m)$	1.24	0.25	0.18	0.06	1.27	0.01	0.40	0.25	0.02

The two BRDF models used for fitting were the Ward and Cook-Torrance models, which were described in Sections 2.2.1.3 and 2.2.2.1, respectively. The fitting method is a non-linear search for the least mean squared error in which all terms were allowed to float. Table 13 shows that for most of IR BRDF measurements, the Ward model

did a poor job of representing the data. The lower the mean squared error, σ_{MSE}, the better the fit is to the data. Another sign that the Ward model did a poor job of representing the data is that often the diffuse reflectance term, ρ_d, is negative. This means that the model was too specular for the data, and the fitting routine is compensating for the error due to the specular term. The Cook-Torrance model does a much better job of fitting to the data with the exception of the RPC®Metalized diffuser, and it also does not produce any negative values for the diffuse reflectance terms. The point to be illustrated here is that when evaluating the diffuseness ratios, the mean squared error must also be considered.

Table 14. Diffuseness Ratios.

	Ward Model		Cook-Torrance Model	
Sample	$\rho_d/(\rho_d + \rho_s)$	σ	$\rho_d/(\rho_d + \rho_s)$	σ
Infragold-LF®Prototype	0.71	0.05	1	0.04
Spectralon®$(\lambda = 633\eta m)$	0.83	0.06	0.99	0.02
Spectralon®	0.66	0.09	0.96	0.02
RPC®Metalized Diffuser	0.01	3.49	0.95	2.64
D51D01	0.07	2.48	0.78	0.74
D51A01	0.04	0.61	0.69	0.10
Infragold®	0.05	1.29	0.55	0.20
D51C01	0.06	0.14	0.42	0.01

Table 14, shows the diffuseness ratios ordered from the most diffuse at the top to the least diffuse at the bottom using the Cook-Torrance model's fit parameters. The Cook-Torrance model is used for this ordering because the fits are generally much better when compared to the Ward fits. These results roughly agree with the previous qualitative assessment of the BRDF profiles in Section 6.4.1. The Infragold-LF®diffuseness ratio is not exactly 1, but rounds to it. The diffuseness ratio for RPC®metalized diffuser is questionable because of its relatively high MSE value, but the other results seem reasonable. These results will be used in a decision matrix to

138

determine which sample is the most suitable for use as a standard in Section 6.4.6.

6.4.4 Repeatability as Percent Difference from the Mean.

This section addresses the importance of repeatability across the sample's face. If a standard cannot be measured more than once without an expectation of getting a reasonably close value each time, it is not a very good standard for measurements. In addition, a wide variance would also require more measurements across the sample's face. Figure 96 shows the average PDM value from $-85° \leq \theta_r \leq 85°$ against θ_i for each sample's set of measurements. Essentially, this allows a much more compact representation of the entire data set's PDM for each sample, and shows its dependence on θ_i. This figure also shows the measurements of Spectralon®at $\lambda = 633\eta m$, as the standard against which to compare. This figure contrasts with the previous PDM plots that show the dependence on θ_r for each individual measurement, which was beneficial when characterizing the phenomena causing the PDM across a sample's surface.

Percent difference is not a bad method to use because it also factors in the magnitude of the sample, whereas the standard deviation alone does not. The limitation with using the PDM is that it is an absolute error, not a squared error, so the distribution of the error is not considered. This must be kept in mind when interpreting the results.

Figure 96 shows that the repeatability of Spectralon®in the visible spectrum is excellent when compared with the IR measurements. It also shows that the samples that have a bulk scatter component perform much better comparatively, and that all the surface scattering samples are grouped much higher on the plot. It is hard to precisely prioritize how all the samples compare to each other given only this plot. Thus, the average PDMs of the entire data set for all measured values of θ_i and θ_r are
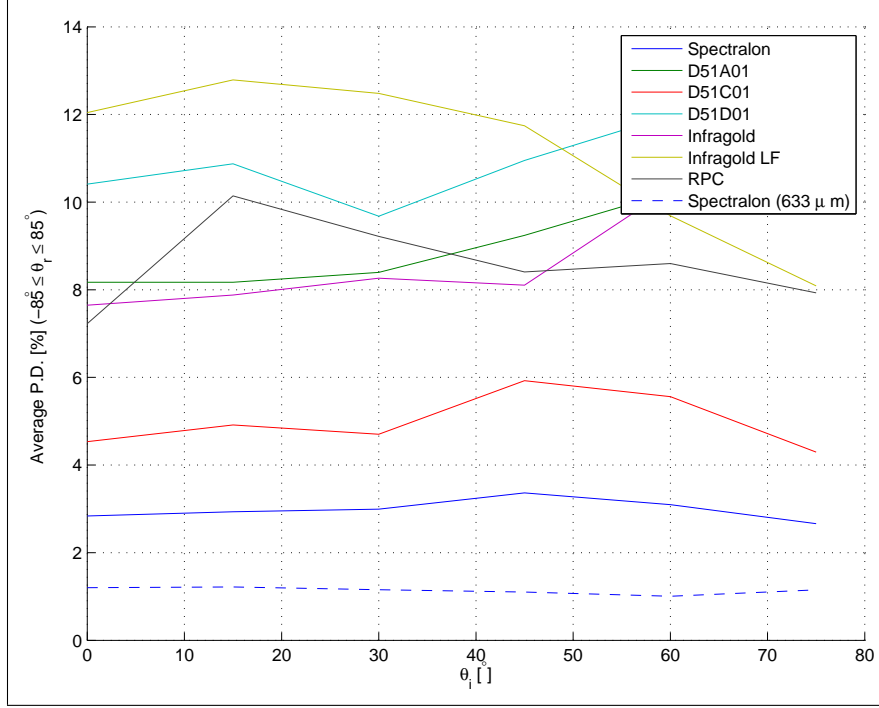
**Figure 96. Average percent difference from the mean of all mea-
surements calculated** $-85° \leq \theta_r \leq 85°$ **versus** θ_i**.**

averaged in Table 15 to provide to a single PDM value to prioritize how the samples
compare for the entire measurement set.

Table 15 is ordered such that the best performers are at the top of the table.
Although the bulk diffusers do perform quite well when compared against the surface
scattering samples, the RPC®metalized diffuser does show some promise of being able
to reduce the variability and increase the repeatability of surface scattering samples.

6.4.5 Repeatability as Standard Deviation.

The last parameter to be considered in this study is the average standard deviation
of each sample. This is important to add to the study because it considers the
distribution of the measurements. Nevertheless, there is a problem if the standard
deviation is presented as it is typically used. The problem is that when measurements
that have large absolute differences are compared, it does not consider the magnitude

140

Table 15. Average Percent Difference from the Mean of All Studied Samples.

Sample $(-85° \leq \theta_r \leq 85°)$	$\theta_i = 0°$	$\theta_i = 15°$	$\theta_i = 30°$	$\theta_i = 45°$
Spectralon®$(\lambda = 633\eta m)$	1.2	1.22	1.15	1.1
Spectralon®	2.84	2.93	2.99	3.36
D51C01	4.53	4.92	4.70	5.92
RPC®Metalized Diffuser	7.23	10.14	9.22	8.41
Infragold®	7.65	7.88	8.26	8.11
D51A01	8.17	8.17	8.40	9.24
D51D01	10.41	10.88	9.68	10.95
Infragold-LF®Prototype	12.04	12.79	12.48	11.74

Sample $(-85° \leq \theta_r \leq 85°)$	$\theta_i = 60°$	$\theta_i = 75°$	$\mu(\theta_i = 0°, 15°, 30°, 45°, 60°, 75°)$
Spectralon®$(\lambda = 633\eta m)$	1.01	1.15	1.14
Spectralon®	3.10	2.66	2.97
D51C01	5.56	4.30	4.96
RPC®Metalized Diffuser	8.60	7.93	8.54
Infragold®	10.31	10.10	8.65
D51A01	10.22	13.11	9.41
D51D01	11.98	11.84	10.93
Infragold-LF®Prototype	9.69	8.09	11.00

when the standard deviation is calculated. Figure 97 illustrates this effect when the average standard deviation for all measurement points within $-85° \leq \theta_r \leq 85°$ versus θ_i is plotted. The Nextel black paint sample has a very small standard deviation because its mean is so small. Conversely, when the rough gold samples become specular at higher incident angles, their standard deviations increase rapidly because their means become very large relatively. The use of these results would provide an inaccurate assessment of their repeatability.

A solution to this problem is to use the Relative Standard Deviation (RSD). The RSD is widely used in analytical chemistry to express precision and repeatability when performing an assay[20]. The RSD allows the comparison of the standard deviation, as a measure of repeatability, when the absolute difference between measurements is
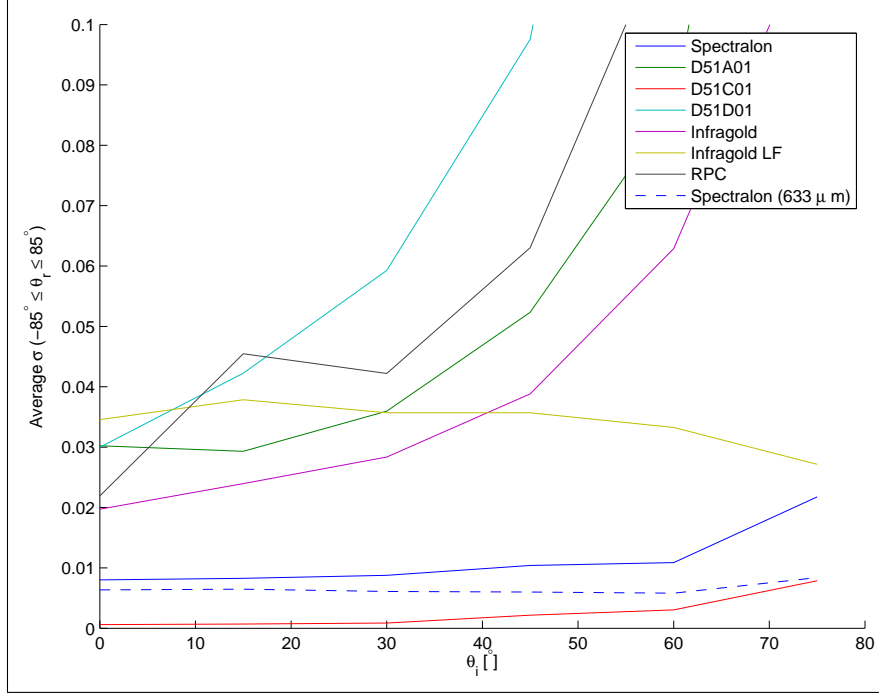
Figure 97. Average standard deviation of all measurements calculated $-85° \leq \theta_r \leq 85°$ **versus** θ_i.

very large. The definition of the RSD, as it is used in this study, is

$$RSD(\theta_i, \theta_r) = \frac{\sigma(\theta_i, \theta_r)}{\mu(\theta_i, \theta_r)}. \tag{50}$$

Figure 98 presents the average RSD from $-85° \leq \theta_r \leq 85°$ plotted as a function of θ_i. This now provides a more accurate assessment of the repeatability for each of the samples. The Nextel black paint sample's RSD has now become much larger relative to the other measured samples. In addition, the rough gold samples do not show the drastic increase with θ_i.

Table 16 shows the average RSD for each sample numerically, and it presents an average for the entire data set in order to make a single numerical comparison between all the samples. The table is ordered with the best performing samples at the top. The results of this agree very well with the PDM results. The exception is that the RPC®metalized diffuser and Infragold®have switched places. This means

142
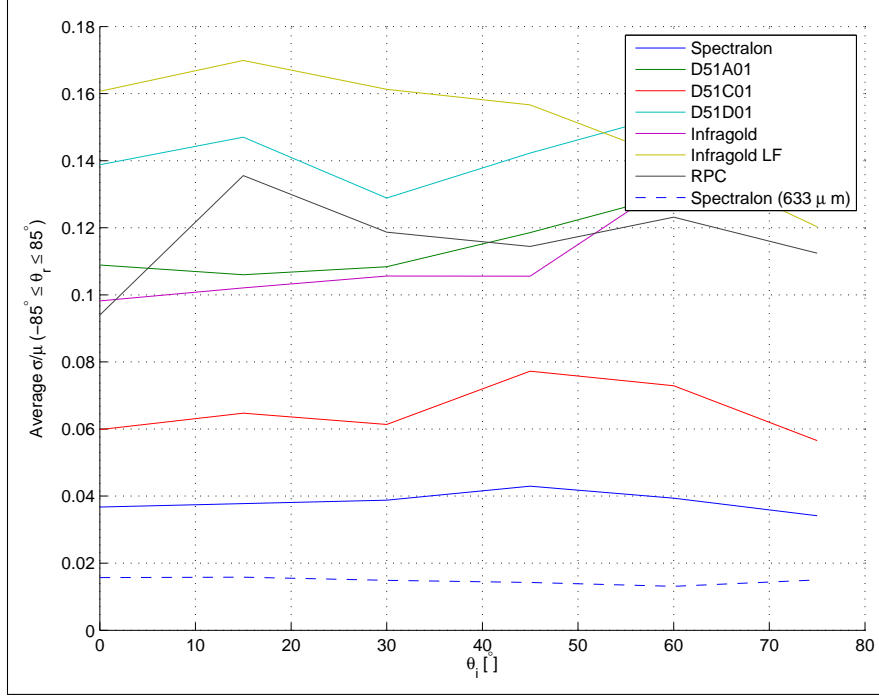
Figure 98. Average scaled standard deviation of all measurements calculated $-85° \leq \theta_r \leq 85°$ **versus** θ_i**.**

that the grouping, or tightness, of the individual measurements is related to the linear PDM error. This need not be the case because the standard deviation method will emphasize outliers more than the PDM, but it is here.

6.4.6   Decision Matrix.

The last step in the analysis is to create a decision matrix to rate all the samples based upon their parameters, and then rank order them based upon their suitability as a diffuse MWIR BRDF standard. This matrix is shown in Table 17. To create this matrix, each parameter was ranked ordered 1 thru 7 according to Section 6.4.1 and Tables 12, 14, 15, and 16. These rankings were then multiplied by a weighting, and these products were summed. The lower the score the better the sample performed. Spectralon®at $\lambda = 633\eta m$ was not included because it was the best performer for every parameter considered. This would have simply give the visible measurements

Table 16. Average Relative Standard Deviation of All Studied Samples.

Sample ($-85° \leq \theta_r \leq 85°$)	$\theta_i = 0°$	$\theta_i = 15°$	$\theta_i = 30°$	$\theta_i = 45°$
Spectralon®($\lambda = 633\eta m$)	0.016	0.016	0.015	0.014
Spectralon®	0.037	0.038	0.039	0.043
D51C01	0.060	0.065	0.061	0.077
Infragold®	0.098	0.102	0.106	0.106
RPC®Metalized Diffuser	0.094	0.136	0.119	0.114
D51A01	0.109	0.106	0.108	0.119
D51D01	0.139	0.147	0.129	0.142
Infragold-LF®Prototype	0.161	0.170	0.161	0.157
Sample ($-85° \leq \theta_r \leq 85°$)	**$\theta_i = 60°$**	**$\theta_i = 75°$**	**$\mu(\theta_i = 0°, 15°, 30°, 45°, 60°, 75°)$**	
Spectralon®($\lambda = 633\eta m$)	0.013	0.015	0.015	
Spectralon®	0.039	0.034	0.038	
D51C01	0.073	0.057	0.065	
Infragold®	0.134	0.130	0.112	
RPC®Metalized Diffuser	0.123	0.112	0.116	
D51A01	0.130	0.163	0.121	
D51D01	0.154	0.148	0.143	
Infragold-LF®Prototype	0.140	0.120	0.151	

of Spectralon®a ranking of 1, and raise all the other measurement's final rankings by one.

The somewhat arbitrary part of this whole process was the justification for the weighting. The diffuseness is important to a BRDF standard because it is more forgiving to alignment errors, and it helps to give relatively constant values for most combinations of incident and reflected angles. This diffuseness requirement recognizes the spatial dependence that separates the BRDF from reflectance measurements. This is why the characterization and diffuseness analysises receive 50% of the total weighting.

The repeatability is also a large issue, because a good standard must provide consistent measurements. This then receives the majority of the remaining weighting,

Table 17. A Decision Matrix to Prioritize Samples.

Weighting	Char. 0.2	Reflec. 0.2	Diff. 0.3	PD 0.15	SD 0.15	Rating
Spectralon®	1	4	2	1	1	1.9
D51A01	3	1	5	5	5	3.8
Infragold-LF®Prototype	2	5	1	7	7	3.8
Infragold®	4	2	6	4	3	4.05
RPC®Metalized Diffuser	6	6	3	3	4	4.35
D51D01	5	3	4	6	6	4.6
D51C01	7	7	7	2	2	5.5

30%. The last consideration is the reflectance. Higher values are more desirable because the are more easily measured, but it is not completely independent of the other requirements. It is also important because the method of using DHR to calibrate the BRDF is more effective with higher values. Nevertheless, it is not necessary for a BRDF standard to have high reflectance values. Thus, it receives the remaining smaller portion of the remaining weighting available, 20%.

The fact that the ranking is somewhat arbitrary would be more of an issue if the ranking was closer, but Spectralon®is the clear winner in this process when only MWIR BRDF measurements are considered. The key here is that the characteristics that make a sample a good spectral reflectance standard do not necessarily make it a good BRDF standard, at the same time. This is because these two measurements are very different. Thus, the gold reflectance standards may have good spectral reflectance characteristics, but their surfaces create much of variance in the BRDF measurements. This is the primary reason Spectralon®performs better than the rough gold standards when considered as an MWIR BRDF standard.

The second related lesson to be illustrated here is the assumption that reflectance standards should be used as BRDF standards, because DHR measurements are used for BRDF calibration, is not valid. It has been shown here that this assumption

should not be made. The drawbacks Spectralon®has as a MWIR BRDF standard is that the reflectance is not as high as desired, and it may not provide consistent BRDF measurements if the bulk properties change over time in the IR. The long-term stability of Spectralon®at this wavelength needs to be studied to confirm that it does not change the BRDF.

6.5 Three Dimensional Modeling

As stated in Chapter I, typically, the end result of a BRDF measurement is its application to a model for use in some type of simulation or scene generation. This section ties the results of the model fitting in the diffuseness comparison to three dimensional representations of each sample's BRDF using the model parameters generated from the data fits.

This is beneficial for an intuitive understanding of the characteristics of the material, and allows a quick and concise understanding of the data. Only the Cook-Torrance model is shown here because the data fits were much better for all the materials. When inspecting the results for the RPC®metalized diffuser, the reader must recall that the results for this model's fit were not very good. Nevertheless, it is still presented for comparison, and Spectralon®at $\lambda = 633\mu m$ is also added for comparative purposes. Figures 99 and 100 show the three dimensional representations for each sample at $\theta_i = 15°$. Figures 101 and 102 show the three dimensional representations for each sample at $\theta_i = 60°$. The varying lobe shapes are due to changes in the Fresnel term and the obscuration function.
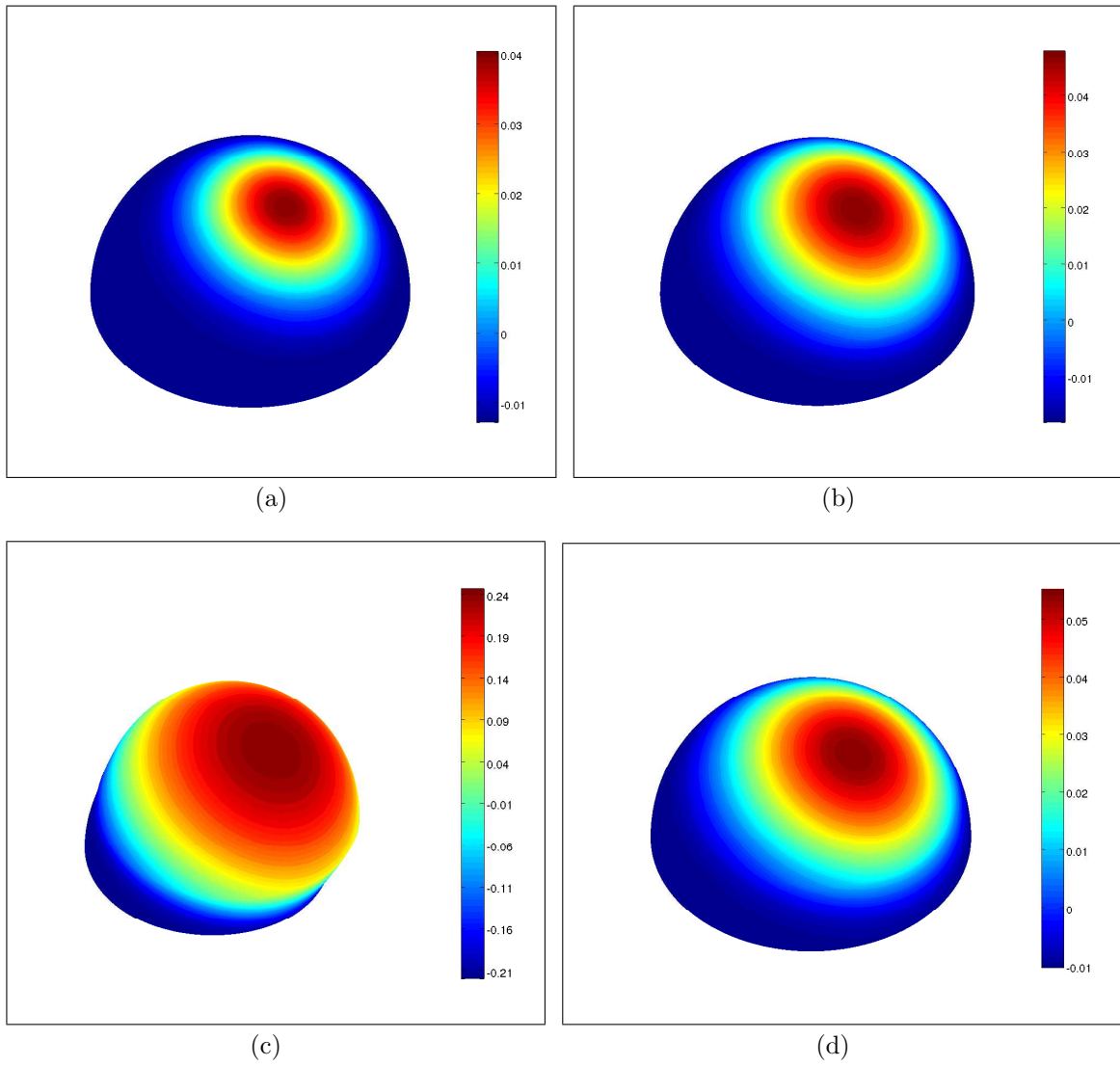
Figure 99. Three dimensional representations of the Cook-Torrance BRDF model fits for $\theta_i = 15°$ for (a) **Spectralon**®at $\lambda = 633\eta m$. (b) **Spectralon**®at $\lambda = 3.39\mu m$. (c) **Rough gold sample, D51A01.** (d) **Infragold-LF**®prototype.
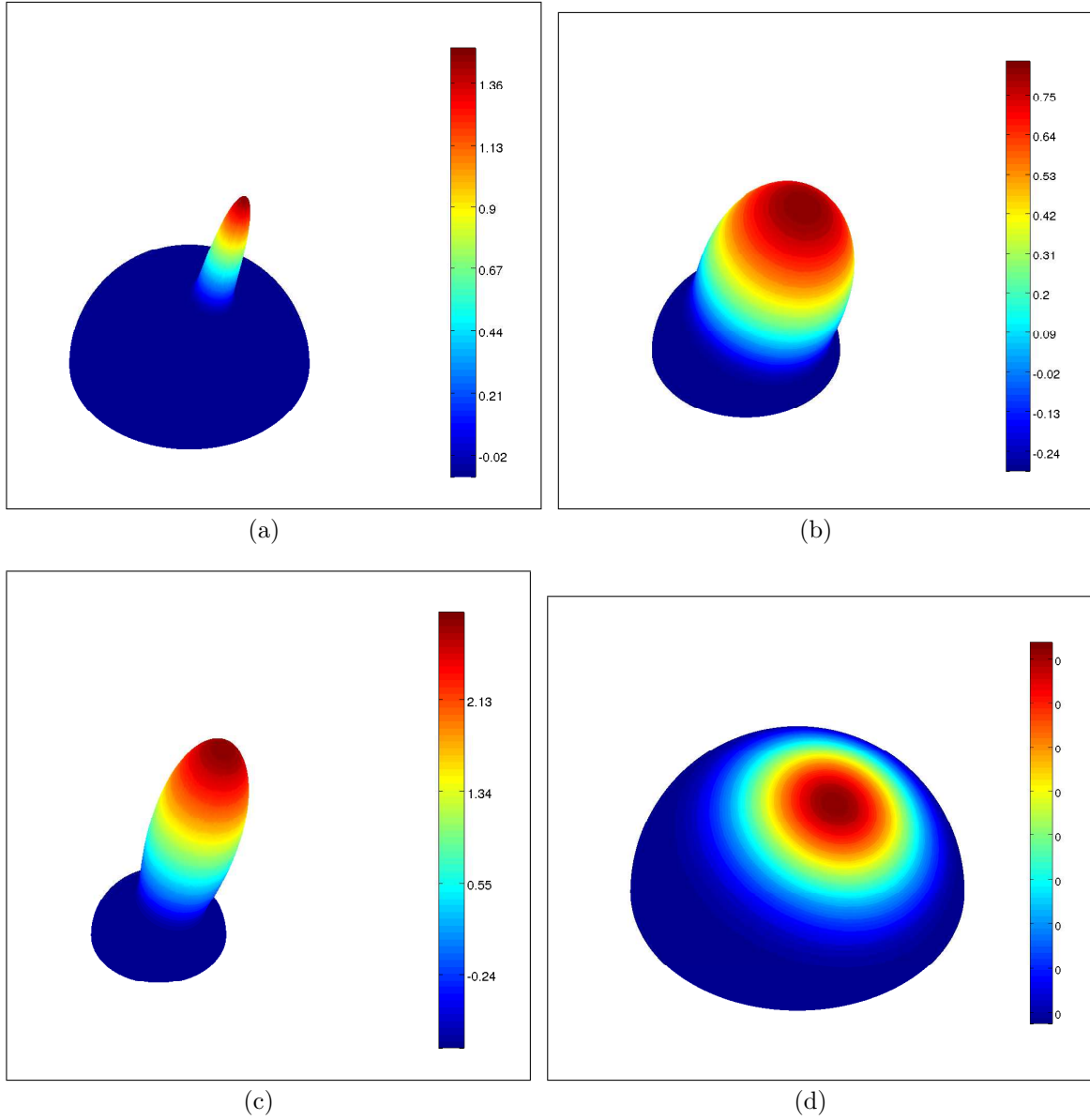
Figure 100. Three dimensional representations of the Cook-Torrance BRDF model fits for $\theta_i = 15°$ for (a) RPC®metalized diffuser. (b) **Infragold**®. (c) rough Krylon silver paint, D51D01. (d) Nextel black paint, D51A01.
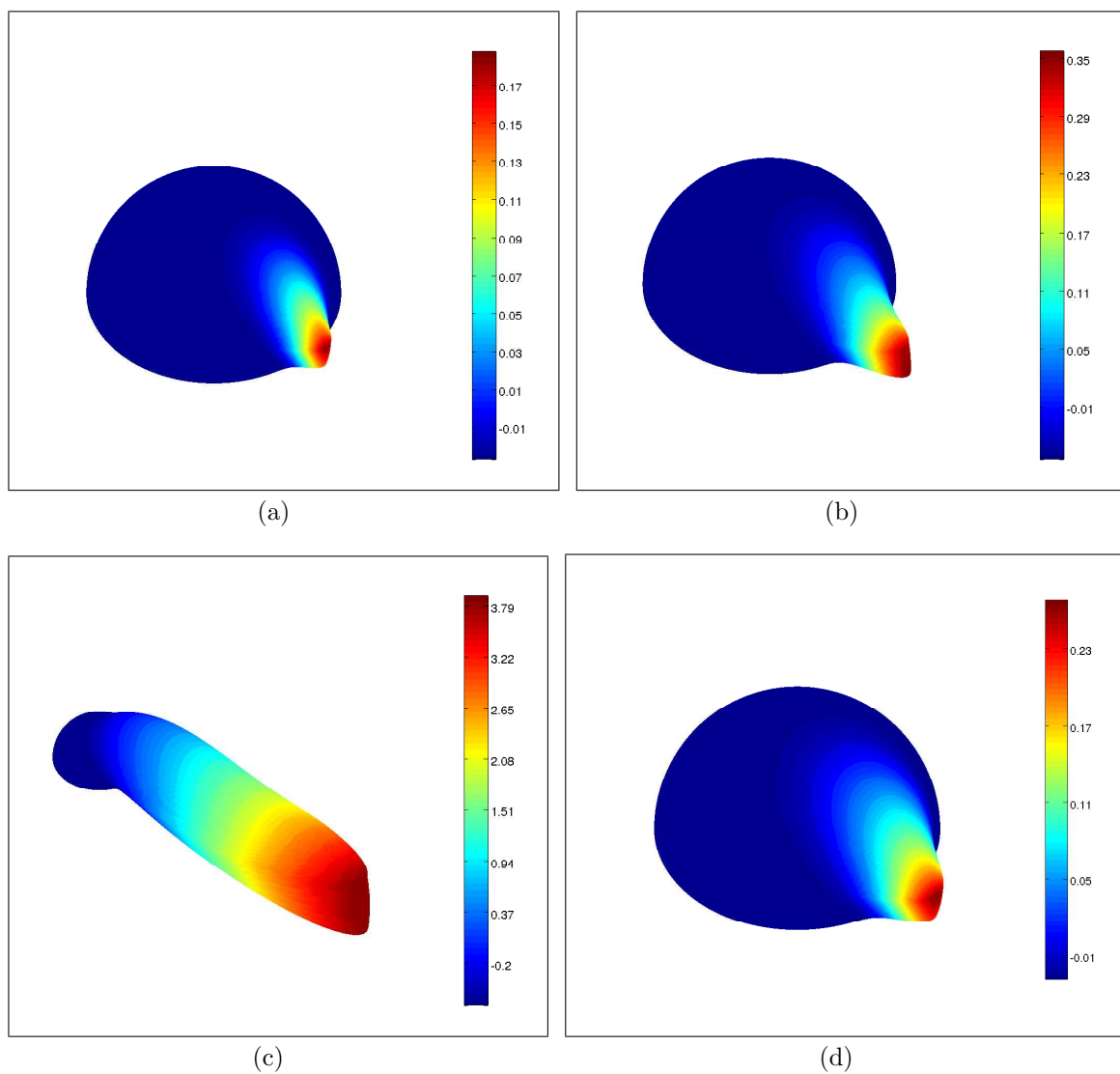
Figure 101. Three dimensional representations of the Cook-Torrance BRDF model fits for $\theta_i = 60°$ for (a) **Spectralon**®at $\lambda = 633\eta m$. (b) **Spectralon**®at $\lambda = 3.39\mu m$. (c) **Rough gold sample, D51A01.** (d) **Infragold-LF**®prototype.
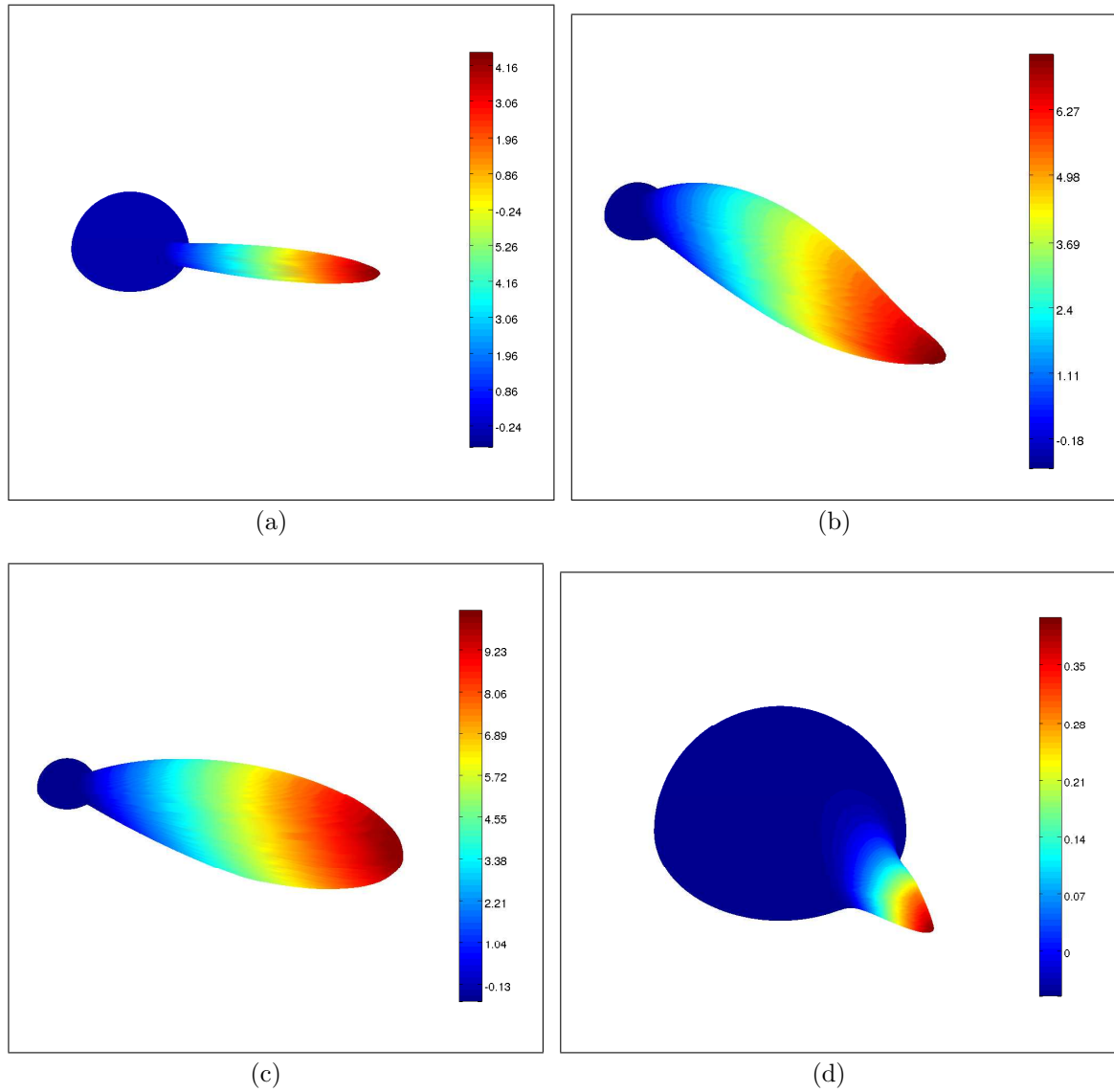
Figure 102. Three dimensional representations of the Cook-Torrance BRDF model fits for $\theta_i = 60°$ for (a) RPC®metalized diffuser. (b) Infragold®. (c) rough Krylon silver paint, D51D01. (d) Nextel black paint, D51A01.

6.6   Chapter Conclusion

This chapter used all of the tools developed previously to measure and quantitatively analyze all of them. Nevertheless, there was some amount judgment to had to be used when all of the measurements were analyzed. First, the comparison of measured DHR and DHR calculated from BRDF data is still an issue that has much higher uncertainty than it should. Second, the fitting process is not a precise measurement of the 'diffuseness', but rather, is one of the ways to quantify it. Also, the possibility of alignment errors creating biases is still a real issue because the sample size of this study was so small. The amount of time required to make IR BRDF measurements forced the smaller sample size so that the study could be completed in the allotted time. Nevertheless, when the samples were analyzed Spectralon®was the clear winner.

VII. Conclusion and Future Research

This is divided into two sections; the first is the conclusion of this document relating each major idea contained in it to the focus of this research, and the second section contains the recommendations for future research related to this study.

7.1 Conclusion

The focus of this research was to compare several different samples with varying surfaces as potential MWIR diffuse BRDF standards. This focus was driven by the ultimate goal of creating a sample and mathematically determining its BRDF before measurement, then verifying the result. The BRDF research conducted ultimately found this to be a futile goal because of the current limitations in computational techniques and mathematics for most types of surfaces, except for surfaces that are nearly optically smooth.

If an *a priori* BRDF was not possible, the next step towards a well defined, scientific BRDF measurement was to be able to verify BRDF measurements based upon DHR and BRDF standards. This proved to be a much more challenging goal than anticipated, which demonstrated the need for a MWIR BRDF standard that is more than just a reflectance standard. This need motivated the focus of this research.

7.1.1 Conclusions from the BRDF Research.

The first objective of this study was to understand the BRDF and find a more physical model that is predictive. Appendix A laid down the radiometry necessary to understand the BRDF, and Chapter II formed the mathematical development of the BRDF. The conducted research motivated a classification of BRDFs based upon the how the model is constructed. The first classification of BRDF models, designated

empirical BRDFs, used brute force data fits. The second classification of models were the phenomenological models which use mathematical formulations based upon physical forms to fit to measured data. The last classification was the deterministic BRDF models, these models are based upon electromagnetics and boundary conditions presented in Appendix B.

Unfortunately, the constraints on where these deterministic solutions are valid are so restrictive, that they only apply to very specular samples. Thus, there is a large void that has yet to be filled between the application of phenomenological models and the more deterministic models. Nevertheless, these models proved useful in the understanding of scattering phenomena and in the analysis of the samples to provide a quantification of their diffuseness.

7.1.2 Conclusions from the BRDF Measurement Calibration and Validation.

Chapters III, IV, and V addressed the general idea of producing repeatable, scientifically accurate, BRDF measurements. Chapter III outlined the transformation of the mathematically based BRDF into a form that can be physically represented in an actual measurement and the process of doing this. This is important to understand what the measurements in this research actually are; with this knowledge demonstrated, the equipment used to take these measurements is explained.

Chapter IV established the methods of BRDF calibration using a well defined reflectance standard called Spectralon®. The research into Spectralon® showed that although the research is thorough, BRDF information presented as a standard is lacking. The techniques used to calibrate BRDF using measured DHR are thoroughly explained in this chapter, and Spectralon® was measured and calibrated according to it's measured DHR. These results were then compared against published BRDF

measurements and the results were very encouraging.

Chapter V used the calibration techniques developed in Chapter IV to perform a calibration of the AFIT CASI® in the MWIR. The samples used had well-verified and published measured DHRs. BRDF measurements for these samples were also available, and they come from a reputable source, AFRL's OMF. The chapter then verified the calibrated AFIT BRDF measurements using the MWIR BRDF measurements made by AFRL's OMF. These results were mixed. Both the AFIT and AFRL measurements did not produce a very consistent corrective factor between the DHR calculated from BRDF and the measured DHRs. Nevertheless, they laid within about 10% of each other which agreed with goals set by the OMF in their final report for their facility. The comparative BRDF measurements allowed the identification of an AFIT alignment error, and subsequently, the corrective factor for this sample was not used in the development of an overall corrective factor for samples in Chapter VI that did not have a measured DHR values available for calibration. Ultimately, this chapter proved the usefulness of an actual BRDF standard, not just a reflectance standard.

> [!] A published set of BRDF standards, with uncertainty data, in the MWIR is necessary in order ensure that BRDF measurements are accurate without any uncertainty.

7.1.3   Results of Comparative MWIR BRDF Standards Study.

The comparative study of the different samples is presented in Chapter VI. The samples included in this study were both experimental, and those currently used as reflectance only standards in the IR. The set of samples included Infragold®, an Infragold-LF®prototype, a sample with electro-plated gold on arc-sprayed aluminum, a sample with Krylon silver paint applied to arc-sprayed aluminum, a sample with

154

Nextel black paint applied directly to a brass substrate, a sample with gold deposited on an RPC®laser beam diffuser, and Spectralon®. They were all measured at $\lambda = 3.39\mu m$.

When the BRDF profiles were qualitatively analyzed and the quantitative parameters of reflectance, diffuseness, repeatability represented as percent difference, and repeatability represented as a relative standard deviation were all considered, the sample discounted as an IR standard, only useful in the visible spectrum, Spectralon®, proved to be the best candidate for a MWIR BRDF standard given the prioritization used in this research.

7.2 Future Research

This experience has proven that the current state of accurate BRDF measurements is not only science, but there is an art to it as well. There are four clear continuations of this research. The first is to quantify the effects of misalignment on calculated DHR and calibration. This has been shown to be a problem in this study. There are really only three methods of alignment: to geometrically measure the sample's position, to align a mirror parallel to the sample's surface and use it to align the specular reflection with the incident beam's path, and to move the sample to very high angles of incidence to create a specular reflection to use for alignment. Each of these methods has problems inherent in the method itself.

A possible solution is to create a jig or mount that would have a mirror for alignment, a reference standard for calibration, and the sample to be measured that are all parallel with each other. The jig would only have to be rastered between the alignment, calibration, and measurement. Thus, the alignment would be preserved, and this effectively solves the problem of calibration and alignment in a single step. A proposal for this mount is shown in Figure 103. It has two open sides to mount
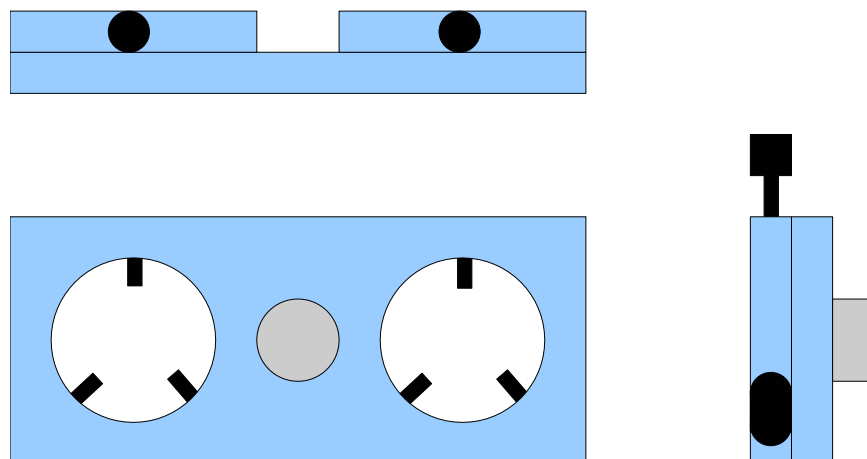
Figure 103. A proposal for a jig that would contain an alignment mirror, a measurement standard, and the sample to be measured.

a circular sample and a standard. The mirror is set in the center. If the jig is set face down on the mirror and both samples are also placed face down and secured, the normal to all three surfaces should be aligned.

The second obvious line of future research is to add other considerations in a similar, but larger, multi-lab study. These other considerations could be the manufacturing, reproducibility, cost, spectral behavior, or other considerations. The third line of related future research would look into Spectralon®as a MWIR BRDF standard. This would require BRDF measurements at multiple wavelengths and a much larger measurement set over time to ensure consistency. Finally, with the knowledge that bulk scattering creates a very diffuse and repeatable BRDF, other materials that have bulk-scattering characteristics could be considered for a diffuse reflectance standards in the IR.

Appendix A. Radiometry Review

This appendix is meant to provide a refresher or primer on radiometry basics, and is necessary to fully understand the BRDF. Radiometry is a quantitative analysis of the flux transfer of light[19, pg. 38]. More colloquially, it is how light is transferred or produced, from a radiant source to an observer.

1.1   The Solid Angle

The BRDF is defined in sr^{-1}, which is a reflectance per steradians, and thus, the solid angle is a key component needed to understand it. To characterize light, three dimensions are required, and this requires the use of a solid angle, which is measured in steradians. This unit is analogous to the two-dimensional, or planar, radian. A planar angle measured in radians is equal to the ratio of arc length on a circle, s, to the radius, r, that traced it,

$$\theta = \frac{s}{r}. \tag{51}$$

From this definition, any planar angle can be measured in radians without knowledge of the arc length or radius because the arc length increases at the same rate as the radius for a given angle.

Extending this definition to three dimensions, a solid angle can be defined in a similar way. Just as the radius traced the arc length in two dimensions, the radius here traces out a spherical surface area in three dimensions. The rigorous definition given by Ferraro[24, pg. 22] is

$$\Omega = \int \int_S \frac{\overrightarrow{r} \cdot \hat{n} dS}{r^3}, \tag{52}$$

where S is the surface area of the projection onto the sphere, dS is the infinitesimal surface area, $\overrightarrow{r}$ is the vector to dS, $\hat{n}$ is the unit vector normal to dS, and r is the

radius.

A simplification of equation (52) is

$$\Omega = \frac{A_{cap}}{r^2},\tag{53}$$

where A_{cap} is the area of a *spherical* cap traced by the radius, r. Using this definition, a sphere with surface area $4\pi r^2$, has 4π steradians of solid angle, Ω [19, pg. 39]. This is a key necessity for radiometric analysis. Another simplification often used with the solid angle is the small angle approximation, this allows the spherical cap area to be approximated by a flat cap, which is useful in real world problems. This geometry is shown in Figure 104; the flat cap approximation holds as long as $r \approx r - h$.
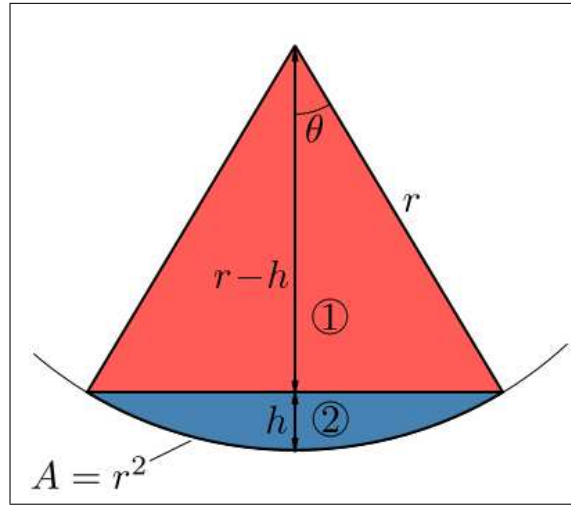
Figure 104. Cross section of a spherical cap and cone inside of a sphere.

The last hip-pocket formula that will later prove useful is the conversion of a planar angle into a solid angle. This is useful because optical detectors always have a finite field of view, FOV. This FOV is typically given in a planar angle that extends from the optic axis to the edge of the field of view, $\theta_{1/2}$. The conversion from Marciniak [42] is simple calculus.

$$\Omega = \int_0^{2\pi} d\phi \int_0^{\theta_{1/2}} sin\theta_{1/2} d\theta_{1/2}$$

$$= 2\pi[-cos\theta_{1/2}]_0^{\theta_{1/2}} \tag{54}$$

$$= 2\pi(1 - cos\theta_{1/2})$$

1.2   Radiometric Quantities

All radiometric quantities first begin with definition of the light ray under consideration. Light is typically quantified with either mks units or in photons in radiometry. The subscript, e, in a radiometric quantity denotes mks, or Joule, units, and a q denotes photon units. Joule quantities will be used for the remainder of the discussion, unless noted, for consistency. This is important because it is not as simple as a dimensional analysis conversion when integrating over a spectral band of light.

The light ray can first be described by the energy it contains, Q_e, and the rate of the energy received, or flux, Φ_e, which is a measurement of the light ray's power. The most easily understood radiometric quantities are those that involve flux density, such as irradiance, E_e, and exitance, M_e, which are fluxes per unit area either incoming or outgoing, respectively. Logically, this is then followed with intensity, I_e, which is flux per solid angle. Intensity is useful for point targets, such as describing how bright a star is.

Lastly, the most complicated, but arguably the most important radiometric quantity is radiance, L_e. This is because all other quantities can be derived from it, and it is the starting point for all radiometric calculations. Radiance as defined by Dereniak [19, pg. 45] is the power, or flux, radiated per unit projected source area per

unit solid angle. The expression for radiance is

$$L_e = \frac{\partial^2 \Phi_e}{\partial A_s cos\theta_s \partial \Omega_d}, \tag{55}$$

where Φ_e is the flux from the source, A_s is the area of the source, Ω_d is the solid angle subtended by the detector, and θ_s is the angle formed by the normal to the source and the optical path. It is a derivative expression because the radiance can, and in reality does, change over the surface of a source and the direction into which light is radiated. The one may find it easier to think of many small points, $\partial \Phi_e / \partial A_s$, each having their own small exitance creating a very small intensity at the detector, $\partial \Phi_e / \partial \Omega_s$, even though this is not quite what it really is. The $cos\theta_s$ term is due to any angular variance of the source. This is needed because of the projection of the surface area. Table 18 summarizes the basic radiometric quantities and typical units used for these quantities.

1.3 Finding Radiometric Quantities

To find any basic radiometric quantity, one must begin with the expression for radiance, rearrange the terms, and integrate to find the quantity needed. This is mostly a question of just having to set up the geometry of the problem within the

Table 18. Basic radiometric quantities.

Symbol	Quantity	Units
Q_e	Energy	Joules
Φ_e	Flux	Watts
I_e	Intensity	Watts sr^{-1}
E_e	Irradiance	Watts cm^{-2}
M_e	Exitance	Watts cm^{-2}
L_e	Radiance	Watts cm^{-2} sr^{-1}

integral. The following quantities are the easiest to obtain because the parts needed are part of the expression for radiance. Recall that intensity, I_e, is relative to the detector solid angle, and exitance, M_e, is relative to the source area.

$$I_e = \frac{\partial \Phi_e}{\partial \Omega_d} = \int_{A_s} L_e \cos\theta_s \, dA_s \tag{56}$$

$$M_e = \frac{\partial \Phi_e}{\partial A_s} = \int_{\Omega_d} L_e \cos\theta_s \, d\Omega_d \tag{57}$$

Next, the expression for the irradiance, E_e, is found. This is slightly more involved because it is relative to the detector area. To find this quantity, we will have to 'disassemble' the solid angle of the detector,

$$d\Omega_d = \frac{dA_d}{R^2} \cos\theta_d, \tag{58}$$

which is then put back into our expression for radiance,

$$L_e = \frac{\partial^2 \Phi_e R^2}{\partial A_s \cos\theta_s \, \partial A_d \cos\theta_d}. \tag{59}$$

Next, one must recombine the range, R, with dA_s to form, $d\Omega_s$, and the result is

$$L_e = \frac{\partial^2 \Phi_e}{\partial A_d \cos\theta_d \partial \Omega_s}. \tag{60}$$

Finally, after rearranging and integrating, the expression for irradiance is

$$E_e = \frac{\partial \Phi_e}{\partial A_d} = \int_{\Omega_s} L_e \cos\theta_s d\Omega_s. \tag{61}$$

The last key part of determining radiometric quantities is knowing when and when

161

not to make approximations to turn the resulting integrals into simple products. The first key assumption is that the source is Lambertian. This means that the source radiance does not vary with position or viewing angle. This is a key assumption that allows the radiance, L_e, to be taken out of the integrand. This assumption is normally valid near normal incidence. The next key assumption is the small angle approximation, or $R^2 >> A_d$ or A_s. Stated more simply, this statement implies that across the surface of the source or detector, the view angle, θ, hardly changes. So little in fact, that it can be considered uniform across the limits of integral. Depending on the radiometric quantity of interest, the entire integral reduces to a product under the correct geometry and situation.

1.4 Blackbody Review

Given the mathematical tools to quantify how light gets to the detector, the source itself must be understood, because without the source, there is no reflectance to measure. The source itself is very important when measuring a BRDF correctly. The BRDF is also directly related to emissivity through Kirchhoff's conservation of energy. Thus, a quick look at blackbody radiation and emissivity will be helpful.

1.4.1 Blackbody Radiance.

A blackbody source emits radiation at the theoretical maximum and is a function of the source temperature and emitted wavelength. The expression for the Joule radiance of a blackbody source is,

$$L_e(\lambda, T) = \frac{2hc^2}{\lambda^5 (e^{hc/\lambda kT} - 1)} \left[\frac{W}{cm^2 - sr - \mu m} \right],$$ (62)

and for the radiance in terms of energy simply divide by hc/λ, the energy of a photon,

$$L_q(\lambda, T) = \frac{2c}{\lambda^4(e^{hc/\lambda kT} - 1)} \left[\frac{photons/sec}{cm^2 - sr - \mu m} \right].$$

(63)

The photon radiance becomes important when describing the detector's response to some source.
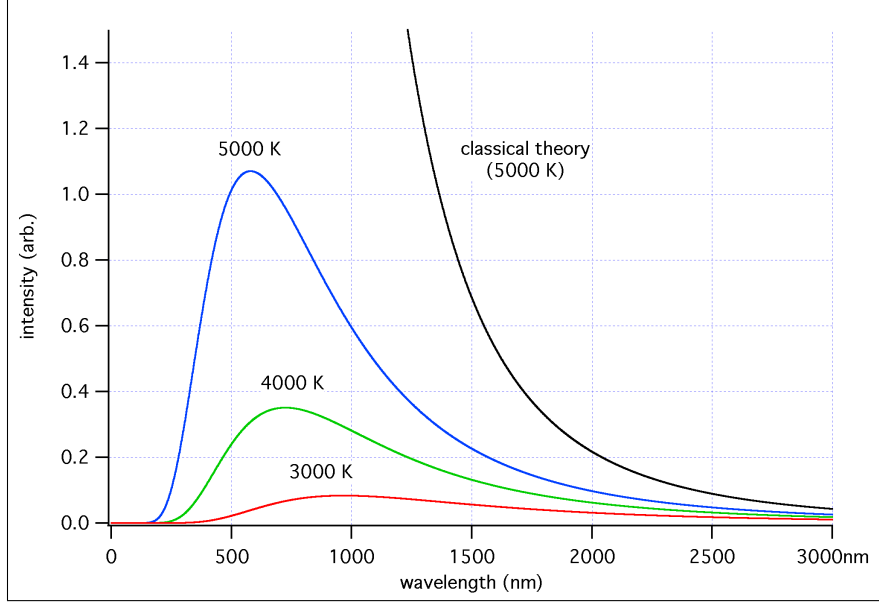
Figure 105. An example of blackbody curves at three different temperatures.

One must remember that the radiance is a function of wavelength and temperature. When it is measured, it is typically integrated over some band by the detector, but not necessarily, which is why it has not been a function of wavelength until now. This is done by integrating the radiance over a band of interest,

$$L_e(T) = \int_{\lambda_1}^{\lambda_2} \frac{2hc^2}{\lambda^5(e^{hc/\lambda kT} - 1)} d\lambda \left[\frac{W}{cm^2 - sr} \right],$$

(64)

or for photon radiance,

$$L_q(T) = \int_{\lambda_1}^{\lambda_2} \frac{2c}{\lambda^4(e^{hc/\lambda kT} - 1)} d\lambda \left[\frac{photons/sec}{cm^2 - sr}\right]. \tag{65}$$

Exitance is a more practical measurement of the source radiance. Therefore, it is a natural extension to define a Lambertian radiance, L_e, relative to the exitance, M_e, of the source,

$$M_e = \int L_e cos\theta_s d\Omega_s \tag{66}$$

$$= L_e \int_0^{2\pi} \int_0^{\pi/2} cos\theta_s cos\theta_s d\theta_s d\phi \tag{67}$$

$$= \pi L_e, \tag{68}$$

This is a key relationship that will often prove handy in deriving radiometric expressions when the source is Lambertian.

In the case where $\lambda_1 = 0$ and $\lambda_2 = \infty$, one can use the relationship between radiance and exitance to obtain the expression for total emitted Joule exitance and reduce it to

$$M_e(T) = \sigma_e T^4 \left[\frac{W}{cm^2 - sr}\right], \tag{69}$$

and total emitted photon exitance can be reduced to

$$M_q(T) = \sigma_q T^3 \left[\frac{photons/sec}{cm^2 - sr}\right]. \tag{70}$$

where $\sigma_e = 5.6704 \times 10^{-12}$ $[W - cm^{-2} - K^{-4}]$ and $\sigma_q = 1.52047 \times 10^{11}$ $[photons - sec^{-1} - cm^{-2} - K^{-3}]$. In this reduction, σ is referred to as the Stefan-Boltzmann constant[42]. Another useful expression is Wein's Displacement Law, where the peak

emission for Joule spectral radiance is given by,

$$\lambda_{max} = \frac{2898 \ (\mu m - K)}{T \ (K)}, \tag{71}$$

and for photon spectral radiance it is

$$\lambda_{max} = \frac{3662 \ (\mu m - K)}{T \ (K)}. \tag{72}$$

They are different because of the extra λ term in the energy expression.

1.4.2 Emissivity and Energy Conservation.

Next, emissivity will be examined as it relates to actual sources and not just blackbodies. This is where blackbody radiation and emissivity become important for the BRDF and accurate scene modeling, especially in the infrared, IR, band.

In reality, few sources will produce the theoretical maximum radiation. To account for this, the emissivity term, ϵ, is introduced. This dimensionless quantity that is always less than or equal to 1 relates the actual radiance to the black body radiance. The emissivity of a blackbody is 1. There are also two other types of sources, a graybody and a selective radiator.

When $\epsilon < 1$ and is a constant, we call the source a graybody, but often this is only an approximation to reality within a band of interest. When emissivity is a function of wavelength, $\epsilon(\lambda)$, i.e., not a constant, the source is a selective radiator. For the BRDF, the emissivity may also be directional, $\epsilon(\lambda, \theta, \phi)$, and this plays a direct role in modeling the diffuse portion of a BRDF.

As with any closed system in thermal equilibrium, it must obey the principles of the conservation of energy. Kirchhoff's Law states this mathematically for radiation

as

$$\Phi_{incident} = \Phi_{absorbed} + \Phi_{reflected} + \Phi_{transmitted}, \tag{73}$$

which reads that the flux incident on some boundary in thermal equilibrium must either be absorbed, reflected, or transmitted. The absorptance, α, reflectance, ρ, and transmittance, τ are then defined as,

$$\alpha = \frac{\Phi_{absorbed}}{\Phi_{incident}} \tag{74}$$

$$\rho = \frac{\Phi_{reflected}}{\Phi_{incident}} \tag{75}$$

$$\tau = \frac{\Phi_{transmitted}}{\Phi_{incident}}. \tag{76}$$

Now, Kirchhoff's law becomes,

$$\alpha(\lambda) + \rho(\lambda) + \tau(\lambda) = 1. \tag{77}$$

Notice that the spectral dependence was included to emphasize that this is also a function of wavelength. If the object is in thermal equilibrium and is opaque, $\tau = 0$, and the result is

$$\alpha + \rho = 1. \tag{78}$$

This has two consequences. First the obvious, if light is not being reflected, it is being absorbed. The second less obvious is that if the light is being absorbed, it must also be re-emitted to stay in thermal equilibrium. Therefore, $\alpha(\lambda, T) = \epsilon(\lambda, T)$, and more importantly for us,

$$\epsilon(\lambda, T) + \rho(\lambda, T) = 1. \tag{79}$$

The temperature dependence is included as a reminder that emissivity is often temperature dependent and so too is the reflectivity. Thus, the BRDF, which is a directional

measure of reflectance, is related to the directional emissivity, and this will be shown in the more physical models of the BRDF, such as the Sandford-Robinson model. Now that the basic radiometry has been established for our analysis of the BRDF, the analytical development of the BRDF is the next step.

Appendix B. Deterministic BRDFs

This appendix covers the theory behind deterministic BRDFs. Although this theory is not directly related to this effort, it does relate to the initial motivation behind this research. The initial motivation was to predict a BRDF *a priori*, and then confirm it with measurements. This appendix covers the two major electromagnetic solutions for the scattering from rough surfaces. These two solutions are commonly known as the Kirchoff diffraction theory and Rayleigh-Rice Vector Perturbation Theory. The notation in this appendix is not the same as the rest of the document, so this should be treated as a separate document notationally. Notation will be described as needed.

2.1   Kirchhoff Diffraction Theory

This solution tends to be more rigorous and precise, but as pointed out by Stover [54], fails at large angles of incidence and scatter. This solution also tends to be more mathematically cumbersome. The strength of this theory is that it allows rough surfaces more than Rayleigh-Rice theory does. There have been many versions of this solution to approximate this geometry, most notably those of Beckmann [12]. Throughout this literature search, it has been a common citation amongst those who are pursuing a more analytic BRDF.

The solution depends upon the geometry of interest, but for this presentation, a square aperture will be approximated. This is because typically a sample used for scattering measurements will be a square coupon. The solution is very similar to that of just a square aperture because given that this solution assumes infinite conductivity at the boundary conditions, reciprocity leads to an 'imaging' of the source behind the aperture. This development also assumes 'far-field' conditions. This development is directly from that of Stover's [53], with sometimes slightly different notation.
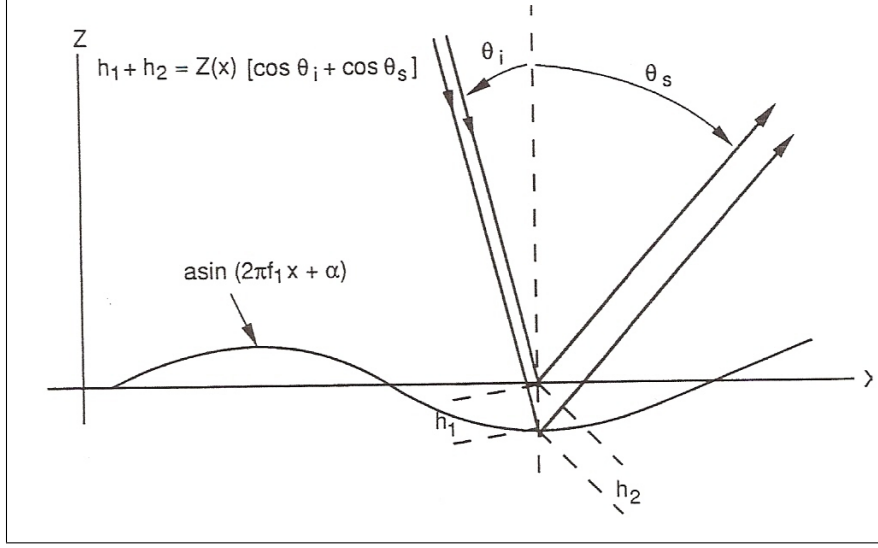
Figure 106. Depiction of the phase modulation by reflection from a rough sinusoidal surface[53].

In Figures 106 and 107, we see diagrams of the phase modulation and aperture, respectively. The phase modulation is derived from the geometry of the diagram. The path length difference leading to a phase delay is,

$$\Delta(x) = \frac{2\pi(h_1 + h_2)}{\lambda} = k(cos\theta_i + cos\theta_s)z(x), \tag{80}$$

where $z(x)$ is the function that describes the surface irregularities. Thus, for a sinusoidal grating, $\Delta(x)$ becomes,

$$\Delta(x) = ka(cos\theta_i + cos\theta_s)sin(2\pi f_g x + \alpha), \tag{81}$$

where a is the amplitude of the grating peak, f_g is the spatial frequency of the grating, and α is the initial offset of the grating. The electric field at the aperture, E_a, is the described by,

$$E_a(x, y, 0) = E_o e^{j(kxsin\theta_i + \Delta(x))} rect(x/L) rect(y/L), \tag{82}$$

169
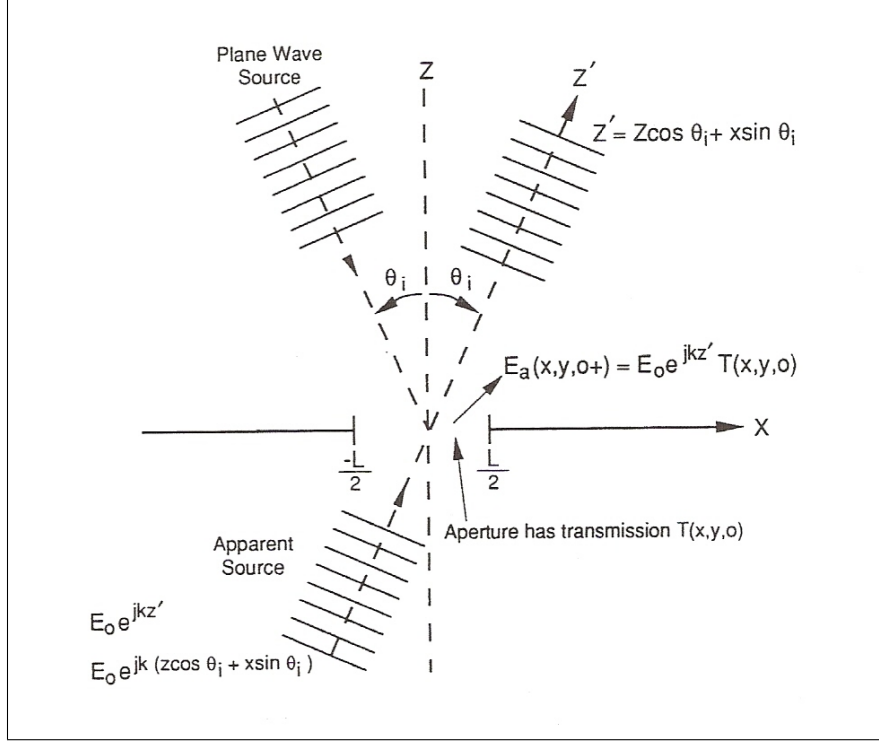
Figure 107. Depiction of the reflection as a aperture in transmission[53].

where E_o is the initial field amplitude. In order to perform the integration, the following identity is used,

$$e^{j\Delta sin\Phi} = \sum_{n=-\infty}^{\infty} J_n(\Delta)e^{jn\Phi},$$ (83)

where J_n is the nth order Bessel function of the first kind, Δ is a constant, and Φ is a variable. The field at the aperture then becomes,

$$E_a(x,y,0) = E_o \sum_{n=-\infty}^{\infty} J_n(\Delta)e^{j(kxsin\theta_i+n2\pi f_g x+n\alpha)}...$$

$$rect(x/L)rect(y/L),$$ (84)

where Δ is the constant portion of $\Delta(x)$.

170

Next, the Franhoffer approximation is used to simplify the radiation integral to find E in the 'far-field' on the plane of observation.

$$E(x_s, y_s) = \frac{cos\theta_s}{j\lambda R} e^{jk[R+(x_s^2+y_s^2)/2R]}...$$
$$\int_{-\infty}^{\infty}\int_{-\infty}^{\infty} E_a(x, y, 0)e^{-j2\pi(f_x x + f_y y)}dxdy, \tag{85}$$

where R is the distance from the aperture to the observation plane. Stover then takes the transform by inspection, and transforms the plane into positions of observation on a sphere. If the result is squared, the field intensity is

$$I(x_s, y_s) = \frac{1}{2\eta_o} \left(\frac{E_o L^2 cos\theta_s}{\lambda R}\right)^2 \sum_{n=-\infty}^{\infty} J_n^2(\Delta)...$$
$$sinc^2 \left[\frac{L}{\lambda}(sin\theta_s cos\phi_s - nf_g\lambda - sin\theta_i)\right]...$$
$$sinc^2 \left(\frac{L}{\lambda}sin\theta_s sin\phi_s\right). \tag{86}$$

where $I(x_s, y_s)$ is the electric field intensity power per unit area and η_o is free space permittivity. In order to convert these to a BRDF, the relationship from Lee's PhD thesis can be applied[39]. This relationship is,

$$f_r = \frac{r^2 \langle I_r \rangle}{|E_i|^2 l^2 cos\theta_i cos\theta_r} \tag{87}$$

where r is the distance to the observer and l is the dimension of one side of a square.

If small scattering angles are used, this result can be reduced to the first-order grating efficiency equation. Thus, these results agree with practice, but only for angles near normal incidence. That is where the approximations of this theory are valid. Thus, this is a rigorous formulation, but it can be very restrictive.

Another notable contribution to this theory not presented here has been provided

by Beckmann [12]. This derivation is called classical Beckmann-Kirchhoff Theory. This is where a tangent plane assumption is made, and this allows the solution to be more accurate than Kirchhoff theory alone at larger angles of incidence.

2.2 Rayleigh-Rice Vector Perturbation Theory

This theory is most accurate for surfaces where the surface variation is much smaller than a wavelength and has a Gaussian distribution. These are normally considered optically smooth surfaces. As noted by Stover, this has been the defacto standard in surface scatter theory in optics and radar since its formulation.

There are few papers that covers the development of this theory. Although most, if not all, papers on the subject have some treatment of Kirchhoff diffraction theory, none pay more than a cite to Rice for its development. As its development was beyond the scope of Stover's scattering 'bible', it will also be presented this way for this research. Nevertheless, a good overview of Vector Perturbation Theory (VPT) is given by Elson in his paper on multilayer optics[23].

Rayleigh-Rice vector perturbation theory gives a resulting equation for the BRDF as,

$$\frac{(dP/d\Omega_s)d\Omega_s}{P_i} = \left(\frac{16\pi^2}{\lambda^4}\right) \; cos(\theta_i) \; cos^2(\theta_s) \; Q \; S(f_x, f_y) \; d\Omega_s, \tag{88}$$

where Q is the Mueller matrix that handles polarization, $S(f_x, f_y)$ is the power spectral density of the reflecting surface, and $d\Omega_s = sin\theta_s d\phi_s d\theta_s$. As noted in Stover [53], it is the same as the cosine corrected BRDF, except that a $d\Omega_s$ has been added to each side and the difference of $(2\pi)^2$ is the result of expressing f_x and f_y as spatial cycles per unit length rather than spatial radians per unit length. The term f_x is

$$f_x = \frac{sin\theta_s cos\phi_s - sin\theta_i}{\lambda}, \tag{89}$$

172

and f_y is

$$f_x = \frac{sin\theta_s sin\phi_s}{\lambda},$$ (90)

when projected onto a hemispherical surface.

The last bit of knowledge to be presented with this theory is the smooth surface limit, which limits it's application. Although there is not a hard and fast limit where results immediately break down, Stover presents this limit as,

$$\left(\frac{4\pi\sigma cos\theta_i}{\lambda}\right)^2 \ll 1,$$ (91)

where σ is the RMS deviation of the surface roughness.

2.3 Deterministic BRDF Domains of Validity
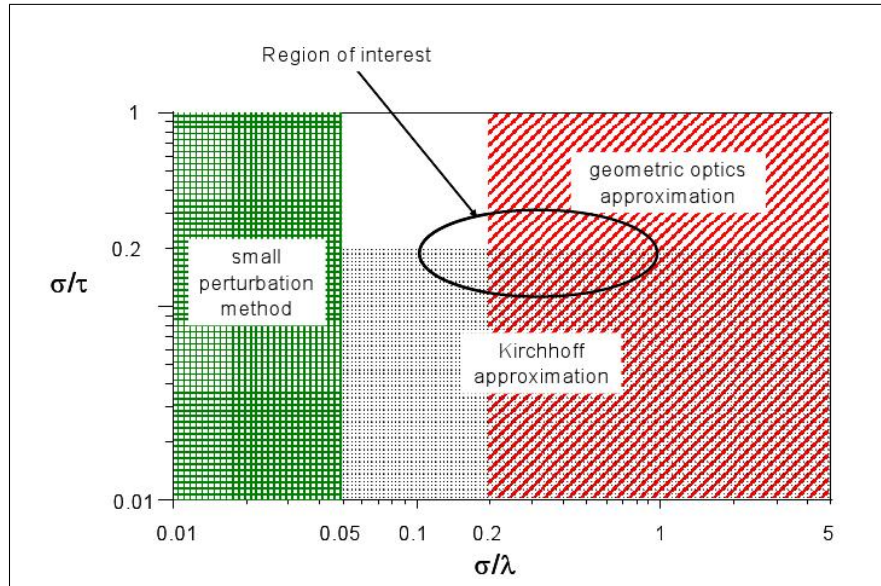
Figure 108. Visual depiction of the domains of validity for different deterministic BRDFs[39].

Lee's PhD thesis presents a nice visualization of where each theory is valid. This is presented in Figure 108, where the small perturbation method is Rayleigh-Rice vector perturbation theory. A newly published method by Stover, et al., presents a unified

173

theory that combines the Kirchoff-Beckman solution and VPT that is applicable and accurate in the domain that either theory is valid[54]. Although these methods do not apply to this study, they are still valid within certain limitations.

Bibliography

[1] "ASTM E1392-96(2002) Standard Practice for Angle Resolved Optical Scatter Measurements on Specular or Diffuse Surfaces (Withdrawn 2003)". URL `http://www.astm.org/DATABASE.CART/WITHDRAWN/E1392.htm`.

[2] "Engauge Digitizer". URL `http://digitizer.sourceforge.net/`.

[3] "Simulation Technologies, Inc." URL `http://www.simtechinc.com/main.html`.

[4] "Spectralon Diffuse Reflectance Standards".

[5] "CASI® Product Literature". November 1998. URL `http://www.schmitt-ind.com/pdf/casi.pdf`.

[6] "Schmitt Measurement Services", 2008. URL `http://www.schmitt-ind.com/products-services-measurement-services.shtml`.

[7] "RPC Photonics Website", February 2009. URL `http://www.rpcphotonics.com/`.

[8] Alexander, C. and D. Flynn. "Polarized surface scattering expressed in terms of a bidirectional reflectance distribution matrix." *Optical Engineering*, volume 34, 1646–1650. June 1995.

[9] Bailey, A. W., E. A. Early, K. S. Keppler, G. Megaloudis, V. I. Villavicencio, and J.J. Zohner. *Dynamic Bidirectional Reflectance Distribution Function Testing and Modeling.* Technical report, Human Effectiveness Directorate, Directed Energy Bioeffects Division, Optical Radiation Branch, Louis Bauer Dr., Brooks City Base, TX 78235, June 2005.

[10] Balanis, C. A. *Advanced Engineering Electromagnetics*. John Wiley & Sons, 1989. ISBN 0-471-62194-3.

[11] Barnes, P Y, E. A. Early, and A. C. Parr. *Spectral Reflectance*, volume 250-48 of *NIST Special Publication*. National Institute of Standards and Technology, Gaithersburg, MD 20899-001, March 1998.

[12] Beckmann, P. and A. Spizzichino. *The Scattering of Electromagnetic Waves From Rough Surfaces*. The Artech House Radar Library. Artech House, Inc., 685 Canton Street, Norwood, MA 02062, 1987. ISBN 0-89006-238-2.

[13] Blinn, J. F. "Models of light reflection for computer synthesized pictures". *Proceedings of the 4th annual conference on computer graphics and interactive techniques*, 196–198. ACM Press, 1977.

[14] Brainard, L., W. Lynn, D. Ramer, and W. Shemano. *Optical Measurements Facility - Final Report*. Technical report, Materials Directorate, Air Force Research Laboratory, Air Force Material Command, 1999.

[15] Byrnes, J. *Unexploded Ordnance Detection and Mitigation*. Springer, 2009. ISBN 9781402092527.

[16] Choquette, S. J., D. L. Duewer, L. M. Hanssen, and E. A. Early. "Standard Reference Material 2036 Near-Infrared Reection Wavelength Standard". *Applied Spectroscopy*, volume 59. Society for Applied Spectrocopy, 2005.

[17] Cook, R. L. and K. E. Torrance. "A reectance model for computer graphics". *Proceedings of the 8th annual conference on Computer graphics and interactive techniques*, 307–316. ACM Press, 1981.

[18] Courreges-Lacoste, G. B., J. G. Schaarsberg, R. Sprik, and S. Delwart. "Modeling of Spectralon diffusers for radiometric calibration in remote sensing". *Optical Engineering*, volume 42, 3600–3607. SPIE, December 2003.

[19] Dereniak, E. L. and G. D. Boreman. *Infrared Detectors and Systems*. Wiley series in pure and applied optics. John Wiley & Sons, Inc., New York, 1996. ISBN 0-471-12209-2.

[20] Dodge, Y. *The Oxford Dictionary of Stastical Terms*. Oxford University Press, 2003. ISBN 0-19-920613-9.

[21] Duer, A. "On the ward model for global illumination". Submitted for review, September 2004.

[22] Early, E. A., P Y Barnes, B C Johnson, J J Butler, C J Bruegge, S F Biggar, P R Spyak, and M M Pavlov. "Bidirectional Reflectance Round-Robin in Support of the Earth Observing System Program". *Journal of Atmospheric and Oceanic Technology*, volume 17, 1077–1091. American Meteorological Society, August 2000.

[23] Elson, J. M. "Multilayer-coated optics: guided-wave coupling and scattering by means of interface random roughness". *Journal of the Optical Society of America*, volume 4, 729–742. Optical Society of America, April 1995.

[24] Ferraro, V. C. A. *Electromagnetic Theory*. FerAthlone Press, University of London, 1962.

[25] Georgiev, Georgi T. and James J. Butler. "Long-term comparison of spectralon BRDF measurements in the ultraviolet". volume 5542, 323–333. SPIE, 2004. URL http://link.aip.org/link/?PSI/5542/323/1.

176

[26] Haner, D. A., B. T. McGuckin, and C J Bruegge. "Polarization Characteristics of Spectralon Illuminated by Coherent Light". *IEEE Transactions on Geoscience and Remote Sensing*. February 1999.

[27] Hanssen, L. M. "Parameters for an infrared diffuse reflectance standard". *Optical Engineering*, 32(4):877–879, April 1993.

[28] Hanssen, L. M. "Integrating-sphere system and method for absolute measurement of transmittance, reflectance, and absorptance of specular samples." *Applied Optics*, volume 40, 3196–3204. Optical Society of America, July 2001.

[29] Hanssen, L. M. and S. G. Kaplan. "Infrared diffuse reflectance instrumentation and standards at NIST". *Analytica Chimica Acta*, volume 380, 289–302. 1999.

[30] Hanssen, L. M. and B. Wilthan. "Results of a NIST-led Inter-laboratory Comparison of Infrared Reflectance", 2008. Conference Presentation.

[31] Harkiss, H. I. *A Study of Bi-Directional Reflectance Distribution Functions and Their Effect on Infrared Signature Models*. Master's thesis, Air Force Institute of Technology, March 2007.

[32] He, X. D., Torrance K.E., F. X. Sillion, and D. P. Greenberg. "A comprehensive physical model for light reflection". *Proceedings of the 18th annual conference on Computer graphics and interactive techniques*, 175–186. ACM Press, 1991.

[33] Hecht, E. *Optics*. Pearson Education, Inc., 1301 Sansome St., San Francisco, CA, 4th edition, 2002. ISBN 0-8053-8566-5.

[34] Jin, G., D. H. Kim, J. Hahn, and D. S. Fraedrich. "Infrared ship signature prediction using measured BRDF data and global illumination rendering".

[35] Kaplan, S. G. and L. M. Hanssen. "Silicon as a standard material for infrared reectance and transmittance from 2 to 5 microns". *Infrared Physics and Technology*, volume 43, 389–396. 2002.

[36] Klicker, K. A., J. C. Stover, D. R. Cheever, and F. M. Cady. "Design review of a unique complete angle-scatter instrument (CASI)". volume 818. SPIE, 1987.

[37] L., Miller J. "Multispectral infrared BRDF forward-scatter measurements of common black surface preparations and materials".

[38] Lamott, R. *Analysis and Application of the Bi-directional Reflectance Distribution Function of Photonic Crystals*. Master's thesis, AFIT, March 2009.

[39] Lee, H. *Radiative Properties of Silicon Wafers with Microroughness and Thin-Film Coatings*. Ph.D. thesis, Georgia Institute of Technology, August 2006.

[40] Leonard, T. "BRDF Round Robin Test of ASTM E1392". *Optical Scattering*, 285–293. SPIE, 1995.

[41] Maga, D. *AFIT Reflectance Lab Procedures*. Dept. of Engineering Physics, 2950 Hobson Way, WPAFB, OH 45431, 1 ed. edition, September 2008.

[42] Marciniak, M. "OENG 650: Radiometry and Detection", January 2008. Course Notes.

[43] Marciniak, M. "OENG 780: Infrared Technology", March 2008. Course Notes.

[44] Maxwell, J. R., J. J. Beard, Weiner S., D. Ladd, and S. Ladd. *Bidirectional reectance model validation and utilization*. Technical Report AFAL-TR-73-303, Environmental Research Institute of Michigan (ERIM), March 1973.

[45] N/A. *A Guide to Reflectance Coatings and Materials*. Technical report, Labsphere, January 2009.

[46] Nayar, S. K. and M. Oren. "Generalization of the Lambertian Model and Implications for Machine Vision". *International Journal on Computer Vision*, volume 14, 227–251. April 1995.

[47] Ngan, W. *Acquisition and Modeling of Material Appearance*. Ph.D. thesis, MIT, 2006.

[48] Nicodemus, F. E., J. C. Richmond, T. Limperis, I. W. Ginsberg, and J. J. Hsia. *Geometrical considerations and nomenclature for reflectance*. National Bureau of Standards, Wash. D.C., 1 ed. edition, October 1977.

[49] Sandford, B. and L. Robertson. "Infrared reectance properties of aircraft paint." *IRIS Targets, Backgrounds and Discrimination*. 1985.

[50] Schlick, C. "An Inexpensive BRDF Model for Physically-based Rendering". *Computer Graphics Forum*, volume 13, 233–246. 1994.

[51] Schmitt Measurement Systems. *SMS Scatterometer Hardware Reference Manual*, June 2007.

[52] Shell, J. R. "Bidirectional Reflectance: An Overview with Remote Sensing Applications & Measurement Recommendations". Rochester, New York, May 2004.

[53] Stover, J. C. *Optical Scattering: Measurement and Analysis*. The International Society for Optical Engineering, Bellingham, Washington, 2 edition, 1995. ISBN 0-8194-1934-6.

[54] Stover, J. C., J. E. Harvey, and A. Krywonos. "Unified Scatter model for Rough Surfaces at Large Incident and Scatter Angles". *Advanced Characterization Techniques for Optics, Semiconductors, and Nanotechnologies III*, volume 6672. The International Society for Optical Engineering, August 2007.

[55] Sun, B., K. Sunkavalli, R. Ramamoorthi, P. Belhumeur, and S. K. Nayar. "Time-Varying BRDFs". *Eurographics Workshop on Natural Phenomena.* The Eurographics Association, June 2006.

[56] Sun, Y. *Analytic Framework for Calculating BRDFs of Randomly Rough Surfaces.* Technical report, Purdue University, W. Lafayette, IN, May 2006.

[57] Torrance, K. E. and H. Li. "Background Data for Validation of the He-Torrance Model", April 2005. TR-PCG-05-02.

[58] Ward, G. J. "Measuring and modeling anisotropic reection". *G. J. In Proceedings of the 19th annual conference on Computer graphics and interactive techniques,* 265–272. ACM Press, 1992.

[59] Weidner, V. R. and J. J. Hsia. "Reflection properties of pressed polytetrafluoroethylene powder". *Journal of the Optical Society of America,* volume 71, 856–861. July 1981.

[60] Weidner, V. R., J. J. Hsia, and B. Adams. "Laboratory intercomparison study of pressed polytetrafluoro ethylene powder reflectance standards". *Optical Society of America,* volume 24 of *Applied Optics,* 2225. July 1985.

REPORT DOCUMENTATION PAGE

Form Approved
OMB No. 0704–0188

1. REPORT DATE *(DD–MM–YYYY)*	2. REPORT TYPE	3. DATES COVERED *(From — To)*
26–03–2009	Master's Thesis	June 2008 — Mar 2009

4. TITLE AND SUBTITLE

A Comparative Study of the
Bidirectional Reflectance Distribution Function
of Several Surfaces as a Mid-wave Infrared
Diffuse Reflectance Standard

5a. CONTRACT NUMBER

Proposal ID 2007-162, JON# 09-317

5b. GRANT NUMBER

5c. PROGRAM ELEMENT NUMBER

6. AUTHOR(S)

Bradley Balling, Capt, USAF

5d. PROJECT NUMBER

5e. TASK NUMBER

5f. WORK UNIT NUMBER

7. PERFORMING ORGANIZATION NAME(S) AND ADDRESS(ES)

Air Force Institute of Technology
Graduate School of Engineering and Management (AFIT/EN)
2950 Hobson Way
WPAFB OH 45433-7765

8. PERFORMING ORGANIZATION REPORT NUMBER

AFIT/GE/ENP/09-M01

9. SPONSORING / MONITORING AGENCY NAME(S) AND ADDRESS(ES)

AFRL/RYS (Jeffery Burks)
2591 K St., Bldg 254
Wright-Patterson AFB, OH 45433
(937)-785-9205 (jeffery.burks@wpafb.af.mil)

10. SPONSOR/MONITOR'S ACRONYM(S)

11. SPONSOR/MONITOR'S REPORT NUMBER(S)

12. DISTRIBUTION / AVAILABILITY STATEMENT

APPROVED FOR PUBLIC RELEASE; DISTRIBUTION IS UNLIMITED.

13. SUPPLEMENTARY NOTES

14. ABSTRACT

The Bi-Directional Reflectance Distribution Function (BRDF) has a well defined diffuse measurement standard in the ultraviolet, visible, and near infrared (NIR), Spectralon. It is predictable, stable, repeatable, and has low surface variation because it is a bulk scatterer. In the mid-wave IR (MWIR) and long-wave IR (LWIR), there is not such a well-defined standard. There are well-defined directional hemispherical reflectance (DHR) standards, but the process of integrating BRDF measurements into DHR for the purpose of calibration is problematic, at best. Direct BRDF measurement standards are needed. This study use current calibration techniques to ensure valid measurements and then systematically investigates the BRDF and its variation for eight potential MWIR diffuse BRDF standards. Diffuseness, repeatability, and reflectance are all considered as required parameters necessary for a diffuse MWIR BRDF standard. This document shows comparatively that Spectralon is an excellent candidate for a diffuse MWIR BRDF standard.

15. SUBJECT TERMS

Bi-Directional Reflectance Distribution Function (BRDF), Directional Hemispherical Reflectance (DHR), Mid-Wave IR (MWIR), IR BRDF Standard, Spectralon

16. SECURITY CLASSIFICATION OF:			17. LIMITATION OF ABSTRACT	18. NUMBER OF PAGES	19a. NAME OF RESPONSIBLE PERSON
a. REPORT	b. ABSTRACT	c. THIS PAGE			Dr. Michael Marciniak
U	U	U	UU	198	19b. TELEPHONE NUMBER *(include area code)* (937) 255–3636, ext 4529 (michael.marciniak@afit.edu)

Standard Form 298 (Rev. 8–98)
Prescribed by ANSI Std. Z39.18